The Dissertation Committee for Gopal Robert Yalla certifies that this is the approved version of the following dissertation:

Numerical Discretization Effects in Large Eddy Simulation of Turbulence

Committee:

Robert Moser, Co-Supervisor

Björn Engquist, Co-Supervisor

Omar Ghattas

Patrick Heimbach

Todd Oliver

Karen Willcox

Numerical Discretization Effects in Large Eddy Simulation of Turbulence

by

Gopal Robert Yalla

Dissertation

Presented to the Faculty of the Graduate School
of the University of Texas at Austin
in Partial Fulfillment
of the Requirements
for the Degree of

Doctor of Philosophy

The University of Texas at Austin
May 2022

To my wife, Melissa.

Acknowledgments

The journey through graduate school is often a turbulent one. Fortunately, I have all my family, friends and colleagues to thank for their endless support throughout this endeavor.

I would first like to thank my advisor Robert Moser for his unwavering guidance and mentorship over the years. For always challenging my ideas and encouraging me to push them further, and of course for teaching me to leave no stone unturned. You have taught me so many lessons that I will carry throughout my career. Thanks are also to my advisor Björn Engquist, especially for all of his advice early in my academic career. Alas, it is only now that I understand your warning about pursuing research in turbulence. I am also grateful to the other members of PECOS: to Todd Oliver for always offering to work through big picture ideas and intricate details alike; to Sigfried Haering for helping me get started in the field of turbulence; and to Prakash Mohan, Bryan Reuter, Teresa Portone, Sean Carney and Clark Pederson for their helpful discussions and continuing friendship. Thanks are also to my other friends from the Oden Institute and beyond, including Samuel Estes, Timothy Smith, Siddhant Wahal, Matthew Mottola, Joseph Testa, Trevor Updike, and numerous others. There are simply too many to name and for that I am grateful. I would also like to thank all of the other teachers and mentors who have inspired me throughout my academic journey, especially the faculty at the College of the Holy Cross including Edward Soares, David Damiano and the rest of the Mathematics and Computer Science Department, and Johnny Guzmán at the Division of Applied Mathematics at Brown University.

Special thanks are to my parents Jamie and Subbarao for their love and support. You have always instilled in me that there is no substitute for hard work and that lesson has guided me throughout my PhD. I am also grateful for my brother Ashok for his constant enthusiasm of my work and for helping me with work-life balance since we were in high school, as well as to my sisters Nina, Minni, and Sapi. Thanks are also to my parents and siblings in law, Linda, Micheal, Kevin, Ryan, Margaret and Lucie for being a constant

source of encouragement, as well as to my grandmothers Dee Dee and Marilynn and to my late grandfather Patrick, from whom I learned to embrace finding a fix for every new problem.

Most importantly I am forever thankful for the love and devotion of my wife Melissa. The work reflected in this thesis was only made possible through your unending support and compassion. You have been by my side since college and contributed so much to my efforts in graduate school. I am truly grateful for your love. And of course, you would not forgive me if I did not thank our golden retriever, Westley, who patiently sat at my feet while I wrote this thesis.

This work was made possible through the generous financial support from the National Aeronautics and Space Administration (cooperative agreement number NNX15AU40A), the National Science Foundation (project number 1904826), the U.S. Department of Energy, Exascale Computing Project (subcontract number XFC-7-70022-01 from contract number DE-AC36-08GO28308 with the National Renewable Energy Laboratory), and the CSEM fellowship from the Oden Institute for Computational Engineering and Sciences. Thanks are also due to the Texas Advanced Computing Center at The University of Texas at Austin for providing HPC resources that have contributed to the research results reported here, and to the entire sysnet team and administrative staff who are the true pillars of the Oden Institute.

Numerical Discretization Effects in Large Eddy Simulation of Turbulence

by

Gopal Robert Yalla, Ph.D.

The University of Texas at Austin, 2022

SUPERVISORS: Robert Moser and Björn Engquist

Large eddy simulation (LES) is now over half a century old and while it has become more widely used as computational capabilities have expanded, its adoption as an engineering tool has arguably been limited by the shortcomings of subgrid models. Most current subgrid models are formulated under the assumption that the subgrid scales are approximately isotropic, and that other complications, such as numerical discretization and inhomogeneous resolution, are negligible. This limits the fidelity of the models when applied in complex flows. For LES to become a robust engineering tool, subgrid models applicable to more complex scenarios will be required. In particular, the effects of numerical discretization must be considered.

In this thesis we develop several analytical and computational tools for identifying the characteristics of an LES introduced by numerical discretization and filtering. First, the effects of numerical dispersion error on the turbulent energy cascade are explored. It is shown that dispersion error due to convection by a large mean velocity causes a decoherence of the phase relationship among interacting Fourier modes, resulting in a reduction of the energy transfer rate from large to small scales. Nonlinear dispersion error due to convection from turbulent fluctuations is also explored through the development of an eddy-damped quasi-normal markovian (EDQNM) type of analysis that is applicable to the filtered turbulence in an LES. EDQNM is shown to be a useful tool for exploring dispersion effects because it exposes the relaxation rate of the third-order velocity correlations. An explicit filtering formulation based on the properties of the underlying numerics is developed to remove the

highly dispersive wavemodes in an LES. Further, the EDQNM LES theory is also used to determine the a priori properties of the subgrid stress needed to recover an inertial range spectrum in the presence of non-spectral numerics and non-cutoff explicit filters.

Second, the convection of turbulence through nonuniform grids is explored. This introduces additional challenges due to so-called commutation error, or neglect of the commutator of the filtering and differentiation operators. We employ a multiscale asymptotic analysis to investigate the characteristics of the commutator. Further, we show how commutation error manifests in simulation and demonstrate its impact on the convection of homogeneous isotropic turbulence through a coarsening grid. A connection is made between the commutation error and the propagation properties of the underlying numerics. A framework for modeling this commutator is proposed that accounts for properties of the discretization. The forcing of turbulence convecting through a refining grid is also explored and a formulation based on divergence-free wavelets is proposed. Results in isotropic turbulence suggest this formulation may be effective at energizing newly resolvable scales and therefore allowing for sharper grid transitions to finer resolved regions.

There are several additional challenges to formulating more broadly applicable subgrid models for LES and we expect that the techniques developed here will also be useful for addressing these wide range of issues.

Contents

Chapter 1

Introduction

The on-going study of turbulence modeling may seem peculiar at first because the equations governing the dynamics of this phenomenon have been known for over a century. These are the celebrated Navier-Stokes equations, which for incompressible flows read

$$\frac{\partial u_i}{\partial t} + \frac{\partial u_i u_j}{\partial x_j} = -\frac{\partial p}{\partial x_i} + \nu \frac{\partial^2 u_i}{\partial x_j \partial x_j} \tag{1.1}$$

$$\frac{\partial u_i}{\partial x_i} = 0, \tag{1.2}$$

where $\mathbf{u}$ is the velocity field, p is the pressure and ν is the kinematic viscosity. So why does the mention of turbulence harbor such feelings of hopelessness, even among histories brightest scientists[1]? To add my own foreboding quote, the devil is quite literally in the details when it comes to turbulence, so perhaps Lamb and Heisenberg should be looking elsewhere for their answers. Several fields of research spanning multiple disciplines are dedicated to understanding the complexities of turbulence and extracting meaningful information from equations (1.1) and (1.2) in the context of a variety of fluid dynamics systems.

This immense research effort is for good reason. Famously dubbed "the most important

[1]Both Horace Lamb and (allegedly) Werner Heisenberg expressed doubt about understanding turbulence even in the heavens. Lamb famously stated, "I am an old man now, and when I die and go to heaven there are two matters on which I hope for enlightenment. One is quantum electrodynamics, and the other is the turbulent motion of fluids. And about the former I am rather optimistic." Similarly, when asked what he would ask God given the opportunity, Heisenberg is said to have replied, "When I meet God, I am going to ask him two questions: Why relativity? And why turbulence? I really believe he will have an answer for the first." Indeed, of these problems, turbulence remains the one unsolved.

unsolved problem of classical physics" by Richard Feynman[2], the importance of turbulence cannot be overstated. This is generally because the flow of fluids in a wide variety of settings (from astrophysical flows, to atmospheric flows, to technological flows, etc.) is often accompanied by turbulence. Best defined through its characteristics, turbulence has a large effect on the high Reynolds number (Re) flows in which it occurs. It greatly enhances mixing and transport, tends to dissipate energy, is composed of a wide range of interacting scales, and is intrinsically chaotic in nature. Therefore, as Moser et al. [1] write, when predicting the evolution of a fluid system (e.g. the earth's atmosphere) or when designing a fluid dynamic system (e.g. an aircraft), it is critical to account for the effects of turbulence. As such, the modeling of turbulent flows has been of primary interest in the study of turbulence since Reynolds [2] identified it as a distinct fluid dynamic phenomenon.

However, the reliable prediction of the effects of turbulence in the flows of most interest remains elusive, and this inability is a significant hindrance to progress in a number of important fields. To see why, consider the approach of simulating equations (1.1) and (1.2) by resolving all relevant length scales and time scales with appropriate boundary and initial conditions, for a single realization of some flow. This is a technique known as Direct Numerical Simulation (DNS). For isotropic turbulence, the total computational complexity of a DNS scales as Re^3, where Re is based on the root-mean-square velocity and integral length scale. As a consequence, the cost of a DNS grows too rapidly with Reynolds number to be computationally feasible for technologically relevant Re.

It is tempting to think that the computational challenge of DNS is a failing of current computing power. However, even with an optimistic projection of the continuing growth in computing power and reduction in computing costs, it will be many decades or even centuries until DNS can be used as a routine tool of fluids engineering. Moreover, the vast majority of computational effort in a DNS is dedicated to resolving the dissipation range,

[2]Ironically it is Feynman who is credited with addressing Lamb's question on quantum electrodynamics.

although the turbulent energy and anisotropy predominantly reside in the larger scales of motion. Moreover, accurately computing statistical properties of a given flow, such as the mean velocity, is usually sufficient for determining most quantities of interests in engineering applications. This objective motivates the use of cheaper computational methods whose goal is only to compute flow statistics.

Decomposition of the velocity field u_i into its mean and fluctuating components as $u_i = \langle u_i \rangle + u_i'$ is referred to as the Reynolds decomposition. Applying the Reynolds decomposition to equations (1.1) and (1.2) and averaging yields the Reynolds Averaged Navier-Stokes (RANS) equations:

$$\frac{\partial \langle u_i \rangle}{\partial t} + \frac{\partial \langle u_j \rangle \langle u_i \rangle}{\partial x_j} = -\frac{\partial \langle p \rangle}{\partial x_i} + \nu \frac{\partial^2 \langle u_i \rangle}{\partial x_j \partial x_j} - \frac{\partial \langle u_j' u_i' \rangle}{\partial x_j} \tag{1.3}$$

$$\frac{\partial \langle u_i \rangle}{\partial x_i} = 0. \tag{1.4}$$

The RANS equations describe the mean velocity field; however, the equations are unclosed due to the last term in equation (1.3), namely the Reynolds stress tensor $\langle u_j' u_i' \rangle$. This term represents an additional mean momentum flux due to the velocity fluctuations. Several models have been proposed for the Reynolds stress tensor, including eddy viscosity models and Reynolds stress transport models. Different choices of eddy viscosity lead to different RANS models, such as the widely used k-ε model [3, 4] the Spalart-Allmaras model [5, 6], and the v^2-f model [7].

Although simulating only the slowly evolving mean flow is within current computational capabilities, RANS suffers from several inadequacies [8, 9, 10]. RANS is particularly insufficient as a model for particular flow features such as unsteady or smooth wall separation [11]. The inadequacies of current RANS models may stem from trying to capture information about turbulent fluctuations using only averaged quantities; however, it is not clear whether

this a fundamental problem with RANS or just a failing of current RANS models.

Since its inception in meteorological modeling in the early 1960's [12, 13], large eddy simulation (LES) of turbulence has held promise as a potentially practical technique to model turbulent flows, addressing the deficiencies of both DNS and RANS. LES is expected to be more reliable than RANS models commonly used in engineering while being orders of magnitude less expensive to compute than DNS, which, as stated above, is widely considered to be highly reliable, but computationally intractable in most applications. In large eddy simulation, one seeks to numerically represent the dynamics of the large scales of motion while modeling the effects of the unrepresented small scales. The rationale for this approach is that the largest scales in any turbulent flow are peculiar to the particulars of the flow and simulating their dynamics avoids the necessity of modeling their effects as in RANS. On the other hand, provided the Reynolds number is sufficiently high, the turbulent fluctuations are expected to become statistically isotropic and therefore universal, as the scale of the fluctuations decreases. Modeling the effects of these small scales should therefore be significantly easier than modeling the large scales, and one might therefore expect such "subgrid scale" (SGS) models to be universally applicable [1].

Unlike the equations for DNS and RANS above, properly formulating the equations for LES has been a complication in the field since its establishment. The difficulty seems to stem from the disconnect between the theoretical foundations of LES and practical considerations. Consequently, this has led to much confusion in the LES literature particularly with how the represented large scales and subgrid scales are defined. As we aim to demonstrate in this thesis, being explicit about the practical considerations of LES is critically important for properly representing the effects of turbulence in flows of interest. In the following section we therefore present a formulation of LES proposed by Moser, Haering, and Yalla [1] for this purpose, which is also general enough to subsume several commonly used LES formulations.

1.1 LES formulation

The fundamental idea of large eddy simulation is simple, that the large scales of turbulence dominate its effect on the mean flow while their effects are more difficult to model than the small scales. So, directly simulating the large scales while modeling the effects of the small scales should be an effective strategy for modeling turbulence. However, there are a number of subtleties to the formulation of an LES that are addressed below. Similar considerations are discussed in Pope [14].

In formulating an LES, one must first define the large scales that are to be simulated. This is accomplished by defining a linear operator $\mathcal{F}$ that maps turbulent fields $\mathbf{u}(\mathbf{x}, t)$ to large-scale (LES) fields $\overline{\mathbf{u}}(\mathbf{x}, t)$. This operator is called the filter, and is commonly written

$$\overline{\mathbf{u}}(\mathbf{x}, t) = \mathcal{F}(\mathbf{u}) = \int_{\mathcal{D}} G(\mathbf{x}, \mathbf{x}')\mathbf{u}(\mathbf{x}', t)\, d\mathbf{x}', \tag{1.5}$$

where $\mathcal{D}$ is the flow domain being simulated and G is the filter kernel. If $\mathcal{F}$ is shift invariant, that is, if it commutes with spatial shift operators with arbitrary shifts, then the filter is homogeneous and the kernel is given by $G(\mathbf{x}, \mathbf{x}') = \tilde{G}(\mathbf{x}-\mathbf{x}')$. The filter is intended to isolate the large scales of turbulent motion, so it should be smoothing; further it must define what information regarding the turbulent field $\mathbf{u}$ is retained in the filtered field $\overline{\mathbf{u}}$. To formulate an LES, an evolution equation for filtered fields will be determined which will be solved numerically. A numerical solution must have a finite-dimensional state space to be solved on a computer, so if the range of $\mathcal{F}$ is infinite dimensional, further discretization will be required, which will project the solution to a finite dimensional space. In this case, it is clearly the operator $\mathcal{F}$ along with the projection that defines the retained information regarding the turbulent field. Thus, to ensure that $\mathcal{F}$ defines the information available in the LES field, it is formulated here to include any required discretization or projection (commonly referred

to as the implicit filter), so that the range of $\mathcal{F}$ is the finite dimensional space of the LES [15, 16].

For ease of notation, a filtered quantity will be designated with an overbar, the expected value with $\langle\cdot\rangle$ as in the RANS equations, and resolved and unresolved fluctuations with $\cdot^>$ and $\cdot^<$, respectively. Accordingly, a filtered velocity is given by $\overline{\mathbf{u}} = \mathcal{F}(\mathbf{u})$ where $\mathbf{u}$ is the velocity field of a real turbulence. Further $\langle\mathbf{u}\rangle = \langle\overline{\mathbf{u}}\rangle$ is the mean velocity, $\mathbf{u}^> = \overline{\mathbf{u}} - \langle\overline{\mathbf{u}}\rangle$ is the resolved fluctuating velocity and $\mathbf{u}^< = \mathbf{u} - \overline{\mathbf{u}}$ is the unresolved fluctuating velocity. The total fluctuating velocity is thus $\mathbf{u}' = \mathbf{u}^> + \mathbf{u}^< = \mathbf{u} - \langle\mathbf{u}\rangle$. A filter is characterized by its filter scale Δ which characterizes the LES resolution. When the resolution is anisotropic, it is characterized by a resolution tensor $\mathcal{M}_{ij}$, which is formally the symmetric part of the Jacobian defining the mapping of a unit cube to a resolution cell [17]. Its eigenvalues are the resolution scales in the directions defined by its eigenvectors.

Applying the filter operator to equations (1.1) and (1.2) yields the filtered (incompressible) Navier-Stokes equations:

$$\frac{\partial\overline{u}_i}{\partial t} + \overline{\frac{\partial u_i u_j}{\partial x_j}} = -\overline{\frac{\partial p}{\partial x_i}} + \nu\overline{\frac{\partial^2 u_i}{\partial x_j \partial x_j}} \tag{1.6}$$

$$\overline{\frac{\partial u_i}{\partial x_i}} = 0. \tag{1.7}$$

Note that $\mathcal{F}$ commutes with time differentiation, because it is a spatial filter, but does not in generally commute with spatial differentiation. This leaves all the remaining terms to be modeled. However, if $\mathcal{F}$ is homogeneous (shift-invariant), then it commutes with differentiation, simplifying the above equations to the Navier-Stokes equations applied to $\overline{\mathbf{u}}$, with the exception of the nonlinear term $\partial_j\overline{u_i u_j}$. In this case, $\overline{u_i u_j}$ is the only term that would need to be modeled in an LES. One can write this as $\widetilde{\overline{u}_i\overline{u}_j} - \tau_{ij}$, where $\tilde{\cdot} = \mathcal{F}'(\cdot)$ is a possibly different filter operator mapping $\overline{u}_i\overline{u}_j$ to the LES solution space, and $\tau_{ij} = -\overline{u_i u_j} + \widetilde{\overline{u}_i\overline{u}_j}$ is the subgrid stress. This formulation applies to $\mathcal{F}$ for which the truncation to a finite dimensional

space is a Fourier truncation, such as a Fourier cut-off filter [18] or a homogeneous Gaussian filter composed with a Fourier cutoff. As an example, using a Fourier cut-off filter for both $\mathcal{F}$ and $\mathcal{F}'$ is equivalent to using a dealiased spectral (or Fourier Galerkin) method, while changing $\mathcal{F}'$ to a collocated projection is equivalent to an aliased pseudo-spectral method [19].

In most LES applications, however, a spectral discretization is not used, and $\mathcal{F}$ is not homogeneous. In this case, all terms in equations (1.6) and (1.7), other than the time derivative, need to be modeled. However, $\mathcal{F}$ can be discretely homogeneous; that is, invariant to shifts by integral multiples of $\Delta_\alpha \mathbf{e}_\alpha$ (no summation on Greek indices), where Δ_α is the "grid spacing" in the direction defined by the unit vector $\mathbf{e}_\alpha$. Examples of the $\mathcal{F}$ operator include finite volume, finite element and spline [20, 21] projections defined on uniform grids, as well as these projections composed with homogeneous continuous filters. The filtered spatial derivative terms can then be approximated by applying a discrete derivative operator appropriate to the LES solution space defined by $\mathcal{F}$ (e.g. a finite volume, finite element, or spline derivative approximation). Denote such discrete derivative operators $\delta/\delta x_i$ or δ_i, then for a generic quantity ϕ, $\overline{\partial_i \phi} \approx \delta_i \overline{\phi}$. The error in this approximation is in principle subject to further modeling, and includes two effects: the usual discretization error associated with the numerical derivative δ_i, and the effect of aliasing when the projection in $\mathcal{F}$ is not a Fourier truncation.

When $\mathcal{F}$ is inhomogeneous, usually because it includes a projection onto a nonuniform grid, the effective resolution scale is spatially dependent. This introduces an additional contribution to the commutator $\mathcal{C}_i(\phi) = \overline{\partial_i \phi} - \delta_i \overline{\phi}$, commonly called "commutation error." Ghosal and Moin [22] analyzed the commutation error by introducing a transformation of the spatial domain to a new set of spatial coordinates $\boldsymbol{\xi}$ in which the grid is uniform. This

then allows $\mathcal{C}(\phi)$ to be decomposed as:

$$\mathcal{C}_i(\phi) = \mathcal{C}_i^I(\phi) + \mathcal{C}_i^H(\phi) \qquad \mathcal{C}_i^I(\phi) = \overline{\frac{\partial \phi}{\partial x_i}} - \overline{\frac{\partial \phi}{\partial \xi_j}} \frac{\partial \xi_j}{\partial x_i} \qquad \mathcal{C}_i^H(\phi) = \overline{\frac{\partial \phi}{\partial \xi_j}} \frac{\partial \xi_j}{\partial x_i} - \frac{\delta \overline{\phi}}{\delta x_i}, \tag{1.8}$$

where $\mathcal{C}^I$ and $\mathcal{C}^H$ are the inhomogeneous and homogeneous contributions to the commutator. Generally, the homogeneous part represents the effects of the numerical discretization error in $\delta/\delta x$ and is non-zero even if the resolution is homogeneous. The inhomogeneous part characterizes the effects of the inhomogeneous resolution and is zero when the resolution is homogeneous or $\mathcal{F}$ is discretely homogeneous. Similarly, there is a commutator for the Laplacian in the viscous term $\mathcal{C}^V(\phi) = \overline{\partial_i \partial_i \phi} - \delta_{ii}^2 \overline{\phi}$, where δ_{ii}^2 is an appropriate numerical approximation to the Laplacian. With this, equations (1.6) and (1.7) can be written

$$\frac{\partial \overline{u}_i}{\partial t} + \frac{\delta \widetilde{\overline{u}_i \overline{u}_j}}{\delta x_j} = -\frac{\delta p}{\delta x_i} + \nu \frac{\delta^2 \overline{u}_i}{\delta x_i \delta x_i} + \frac{\delta \tau_{ij}}{\delta x_j} - \mathcal{C}_j^I(u_i u_j) - \mathcal{C}_j^H(u_i u_j) - \mathcal{C}_i(p) + \nu \mathcal{C}^V(u_i) \tag{1.9}$$

$$\frac{\delta \overline{u}_i}{\delta x_i} = -\mathcal{C}_i(u_i). \tag{1.10}$$

It will be convenient to refer to the sum of all the model terms in equation (1.9) as M_i. Here the nonlinear terms are written in conservative form, although a similar formulation holds for the convective, skew-symmetric, and rotational forms as well (see chapter 3).

It should be noted that there is a subtlety to this formulation when the filter is discretely homogeneous in $\boldsymbol{\xi}$ since discretely homogeneous filters can be decomposed into a homogeneous filter followed by sampling on a uniform grid. If the homogeneous filter is defined to include a Fourier cutoff with cutoff wavenumber less than the Nyquist wavenumber for the grid, the sampling does not discard information, and this is usually what is intended when defining the filter. When applying this to the decomposition given by equation (1.8), we can choose to include the effect of sampling as part of $\mathcal{C}^I$ or $\mathcal{C}^H$. Here, we will generally choose the latter, so that $\mathcal{C}^I$ is expressed in terms of a non-invertible homogeneous filter in ξ.

Further, equations (1.9) and (1.10) are intended to be general enough to subsume all LES formulations and their numerical discretizations. One way this may not be obvious is the $\delta_j \widetilde{\overline{u}_i \overline{u}_j}$ term, which can be interpreted as a binary operator $B(\overline{u}_i, \overline{u}_j)$ that maps into the LES solution space. This binary operator will be designated as $\tilde{\delta}_j$, and can subsume all finite volume and finite element flux estimates, numerical schemes that employ non-linear derivative approximations (e.g. TVD, WENO), various deconvolution, reconstruction, and explicit filtering techniques.

1.2 Statistical requirements of LES models

In addition to formulating an LES, realistic goals for LES and LES modeling should also be made explicit. A discussion from Moser, Haering, and Yalla [1] is presented here for this purpose. Early investigations of the fundamentals of SGS modeling showed that the model proposed by Smagorinsky [12] could be quite effective in the LES of isotropic turbulence [23, 24, 25, 26], producing reasonable predictions of both the decay of turbulent kinetic energy and the energy spectra. However, by applying the model in large-scale (filtered) fields derived from DNS, it was found that the Smagorinsky model output was poorly correlated with the exact subgrid term computed from the DNS [27, 28]. Further, the similarity model proposed by Bardina et al. [29] correlated much better with the exact subgrid term [30], but performed poorly as an LES model for isotropic turbulence because it was insufficiently dissipative [29]; that is, it did not adequately represent the transfer of energy from the resolved large scales to the unresolved small scales. Clearly, at least for these models and for performance in predicting the low-order statistics of isotropic turbulence, the dissipative characteristics of the model were more important than accurately representing the subgrid term as determined from DNS.

This supposed disconnect between representing the instantaneous subgrid term as determined from DNS and the actual performance of an SGS model in LES can be understood by

observing that an LES field, which only includes the large scale turbulent fluctuations, does not generally include enough information to reconstruct the missing small scale turbulence. This is a direct consequence of the implicit filter included in $\mathcal{F}$. Following the nomenclature used in Pope [14] and Langford and Moser [15], let an LES solution be denoted $\mathbf{w}$, to distinguish it from a filtered turbulence. Both $\overline{\mathbf{u}}$ and $\mathbf{w}$ reside in the same finite-dimensional LES solution space, and clearly the objective of an LES must be for the evolution of $\mathbf{w}$ to resemble that of $\overline{\mathbf{u}}$ to the extent possible. However, it is not possible for their evolutions to match in detail because there are many turbulent fields $\mathbf{u}$ with the same filtered field $\overline{\mathbf{u}}$; and further, both the turbulence and the LES are chaotic. Knowledge of the resolved field $\overline{\mathbf{u}}$ is thus insufficient to uniquely determine its evolution in time. The best possible evolution of $\mathbf{w}$ can "only" ensure that the single-time statistics of $\mathbf{w}$ match those of $\overline{\mathbf{u}}$ [15]. This is the ideal LES, which is obtained when at each time, $\partial_t \mathbf{w}$ of the LES is the average of $\partial_t \overline{\mathbf{u}}$ over all $\mathbf{u}$ for which $\mathcal{F}(\mathbf{u}) = \mathbf{w}$. However, this ideal LES evolution is practically unattainable, so the LES modeling challenge is to approximate it. The LES evolution equations are therefore obtained by substituting w_i for $\overline{u}_i$ in equations (1.6) and (1.7) and posing models for τ_{ij} and the $\mathcal{C}$'s in terms of w_i.

Since there are an infinite number of small-scale fields that are consistent with a given large-scale (filtered) turbulence, there is a distribution of possible subgrid terms [15]. This suggests that an appropriate model for the subgrid term may be the average over this distribution (that is, a conditional average). Such a model was called an ideal LES model by Langford and Moser [15] because it will yield an LES whose statistics match those of the filtered real turbulence and will minimize the mean-square error in the subgrid term. Furthermore, the ideal SGS model will correctly represent any correlation between the subgrid term and the resolved turbulent field that is linear in the subgrid term. In particular, the

ideal SGS model guarantees that

$$\langle \mathcal{G}(\overline{\mathbf{u}}) m(\overline{\mathbf{u}}) \rangle = \langle \mathcal{G}(\overline{\mathbf{u}}) M(\mathbf{u}) \rangle \tag{1.11}$$

and

$$\langle \mathcal{G}(\mathbf{w}) m(\mathbf{w}) \rangle = \langle \mathcal{G}(\overline{\mathbf{u}}) M(\mathbf{u}) \rangle \tag{1.12}$$

where $\mathcal{G}$ is any operator acting on the LES solution space (space of filtered velocity fields). A SGS model m that satisfies the *a priori* condition of equation (1.11) for all operators $\mathcal{G}$ is both necessary and sufficient for the model to be ideal. This then ensures that the *a posteriori* condition Equation 1.12 will be satisfied, with w an LES solution [15]. Hence, the ideal LES is statistically defined and is sufficient for *a posteriori* consistency of all single-time resolved statistical quantities.

Unfortunately, the ideal LES model is not attainable because it requires knowledge of an infinite-dimensional set of statistics. However, the existence of an ideal SGS model and its statistical definition and properties suggest that it is the statistical characteristics of an SGS model that are important, rather than its instantaneous representation of the subgrid term. Moreover, in a practical LES, we have more modest objectives than the ideal LES. As discussed above, we may, for example, only need an LES to provide an accurate prediction of the mean velocity and/or energy spectrum, and so naturally ask whether there are specific $\mathcal{G}$, for which satisfying equation (1.11) is either necessary or sufficient for accurate predictions. Identifying such an *a priori* requirement would allow models to be designed and tested based on *a priori* information from DNS or theory [31].

In some cases, it may be possible to analytically identify a $\mathcal{G}$ for which $\langle \mathcal{G}(w) m(w) \rangle$ is dynamically important to the statistical quantity to be predicted so that satisfying equation (1.12) is necessary for accurate predictions. This may imply that satisfying equation (1.11) is necessary, but even if not, it is a good candidate for an *a priori* condition

on the model. Finally, for some prediction quantities, there may be no analysis available that provides a closed necessary statistical condition [e.g. see 31]. In this case, it is still a reasonable hypothesis that there are some statistical quantities (i.e. $\mathcal{G}$'s) for which *a priori* consistency is important, though they may need to be discovered empirically.

1.3 Research motivation

Large eddy simulation is now over half a century old and while it has become more widely used as computational capabilities have expanded, its adoption as an engineering tool has arguably been limited by the shortcomings of subgrid models. In equation (1.9) all of the commutators and the subgrid stress generally require modeling. However, most current subgrid models were formulated under the assumption that the subgrid scales are approximately isotropic, and that other complications, such as numerical discretization and inhomogeneous resolution, are negligible. As such LES modeling efforts have largely been limited to τ_{ij} and all the commutator terms are typically neglected. The commutator on the viscous term $\nu\mathcal{C}^V$ is expected to be small when the Reynolds number is high, and so can safely be neglected except in low Reynolds number regions such as near a wall. Similarly, errors in the pressure term may be subsumed in the treatment of continuity. However, the nonlinear commutators $\mathcal{C}_j^I$ and $\mathcal{C}_j^H$ are generally important in an LES, but are commonly neglected nonetheless. This limits the fidelity of the models when applied in complex flows, and these limitations require simulations to have finer resolution than they would otherwise to ensure reliable results. For LES to become a widely applicable engineering tool, subgrid models applicable with much coarser resolution will be required. The complexities introduced by numerical discretization through the commutators must therefore be addressed in subgrid modeling.

To circle back to the somewhat rhetorical question posed at the beginning of this section, the overarching challenges facing the development of more broadly capable LES models are: (1) to identify a set of *a priori* statistical characteristics that are important for subgrid

models in complex scenarios, and (2) to acquire adequate statistical information to inform the development of models that are capable of representing these characteristics [1]. These challenges, in the context of the commutators identified in section 1.1, motivate the work in this dissertation. We aim to identify, either analytically or empirically, the important effects introduced by numerical discretization in an LES and develop corresponding LES models for the commutators that directly account for the properties of the underlying numerics. Moreover, we aim to gain a better understanding of the flow physics represented in an LES, which has typically been analyzed only in terms of isotropic turbulence represented on a uniform grid with Fourier-spectral numerics and cutoff filters.

The remainder of this dissertation is organized as follows: A review of known statistical subgrid properties and subgrid stress models is provided in chapter 2. The homogeneous commutator is then explored in chapter 3, with a particular focus on the effects of numerical dispersion error on the energy cascade in LES, as well as explicit filtering formulations that aim to address these errors. An EDQNM type of analysis that is applicable to the filtered turbulence in an LES is then developed in chapter 4, which is used to further explore numerical dispersion effects and determine the a priori requirements of subgrid stress models in the presence of non-spectral numerics and non-cutoff explicit filters. The characteristics of the inhomogeneous commutator are then explored analytically in chapter 5, followed by a numerical investigation of commutation error and commutator modeling for turbulence convecting through a coarsening grid in chapter 6. Lastly, forcing formulations for turbulence convecting through refining grids are explored in chapter 7. Concluding remarks are offered in chapter 8.

Chapter 2

Statistical properties of the subgrid stress

The subgrid stress term τ_{ij} has widely received the most modeling attention in LES. In this chapter we therefore present a review of the known statistical properties and models as mainly related to τ_{ij}. This review was previously published in the recent Annual Review of Fluid Mechanics paper by Moser, Haering, and Yalla [1] and will be useful in later chapters when exploring the homogeneous and inhomogeneous commutators.

2.1 Dissipative models

It has long been appreciated that the mean rate of energy transfer to the unresolved scales (dissipation) is a critical statistical characteristic of a SGS model. In stationary forced isotropic turbulence, and by extension in LES of stationary flows in which the turbulence at the resolution scale is approximately isotropic, the subgrid dissipation must similarly be equal to the rate of production. However, this will be trivially true *a posteriori* if the LES is stationary. The important question is whether the modeled subgrid dissipation matches production when evaluated in an *a priori* sense, that is, when evaluated using data from DNS or theory. This is then a necessary condition for a stationary LES or an LES with the correct decay rate to match the statistical characteristics of the filtered real turbulence. As an example, in a constant eddy viscosity SGS model, *a priori* consistency of the dissipation is necessary for *a posteriori* consistency of the energy spectrum. The mean rate of turbulence

kinetic energy dissipation is the most obvious statistical characteristic of an SGS model and many SGS models are therefore designed specifically to dissipate kinetic energy. These models are discussed here.

2.1.1 Eddy diffusivity

By far, the most commonly used class of LES subgrid models are eddy viscosity models. For modeling the mean momentum transport, as in RANS, an eddy viscosity form can be justified by gradient diffusion arguments. Consider convective transport of some fluctuating conserved quantity ϕ by a fluctuating velocity field. Using the first term in a Taylor expansion of a stochastic fluid particle location, χ_i', and assuming isotropic turbulence, one obtains [32] an eddy viscosity representation for $\langle u_j'\phi'\rangle$ with the eddy viscosity given by $\nu_t = C\langle k\rangle T_c$, where T_c is a velocity correlation time. Such a formulation based on the expected energy and correlation timescale suggests an eddy viscosity model is justified in the mean, but in an LES, the SGS τ_{ij} is a fluctuating quantity. The physical justification for an eddy viscosity representation of τ_{ij} fluctuations is thus questionable.

In an LES, however, the subgrid scale fluctuations are critical, since the rate of turbulent energy transfer to the small scales (dissipation) is given by $\langle\varepsilon^s\rangle = \langle S_{ij}^{>}\tau_{ij}'\rangle$, which is one of the critical *a priori* model characteristics. While gradient transport arguments do not justify an eddy viscosity model for τ_{ij}', such a model is guaranteed to be dissipative, and is useful for this reason. Particularly, with $\tau_{ij}^d \approx \nu_t\overline{S}_{ij}$, where $\tau_{ij}^d = \tau_{ij} - \frac{1}{3}\tau_{kk}\delta_{ij}$, [see e.g. 33] the mean subgrid stress and the dissipation are given by

$$-\tfrac{1}{2}\langle\tau_{ij}^d\rangle \approx \langle\nu_t\rangle\langle S_{ij}\rangle + \langle\nu_j' S_{ij}^{>}\rangle \tag{2.1}$$

$$\tfrac{1}{2}\langle\varepsilon^s\rangle \approx \langle\nu_t\rangle\langle S_{ij}^{>}S_{ij}^{>}\rangle + \langle\nu_t' S_{ij}^{>}\rangle\langle S_{ij}\rangle + \langle\nu_j' S_{ij}^{>}S_{ij}^{>}\rangle. \tag{2.2}$$

The function of a subgrid model is often considered to be providing the total subgrid energy

flux, $\langle \tau_{ij} \overline{S}_{ij} \rangle = \langle \tau_{ij} \rangle \langle S_{ij} \rangle + \langle \varepsilon^s \rangle$. But this is conflating two of the distinct *statistical roles* of the subgrid scale model; to transport mean momentum via $\langle \tau_{ij} \rangle$ and to transfer resolved turbulent energy to the subgrid through $\langle \varepsilon^s \rangle$.

Note first that if the eddy viscosity fluctuations and the resolved strain rate are correlated, they contribute to the mean momentum transport, which is not consistent with the gradient transport argument above. Second, the eddy viscosity need not fluctuate for the model to be dissipative. Also, note that use of the standard model form, $\tau_{ij}^d \approx \nu_t \overline{S}_{ij}$, with fluctuating ν_t results in the mean strain contributing to ε^s, which is inconsistent with ε^s representation of nonlinear transfer of energy across turbulence scales [34]. This has led to much difficulty when using eddy viscosity subgrid models in mean-shear-dominated regions such as near walls [35, 36] and often necessitates ad-hoc damping. Use of this model form to represent $\langle \tau_{ij} \rangle$ while representing $\langle \varepsilon_s \rangle$ is also inconsistent since the required eddy viscosities scale differently [37]. Models of this form therefore require the LES resolution be sufficiently fine to make the mean subgrid stress negligible. An alternative is to use a different eddy viscosity for the mean momentum transport and the dissipation [38, 39, 40] as will be discussed in section 2.2.1.

Generally in LES then, eddy viscosity models for the mean subgrid stress $\langle \tau_{ij} \rangle$ are justified by gradient transport arguments, and eddy viscosity models for τ'_{ij} are useful because they are inherently dissipative. In most LES formulations, it is the dissipative characteristics of eddy viscosity models that are of greatest interest, and these are discussed in the following subsections. Such models have been used successfully in LES of a wide variety of complex turbulent flows [41, 42, 43, 44, 45]. The success of eddy viscosity models can usually be attributed to the use of an LES resolution fine enough to ensure that only the dissipative properties of the model are important. They are likely to continue to be valuable in ensuring that subgrid models represent the transfer of energy to the small scales. However, additional or alternative model forms may be needed to represent other statistical characteristics of the

subgrid terms. Fluctuations in the eddy viscosity are not justified on physical grounds nor do they appear to be necessary. Indeed, subgrid models with non-fluctuating eddy viscosities have been used successfully [46, 17], though most subgrid models employ a fluctuating eddy viscosity (e.g. the Smagorinsky model). Finally, real space eddy viscosity models do not provide the well-known spectral cusp behavior resulting from incomplete wavenumber triad interactions near the cutoff [47, 48]. This fact motivates the use of hyperviscosity models as discussed in section 2.1.3 and further in chapter 4.

Mean dissipation formulations

When considering only the exchange of energy from the resolved to unresolved scales, it is natural to formulate an eddy viscosity directly in terms of the dissipation. If the eddy viscosity is presumed to not fluctuate, it can be simply defined as

$$\nu_t = \frac{\langle \varepsilon \rangle}{2\langle S_{ij}^{>} S_{ij}^{>} \rangle}, \tag{2.3}$$

which guarantees that the model will have dissipation $\langle \varepsilon \rangle$ *a priori*. Notice that ν_t from equation (2.3) grows without bound as filter scale Δ increases. Equation 2.3 is not particularly useful by itself; additional modeling is required before it can be employed in an LES. The denominator $\langle |S^{>}|^2 \rangle$ in Equation 2.3 can be computed *a priori* from the spectrum tensor, if known. Assuming an isotropic inertial range spectrum, we have [49]

$$\langle \partial_k u_i^{>} \partial_l u_j^{>} \rangle = \frac{C_k \langle \varepsilon \rangle^{2/3}}{4\pi} \int_{\mathcal{D}} \kappa_k \kappa_l \hat{\mathcal{F}}^2(\boldsymbol{\kappa}) |\boldsymbol{\kappa}|^{-11/3} \left(\delta_{ij} - \frac{\kappa_i \kappa_j}{|\boldsymbol{\kappa}|^2} \right) d\boldsymbol{\kappa}, \tag{2.4}$$

where $\hat{\mathcal{F}}$ is the Fourier transform of the filter operator $\mathcal{F}$ defined in section 1.1. Assume that $\mathcal{F}$ is simply a Fourier cutoff at wavenumber $\kappa_c = \pi/\Delta$ so that $\hat{\mathcal{F}}(\boldsymbol{\kappa}) = 1$ for $|\boldsymbol{\kappa}| < \kappa_c$, and 0 otherwise, and that the inertial range extends to wavenumbers as low as $|\boldsymbol{\kappa}| = \pi/L$, where L is proportional to the integral scale. The domain of integration in equation (2.4)

can then be set to $\mathcal{D} = \{\boldsymbol{\kappa} \,|\, \pi/L < |\boldsymbol{\kappa}| < \kappa_c\}$, and the integral performed to determine $\langle |S^>|^2 \rangle = C_k \pi^{4/3} \langle \varepsilon \rangle^{2/3} (\Delta^{-4/3} - L^{-4/3})$, where C_k is the Kolmogorov constant. For $L \gg \Delta$, we get the simple result

$$\nu_t = C \langle \varepsilon \rangle^{1/3} \Delta^{4/3}, \tag{2.5}$$

with $C = 0.11/C_k$ [17], showing that provided Δ is sufficiently small, the eddy viscosity is insensitive to the details of the large scales, as expected. It remains only to specify $\langle \varepsilon \rangle$, which unfortunately is generally not known *a priori*. A more sophisticated theoretical spectrum can be used in a similar analysis to obtain a model constant that accounts for effects of finite Reynolds number and small L/Δ [50].

Through approximations of $\langle \varepsilon \rangle$, many subgrid models can be cast into the form of equation (2.5). First, the "Kolmogorov expression" model of Carati et al. [51] and Dantinne et al. [46] is basically equation (2.5), though they do not apply the expected value to the dissipation. Second, assuming equilibrium, *i.e.* $\langle \varepsilon \rangle = \langle \varepsilon^s \rangle = 2\nu_t \langle S_{ij}^> S_{ij}^> \rangle$, a variant of the Smagorinsky model [12] is recovered, $\nu_t = C(2\langle S_{ij}^> S_{ij}^> \rangle)^{1/2} \Delta^2$. This is the argument put forward by Deardorff [52] to justify use of the Smagorinsky model. Note that the more standard Smagorinsky form, $\nu_t = C(2\langle \overline{S}_{ij} \overline{S}_{ij} \rangle)^{1/2} \Delta^2$, is recovered only if we conflate subgrid statistical roles and require $\langle \varepsilon \rangle \approx \langle \varepsilon^s \rangle + \langle \tau_{ij} \rangle \langle S_{ij} \rangle$. Alternatively, $\langle \varepsilon \rangle$ in equation (2.5) could be determined through an approximation of the second order structure function, $F_2(r)$ and the Kolmogorov 2/3-law, $F_2(r) = C(\langle \varepsilon \rangle r)^{2/3}$ [53] where r is the separation. With the filtered structure function related to the total F_2 through a coefficient in the inertial range [54, 11] and setting $r = \Delta$, we have $\nu_t = C(\overline{F}_2(\Delta))^{1/2} \Delta$, which is a variant of the structure function model of Métais and Lesieur [54]. Assuming isotropic resolution and the 2/3 law simply yields $\langle \varepsilon \rangle = C \langle \partial_j u_i^> \partial_j u_i^> \rangle^{3/2} \Delta^2$ and $\nu_t = C \langle \partial_j u_i^> \partial_j u_i^> \rangle^{1/2} \Delta^2$ which is similar to the Smagorinsky form and is another variant of the structure function model [48]. Thus, many common models, when formulated as an expected value, differ only in how they approximate the dissipation.

Rarely are LES models formulated in terms of expected values, even when the underlying assumptions only hold in expectation. Instead, instantaneous gradients are used to define a subgrid time scale so that ν_t fluctuates and the ν_t' terms in equation (2.2) affect model behavior. For instance, in the analysis of the dissipation due to the Smagorinsky model, Lilly [55] neglects these terms under the assumption that ν_t has undergone "some form of averaging sufficient to assure stability of velocity covariances." However, this fluctuating term does contribute to the dissipation and its neglect in Lilly's *a priori* analysis leads to an overestimate of the Smagorinsky constant through $\langle \nu_j' S_{ij}^{>} S_{ij}^{>} \rangle$ and especially through $\langle \nu_t' S_{ij}^{>} \rangle \langle S_{ij} \rangle$ in regions of high mean shear. Furthermore, the use of numerical derivative operators to estimate $S_{ij}^{>}$ adds further complication to estimating the constant. As a consequence of these complications, the constants in the Smagorinsky model and other models with fluctuating ν_t generally need to be adjusted for *a priori* consistency of the dissipation.

The eddy viscosity models described in this section are formulated in terms of average quantities, making it straight-forward to ensure *a priori* consistency with dissipation. In the remainder of section 2.1.1 we consider ensuring *a priori* statistical consistency when the eddy viscosity fluctuates.

The dynamic procedure

The dynamic procedure [56] has been widely used to determine constants in subgrid models. The procedure relies on a second filter $\mathcal{F}^d$ at scale d (a test filter, signified by $\widehat{\cdot}$) that is coarser than the "grid filter" $\mathcal{F}^\Delta$ at scale Δ ($d > \Delta$). The Germano identity relates the subgrid stress determined for the composite filter $\mathcal{F}^{\widehat{\Delta}} = \mathcal{F}^d \mathcal{F}^\Delta$ ($\widehat{\Delta}$ is the effective scale of the composite filter) evaluated for the LES filter, and the "resolved stress" (Leonard stress). Letting $\mathcal{F}^d(u) = \hat{u}$, the identity reads:

$$\tau_{ij}^{\widehat{\Delta}} - \hat{\tau}_{ij}^{\Delta} = \widehat{\overline{u}_i \overline{u}_j} - \hat{\overline{u}}_i \hat{\overline{u}}_j = \mathcal{L}_{ij} \tag{2.6}$$

where $\tau^{\widehat{\Delta}}$ and τ^{Δ} are the subgrid stresses determined for the composite and grid filters respectively. The resolved stress can be evaluated from an LES solution, and if $\tau^{\widehat{\Delta}}$ and τ^{Δ} are modeled using the same model, evaluated for the different filters, equation (2.6) can be used to determine an overall multiplicative constant in the model (e.g. the Smagorinsky constant). Let $m_{ij} = (\tau_{ij}^{\widehat{\Delta}} - \hat{\tau}_{ij}^{\Delta})/C$, as determined by the model, with C the multiplicative constant. Then the Germano identity requires $Cm_{ij} = \mathcal{L}_{ij}$, which in principle should be true locally in space and instantaneously in time.

As an expression for C this relation is over-determined, since C is just a scalar in a tensor equation. Germano et al. [56] originally proposed contracting this equation with $\hat{\overline{S}}_{ij}$ to obtain a scalar equation, and later Lilly [57] and Ghosal et al. [58] proposed contracting it with m_{ij}. The former is motivated by the fact that $\tau_{ij}^{\widehat{\Delta}}\hat{\overline{S}}_{ij}$ is the dissipation for the composite filtered turbulence, while C determined from the latter minimizes the square error [57]. In either case, C varies wildly in space and time [58], resulting in regions with large negative eddy viscosity, and the resulting instabilities in an LES. This is generally avoided by averaging, resulting in

$$C = \frac{\langle \mathcal{L}_{ij}\hat{\overline{S}}_{ij}\rangle}{\langle m_{ij}\hat{\overline{S}}_{ij}\rangle} \quad \text{or} \quad \frac{\langle \mathcal{L}_{ij}m_{ij}\rangle}{\langle |m|^2\rangle}. \tag{2.7}$$

In an LES, the averages have been defined as over homogeneous spatial dimension, as Lagrangian time averages [59, 60] and as averages in local spatial neighborhoods. By far, the most common model to which the dynamic procedure has been applied is the Smagorinsky model [12]. However, the dynamic procedure can be used for any subgrid stress model and is not limited to simple multiplicative constants. Other subgrid models to which it has been applied include the Vreman model [61, 62], transport-based subgrid kinetic energy [63] and mixed models, both similarity-based [64, 65] and gradient-based [66, 67] The dynamic procedure has also been used to determine $\langle C\varepsilon^{1/3}\rangle$ in equation (2.5) which was shown to perform equally well to dynamic Smagorinsky with fewer operations [46].

Given the low correlation between the resolved stress and strain [68, 69], the scaling of the eddy viscosity by the dynamic procedure can only adjust the amount of energy removed by the model. Jimenez and Moser [37] analyzed the Lilly form of the dynamic procedure applied to the Smagorinsky model and noted that the expression for C was essentially a relation between production of turbulent energy at scales smaller than the test filter ($\mathcal{L}_{ij}\hat{\overline{S}}_{ij}$) to the dissipation provided by the model formulated for the grid filter due to the fluctuations at scales between the grid and test filter. This connection can be seen more clearly through an *a priori* analysis for models with non-fluctuating eddy viscosity, such as those mentioned in section 2.1.1, applied to isotropic turbulence with a Kolmogorov inertial range with Fourier cutoff filters. With a non-fluctuating eddy viscosity, the Germano and Lilly forms of the contracted Germano identity (equation (2.7)) are equivalent because in this case $Cm_{ij} = (\nu_t^{\widehat{\Delta}} - \nu_t^{\Delta})\hat{\overline{S}}_{ij}$. Further with the Fourier cutoff filters, $\hat{\overline{S}}_{ij} = \hat{S}_{ij}$, and with a Kolmogorov inertial range, one can easily determine that $\langle|\overline{S}|^2\rangle/\langle|\hat{S}|^2\rangle = \widehat{\Delta}^{4/3}/\Delta^{4/3}$ and that for each of the model forms mentioned in section 2.1.1 $\nu_t^{\widehat{\Delta}}/\nu_t^{\Delta} = \widehat{\Delta}^{4/3}/\Delta^{4/3}$. Using these results, the Germano and Lilly relationships reduce to $\langle\mathcal{L}_{ij}\hat{S}_{ij}\rangle = \nu_t^{\Delta}(\langle|\overline{S}|^2\rangle - \langle|\hat{S}|^2\rangle)$. The left hand side is the production of energy at scales less than $\widehat{\Delta}$ and the right hand side is precisely the dissipation of the model for τ^{Δ} due to the scales between $\widehat{\Delta}$ and Δ.

In regions of flow where the filter is not well within the inertial subrange, Pope [14] has argued that the dynamic procedure functions by minimizing the dependence of the statistical characteristics of the model on the filter width. Porté-Agel et al. [70] propose using multiple test filters to infer the dependence on Δ in this situation.

Representing dissipation in inhomogeneous flows

The broad success of the dynamic procedure arises from its ability to overcome a number of deficiencies in the base model. One such deficiency arises when the Smagorinsky model is applied to inhomogeneous flows, especially wall-bounded flows. The Smagorinsky eddy

viscosity does not go to zero as it should near the wall because of the asymptotic limits of the velocity gradients at the wall, and in laminar flows because of the contributions of the mean to $|\overline{S}|$. The dynamic procedure corrects for this by adjusting the constant. The discussion in section 2.1.1 suggests that the important characteristic of the $|S|$ factor in the Smagorinsky eddy viscosity is that it scales with $\langle\varepsilon\rangle^{1/3}$ for filter widths in an inertial range. However, the contribution of the mean to $\overline{S}$ spoils this, which is a fundamental reason for the poor behavior in laminar flows. Alternatives to Smagorinsky eddy viscosity that attain the required ε scaling with different scalar functions of the velocity gradient have been formulated to produce the correct wall behavior and reduce sensitivity to specific mean characteristics. These include the wall adaptive large eddy (or WALE) model of Nicoud and Ducros [71] which corrects the behavior near walls, the Vreman model [61] which is insensitive to pure shear, and the σ-model [72] which has both these features plus insensitivity to solid body rotation, axisymmetric strain and pure dilatation. The particular behaviors of such models in response to different mean flow conditions have been thoroughly examined [36]. Consistent with the expectations for such models, when the dynamic procedure is applied to the Vreman model, the coefficient is significantly less variable than Smagorinsky [62].

To completely eliminate the dependence of the eddy viscosity on the mean, which would be most consistent with parameterizing it for dissipation of resolved turbulence, it can be made proportional to $|S^{>}|$ as done by Schumann [38] and Moin and Kim [39]. Similarly, Lévêque et al. [35] formulate the eddy viscosity in terms of $|\overline{S}| - |\langle S\rangle|$ which also vanishes in laminar flows, and is designed to represent the total energy transfer to the subgrid scales including both the production by the mean and the dissipation of the resolved fluctuations.

Minimum dissipation models

The motivation for the eddy viscosity formulations discussed above is arguably to yield a good approximation of the mean dissipation when evaluated *a priori*. An alternative approach is

to target the local resolved dynamics, which if correctly represented would naturally produce the *a priori* statistics. The minimal dissipation (MD) family of models [73, 74, 75] are of this type. They shed any pretense of representing the subgrid and instead pose a model that counteracts the formation of fluctuations smaller than the specified filter scale. Through the Poincaré-Wirtinger inequality, the production of subfilter energy is bound above by the production of filtered gradient energy ($\partial_i \overline{u}_j \partial_i \overline{u}_j$), so limiting filtered gradient growth is sufficient to limit production of subfilter energy in the resolved subspace. A "production of subfilter scales" in the resolved space would physically manifest in an increasing pile-up of energy at the cutoff. The fact that only the resolved scales are considered is the reason the Poincaré-Wirtinger inequality can be used with the resolved gradient, since otherwise explicit knowledge of the unfiltered velocity gradients would be required.

The MD models consider the evolution equation of the filtered gradient energy with an eddy viscosity subgrid model integrated over a grid cell [73]. Assuming negligible transport, variation of eddy viscosity ν_t and resolved viscous dissipation, a zero time derivative of the gradient energy requires

$$\nu_t \geq C_\Delta \frac{r}{q} \tag{2.8}$$

where $q = \frac{1}{2} S_{ij} S_{ij}$, $r = -\frac{1}{3} S_{ik} S_{kj} S_{ji}$. In practice, r is clipped at zero to prevent negative ν_t, and equation (2.8) is taken as an equality with $C_\Delta = 0.2\Delta^2$. Models stemming from equation (2.8) have been tested on decaying turbulence and mixing layers [74] in addition to channel flow [73, 75] and the anisotropic MD model (AMD) [74] has been shown to produce remarkably accurate energy spectra in isotropic turbulence with anisotropic resolution [17].

It appears that the correlations between ν_t', and $S_{ij}^{>}$ account for the AMD model performance, but it is not clear how. One insight is derived by comparing the AMD eddy viscosity with equation (2.3), which suggests that the AMD eddy viscosity produces local dissipation consistent with the nonlinear gradient model [27, 68, 33], when it is dissipative. Note that an anisotropic resolution generalization of the gradient model is given by

$\tau_{ij}^C = C\mathcal{M}_{kl}\partial_l\overline{u}_i\mathcal{M}_{kp}\partial_p\overline{u}_j$, and that $\varepsilon^C = \tau_{ij}^C\overline{S}_{ij}$ is the energy transfer due to that stress and the value of r in AMD. An alternate interpretation is that τ_{ij}^C arises from contracting an approximation of the two-point second-order structure function. In the AMD model then, the resulting energy transfer is $\varepsilon = \tau_{ij}\overline{S}_{ij} = C\varepsilon^C/(\overline{S}_{kl}\overline{S}_{kl} + \overline{\Omega}_{mn}\overline{\Omega}_{mn})(\overline{S}_{ij}\overline{S}_{ij}) \leq C\varepsilon^C$ due to $(\overline{\Omega}_{mn}\overline{\Omega}_{mn}) \geq 0$. However, the gradient model is known to be unstable [66]. It seems then, that minimum dissipation models provide a convenient vehicle for stabilizing such gradient models. Clipping of r is justified because the processes responsible for inverse energy transfer, which would be represented by negative viscosity, is not consistent with the characteristics of negative diffusivity. In particular, the former enhances energy in larger scales while the latter amplifies energy in smaller scales. In any case, equation (2.8) is an eddy viscosity formulated to match a model of local dissipation variations.

The success of MD models indicates more careful consideration of gradient energy transport is warranted. Though the resulting models are all of the eddy viscosity type, and therefore act on all scales of motion, MD arguments suggest the energy transfer role of the subgrid turbulence could be replaced by preventing the formation of subfilter scales of motion by the nonlinear product. This perspective is shared by implicit LES (Section 2.1.2), explicit filtering (Section 3.6), and Leray regularization [76] methods.

Transport-based eddy viscosity

The algebraic eddy viscosity models described in the previous subsections were formulated based on the assumption that the subgrid turbulence is in statistical equilibrium with the resolved turbulence. If this condition does not hold, the statistical evolution of the subgrid scales will be important, prompting the use of transport models for the state of the subgrid turbulence. For example, to address the effects of stratification, Deardorff [77] introduced evolution equations for the subgrid stress, analogous to the Reynolds stress transport equations. More common has been the use of the equation for subgrid kinetic energy $k^> = \frac{1}{2}\tau_{kk}$

[38, 78], which can be written:

$$\frac{\partial k^{>}}{\partial t} + \overline{u}_i \frac{\partial k^{>}}{\partial x_i} = \tau_{ij}\overline{S}_{ij} - 2\nu|S^{>}|^2 - \varepsilon + \frac{\partial}{\partial x_i}\Big(\nu + \sigma_k \nu_t)\frac{\partial k^{>}}{\partial x_i}\Big), \tag{2.9}$$

where σ_k is a model constant representing the inverse of the Prandtl number relating transport of momentum and $k^{>}$, and ε must be modeled. The eddy viscosity and dissipation can then be written in terms of $k^{>}$ and Δ:

$$\nu_t = C_\mu (k^{>})^{1/2}\Delta \qquad \varepsilon = C_\varepsilon (k^{>})^{3/2}/\Delta. \tag{2.10}$$

If the subgrid turbulence is in equilibrium so that $\partial_t k^{>} = 0$, the Reynolds number is high so that viscous dissipation due to the resolved scales is negligible and turbulence is homogeneous, then equation (2.9) with $\tau_{ij} = \nu_t \overline{S}_{ij}$ can be solved for $k^{>}$, resulting in $\nu_t = (C_\mu/C_\epsilon)^{1/2}\Delta^2|S|$, which is just the Smagorinsky model. Other choices for the closure models for ν_t and ε could also be made, which could be formulated to yield an equilibrium consistent with the other algebraic models discussed in the previous subsections. However, because the subgrid production term is written $\tau_{ij}\overline{S}_{ij}$ rather than $\langle \tau_{ij}\overline{S}_{ij}\rangle$ and because of the convective velocity fluctuations, $k^{>}$ is a fluctuating quantity, and equation (2.9) will generally not be in equilibrium. The resulting eddy viscosity will fluctuate differently from Smagorinsky (using equation (2.10)), due to the dynamics introduced by equation (2.9).

However, there is no reason to expect these fluctuations to contribute to the fidelity of the model in representing τ_{ij} any more than they do for Smagorinsky, especially since the closure models of equation (2.10) are in essence only valid statistically. However, one likely consequence of the change in the fluctuations is a reduction in the correlation between ν_t and $S^{>}$, which is generally unrealistically high in the algebraic models like Smagorinsky.

While originally used extensively for atmospheric simulations [77], transport-based subgrid models have seen more recent application in so-called "bridging" models [79]. The par-

tially averaged Navier-Stokes (PANS) [80] and partially integrated transport model (PITM) [81] models are intended for use in hybrid RANS/LES simulations, but, in practice, are generally used with coarse LES throughout a simulated domain. In both approaches, RANS-like transport models are made a function of the level of resolved turbulence, often specified *ab initio*. Bridging methods have been used to varying degrees of success in a number of flows with wide ratios of unresolved to total turbulent kinetic energy as high as 70% [80] but typically show good results with levels in the vicinity of 20% (see Chaouat and Schiestel [82], Razi et al. [83] for instance). Such resolution levels are well past the typical limits of $< 10\%$ for a well-resolved LES [37]. A reduction in the correlation between ν_t and $S^{>}$ and the resulting improvement in representing the Reynolds stress may be the reason.

Dissipation anisotropy

In the analysis of eddy viscosity models in the previous subsections, only the kinetic energy dissipation (transfer to unresolved scales) has been considered. However, another necessary condition for correct first, second and third order resolved velocity correlations is an *a priori* consistent dissipation tensor $\varepsilon_{ij} = \langle \partial_k u_i^{>} \tau_{kj} + \partial_k u_j^{>} \tau_{ki} \rangle$ [31]. If the unresolved scales are isotropic, ε_{ij} consistency will follow from consistency of ε_{kk}. However, if the LES resolution is coarse or anisotropic, this will not be the case [84]. There has unfortunately been little work towards developing models that capture dissipation anisotropy. It is possible that similarity models (section 2.2.1) are improving representation of dissipation anisotropy but, to the authors knowledge, this conjecture has not been examined to date.

Two exceptions are the M43 model [17] and the AMD model [74], which were both designed to account for resolution anisotropy. The AMD model was described briefly in section 2.1.1. It employs a fluctuating scalar eddy viscosity determined from a triple product of the velocity gradients. The M43 model on the other hand employs a non-fluctuating tensor eddy viscosity determined from an estimate of $\langle \varepsilon \rangle$. Both models depend explicitly on

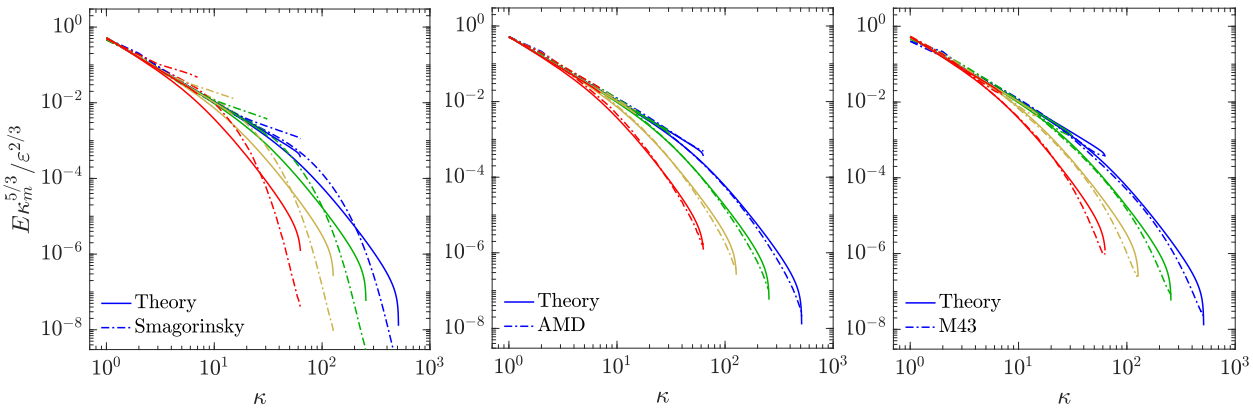

Figure 2.1: Normalized one-dimensional energy spectra from LES of forced isotropic turbulence at infinite Re in a periodic box using the Smagorinsky, AMD, and M43 models, and anisotropic resolution with of $(8:8:1)$ aspect ratio cells and varying ratios of cutoff wavenumber (grid size) to box size, κ_{cc}/κ_m, compared with the equivalently filtered $|\boldsymbol{\kappa}|^{-5/3}$ Kolmogorov inertial energy spectra [see 17, for details]. Shown are spectra in both the fine and coarse directions. All models yield virtually identical results for isotropic resolution. Values of κ_{cc}/κ_m are: 8, 16, 32, 64.

an anisotropic tensor measure of the resolution, and both do an excellent job of capturing the kinetic energy spectrum over a wide range of grid aspect ratios (see figure 2.1). With regard to ε_{ij}, the M43 model is qualitatively consistent *a posteriori* as a function of aspect ratio, while with AMD, ε_{ij} remains approximately isotropic [17]. Also, the formulation and function of the models is significantly different. The AMD model is formulated based on the minimum dissipation considerations described in section 2.1.1, and it's good performance in reproducing spectral anisotropy must be a consequence of the correlations of the eddy viscosity fluctuations with the fluctuations of $S_{ij}^{>}$, since the eddy viscosity is a scalar. On the other hand, the M43 model is formulated as a straight-forward generalization of the Kolmogorov model [51, 46], based on *a priori* consideration of the fourth rank velocity gradient tensor $\langle \partial_k u_i \partial_l u_j \rangle$, and the eigenstructure of the modified dissipation tensor $\langle \partial_i u_k^{>} \tau_{jk} + \partial_j u_k^{>} \tau_{ik} \rangle$. Its good performance reproducing the spectral anisotropy arises from its use of a tensor eddy viscosity. It suggests that a tensor eddy viscosity could be formulated to represent the effects of turbulence anisotropy as well.

2.1.2 Implicit LES

An alternative approach to modeling the subgrid dissipation is to design the numerical divergence operator, $\tilde{\delta}_i$, to include the dissipation usually provided by eddy diffusivity models of τ_{ij}. This leads to implicit LES models (ILES), in which the goal is essentially to define the $\tilde{\delta}_i$ operator so that $\delta_j \tau_{ij} + \mathcal{C}_j^H(u_i u_j)$ can be neglected. However, τ_{ij} may still need to be modeled to represent important statistical properties other than dissipation, such as subgrid Reynolds stress. As pointed out by Fureby and Grinstein [85], the ILES approach simply shifts the modeling challenge from τ_{ij} to $\tilde{\delta}_i$ where concerns for the consistency of statistical properties remain.

The most common ILES model exploits the leading order dissipation term introduced by numerical upwinding of the convection term. Boris [86] introduced this approach in the Monotone Integrated LES (MILES) model based on flux-limiting finite volume discretizations. A connection between the dissipation of the ILES $\tilde{\delta}_i$ operator and dissipative models of τ_{ij} can be established with modified equation analysis [87]. Also, *a priori* consistency of the dissipative and transport properties of $\tilde{\delta}_i$ can be tested with DNS data, though to the authors' knowledge this has not been pursued. Implicit models can also be built from the high-order adaptive flux reconstruction techniques used in finite volume methods [88], which has features of the deconvolution methods described in section 3.7. See Grinstein et al. [89] for a more detailed review of ILES models.

Finally, note that the ILES modeling considerations are different from the approaches to ameliorate the effects of discretization error described in chapter 3. The objective of the former is to replace models for τ_{ij} while the objective of the latter is to minimize $\mathcal{C}^H$.

2.1.3 Hyperviscosity models

Applying the analysis of Meneveau [31] to the equation for the energy spectrum in isotropic turbulence yields the necessary condition that the subgrid dissipation spectrum be *a priori* consistent. With a Fourier cutoff filter, it is well known that the *a priori* dissipation spectrum has a cusp near the cutoff [48, 90, 91]. A wavenumber-dependent eddy viscosity to represent this cusp has been proposed [92]; however, such an eddy viscosity is only easily applicable with Fourier spectral methods. To approximate the cusp in the dissipation spectrum, hyperviscosity models have been proposed by several authors [see 34]. Moreover, Cerutti et al. [93] showed that a fourth order hyperviscosity model is the simplest model that correctly represents the dissipation of resolved enstrophy.

Hyperviscosity models are formulated as a sum of Laplacian operators of various orders, providing an approximation of a wavenumber-dependent eddy viscosity. They have been evaluated *a priori* using both experimental [93] and computational data [46, 94, 95].

2.2 Beyond dissipation

There are statistical characteristics beyond dissipation that the subgrid model needs to satisfy to enable reliable simulations. However, these have received much less attention in both modeling and analysis. One such characteristic, the mean subgrid stress is discussed in the following subsection. Lastly, the Optimal LES modeling technique of Langford and Moser [15] is discussed, which is guaranteed to produce a model that satisfies a given statistical requirement in the *a priori* sense. However, the burden is still on identifying the important statistical characteristics.

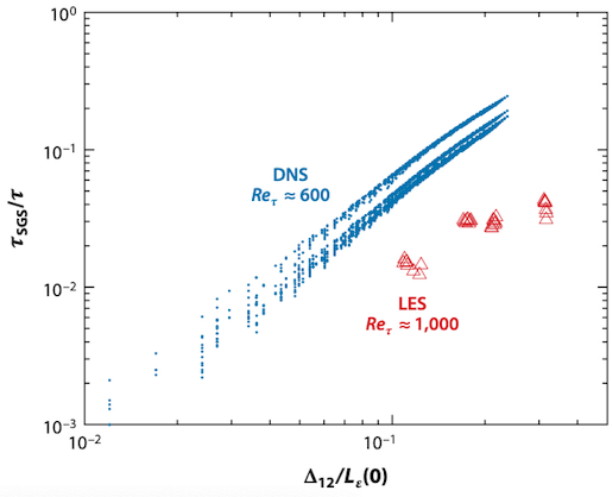

Figure 2.2: Mean subgrid shear stress, τ_{SGS} normalized by the total Reynolds stress, τ, as a function of the filter width, Δ_{12}, normalized by the local integral scale, $L_\varepsilon(0)$ in channel flow. Data is obtained a priori from a DNS at $Re_\tau \approx 600$, and Δ a posteriori from an LES at $Re_\tau \approx 1000$ using dynamic Smagorinsky model [from 37].

2.2.1 Mean subgrid stress

The main limitation preventing modeling both stress and dissipation with a single eddy viscosity is the single degree of freedom that an eddy viscosity affords to adjust the behavior of the model. In essence, we can adjust the viscosity to provide either the correct mean subgrid stress or the correct dissipation, but not generally both [96, 37, 97]. This is problematic because, as pointed out by Meneveau [31], both are necessary to predict the mean velocity and the resolved Reynolds stress.

Jimenez and Moser [37] measured the magnitude of the problem in an *a priori* analysis of turbulence channel flow using box filters. They found that when tuned for dissipation, the Smagorinsky model yielded a mean subgrid stress that is too small by about a factor of 5, with the discrepancy increasing with the fraction of unresolved turbulent kinetic energy (see figure 2.2). This suggested that when using a simple Smagorinsky model, the filter width needed to be small enough to ensure that the subgrid contribution to the mean subgrid stress is negligible. Similarly, using Gaussian filters on a theoretical energy spectrum representing

turbulence in shear flow [98], Li and Meneveau [97] showed that in the limit of weak shear the Smagorinsky eddy viscosity needed for consistency with the mean subgrid stress is a factor of 2.6 larger than that needed for consistency with dissipation. With Fourier cutoff filters, however, consistency of mean subgrid stress and dissipation yield nearly the same model constant. Except possibly in this special case, *a priori* consistency of mean subgrid stress and dissipation are distinct requirements that are incompatible for a single eddy viscosity model.

One approach to addressing this problem is to use a different eddy viscosity to represent the mean subgrid stress and the dissipation [38, 39, 40, 99]. In this approach, the resolved strain rate is decomposed into mean and fluctuating components, and a different eddy viscosity is applied to each, as in:

$$\tau_{ij}^d \approx -2(\nu_s \langle S \rangle_{ij} + \nu_e S_{ij}^{>}). \tag{2.11}$$

Most applications of this formulation have been motivated by coarse near-wall resolution with ν_s made a function of wall distance [38, 39, 100]. The mean part of the model is then only active near the wall so that the model reverts to a form similar to that of Lévêque et al. [35] over most of the domain. However, this split model approach is not limited to near-wall regions and may be useful anywhere in a simulation with coarse local resolution. More recently, hybrid RANS/LES methods have emerged [40, 99] that use a RANS-like formulation of ν_s. If a standard fluctuating eddy viscosity model is used for ν_e (*e.g.* Smagorinsky), $\langle \nu_e S_{ij}^{>} \rangle$ will contribute to the mean subgrid stress when ν_e' and $S^{>}$ are correlated, and would have to be taken into account in formulating ν_s. However, if both ν_s and ν_e are formulated as expected values, as with the models described in section 2.1.1, then mean subgrid stress and

dissipation reduce to

$$\langle \tau_{ij}^d \rangle \approx -2\langle \nu_s \rangle \langle S_{ij} \rangle \qquad \langle \varepsilon^s \rangle \approx 2\langle \nu_e \rangle \langle S_{ij}^> S_{ij}^> \rangle \tag{2.12}$$

and the mean stress and energy transfer roles of the subgrid model become distinct [40]. This split-τ approach has the additional benefit of allowing the dissipative and momentum transport roles of the subgrid to be represented by models best suited for these effects.

Another approach to obtaining consistency with both the mean subgrid stress and the dissipation is with a mixed model, in which the subgrid model consists of the sum of two different models with different characteristics. For example, Li and Meneveau [97] interpreted the inconsistency of the eddy viscosity for mean stress and dissipation as arising from the Leonard stress, and so proposed addressing it with a mixed model consisting of the quadratic gradient model [27, 68, 33] plus Smagorinsky:

$$\tau_{ij}^d = -2C_1\Delta^2|\overline{S}|\overline{S}_{ij} + C_2\Delta^2\big(\partial_k\overline{u}_i\partial_k\overline{u}_j - \tfrac{1}{3}\partial_k\overline{u}_l\partial_k\overline{u}_l\delta_{ij}\big) \tag{2.13}$$

They were able to satisfy both the *a priori* dissipation and mean stress, through production, consistency requirements for weak mean deformation, based on a theoretical spectrum as discussed above. However, the coefficients in equation (2.13) were found to depend on the strength and structure of the mean velocity gradient tensor. This dependence was strong for sharp spectral filters but reduced for Gaussian filters. For stronger mean gradients, where the assumptions of Ishihara et al. [98] are invalid, this strong coefficient dependence on the mean is expected to increase. Practical application of this model would require developing robust broadly applicable coefficients as a function of the invariants of the mean velocity gradient tensor and, potentially, statistics of the resolved scales. Finally, in Gaussian filtered isotropic turbulence, the nonlinear gradient term is highly correlated with the true subgrid stress, to the extent that Borue and Orszag [69] referred to them as "statistically equivalent".

Therefore, enforcing *a priori* consistency of $\langle\tau_{ij}\rangle\langle S_{ij}\rangle$ through the nonlinear gradient term, as in Li and Meneveau [97], may also minimize the error in the modeled subgrid stress alignment Explicit algebraic subgrid stress models (EASSM) [101] might also be useful for this approach as they have similar forms to equation (2.13).

Another class of mixed models that should effectively represent the mean stress is the scale similarity model, which is usually paired with the Smagorinsky model [29, 68],

$$\tau_{ij}^d \approx -2C_1\Delta^2(\overline{S}_{kl}\overline{S}_{kl})^{1/2}\overline{S}_{ij} + \widehat{\overline{u}_i\overline{u}_j} - \widehat{\overline{u}}_i\widehat{\overline{u}}_j, \tag{2.14}$$

where, as in section 2.1.1, $\widehat{\cdot}$ signifies a secondary filter. Such models were reviewed by Meneveau and Katz [33]. The scale similarity term is much better correlated with exact subgrid stress *a priori* than the Smagorinsky model, with correlation coefficients as large as 0.6 [68, 33], except when used with Fourier cutoff filters. However, the authors are not aware of studies that have measured the *a priori* consistency of the mean stress. Nonetheless, it is expected that models such as equation (2.14) will enable *a priori* consistency of the mean stress and dissipation since the gradient model discussed above can be considered a first-order Taylor series approximation of the similarity model [68].

It appears then that to enable accurate LES with the coarsest possible resolution with eddy viscosity models, one of the modeling enhancements discussed above should be employed, as they allow simultaneous representation of both dissipation and mean stress.

2.2.2 Optimal LES

An LES modeling technique called "optimal LES" was introduced by Langford and Moser [15] as a formal approximation to the ideal LES described briefly in section 1.2. The ideal LES is obtained when the model term $\mathbf{M}(w)$ in the LES equation is modeled as

$$\mathbf{m}(w) = \langle\mathbf{M}(u)|\overline{u} = w\rangle \tag{2.15}$$

whereas in section 1.1, $\mathbf{M}(u)$ is the exact subgrid force associated with a real turbulent field. Notice that the conditional average in equation (2.15) is conditioned on the entire filtered field $\overline{u}$ being the same as the entire LES field w. With this definition, the evolution of the probability density of an ensemble of LES fields w will be the same as that of the filtered real turbulence. Unfortunately, because the condition is on the equality of the entire filtered field, it is essentially impossible for the conditional average in equation (2.15) to be determined.

To obtain an optimal LES model, we formally approximate the conditional average in equation (2.15) using stochastic estimation [102, 103, 104, 105]. In this approach, one postulates a restricted dependence of $\mathbf{m}$ on w as a linear operator acting on a specified vector of possibly non-linear functions of w (an event vector). The linear operator is then determined by minimizing the mean-square error between the estimate and the conditional average [106, 102], which also minimizes the mean-square discrepancy between and optimal model and the exact subgrid term. It is the latter that is actually optimized using theory [107] or data from DNS. As a generalization of this approach, optimal estimates of subgrid terms formulated in terms of neural networks have been proposed by several authors [108, 109, 110].

However, most interesting in the context of the current review is another property of optimal LES models. The model is guaranteed to produce the correct statistical correlations between the model term and the elements of the event vector, in an *a priori* sense [15]. This has two important implications. First, if one has a statistical requirement for the model term as discussed in section 1.2, then one can use the optimal LES formulation to construct a model that satisfies this requirement *a priori*. Second, one can use this property of optimal LES formulations to help identify important *a priori* statistical properties of LES models through *a posteriori* testing of a variety of optimal LES models formulated to have different *a priori* statistical properties.

These ideas were applied to isotropic turbulence with Fourier cutoff filters by Langford

and Moser [15]. A general linear model that ensured *a priori* consistency of the subgrid dissipation spectrum was found to be equivalent to the well-known wavenumber-dependent eddy viscosity with a cusp at the cutoff [47, 90, 111], and was in excellent *a posteriori* agreement with DNS energy spectra and third-order structure functions [112]. Introducing higher order terms to the optimal model did not significantly improve *a priori* correlation with the exact subgrid term or *a posterior* agreement with DNS.

A similar study was conducted in channel flow at $Re_\tau = 590$ by Völker et al. [113], using DNS data. A number of optimal LES formulations were explored. It was found that those formulated for *a priori* consistency of mean subgrid stress, the subgrid wall-normal transport of resolved kinetic energy, and the dissipation yielded the best LES solutions, with accurate wall shear stress, mean velocity, and one-dimensional spectra. This is consistent with the analysis of Meneveau [31] who identified these *a priori* necessary conditions.

When optimal LES is applied with finite volume or box filters, it is most natural to pose the model in terms of stochastic estimates of both viscous and convective momentum fluxes. This effectively treats the numerical operators and the model terms together. In isotropic turbulence, a model of this type that conserves momentum and is formulated for *a priori* consistency of dissipation out-performs dynamic Smagorinsky [56] for both the energy spectrum and the third-order structure function at both finite and infinite Reynolds number [114, 107]. In channel flow with unresolved wall-layers, an optimal model formulated for *a priori* consistency of mean convection and production terms, in addition to mean stress, wall-normal transport and dissipation was needed to attain good *a posteriori* agreement with DNS [115].

The extensive statistical information required to formulate the optimal models described above has generally been obtained from DNS, which makes them unsuitable for use in practical applications. Instead, these models are interesting because of what they say about important *a priori* statistical characteristics of the subgrid model. Possible exceptions are

optimal models constructed based on inertial range models of the statistics for isotropic turbulence as in [107], which may be more generally applicable, provided the filter scale is small enough and the Reynolds number is high enough. An alternative approach proposed by [116] is to determine the optimal estimate dynamically based on information from a coarser filtering of the LES solution, as in the dynamic model [56]. In addition, Park et al. [117] and Fabre and Balarac [67] used optimal estimation models as standards by which to assess errors in other models.

2.2.3 Discussion

The review in the chapter makes it clear that the majority of effort in LES modeling has largely been dedicated toward constructed SGS models that represent the mean rate of kinetic energy dissipation. Progress in subgrid model development to address other challenges in LES has been painfully slow, albeit for a few notable exceptions mentioned above. To move past the "well-resolved" barrier in LES where the majority of the turbulence is resolved, subgrid models must do more for us than dissipate energy. The less the turbulence is resolved, the more the subgrid motions contribute to mean momentum and energy transport. The effects of numerical discretization and resolution inhomogeneity/anisotropy cannot be ignored since the smallest resolved scales, which are the ones impacted, will also be the important energy-containing scales. The statistical characteristics introduced by these complexities are explored in the follow chapters along with corresponding subgrid model developments.

Chapter 3

Numerics and filtering in LES

We turn our attention now to the commutators introduced in equation (1.9), beginning with the homogeneous commutator $\mathcal{C}_j^H(u_i u_j)$. We will consider the case of uniform resolution in this chapter so that $\mathcal{C}_j^I$ is zero. $\mathcal{C}_j^H$ arises because the numerical properties of the discrete derivative operator $\tilde{\delta}_j$ usually differ from those of the partial derivative ∂_j, with the sole exception being for Fourier spectral methods. In numerical analysis, one generally aspires to make the resolution sufficiently fine so that discretization error (and thus $\mathcal{C}^H$) is negligible, however, LES is, by definition, under-resolved. As discussed in section 1.1, information about the small-scale turbulence is discarded through the process of numerical discretization in practice. This includes the projection of the infinite-dimensional velocity field onto a finite-dimensional solution space (often referred to as the implicit filter) and the introduction of numerical derivative operators, which together characterize the scales in the resolved field whose dynamics are accurately represented. In practical applications, numerical projection is typically the only "filter" used to define the LES. Since the resolution scale in an LES often lies in the energy-containing inertial range, the effects of discretization error must generally be considered (again with the sole exception being for Fourier-spectral methods).

Moreover, we are particularly focused on the effects of discretization error in this chapter; however, the non-linearity of the convection term also leads to aliasing, which introduces additional errors in the small-scale features of the approximate convection term ($\tilde{\delta}_j \overline{u}_i \overline{u}_j$). When Fourier analyzed, this aliasing error affects the Fourier modes of the derivative with

$\kappa > 2\pi/3\Delta$. The analysis of Ghosal [118] indicates that aliasing error can overwhelm subgrid stress modeling error and can corrupt the entirety of the resolved turbulence, which was demonstrated experimentally by Kravchenko and Moin [119] and Chow and Moin [120] in simulations of channel flow and stably stratified shear flow, respectively. Thus the effects of aliasing should generally be considered in addition to the discretization errors explored here.

3.1 The effective wavenumber

Numerical approximations to differential operators are typically characterized by the leading order term in their local truncation error e.g, the standard finite difference formula

$$\frac{df}{dx} = \frac{f_{j+1} - f_{j-1}}{2\Delta} + \mathcal{O}(\Delta^2) \tag{3.1}$$

is considered a *second-order* centered difference approximation to the first derivative on a uniform grid of spacing Δ, indicating that the local truncation error will reduce by a factor of four if the mesh spacing is halved. For most applications, this is a sufficient means of characterizing discretization error. However, as discussed above, the resolution scale in LES is fixed significantly above the Kolmogorov scale, so discretization error cannot be resolved away without approaching DNS limits.

It will therefore be more useful to understand how well numerical derivatives $\delta/\delta x$ approximate analytical derivatives $\partial/\partial x$ across the range of resolved spatial scales in LES. The appropriate tool is known as the *effective* or *modified* wavenumber and corresponds to the eigenvalue $i\tilde{\kappa}(\kappa)$ of the numerical derivative operator associated with the eigenfunction $e^{i\kappa x}$. For example, substituting $f = e^{i\kappa x}$ into equation (3.1) yields the effective wavenumber

$$\tilde{\kappa}(\kappa) = \frac{\sin(\kappa\Delta)}{\Delta}, \tag{3.2}$$

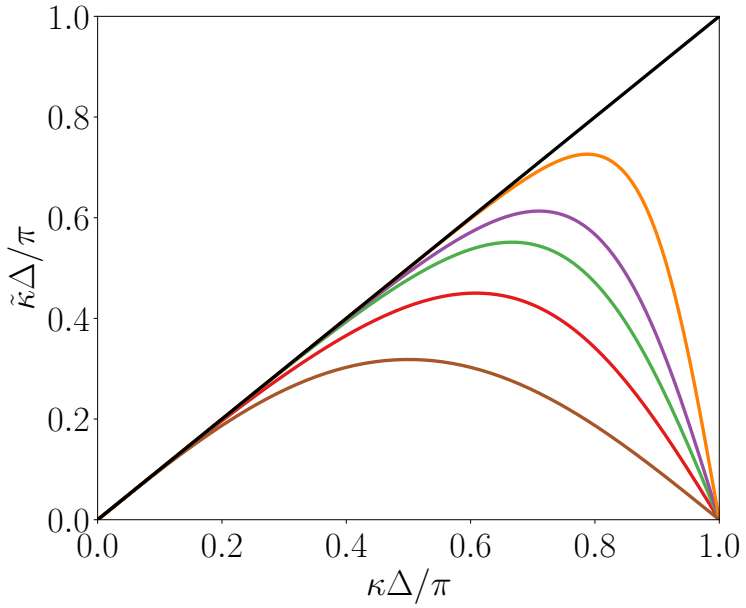

Figure 3.1: The effective wavenumbers corresponding to the first derivative operators for a Fourier-spectral method (——), 7th order B-spline collocation method (——), 4th order B-spline collocation method (——), 3rd order B-spline collocation method (——), 2nd order B-spline collocation method (——), and 2nd order centered difference method (——).

which is plotted in figure 3.1. Clearly, equation (3.1) is an appropriate approximation to the derivative only for the smallest wavenumbers.

Similarly, the effectiveness of a numerical second derivative operator can be examined through its spectrum. In this case, there are two approximations to the second derivative $\partial^2/\partial x^2$ we will consider. The first is repeated applications of the numerical first derivative operators, denoted $\frac{\delta}{\delta x}\frac{\delta}{\delta x}$ with spectrum $-\tilde{\kappa}\tilde{\kappa}$. For the second order centered difference case

$$\frac{\delta}{\delta x}\left(\frac{\delta f}{\delta x}\right) = \frac{f_{j+2} - 2f_j + f_{j-2}}{4\Delta^2}, \qquad \text{and} \qquad \tilde{\kappa}\tilde{\kappa} = -\frac{\sin(\kappa\Delta)^2}{\Delta^2}, \tag{3.3}$$

which is plotted in figure 3.2b. The second is the usual approximation to the second derivative denoted $\frac{\delta^2}{\delta x^2}$ with spectrum $-\widetilde{\kappa^2}$. For the second order centered difference case

$$\frac{\delta^2 f}{\delta x^2} = \frac{f_{j+1} - 2f_j + f_{j-1}}{\Delta^2}, \qquad \text{and} \qquad \widetilde{\kappa^2} = -\frac{2(\cos(\kappa\Delta) - 1)}{\Delta^2}, \tag{3.4}$$

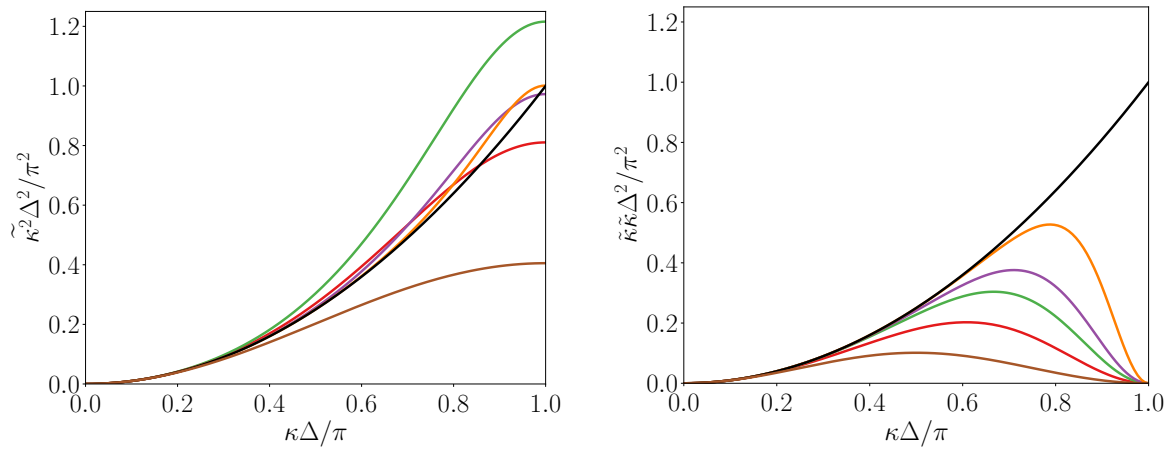

(a) (b)

Figure 3.2: The (negative) spectrum of the second derivative operators corresponding to a Fourier-spectral method (——), 7th order B-spline collocation method (——), 4th order B-spline collocation method (——), 3rd order B-spline collocation method (——), 2nd order B-spline collocation method (——), and 2nd order centered difference method (——). (a) is the standard compact approximation to the second derivative, while (b) is repeated applications of the first derivative operator.

which is plotted in figure 3.2a.

In multiple dimensions a corresponding effective wave "vector" $\tilde{\boldsymbol{\kappa}}$ can be defined with components $\tilde{\kappa}_i$. Similarly, the spectrum of the numerical Laplacian operator can defined as either $-\widetilde{\kappa_j\kappa_j}$ if second derivative operators are used, or $-\tilde{\kappa}_j\tilde{\kappa}_j$ if repeated application of the first derivative is used.

In addition to second order centered difference methods, a periodic B-spline collocation scheme will be used throughout this work, as it provides a convenient numerical treatment for both homogeneous and inhomogeneous resolutions and offers easy access to a range of orders of accuracy. Although second order schemes largely remain the most popular choice among LES practitioners, B-splines have also seen significant use in turbulence simulations [119, 121, 122, 123, 124]. Unlike finite-difference formulas, or more generally any Padé approximation, the effective wavenumber for a periodic B-spline collocation method is most readily determined numerically, with the peculiar exception of cubic B-splines whose first

derivative approximation exactly matches the standard fourth-order compact Padé approximation [125]. Specifically, let B_n^k denote the nth derivative B-spline operator of order k (as defined in, e.g., [20]). In the periodic case, B_n^k is a circulant matrix, so its eigenvalues can be determined through the Fourier analysis. On the domain $[0, 2\pi]$ divided into N intervals, let $\mathbf{F}^{\mathrm{DFT}}$ be the standard discrete Fourier transform matrix whose j, ℓ component is $e^{-2j\ell\pi i/N}$ for $0 \leq j, \ell \leq N$ and let b_n^k be a column of B_n^k. The spectra for the first derivative operator B_1^k and the second derivative operator B_2^k can be computed as $\mathbf{F}^{\mathrm{DFT}} b_1^k / i\mathbf{F}^{\mathrm{DFT}} b_0^k$ and $-\mathbf{F}^{\mathrm{DFT}} b_2^k / \mathbf{F}^{\mathrm{DFT}} b_0^k$, respectively. These spectra are plotted in figure 3.1 and figure 3.2 for various orders of B-splines.

The effective wavenumbers indicate that, for non-spectral numerics, the dynamics of all the resolved scales cannot accurately be represented by the numerical derivative operators. In the following subsections we explore the profound effects this has on implicitly filtered LES, particularly with the representation of the convection term.

Finally, we note that although the numerical experiments here are limited to collocation schemes, similar considerations carry over to Galerkin formulations. In this case, although the derivatives that appear on the basis functions are exact, the associated "discretization error" comes from the properties of the particular discrete basis used. For instance, uniform hat basis functions lead to the same derivative matrices as equations (3.1) and (3.4). Moreover, projecting the resulting first derivative approximation back onto the hat functions and approximating the first derivative again yields the same matrix as equation (3.3), as expected. Further, the extension to multiple dimensions is more straightforward in Galerkin formulations, particularly with non-Cartesian grids, suggesting that this may be a worthwhile approach to explore in extending the work here to more practical three-dimensional applications.

3.2 Numerical energy transfer spectra

Note that much of the material here and in section 3.3 was published previously by Yalla, Oliver, and Moser [126].

A simple flow in which to explore dispersion error effects is infinite Reynolds number forced homogeneous isotropic turbulence with fluctuating velocities $\mathbf{u}$ transported with a uniform convection velocity $\mathbf{U}$, with magnitude U. We consider an LES with homogeneous isotropic resolution Δ, and solve

$$\frac{\partial \overline{u}_i}{\partial t} + U_j \frac{\delta \overline{u}_i}{\delta x_j} + \frac{\delta \mathcal{F}'(\overline{u}_i \overline{u}_j)}{\delta x_j} = -\frac{\delta \overline{p}}{\delta x_i} + \frac{\delta \tau_{ij}}{\delta x_j} + f_i \tag{3.5}$$

$$\frac{\delta \overline{u}_i}{\delta x_i} = 0 \tag{3.6}$$

with periodic boundary conditions, where f_i is the forcing. The homogeneous commutators that should appear in equations (3.5) and (3.6) have been neglected, as is typical in LES, to assess the effects of discretization error. Both filters $\bar{\cdot}$ and $\mathcal{F}'(\cdot)$ are defined to be Fourier cutoff filters, to allow us to isolate dispersion effects from aliasing effects. However, simulations using a collocation projection for $\mathcal{F}'$ yielded results similar to those presented here.

All the operators are implemented in a modified version of the Fourier spectral code POONGBACK [124] by substituting the effective wavenumbers associated with each method for the true wavenumber when evaluating derivatives in Fourier-space. A third-order low storage Runge-Kutta method [127] is used for time advancement, with time step selected to maintain CFL=0.5 as defined in Spalart et al. [127]. The filtered Navier-Stokes equations are solved using the vorticity-velocity formulation of Kim et al. [128]; see appendix A for more details regarding the implementation of the vorticity-velocity formulation for non-spectral numerics.

The forcing f_i is formulated to inject energy at a constant rate ε as in [129] and the simulations are performed in a cubical domain of size L. Because the turbulence is statistically stationary, ε is also the mean rate of kinetic energy dissipation. Unless otherwise indicated, all quantities are reported in units in which $\varepsilon = 1$ and $L = 2\pi$. The filtered velocity will typically be represented with either 32 or 16 Fourier modes in each direction (as specified), for an effective uniform resolution of $\Delta = 2\pi/32$ or $\Delta = 2\pi/16$, and the forcing f_i is active only in the wavenumber range $0 < |\boldsymbol{\kappa}| \leq 2$. The filter $\mathcal{F}(\cdot)$ (a Fourier cutoff) is applied to the nonlinear terms as in a dealiased pseudo-spectral method, by evaluating the nonlinear product on a grid with 3/2 the number of grid points as the number of Fourier modes, and truncating the discrete Fourier transform of the result back to the original number of Fourier modes (the 3/2 rule) [130]. The subgrid stress is approximated by a Kolmogorov model $\tau_{ij} = 2\nu_t S_{ij}$, where $\nu_t = C_m \Delta^{4/3} \varepsilon^{1/3}$ is the eddy viscosity and $S_{ij} = \frac{1}{2}(\delta_i \overline{u}_j + \delta_j \overline{u}_i)$ is the filtered strain rate tensor as in section 2.1.1. The requirements of the subgrid stress model in the context of numerics and filtering will be more closely analyzed in chapter 4. Further, note that the dispersion phenomena reported here is not dependent on this choice of the subgrid model. To isolate the effects of numerical dispersion error the Laplacian that arises from the eddy viscosity model for the subgrid stress because ν_t is constant is treated spectrally. In this case, $C_m = 0.065$ [131, 17].

The statistical effects of dispersion error can be assessed by considering the evolution equation for the instantaneous resolved energy spectrum $\overline{E}(\boldsymbol{\kappa}, t) = \frac{1}{2}\hat{\overline{u}}_j^*(\boldsymbol{\kappa}, t)\hat{\overline{u}}_j(\boldsymbol{\kappa}, t)$. In this setting,

$$\frac{\partial \overline{E}(\boldsymbol{\kappa}, t)}{\partial t} = T_{\mathrm{N}}(\boldsymbol{\kappa}, t) - 2\nu_t |\boldsymbol{\kappa}|^2 \overline{E}(\boldsymbol{\kappa}, t) + F(\boldsymbol{\kappa}, t), \tag{3.7}$$

where $T_{\mathrm{N}}(\boldsymbol{\kappa}, t)$ is a numerical approximation to the resolved transfer spectrum $T^{>}(\boldsymbol{\kappa}, t)$ that represents the exchange of energy between wavenumbers due to triad interactions in the presence of numerical dispersion error, and $F = \mathrm{Re}\left\{\hat{\overline{u}}_j^*(\boldsymbol{\kappa}, t)\hat{f}_j(\boldsymbol{\kappa}, t)\right\}$ is the spectrum of the energy production arising from the forcing.

One-dimensional energy spectra $E_{1\mathrm{D}}(\kappa_1) = \sum_{\kappa_2,\kappa_3} \langle \overline{E}(\boldsymbol{\kappa}, t) \rangle$ and analogous one-dimensional transfer spectra $T_{1\mathrm{D}}(\kappa_1) = \sum_{\kappa_2,\kappa_3} \langle T_{\mathrm{N}}(\boldsymbol{\kappa}, t) \rangle$ are reported here, where the expected value $\langle \cdot \rangle$ is approximated as a time average. When $\mathbf{U} \neq 0$, the convection velocity is chosen to be aligned with the grid direction ($i = 1$) so the one-dimensional spectra reported are in the direction of convection.

Four different forms of the nonlinear terms are commonly used for numerical discretization of the filtered or unfiltered Navier-Stokes equations. While they are equivalent analytically, they are not equivalent in the presence of discretization error, and so result in different forms of the discrete energy transfer spectra. These forms and associated transfer spectra are listed below. For generality, u_i represents the filtered or unfiltered velocity, depending on whether the equations being solved are filtered, for just the remainder of this subsection.

1. Conservative form, $\delta_j(u_j u_i)$:

$$T_{\mathrm{cons}}(\boldsymbol{\kappa}, t) = -\mathrm{Im}\left\{ \sum_{\boldsymbol{\kappa}'} \tilde{\kappa}_\ell \hat{u}_k(\boldsymbol{\kappa}, t) \hat{u}_k^*(\boldsymbol{\kappa}', t) \hat{u}_\ell^*(\boldsymbol{\kappa} - \boldsymbol{\kappa}', t) \right\} \tag{3.8}$$

2. Convective form, $u_j \delta_j(u_i)$:

$$T_{\mathrm{conv}}(\boldsymbol{\kappa}, t) = -\mathrm{Im}\left\{ \sum_{\boldsymbol{\kappa}'} \widetilde{\kappa'_\ell} \hat{u}_k(\boldsymbol{\kappa}, t) \hat{u}_k^*(\boldsymbol{\kappa}', t) \hat{u}_\ell^*(\boldsymbol{\kappa} - \boldsymbol{\kappa}', t) \right\} \tag{3.9}$$

3. Skew-Symmetric form, $\frac{1}{2}\left(\delta_j(u_j u_i) + u_j \delta_j(u_i)\right)$:

$$T_{\mathrm{skew}}(\boldsymbol{\kappa}, t) = -\frac{1}{2}\mathrm{Im}\left\{ \sum_{\boldsymbol{\kappa}'} (\widetilde{\kappa'_\ell} + \tilde{\kappa}_\ell) \hat{u}_k(\boldsymbol{\kappa}, t) \hat{u}_k^*(\boldsymbol{\kappa}', t) \hat{u}_\ell^*(\boldsymbol{\kappa} - \boldsymbol{\kappa}', t) \right\} \tag{3.10}$$

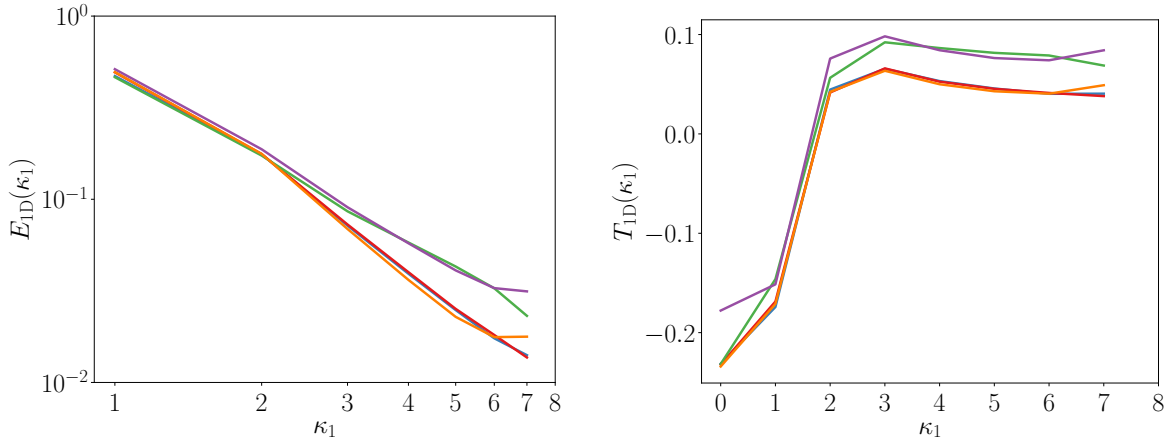

(a) (b)

Figure 3.3: One dimensional spectra of energy E_{1D} and energy transfer rate T_{1D} with a convection velocity of $U = 0$ and effective resolution $\Delta = 2\pi/16$. Shown are spectra from a Fourier-spectral method (———), and 4th order B-spline collocation method using the skew-symmetric form (———), conservative form (———), convective form (———), and rotational form (———). In this case, $\langle \sum_{\boldsymbol{\kappa}} T_{conv} \rangle \approx 0.5$, $\langle \sum_{\boldsymbol{\kappa}} T_{cons} \rangle \approx 0.4$, $\langle \sum_{\boldsymbol{\kappa}} T_{skew} \rangle = 0$, and $\langle \sum_{\boldsymbol{\kappa}} T_{rot} \rangle = 0$.

4. Rotational form, $u_j \delta_j(u_i) - u_j \delta_i(u_j) + \frac{1}{2}\delta_i(u_j u_j)$:

$$T_{\text{rot}}(\boldsymbol{\kappa}, t) = -\text{Im}\left\{ \sum_{\boldsymbol{\kappa}'} \tilde{\kappa}'_\ell \hat{u}_k(\boldsymbol{\kappa}, t) \hat{u}_k^*(\boldsymbol{\kappa}', t) \hat{u}_\ell^*(\boldsymbol{\kappa} - \boldsymbol{\kappa}', t) - \tilde{\kappa}'_k \hat{u}_k(\boldsymbol{\kappa}, t) \hat{u}_\ell^*(\boldsymbol{\kappa}', t) \hat{u}_\ell^*(\boldsymbol{\kappa} - \boldsymbol{\kappa}', t) \right\} \tag{3.11}$$

The transfer spectrum $T(\boldsymbol{\kappa}, t)$ is responsible for transferring energy between resolved modes so $\sum_{\boldsymbol{\kappa}} T(\boldsymbol{\kappa}, t) = 0$ for all t, reflecting conservation of energy. However, it is well known that in the presence of discretization error, both the conservative and convective forms do not satisfy this condition [132, 133, 120, 134]. To analyze this error in the context

of LES, notice that for the conservative form

$$\begin{aligned}\sum_{\boldsymbol{\kappa}} T_{cons}(\boldsymbol{\kappa},t) &= -\mathrm{Im}\left\{\sum_{\boldsymbol{\kappa}}\sum_{\boldsymbol{\kappa}'} \tilde{\kappa}_\ell \hat{\overline{u}}_k(\boldsymbol{\kappa},t)\hat{\overline{u}}_k^*(\boldsymbol{\kappa}',t)\hat{\overline{u}}_\ell^*(\boldsymbol{\kappa}-\boldsymbol{\kappa}',t)\right\} \\ &= -\frac{1}{2}\mathrm{Im}\left\{\sum_{\boldsymbol{\kappa}}\sum_{\boldsymbol{\kappa}'} (\tilde{\kappa}_\ell - \tilde{\kappa'}_\ell)\hat{\overline{u}}_k(\boldsymbol{\kappa},t)\hat{\overline{u}}_k^*(\boldsymbol{\kappa}',t)\hat{\overline{u}}_\ell^*(\boldsymbol{\kappa}-\boldsymbol{\kappa}',t)\right\} \\ &= -\frac{1}{2}\mathrm{Im}\left\{\sum_{\boldsymbol{\kappa}}\sum_{\boldsymbol{\kappa}'} (\tilde{\kappa}_\ell - \tilde{\kappa}'_\ell - \widetilde{(\kappa-\kappa')}_\ell)\hat{\overline{u}}_k(\boldsymbol{\kappa},t)\hat{\overline{u}}_k^*(\boldsymbol{\kappa}',t)\hat{\overline{u}}_\ell^*(\boldsymbol{\kappa}-\boldsymbol{\kappa}',t)\right\}\end{aligned} \quad . \tag{3.12}$$

Similarly, for the convective form,

$$\sum_{\boldsymbol{\kappa}} T_{\mathrm{conv}}(\boldsymbol{\kappa},t) = -\frac{1}{2}\mathrm{Im}\left\{\sum_{\boldsymbol{\kappa}}\sum_{\boldsymbol{\kappa}'} \left(\widetilde{\kappa'_\ell} - \tilde{\kappa}_\ell + \widetilde{(\kappa-\kappa')}_\ell\right)\hat{u}_k(\boldsymbol{\kappa},t)\hat{u}_k^*(\boldsymbol{\kappa}',t)\hat{u}_\ell^*(\boldsymbol{\kappa}-\boldsymbol{\kappa}',t)\right\}. \tag{3.13}$$

For numerical methods other than Fourier spectral, $\tilde{\boldsymbol{\kappa}}$ is a nonlinear function of $\boldsymbol{\kappa}$ (see figure 3.1), so $\tilde{\boldsymbol{\kappa}} - \widetilde{\boldsymbol{\kappa}'} - \widetilde{(\boldsymbol{\kappa}-\boldsymbol{\kappa}')} \neq 0$. Therefore, the violation of conservation of energy for the conservative and convective forms can be directly attributed to the fact that the effective wavenumbers of triad interacting wavemodes do not sum to zero. Thus, the conservative and convective forms will act as an additional source term to the energy balance equations. Interestingly, the velocity field seems to adjust in such a way that both the conservative and convective forms add energy into the system, despite equations (3.12) and (3.13) being equal and opposite, leading to a significant pile up in energy in the dispersion wavemodes in both cases (see figure 3.3). However, the skew-symmetric form does indeed satisfy $\sum_{\boldsymbol{\kappa}} T_{\mathrm{skew}}(\boldsymbol{\kappa},t) = 0$ (with the convective part adding energy and the conservative part removing energy) and therefore avoids any energy pile up in the spectrum (figure 3.3). Similarly, the rotational form is energy conserving by construction so $\sum_{\boldsymbol{\kappa}} T_{\mathrm{rot}}(\boldsymbol{\kappa},t) = 0$. In more complex settings, non-conservative numerics can lead to a blow-up of the numerical simulation and so the skew-symmetric or rotational form is generally preferred. Alternatively, this ad-

ditional energy source must be taken into account in the formulation of the subgrid model (see chapter 4). It should be noted that although the skew-symmetric and rotational forms lead to the correct energy characteristics, they do not correct the underlying dynamics of the dispersive modes, as seen in the following subsection.

3.3 Numerical dispersion effects in LES

The effects of numerical dispersion error are examined in the context of equations (3.5) and (3.6) with a zero and non-zero mean convection velocity. The convection velocity is chosen to be aligned with the grid direction ($i = 1$) so the one-dimensional spectra reported here are in the direction of convection. When the convection velocity is not aligned with the grid, dispersive effects on the one-dimensional spectra similar to those reported here occur in each grid direction in which $\mathbf{U}$ has a non-zero component. The skew-symmetric form of the nonlinear terms is used so energy is conserved between nonlinear interactions. Additionally, six different discrete first derivative operators $\delta/\delta\mathbf{x}$ are used: a Fourier-spectral method, a 2nd order centered difference method, and 2nd, 3rd, 4th, and 7th order B-spline collocation methods (see figure 3.1). The effective resolution is set at $\Delta = 2\pi/32$ so that each of these schemes can adequately represent the forcing modes $|\boldsymbol{\kappa}| \in (0, 2]$.

In the absence of mean convection ($U = 0$), each numerical scheme produces spectra that roughly agree with an equivalently filtered $\kappa^{-5/3}$ theoretical inertial range spectrum (see figure 3.4a). Furthermore, the transfer spectra are identical to that for the Fourier-spectral case for all the numerical approximations (see figure 3.4b). For reference, the statistical characteristics of the turbulence for the $U = 0$, Fourier-spectral case are reported in Table 3.1.

To demonstrate numerical dispersion effects, consider the case with mean convection velocity $U = 35$. In this case, the value of $U/u' \approx 27$ (u' is the root-mean square velocity as defined in table 3.1) is comparable to that at the centerline of a turbulent channel flow, where U/u' ranges from 23 to 30 for friction Reynolds number ranging from 180 to 5200

Table 3.1: Statistical characteristics of LES turbulence averaged over 500 eddy turnover times for the $U = 0$ case with Fourier spectral numerics. Values are normalized by ε and $L/2\pi$.

Resolved Kinetic Energy, $k_{res} = \frac{1}{2}\langle \overline{u}_i \overline{u}_i \rangle$	2.467
RMS Velocity, $u' = \sqrt{(2/3)k_{res}}$	1.282
Integral Scale, $\mathcal{L} = \frac{\pi E_{1\mathrm{D}}(0)}{u'^2}$	1.129
Large Eddy Turnover Time, $T_L = \mathcal{L}/u'$	0.880

[124]. As expected, for spectral numerics, no change from the $U = 0$ case occurs in either the energy spectrum or transfer spectrum. However, for all other numerical schemes, the one-dimensional energy spectra in the direction of convection are significantly reduced over a range of the highest resolved wavenumbers (see figure 3.4c). The corresponding transfer spectra in the direction of convection tend to zero over this range of resolved modes (see figure 3.4d). In effect, numerical dispersion error prevents energy from transferring at the appropriate rate from the largest to smallest resolved scales. As a consequence, energy also piles up in the larger resolved scales as energy is not transferred to the smallest resolved scales at the correct rate for the subgrid model to dissipate (see figure 3.4c). For energy conserving numerics, we must have $\sum_{\boldsymbol{\kappa}} T_{\mathrm{N}}(\boldsymbol{\kappa}, t) = 0$ for all t. To maintain this balance, the energy transfer spectrum at all wavenumbers is affected by the dispersion error that is primarily in the largest wavenumbers (see figure 3.4d). Moreover, the energy transfer rates in directions orthogonal to convection are not degraded, however, the energy spectra in the orthogonal directions are impacted by the errors in the convection direction (not shown).

The reason for the observed degradation of energy transfer to the smallest resolved scales can be understood through analysis of a case in which $U \gg u'$. Let $\epsilon = u'/U \ll 1$ be a small parameter (not to be confused with the mean dissipation rate ε). Then the velocity Fourier coefficients $\hat{\overline{u}}_i$ vary on a fast and a slow time scale. Using a multiscale asymptotic

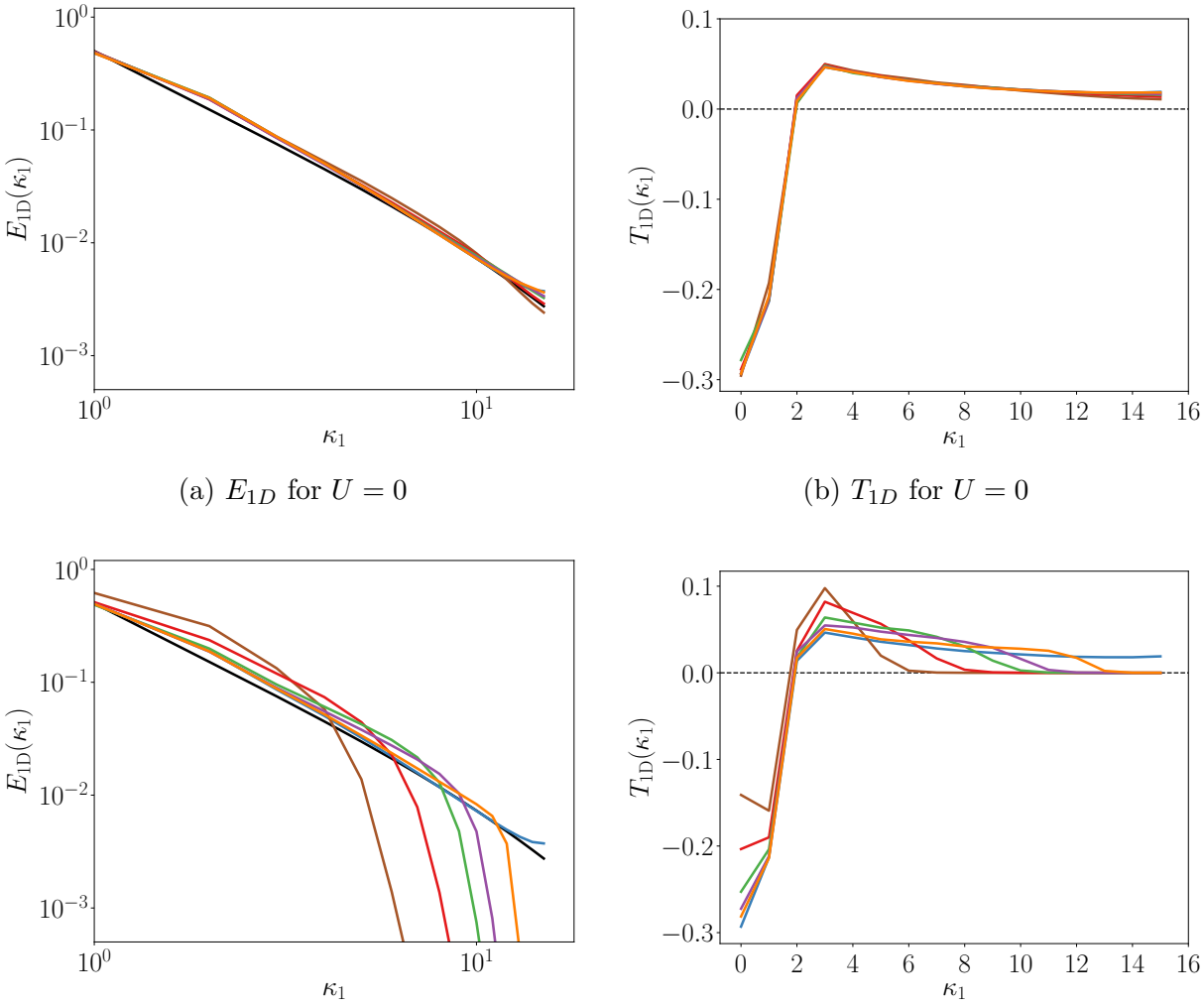

(a) E_{1D} for $U = 0$

(b) T_{1D} for $U = 0$

(c) E_{1D} for $U = 35$

(d) T_{1D} for $U = 35$

Figure 3.4: One dimensional spectra in the convection direction of energy E_{1D} and energy transfer rate T_{1D}, with convection velocities $U = 0$ and 35. Shown are spectra from theory (——), Fourier-spectral method (——), 7th order B-spline collocation method (——), 4th order B-spline collocation method (——), 3rd order B-spline collocation method (——), 2nd order B-spline collocation method (——), 2nd order centered difference method (——).

representation, $\hat{\bar{u}}_i$ can be said to depend on a fast time variable $t_f = t/\epsilon$ and a slow time variable $t_s = t$. Further, as with Taylor's hypothesis, in the continuous case, $\partial/\partial t_f = \epsilon U_j \partial/\partial x_j$ is order one in ϵ. But, when using discrete derivatives as in equation (3.5), the

same analysis yields $\partial/\partial t_f = \epsilon U_j \delta/\delta x_j$. Therefore, $\hat{\overline{u}}_i$ can be written:

$$\hat{\overline{u}}_i(\boldsymbol{\kappa}, t_f, t_s) = \hat{\overline{u}}_i(\boldsymbol{\kappa}, t_s) e^{-i\epsilon \mathbf{U}\cdot\tilde{\boldsymbol{\kappa}} t_f} + \mathcal{O}(\epsilon), \tag{3.14}$$

where $\hat{\overline{u}}_i(\boldsymbol{\kappa}, t_s)$ is simply the fast time average of $\hat{\overline{u}}_i$, which varies in slow time due to the nonlinear turbulent processes. The instantaneous energy transfer rate for the skew-symmetric form as used here (see equation (3.10)) is then

$$T_{\text{skew}}(\boldsymbol{\kappa}, t_f, t_s) = -\frac{1}{2}\text{Im}\left\{\sum_{\boldsymbol{\kappa}'} (\widetilde{\kappa'_\ell} + \tilde{\kappa}_\ell)\hat{\overline{u}}_k(\boldsymbol{\kappa}, t_s)\hat{\overline{u}}^*_k(\boldsymbol{\kappa}', t_s)\hat{\overline{u}}^*_\ell(\boldsymbol{\kappa} - \boldsymbol{\kappa}', t_s) e^{i\epsilon\mathbf{U}\cdot(\tilde{\boldsymbol{\kappa}'} - \tilde{\boldsymbol{\kappa}} - (\widetilde{\boldsymbol{\kappa}' - \boldsymbol{\kappa}}))t_f}\right\} + \mathcal{O}(\epsilon). \tag{3.15}$$

Since the turbulence is assumed to be stationary and ergodic, the expected value $\langle T(\boldsymbol{\kappa})\rangle$ is time independent and can be estimated as a time average as follows:

$$\langle T_{\text{skew}}(\boldsymbol{\kappa})\rangle = -\frac{1}{2}\text{Im}\left\{\sum_{\boldsymbol{\kappa}'} (\widetilde{\kappa'_\ell} + \tilde{\kappa}_\ell)\langle\hat{\overline{u}}_k(\boldsymbol{\kappa}, t_s)\hat{\overline{u}}^*_k(\boldsymbol{\kappa}', t_s)\hat{\overline{u}}^*_\ell(\boldsymbol{\kappa} - \boldsymbol{\kappa}', t_s)\rangle \left\langle e^{i\epsilon\mathbf{U}\cdot(\tilde{\boldsymbol{\kappa}'} - \tilde{\boldsymbol{\kappa}} - (\widetilde{\boldsymbol{\kappa}' - \boldsymbol{\kappa}}))t_f}\right\rangle_{t_f}\right\} + \mathcal{O}(\epsilon), \tag{3.16}$$

where $\langle\cdot\rangle_{t_f}$ is the fast time average, and the (slow) time average of the $\hat{\overline{u}}_i$ triple product has been replaced by the expected value by ergodicity.

Clearly, the fast time average in equation (3.16) is zero unless

$$\omega_T = \mathbf{U}\cdot(\tilde{\boldsymbol{\kappa}'} - \tilde{\boldsymbol{\kappa}} - (\widetilde{\boldsymbol{\kappa}' - \boldsymbol{\kappa}})) = 0, \tag{3.17}$$

in which case it is one. When using Fourier spectral numerics, $\tilde{\boldsymbol{\kappa}} = \boldsymbol{\kappa}$ and equation (3.17) is satisfied identically for all the triad interactions represented in equation (3.16). However, for other numerical schemes, such as those analyzed in figure 3.1, $\tilde{\boldsymbol{\kappa}}$ is a nonlinear function of $\boldsymbol{\kappa}$, and so (3.17) will generally not be satisfied unless $|\mathbf{U}\cdot\boldsymbol{\kappa}| = |\mathbf{U}\cdot\boldsymbol{\kappa}'|$, severely limiting the triad interactions that contribute to net energy transfer among wavenumbers. This occurs because the spatial Fourier modes that can interact to transfer energy are determined by

the wavenumbers $\boldsymbol{\kappa}$, while the convective dynamics of those modes are determined by $\tilde{\boldsymbol{\kappa}}$. The result is that the interacting wavemodes do not maintain consistent phase relationships, essentially shutting down the energy transfer and producing spectral anomalies like those shown in Fig. 3.4. The inhibition of energy transfer due to phase scrambling discussed here is similar to that caused by rapid rotation as described, for example, in [135, 136].

Of course, this analysis is asymptotic for $\epsilon \to 0$. For any finite ϵ, there will be $\mathcal{O}(\epsilon)$ corrections because the phase scrambling effect of the mean convective dispersion errors as described above will compete with the nonlinear evolution of the Fourier modes. In this case, one would expect that triad interactions for which $\omega_T \neq 0$ in (3.17) would be weakened, rather than completely excluded, depending on the magnitude of ω_T. This may be the reason the spectra in Fig. 3.4 roll off smoothly for wavenumbers with significant dispersion error.

The condition (3.17) suggests that the strength of the dispersion effect on the energy transfer at any wavenumber is determined by $U(\kappa - \tilde{\kappa}) = U\Delta\kappa$, which measures the rapidity of the phase scrambling. Provided $U\Delta\kappa$ at some wavenumber is sufficiently small compared to the rate of other processes, one would expect the dispersion effects on the energy transfer at that wavenumber to be negligible. This is supported by the observation that, for the third, fourth and seventh order B-splines [1], the value of $\Delta\kappa$ at the wavenumbers where the transfer spectrum crosses that for spectral numerics in Figure 3.4d is approximately the same (~ 0.4). In addition, in simulations with the convection velocity increased (decreased) by a factor of two (not shown), $\Delta\kappa$ at this cross-over is decreased (increased) by about a factor of two.

While the above analysis was performed for the skew-symmetric form of the nonlinear terms, the structure of the transfer spectrum is similar for other forms (see section 3.2), and the same analysis applies. This suggests that the same dispersion effects should occur for the convective, conservative and rotational form of the nonlinear terms, and this was confirmed

[1] The lower order approximations do not have a wide enough range of non-dispersive scales for the scaling to hold.

numerically. In particular, when $U \gg u'$, dispersion errors due to mean convection dominate the energy pile-up introduce by non-conservative numerics, and the results are similar to those presented here for the skew-symmetric form.

In many LES applications, the turbulence is convected with a velocity large compared to the turbulence fluctuations (e.g., turbulent boundary layers [137], flow through a wind turbine [138]). In LES of such turbulent flows, numerical dispersion error causes a decoherence of the phase relationship among interacting Fourier modes, which results in a reduction of the energy transfer rate from large to small resolved scales in the direction of convection. This leads to nonphysical changes in the energy distribution across all resolved scales.

On the other hand, the $U = 0$ results indicate that the nonlinear dispersion error has little effect on the LES spectra, despite an inaccurate representation of the resolved scale dynamics (see Figures 3.4a and 3.4b). This is interesting because one might expect the energy transfer to be affected by phase scrambling due to convection of the small scales by the large scales even when $U = 0$. By analogy with the scaling with the mean convection velocity, the strength of this effect should scale with u' so that, provided $u'\Delta\kappa$ is sufficiently small compared to the rate of other processes, the impact of dispersion on energy transfer should be negligible. Presumably this is the case for all scales in the $U = 0$ simulations shown in Figure 3.4. However, the good $U = 0$ results presented here should be interpreted with caution, since the highly dispersive scales can have a damaging effect in more complex flows [118, 119, 120, 139]. Consequently, in an LES, we generally cannot expect the scales with significant dispersion error to be dynamically meaningful.

In later subsections we explore approaches to addressing the consequences of discretization error in LES. The results here make it clear that the standard for sufficiently small dispersion error depends on the convection velocity and possibly other flow characteristics, not just the characteristics of the derivative approximation. As such, the effective range of dynamically resolved scales is not defined by the grid spacing, but rather the dispersive

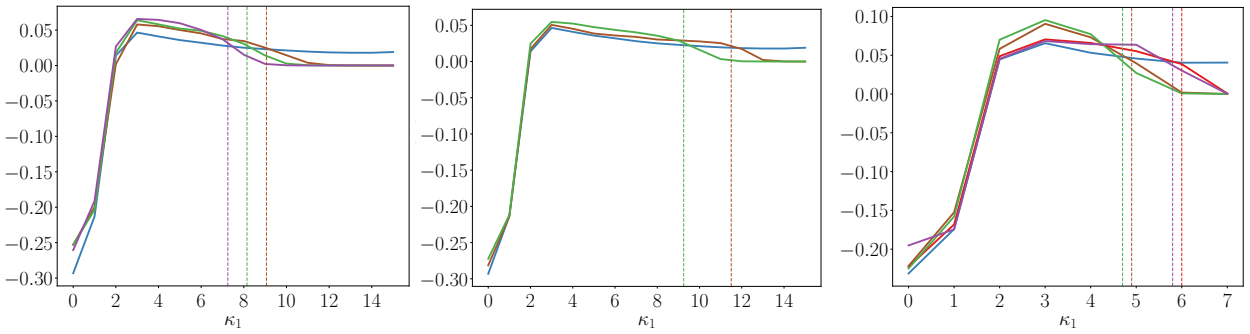

(a) (b) (c)

Figure 3.5: One-dimensional energy transfer spectra in the direction of mean convection for the following cases. (a) 3rd order Bspline collocation method with $U = 70$ (——) with $U = 35$ (——) with $U = 17.5$ (——) and $\kappa_c = 16$. (b) 4th (——) and 7th (——) order Bspline collocation method with $\kappa_c = 16$ and $U = 35$. (c) 4th order Bspline collocation with $U = 35$ (——) and $U = 25$ (——) and 7th order Bspline collocation with $U = 35$ (——) and $U = 25$ (——). In all plots the Fourier-spectral case is shown in (——). The vertical dashed lines represent the scaling $U\Delta\kappa \sim \varepsilon^{1/3}\kappa^{-2/3}\kappa_c^{4/3}$ for each case of the corresponding color (see table 3.2).

properties of the numerical approximation to the convection term.

3.4 Scaling of the dispersive timescale

In the previous section the timescale $1/U\Delta\kappa$ was identified as a measure of the rapidity of the phase scrambling introduce by numerical dispersion. In this section we present preliminary results that are suggestive of a scaling law for this timescale.

Nine simulations were performed in the same setting as in section 3.3 for various mean convection velocities, numerical schemes, and cutoff wavenumbers. We use the wavenumber region where the one dimensional energy transfer spectra crosses that for the Fourier-spectral case as an indicator for the scale at which dispersion error shuts down the energy transfer rate to higher wavenumbers (see figure 3.5). The data is suggestive of the scaling

$$U\Delta\kappa \sim \varepsilon^{1/3}\kappa^{-2/3}\kappa_c^{4/3} \tag{3.18}$$

Table 3.2: Data for the scaling $U\Delta\kappa = C\varepsilon^{1/3}\kappa^{-2/3}\kappa_c^{4/3}$ for the cases shown in figure 3.5

U	κ	$\Delta\kappa$	κ_c	C
70	7.25	0.21	16	1.36
35	8.15	0.38	16	1.33
17.5	9.06	0.73	16	1.37
35	9.25	0.36	16	1.37
35	11.5	0.31	16	1.37
25	4.9	0.29	8	1.31
25	6.0	0.26	8	1.34
35	4.7	0.22	8	1.35
35	5.8	0.19	8	1.34

with constant of proportionality $C \approx 1.3$ (see table 3.2), although it is not clear why this scaling is appropriate. More work is needed to make this scaling robust, however, this result may be helpful for suggesting model dependencies for the timescale $U\Delta\kappa$. This timescale will be explored further in chapter 4.

3.5 Numerical adjustments to the subgrid stress model constant

Although the focus here is primarily on the effects of dispersion error introduced through the numerical approximation to the first derivative operator, the dissipative effects of the numerical approximation to the second derivative operator are also worth discussing. This is particularly important because the numerical approximation to the Laplacian affects the dissipation of the subgrid stress term and the dissipation rate was identified as the most critically important statistical characteristic to satisfy in LES modeling in chapter 2. The effects of dissipative numerical approximations to the nonlinear terms are not considered here (see section 2.1.2).

The Kolmogorov eddy viscosity model of the SGS term leads to $-T^{<}(\boldsymbol{\kappa}, t) = 2C_m\varepsilon^{1/3}\Delta^{4/3}|\boldsymbol{\kappa}|^2 E(\boldsymbol{\kappa}, t)$. Therefore, setting the constant based on equations (2.3) and (2.4) will guarantee the model

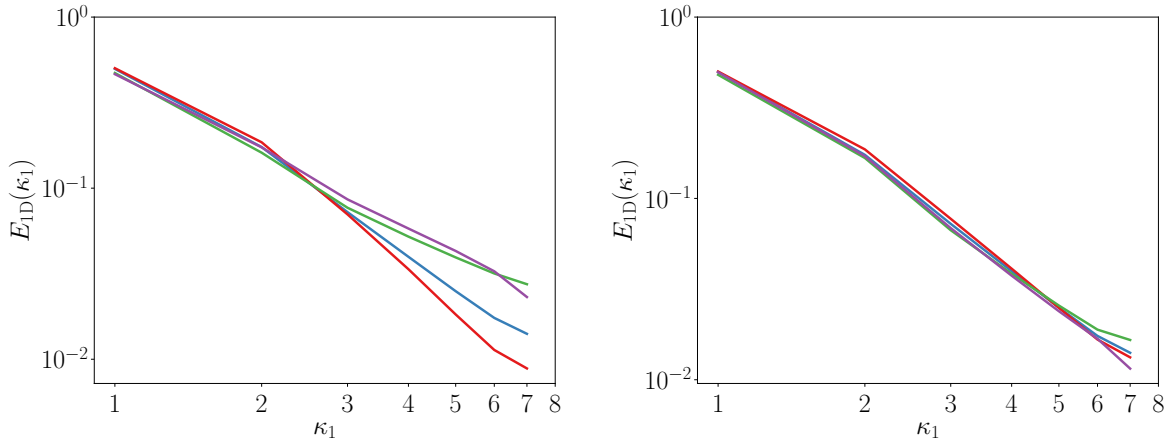

Figure 3.6: One dimensional energy spectra for an LES computed with Fourier-spectral first derivatives operators and 3rd order B-spline second derivatives (——), and 2nd order centered difference second derivatives (——). An LES with 4th order B-spline first derivatives, Fourier-spectral second derivatives and the conservative form of the nonlinear terms is also shown (——). In (a) the spectral value of $C_m = 0.065$ is used. In (b) the constants correspond to those calculated from equations (3.19) and (3.20). The theoretical energy spectra are shown in ——.

produces a dissipation rate of ε *a priori* for isotropic turbulence. However, the dissipative characteristics of the numerical approximation to the second derivative operators must be taken into account (see figure 3.6a). If the goal of the SGS model is solely to represent the dissipation rate correctly and an energy-conserving approximation to the nonlinear terms is used, numerical second derivative approximations can be incorporated into the model by setting

$$C_m = \frac{2\pi}{C_{kol}\Delta^{4/3}} \int_{\mathcal{D}} \widetilde{\kappa_\ell \kappa_\ell} |\boldsymbol{\kappa}|^{-11/3} d\boldsymbol{\kappa}, \tag{3.19}$$

where C_{kol} is the Kolmogorov constant. Values for the numerical schemes shown in figure 3.2a are listen in table 3.3. This formulation will guarantee the SGS model produces the correct dissipation in the presence of numerical dissipation a priori. To demonstrate the effects of this a posteriori, consider an LES of isotropic turbulence represented with uniform resolution of $\Delta = 2\pi/16$, Fourier-spectral first derivative operators, and lower-order

Table 3.3: Subgrid stress model constants for $\nu_t = C_m \varepsilon^{1/3} \Delta^{4/3}$ based on equation (3.19) and $C_{kol} = 1.75$.

Numerics for $\widetilde{\kappa_j \kappa_j}$	C_m
Fourier-spectral	0.065
2nd order centered difference	0.085
2nd order B-splines collocation	0.063
3rd order B-splines collocation	0.053
4th order B-splines collocation	0.062
7th order B-splines collocation	0.064

numerical approximations to the second derivative operator that appears on the subgrid stress term (see figure 3.6a). Clearly for over-dissipative numerics (e.g., 3rd-order B-splines) or under-dissipative numerics (e.g., 2nd-order centered difference) setting the constant this way restores balance to energy equation, leading to five-thirds inertial range spectrum (see figure 3.6b).

This restorative property of the SGS can be pushed further by incorporating other information from the energy balance equation into the model constant. For instance recall that the conservative form of the nonlinear term leads to the energy source $\sum_{\boldsymbol{\kappa}} T_{cons} > 0$. Considering the same example as in figure 3.3 but setting the subgrid stress model constant C_m as

$$C_m = \frac{2\pi \left(\varepsilon + \sum_{\boldsymbol{\kappa}} T_{cons}\right)}{C_{kol} \Delta^{4/3} \varepsilon} \int_{\mathcal{D}} \widetilde{\kappa_\ell \kappa_\ell} |\boldsymbol{\kappa}|^{-11/3} d\boldsymbol{\kappa} \tag{3.20}$$

also leads to five-thirds inertial range spectrum, appropriately reducing the energy pile up introduced by the conservative form (see figure 3.6). Here we are not advocating for correcting dispersive errors simply through the SGS constant, but that the energy injection/dissipation rate introduced by numerical approximations to $T^<$ must be accounted for in the energy balance (in this case, through the subgrid stress model for $T^>$). One cannot expect equa-

tion (3.19) or equation (3.20) to work for all cases, i.e., producing a five-thirds spectrum cannot always be done by simply adding or removing energy through an eddy viscosity. In chapter 4 the requirements of the subgrid stress to produce a Kolmogorov spectrum for given numerics and filter are explored further. An a priori estimate of the numerical approximation to $\sum_{\boldsymbol{\kappa}} T^{<}(\boldsymbol{\kappa})$ for a general form of the nonlinear terms is also derived so that adjusting the subgrid stress constant as equation (3.20) may be computed a priori.

3.6 Explicit filtering

To mitigate discretization error, the large scales to be simulated can be defined using an explicit filter, acting in addition to the implicit filter defined by the numerical discretization, to ensure that the scales with significant dispersion error are not energized [140, 141, 142, 143, 144, 145, 146, 147, 148, 149]. In this case the filter $\mathcal{F}' = \tilde{\cdot}$ includes an explicit smoothing filter with filter kernel $\tilde{G}$ and filter width $\tilde{\Delta} \geq \Delta$. Although the explicit filter is only directly applied to the nonlinear terms, the velocity field is considered to be effectively filtered by $\tilde{G}$, because the nonlinear terms are responsible for transferring energy to larger modes. As such, the frequency content of the filter velocity field $\overline{\mathbf{u}}$ is dictated by the properties of filter $\tilde{\cdot}$. It is important to note that this procedure is different from the approach of filtering the velocity field after a certain number of time steps, which should generally be avoided because the filter will then depend on the temporal discretization and result in a cumulative effect of multiple filterings of the velocity field [140, 1].

Explicit filters are commonly not used in practice to maximize the range of scales being represented — it is argued that removing resolved scales is a waste of computational effort that could be spent performing an LES on a finer grid. To explore this, consider the idealized case of a Fourier cutoff explicit filter applied to the nonlinear terms in the convecting homogeneous isotropic turbulence examples shown in figure 3.4. By using an explicit filter width corresponding to the wavenumber at which the energy transfer rate shuts down due

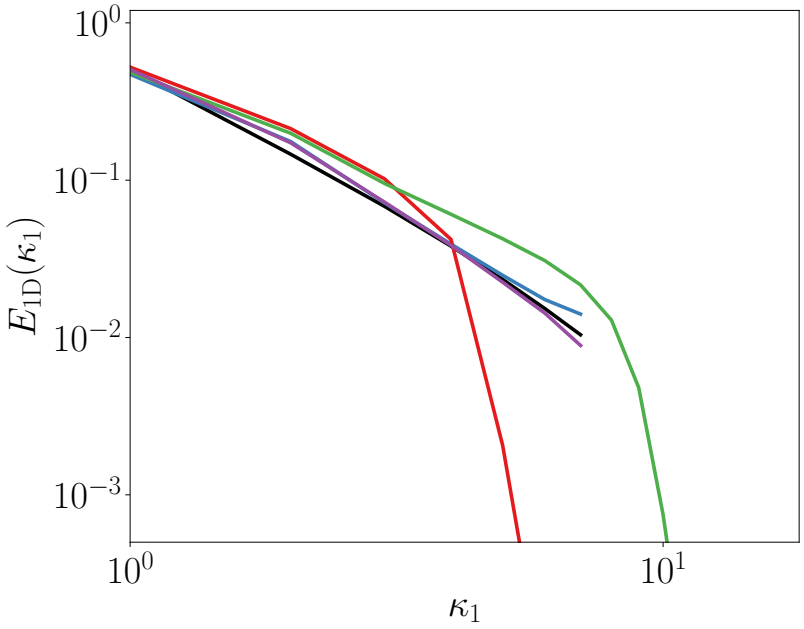

Figure 3.7: One-dimensional energy spectra in the convection direction with a mean convection velocity of $U = 35$: Theory (——); Fourier-spectral method for a resolution scale of $\Delta = 2\pi/16$ (——); 3rd order Bsplines at a resolution scale of $\Delta = 2\pi/16$ (——); 3rd order Bsplines at a resolution scale of $\Delta = 2\pi/32$ (——); 3rd order Bsplines at a resolution scale of $\Delta = 2\pi/32$ with a Fourier-cutoff filter applied at an effective filter width of $\Delta = 2\pi/16$ (——).

to dispersion, the explicit filter removes the highly dispersive modes and thus corrects the energy dynamics in the well resolved modes (see figure 3.7). Simply increasing the resolution without introducing an explicit filter leads to an LES without meaningful statistics at any resolved scale, because the dispersive modes interact with the well represented modes in a way that is damaging to the entire spectrum. As such the cost penalty truly comes from using numerical schemes with poor dispersive characteristics and explicit filters serve as a potential remedy for a range of the resolved scales. We note that it may also be possible to address discretization error through further refinements to the subgrid model as will be explored in chapter 4. In either case, the dispersion characteristics place a fundamental limit on the range of scales that are dynamically meaningful in an LES.

The goal of explicit filtering needs to be examined. The literature, e.g., [148], often

suggest that explicit filters are needed to obtain "grid independent" LES solutions so that LES models and flow statistics are decoupled from the computational grid resolution. This goal is not very useful to practical LES and convergence studies often require resolutions that approach DNS limits. Instead, the aim here is to formulate an LES that maximizes the range of meaningful statistics across the resolved scales for a given computational grid.

Many of the considerations regarding numerics carry over to explicit filtering. For instance, applying an explicit filter to the nonlinear term in conservative form $\delta_j\widetilde{\overline{u}_i\overline{u}_j}$ leads to the energy transfer function

$$\tilde{T}_{\text{cons}}(\boldsymbol{\kappa},t) = -\text{Im}\left\{\sum_{\boldsymbol{\kappa}'}\tilde{G}(\boldsymbol{\kappa})\tilde{\kappa}_\ell\hat{\overline{u}}_k(\boldsymbol{\kappa},t)\hat{\overline{u}}_k^*(\boldsymbol{\kappa}',t)\hat{\overline{u}}_\ell^*(\boldsymbol{\kappa}-\boldsymbol{\kappa}',t)\right\}. \tag{3.21}$$

The combined energy injection rate introduced by numerics and filtering in this formulation is then

$$\sum_{\boldsymbol{\kappa}}\tilde{T}_{\text{cons}}(\boldsymbol{\kappa},t) = -\frac{1}{2}\text{Im}\left\{\sum_{\boldsymbol{\kappa}}\sum_{\boldsymbol{\kappa}'}(\tilde{G}(\boldsymbol{\kappa})\tilde{\kappa}_\ell - \tilde{G}(\boldsymbol{\kappa}')\tilde{\kappa}'_\ell - \tilde{G}(\boldsymbol{\kappa}-\boldsymbol{\kappa}')\widetilde{(\kappa-\kappa')}_\ell)\hat{\overline{u}}_k(\boldsymbol{\kappa},t)\hat{\overline{u}}_k^*(\boldsymbol{\kappa}',t)\hat{\overline{u}}_\ell^*(\boldsymbol{\kappa}-\boldsymbol{\kappa}',t)\right\}. \tag{3.22}$$

Therefore non-Fourier cutoff explicit filters destroy the symmetries necessary to conserve energy in the same way as non-Fourier spectral numerics. The equivalent skew-symmetric form needed to restore conservation of energy in this context reads $\frac{1}{2}(\delta_j\widetilde{\overline{u}_i\overline{u}_j} + \overline{u}_j\widetilde{\delta_j\overline{u}_i})$ so that the convective part introduces an energy injection rate of

$$\sum_{\boldsymbol{\kappa}}\tilde{T}_{\text{conv}}(\boldsymbol{\kappa},t) = -\frac{1}{2}\text{Im}\left\{\sum_{\boldsymbol{\kappa}}\sum_{\boldsymbol{\kappa}'}(\tilde{G}(\boldsymbol{\kappa}')\tilde{\kappa}'_\ell + \tilde{G}(\boldsymbol{\kappa})\tilde{\kappa}_\ell - \tilde{G}(\boldsymbol{\kappa}'-\boldsymbol{\kappa})\widetilde{(\kappa'-\kappa)}_\ell)\hat{\overline{u}}_k(\boldsymbol{\kappa},t)\hat{\overline{u}}_k^*(\boldsymbol{\kappa}',t)\hat{\overline{u}}_\ell^*(\boldsymbol{\kappa}-\boldsymbol{\kappa}',t)\right\}, \tag{3.23}$$

exactly canceling equation (3.22). However, note that $\overline{u}_j\widetilde{\delta_j\overline{u}_i}$ does not necessarily reside in the LES solution space and so it may generally not be possible to correct the energy balance in this way without introducing additional aliasing errors. Instead, the additional energy source/sink introduced by graded explicit filters must be accounted for in the formu-

lation of the dissipative model for the subgrid stress. Clearly for Fourier-spectral numerics equations (3.22) and (3.23) approach zero as $\tilde{G}(\boldsymbol{\kappa})$ approaches a Fourier cutoff filter.

Further, non-Fourier cutoff filters introduce an additional operator to the nonlinear terms that is not Galilean invariant, as with non-Fourier spectral numerics. As such, we can expect the same dispersive effects from section 3.3 to carry over to explicit filters. Introducing the same type of multiscale assumption, the explicitly filtered velocity field can be written

$$\hat{\overline{u}}_i(\boldsymbol{\kappa}, t_f, t_s) = \hat{\overline{u}}_i(\boldsymbol{\kappa}, t_s) e^{-i\epsilon \mathbf{U}\cdot\tilde{G}(\boldsymbol{\kappa})\tilde{\boldsymbol{\kappa}} t_f} + \mathcal{O}(\epsilon), \tag{3.24}$$

and the expected value $\langle \tilde{T}(\boldsymbol{\kappa}) \rangle$ can be estimated to leading order as

$$\langle \tilde{T}_{\text{cons}}(\boldsymbol{\kappa}) \rangle = -\text{Im}\left\{ \sum_{\boldsymbol{\kappa}'} \tilde{G}(\boldsymbol{\kappa}) \tilde{\kappa}_\ell \langle \hat{\overline{u}}_k(\boldsymbol{\kappa}, t_s) \hat{\overline{u}}_k^*(\boldsymbol{\kappa}', t_s) \hat{\overline{u}}_\ell^*(\boldsymbol{\kappa} - \boldsymbol{\kappa}', t_s) \rangle \left\langle e^{i\epsilon \mathbf{U}\cdot(\tilde{G}(\boldsymbol{\kappa}')\tilde{\boldsymbol{\kappa}}' - \tilde{G}(\boldsymbol{\kappa})\tilde{\boldsymbol{\kappa}} - \tilde{G}(\boldsymbol{\kappa}'-\boldsymbol{\kappa})\widetilde{(\boldsymbol{\kappa}'-\boldsymbol{\kappa})}) t_f} \right\rangle_{t_f} \right\}. \tag{3.25}$$

As in equation (3.16), this is zero unless

$$\omega_T = \mathbf{U}\cdot(\tilde{G}(\boldsymbol{\kappa}')\tilde{\boldsymbol{\kappa}}' - \tilde{G}(\boldsymbol{\kappa})\tilde{\boldsymbol{\kappa}} - \tilde{G}(\boldsymbol{\kappa}'-\boldsymbol{\kappa})\widetilde{(\boldsymbol{\kappa}'-\boldsymbol{\kappa})}) = 0. \tag{3.26}$$

For example, consider a spherical Gaussian filter with filter width equal to twice the resolution scale

$$\tilde{G}^{\text{gauss}}(\boldsymbol{\kappa}) = \exp\left(-\frac{|\boldsymbol{\kappa}|^2(2\Delta)^2}{24}\right), \tag{3.27}$$

which has been commonly advocated as an explicit filter in LES [120, 144]. We apply this filter to the nonlinear terms in conservative form with Fourier-spectral numerics in the same setting as section 3.3 with the subgrid stress model length scale now defined through $\tilde{\Delta} = 2\Delta$ (see figure 3.8). In the presence of a mean convection velocity, the explicit filter disrupts the phase relationship between velocity Fourier modes, in the same way as numerical dispersion error, leading to a further degradation of the energy spectrum in the larger wavenumbers

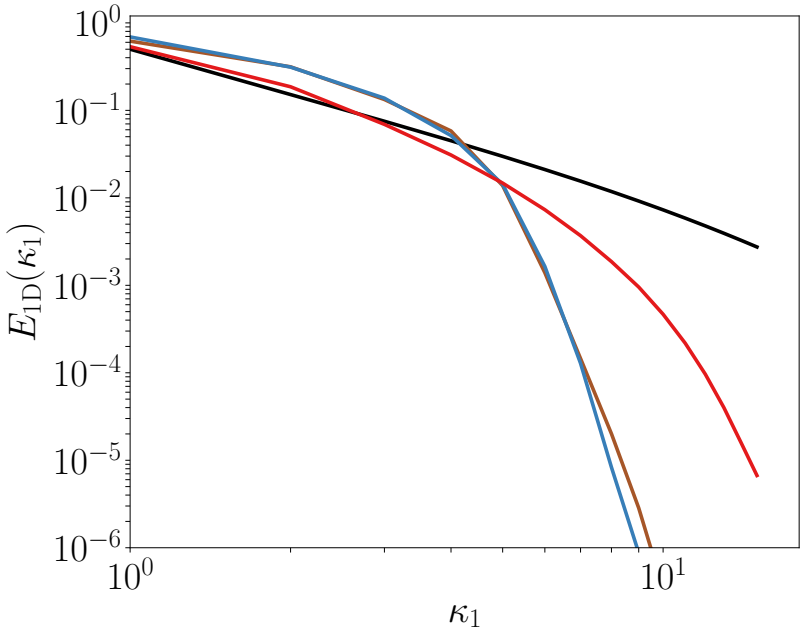

Figure 3.8: One-dimensional energy spectra in the direction of the mean convection velocity U. Filtered five-thirds spectrum (——); 2nd order centered difference method in the skew-symmetric form with $U = 35$ from figure 3.4 (——); Fourier-spectral numerics with a spherical Gaussian explicit filter applied to the conservative form of the nonlinear terms with an effective filter width of $\tilde{\Delta} = 2\Delta$ and a mean convection velocity of $U = 0$ (——) and $U = 35$ (——).

(see figure 3.8). This may not sound problematic at first since the goal of an explicit filter *is* to shut down the energy transfer rate to large wavenumbers. However, for non-cutoff filters, wavenumbers greater than $\pi/\tilde{\Delta}$ are still energized and interact with the well resolved modes in a way that must be accounted for. Clearly in the case of mean convection, the further shut down of the energy transfer rate by the explicit filter leads to an energy pile up in the well resolved modes, corrupting the energy distribution throughout the entire range of resolved modes (see figure 3.8).

As shown here, although explicit filters offer a potential remedy to the issues introduced by numerical discretization error, unless properly constructed they can lead to the same type of errors in LES. In the following sections we explore the construction of practical explicit filters that closely approximate a Fourier cutoff filter, as has been advocated in the literature

[146, 150, 147], so that the errors in equations (3.21) and (3.26) are small. In chapter 4, we develop an a priori estimate of what is required from the subgrid stress model for a given numerics and filter to lead to meaningful second order statistics in an LES.

Before proceeding we note that, despite their similarities, there is a fundamental difference between filtering and numerical dispersion. In one-dimension we can cast the numerical errors as filters through the filter $G^{\text{num}}(\kappa) = \tilde{\kappa}/\kappa$. For the second order centered difference case, $G^{CD} = \sin(\kappa\Delta)/\kappa\Delta$ and, in fact,

$$G^{CD}(\kappa) \approx 1 - \frac{(\Delta\kappa)^2}{6} + \mathcal{O}(\Delta\kappa)^4 \approx G^{\text{gauss}}(\kappa). \tag{3.28}$$

Therefore we expect the errors in equations (3.21) and (3.26) to be similar for second order centered difference numerics and a Gaussian filter with filter width at twice the resolution scale, which is indeed the case for the dispersion results shown in figure 3.8. However, in three dimensions the process of numerical discretization introduces an inherent anisotropy that cannot be represented by an effective three-dimensional filter operator acting on the velocity field [140]. As such, the implicit filter essentially acts on each coordinate direction whereas the explicit filter can be defined as a three dimensional operator as in equation (1.5). This fact has been used as an argument against implicitly filter LES [140], however, it should be noted that an implicit filter always exists whether or not an explicit filter is applied.

3.7 Filtering in practice

The theoretical developments of several filtering techniques in LES (beyond just explicit filtering) rely on being able to apply analytical filters in wavespace whose transfer function is known. However, for simulations performed in physical space, applying a convolution filter is computational infeasible. There are generally only two approaches that are used in LES for applying a filter in physical space, which will be discussed in this section.

The first approach involves constructing discrete filters whose value at a point is defined as linear combinations of weights at the neighboring points [146, 147, 151]. In one-dimension, the filter value of the variable u at the grid point of index i is

$$\overline{u}_i \equiv \sum_{j=-N}^{N} w_j u_{i+j} \tag{3.29}$$

where N is the radius of the discrete filter stencil and $\sum_j w_j = 1$. The larger N, the better 3.29 can approximate a Fourier cutoff filter. An additional requirement is usually placed on the values of w_j so that the discrete filter also has N vanishing moments to reduce commutation error, although this requirement does not seem necessary (see section 5.4). Common values for the weight w_j can be found in, e.g., Vasilyev et al. [146]. However, a straightforward extension of this approach is often not possible in multiple dimensions, especially when considering non-uniform or unstructured grids where an obvious dimensional splitting is not available. Bose et al. [149] provides a nice summary of the difficulties with discrete filtering in multiple dimensions and writes,

> "Marsden et al. [147], Haselbacher and Vasilyev [151] have suggested the unstructured generalization of the structured grid approach where the filtering operator relies on a weighted sum of neighboring values. The primary difficulty of both these approaches is that there is no way to ensure that the filtering operator is well behaved (i.e., $0 \leq G(\boldsymbol{\kappa}) \leq 1 \ \ \forall \boldsymbol{\kappa}$), and moreover the exact behavior of the filter kernel is strongly controlled by the distribution of the surrounding mesh points. The algorithm of Marsden et al. [147] additionally requires a careful selection of a subset of neighboring grid points, but it is not obvious that a reasonable subset of neighboring mesh points will exists in the presence of badly skewed and stretched grids. Another difficulty is that there is no clear way to fix the filter width in physical space when the grid is refined even if the data

structures of the unstructured solvers are altered in order to allow for more neighbors."

Another approach to explicit filtering that circumvents the issues mentioned above is to specify a continuous filter kernel and discretize the associated filter operator. This can be thought of as a discrete filter whose weighted coefficients of the neighboring nodes are the coefficients of the discrete scheme associated with the given differential operator [34]. A common choice is to define the filtering operator through the solution of an elliptic relaxation equation, i.e.,

$$\left(1 - \alpha\tilde{\Delta}^2 \frac{\partial^2}{\partial x_j \partial x_j}\right) \overline{u} = u \tag{3.30}$$

where α is a positive constant usually taken to be 1 and $\tilde{\Delta}$ is the desired cutoff length [144]. In this case, the actual filter operator is defined through the Green's function of the associated elliptic operator [144]. The transfer function associated with the filter in equation (3.30) can be analyzed by considering

$$\hat{\overline{u}}(\kappa) = \left(\frac{1}{1 + \alpha\tilde{\Delta}^2\kappa^2}\right) \hat{u}(\kappa), \tag{3.31}$$

which is shown in figure 3.9 for various choices of filter width.

Although equation (3.30) seems to be the most common type of explicit filter used in practice in LES [149, 143, 152], the filters are not particularly sharp and would therefore introduce significant errors in the energy balance as discussed in section 3.6. Mullen and Fischer [150] recognized the need for filters sharper than a second order elliptic relaxation and proposed the general higher order case

$$\left(I - p(\nabla^2)^m\right) \overline{u} = u \tag{3.32}$$

where p is a dimensional constant, I is the identity operator, and $m > 1$. Because the higher order operators $(\nabla^2)^m$ are generally not available in practical LES codes, the work in [150]

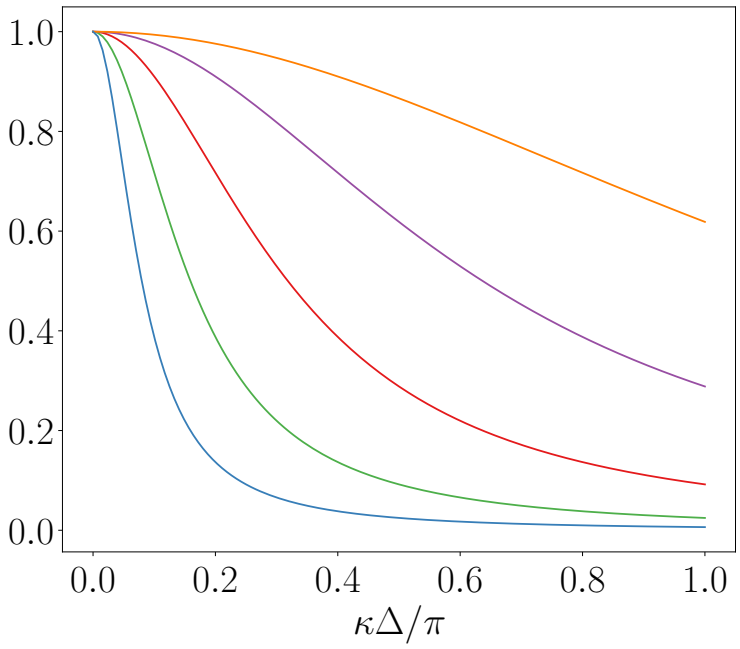

Figure 3.9: Transfer functions for differential filters of the form $\left(1 - \tilde{\Delta}^2 \frac{\partial^2}{\partial x_j x_j}\right) \tilde{\overline{u}} = \overline{u}$ for: $\tilde{\Delta} = \Delta/4$ (——), $\tilde{\Delta} = \Delta/2$ (——), $\tilde{\Delta} = \Delta$ (——), $\tilde{\Delta} = 2\Delta$ (——), $\tilde{\Delta} = 4\Delta$ (——),

focused on approximating solutions to equation (3.32) through a Poisson equation with a particular choice of preconditioner and conjugate gradient method, however, it was noted that much more work was needed to make the formulation robust (in particular, incompressibility was lost). In the work here, we use this discussion as motivation for developing higher order filters that are accessible in practical LES applications. Before constructing such filters, we briefly discuss two other general techniques that are related to filtering in LES that will be useful.

First, an alternative to explicitly filtering the nonlinear terms is to introduce a hyperviscosity or similar term into the LES evolution equations as in section 2.1.3, which has the effect of damping small-scale motions [153, 139]. Such a hyperviscosity can be considered part of the model for $\delta_j \tau_{ij}$, and has the advantage of directly controlling the growth of fluctuations at scales too small to be well represented numerically. However, this approach has the disadvantage that the smoothing filter defining $\overline{u}_i$ is effectively being determined

implicitly through the action of the small-scale damping process and has an inherent time scale dependence.

Second, when an explicit smoothing filter is used, there may be an opportunity to improve the fidelity of the convective term $\tilde{\delta}_j \overline{u}_i \overline{u}_j$ as a model for $\overline{\partial_j u_i u_j}$, and thereby reduce the burden on the subgrid stress model. One can reformulate the $\tilde{\delta}_j$ operator to include applying an inverse filter to $\overline{u}$ before forming the nonlinear product and then applying the explicit filter $\mathcal{F}'$ to the result. This could provide a better approximation of $\overline{u_i u_j}$. Of course, one cannot invert the finite-dimensional projection, so these techniques are only applicable to the explicit filter. In the following, $\mathcal{F}$ includes a homogeneous smoothing filter operator $\mathcal{G}$ in addition to the finite dimensional projection, which is expressed as a convolution with a filter kernel $\tilde{G}$ with filter width Δ_G as in equation (1.5).

One way to approximate the deconvolution operator is to expand $\overline{u}$ in a Taylor series in the filter width Δ_G to obtain

$$\overline{u}(x) = \sum_{k=0}^{\infty} \frac{(-1)^k}{k!} \Delta_G^k M_k(x) \frac{\partial^k \mathcal{G}^{-1} \overline{u}}{\partial x^k}, \tag{3.33}$$

where M_k is the kth order moment of $\tilde{G}$ [154]. By truncating and approximately inverting equation (3.33) we obtain a differential expression for the unfiltered field in terms of the filtered field. The second-order expansion, for example, leads to the gradient model discussed in section 2.2.1 [144, 27]. An alternative approximation comes from a formal expansion of $\mathcal{G}^{-1}$, assuming it exists, about the identity to obtain

$$\mathcal{G}^{-1} = \sum_{n=0}^{\infty} (I - \mathcal{G})^n. \tag{3.34}$$

Truncating this expansion provides an approximate inverse, leading to the approximate deconvolution method (ADM). Stolz et al. [155] showed that these two inversion techniques were practically equivalent. In general, the inverse filter operation will be ill-conditioned, so

the inverse filter is approximate. Mathew et al. [156] showed that approximately inverting the smoothing filter through truncation of equation (3.33) or 3.34 allows for reconstruction of the large scales while keeping the small scales damped, thus preserving the effect of the explicit filter. Because the finite-dimensional projection cannot be inverted, the subgrid stress still needs to be modeled, and Smagorinsky is commonly used. So in many ways, these approximate reconstruction models are similar to scale similarity models and the gradient model.

Formal reconstruction methods of this type were reviewed by Domaradzki and Adams [157]. Here we simply note that, as with explicit filtering methods in general, *a priori* tests of the ability of the $\tilde{\delta}_j$ and τ_{ij} to maintain the expected filtered energy spectrum, as required to minimize numerical artifacts, would be useful as is explored in chapter 4.

3.8 The $B_2 - B_1B_1$ operator

In this section we introduce an operator that is useful for addressing a wide range of numerical and discretization issues in LES. This operator is given by the difference between the numerical second derivative operator, $B_2 = \frac{\delta^2}{\delta x \delta x}$, and repeated application of the numerical first derivative operator, $B_1B_1 = \frac{\delta}{\delta x}\frac{\delta}{\delta x}$, for a general numerical scheme. The spectrum of this operator is shown in figure 3.10 for several choices of numerics. In three dimensions this operator is $\frac{\delta^2}{\delta x_j \delta x_j} - \frac{\delta}{\delta x_j}\frac{\delta}{\delta x_j}$, namely the difference between the numerical Laplacian made up of numerical second derivatives and the numerical divergence of the gradient made up of repeated numerical first derivatives.

It is intuitively reasonable that such an operator would be useful. For numerically well-resolved wavenumbers, the B_2 and B_1B_1 operators are almost identical, and they cancel out. However, for insufficiently resolved wavenumbers, their difference is nonzero and can be used to filter out highly dispersive wavenumbers. Moreover, the operator naturally adapts to the underlying numerics. Further, a simple Taylor expansion for second-order centered

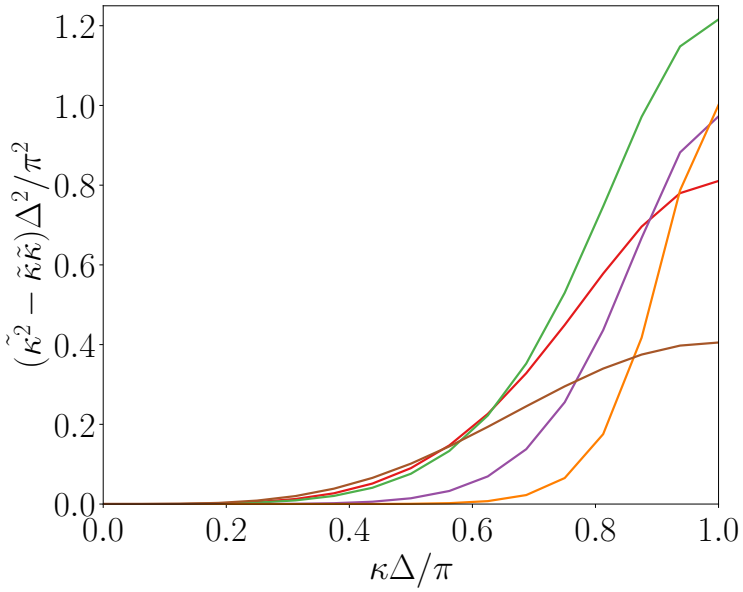

Figure 3.10: The spectrum of the $B_2 - B_1B_1$ operator for a 7th order B-spline collocation method (——), 4th order B-spline collocation method (——), 3rd order B-spline collocation method (——), 2nd order B-spline collocation method (——), and 2nd order centered difference method (——).

difference numerics shows that

$$(B_2^{CD} - B_1^{CD}B_1^{CD})u \equiv \frac{-u_{j+2} + 4u_{j+1} - 8u_j + 4u_{j-1} + u_{j-2}}{4\Delta^2} = -\frac{\Delta^2}{4}\frac{d^4u}{dx^4} + \mathcal{O}(\Delta^4). \quad (3.35)$$

Similarly, it can be shown that $(B_2^7 - B_1^7B_1^7)u \approx \Delta^8 \frac{d^{10}u}{dx^{10}}$ and $(B_2^2 - B_1^2B_1^2)u \approx -\Delta^2 \frac{d^4u}{dx^4}$. Therefore, the $B_2 - B_1B_1$ operator essentially mimics higher order differential operators. Additionally the $B_2 - B_1B_1$ operator is particularly useful because the first and second differential operators are already required by the governing equations, and are thus readily available in practical applications.

We consider two ways in which the $B_2 - B_1B_1$ operator could be used in LES modeling. First, the operator could be added to the right hand side of the governing equations as with the SGS model with appropriate length and time scale dependencies. The analysis above indicates this is roughly equivalent to filtering via a hyperviscosity, however, the $B_2 - B_1B_1$

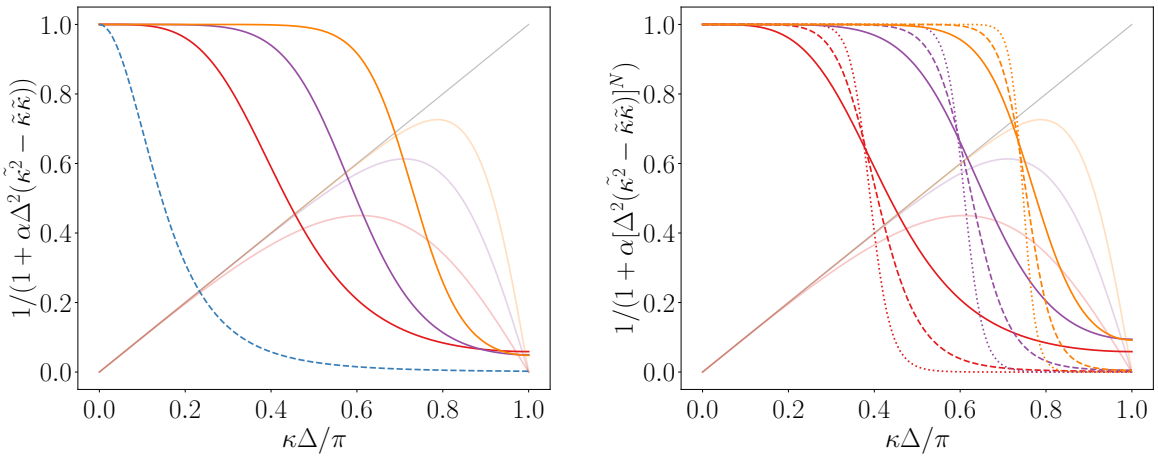

Figure 3.11: The transfer function $\left(\frac{1}{1+\alpha\left[\tilde{\Delta}^2\left(\tilde{\kappa^2}-\tilde{\kappa}\tilde{\kappa}\right)\right]^N}\right)$ of differential filters with the $B_2-B_1B_1$ operator for 7th order B-spline collocation method (——), 4th order B-spline collocation method (——), and 2nd order B-spline collocation method (——). In (a) $\alpha = 2$ and $N = 1$. In (b) α is tuned so that the filters roughly roll off around the wavenumber at which $\Delta\kappa = 0.4$ for a resolution of $\Delta = 2\pi/32$ as in section 3.3, and N is taken to be 1 (solid lines) and 2 (dashed lines), and 3 (dotted lines). The corresponding effective wavenumber for each numerical scheme is shown opaquely in the background and the standard second order differential filter of [144] is also shown (– – –).

operator does not change the order of the differential equation, avoiding the need to explicitly define higher order derivative approximations and additional boundary conditions, which are the typical shortcomings of hyperviscosity models [153]. This will be explored in section 6.3.

Second, the $B_2 - B_1B_1$ operator can be used to construct higher order differential filters approximating the form given in equation (3.32). In one-dimension, consider the explicit filter defined as

$$\left(1 - \alpha\Delta^2\left(\frac{\delta^2}{\delta x\delta x} - \frac{\delta}{\delta x}\frac{\delta}{\delta x}\right)\right)\tilde{\overline{u}}_i = \overline{u}_i \tag{3.36}$$

with transfer function

$$\hat{\tilde{\overline{u}}}_i(\kappa) = \left(\frac{1}{1+\alpha\Delta^2\left(\tilde{\kappa^2}-\tilde{\kappa}\tilde{\kappa}\right)}\right)\hat{\overline{u}}_i(\kappa). \tag{3.37}$$

These filters are significantly sharper than the standard second order differential filter of

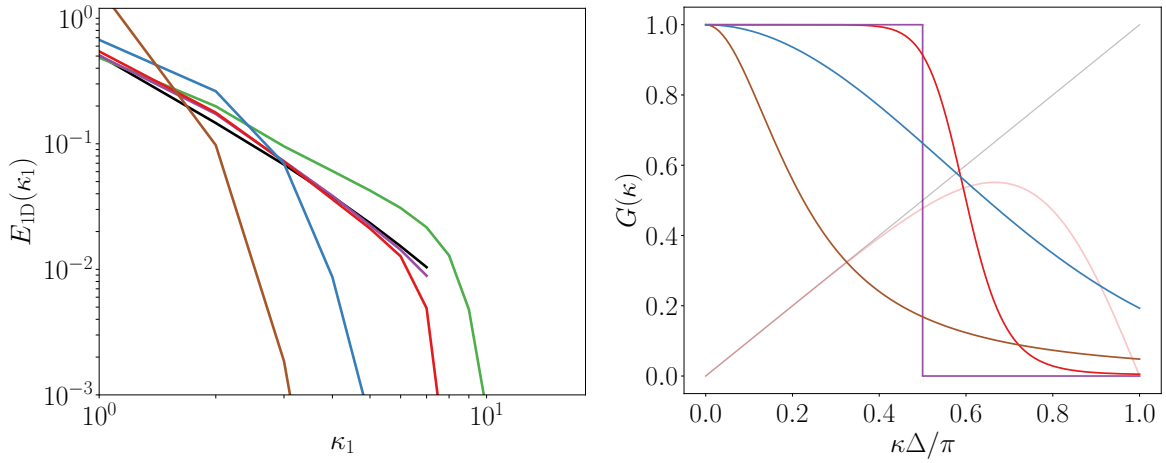

(a) (b)

Figure 3.12: (a) One-dimensional energy spectra in the convection direction with a mean convection velocity of $U = 35$, 3rd order Bspline collocation method, and a resolution scale of $\Delta = 2\pi/32$. (b) The transfer function of the explicit filters used in (a). Theory (——); No explicit filter (——); A Fourier-cutoff explicit filter applied at an effective filter width of $\Delta = 2\pi/16$ (——); A $B_2 - B_1B_1$ differential explicit filter with $\alpha = 2$ and $N = 2$ (——); A Gaussian explicit filter with an effective filter width of $\Delta = 2\pi/16$ (——); The standard second order differential filter of [144] with $\alpha = 1$ (——). The effective wavenumber a 3rd order Bspline collocation method is shown opaquely in the background.

[144, 149] and clearly behave appropriately with respect the underlying numerics, i.e., filtering the dispersive wavemodes while preserving the well resolved modes (see figure 3.11a). Further, Mullen and Fischer [150] found that repeated application of the standard second order differential filter (equation (3.30)) converges to a Gaussian filter. Interestingly, repeated application of the $B_2 - B_1B_1$ operator in the form of:

$$\hat{\bar{\bar{u}}}_i(\kappa) = \left(\frac{1}{1 + \alpha \left[\Delta^2 \left(\tilde{\kappa^2} - \tilde{\kappa}\tilde{\kappa} \right) \right]^N} \right) \hat{\bar{u}}_i(\kappa). \tag{3.38}$$

converges to a Fourier cutoff filter as N increases (see figure 3.11b).

The utility of these filters is demonstrated in the convecting homogeneous isotropic turbulence case as in figures 3.4 and 3.7. A mixed $B_2 - B_1B_1$ differential filter with 3rd order

Bsplines first derivatives and Fourier-spectral second derivatives (see section 3.3) and $\alpha = 2$ and $N = 2$ is used in each coordinate direction (see figure 3.12b). A Gaussian explicit filter with filter width of $\tilde{\Delta} = 2\Delta$ is also tested along with the standard second order differential filter of [144] with $\alpha = 1$ (see figure 3.12b). In each case the length scale of the subgrid stress model corresponds to the effective filter width of 2Δ, which is the wavenumber at which the energy transfer rate shuts down due to dispersion. The $B_2 - B_1 B_1$ differential filter effectively reduces the highly dispersive modes and leads to the correct energy spectrum in the modes up the effective filter width (see figure 3.12a). The results vary only slightly from the Fourier-cutoff explicit filter. The Gaussian explicit filter suffers from the same dispersion errors as in figure 3.8 as does the standard second order differential filter which is simply not suitable for this purpose. However, we do not want to claim too much for these results yet, as we still need to understand what's required of the subgrid stress model for a given filter and numerics in LES (this will be explored in the following chapter). As demonstrated here, for filters that are close to a Fourier-cutoff filter, modifying the length scale of the constant eddy viscosity model to the effective filter width and adjusting the constant to provide the correct a priori dissipation rate over the resolved scales seems sufficient for representing second order statistics. The results here do highlight the importance of considering numerics and filtering together and designing explicit filters that account for the properties of the underlying numerics.

Lastly we note that while the $B_2 - B_1 B_1$ differential filters presented here have several desirable properties of an explicit filter, they do involve inverting the $B_1 B_1$ operator. For finite difference formulas this is not much of an issue, however, for any projective numerical schemes such as B-spline collocation/Galerkin, this involves a dense matrix solve since the inverse of the matrix mass matrix B_0^{-1} is needed when computing repeated first derivative approximations, i.e., the operator is really $B_2 - B_1 B_0^{-1} B_1$. Since the low-order KMM formulation described in appendix A was used in the simulations here, inverting the $B_1 B_0^{-1} B_1$

matrix was already required by the governing equations so the differential filters did not introduce additional computational cost. If this cost is prohibitive, the $B_2 - B_1 B_1$ operators can be used as a term on the right hand side of the equations in the hyperviscosity fashion described above, although this requires additional modeling. It may also be possible to design numerical operators/explicit filters that avoid this computational issue but still respond the properties of the underlying numerics in a similar way. One may also be tempted to directly filter the nonlinear terms with an operator of the form $(I - (B_2 - B_1 B_1))$ where I is the identity, however there is generally no guarantee this will lead to a well defined filter $(0 \leq G(\boldsymbol{\kappa}) \leq 1)$; the differential form in equation (3.36) ensures this property is satisfied.

Chapter 4

An eddy-damped quasi-normal markovian model for LES

The discussion in chapter 3 on numerics and filtering in LES raises the question of how the formulation of an LES — including explicit and implicit filtering, numerical approximations to the differential operators, and the form of the nonlinear terms — affect the requirements for subgrid scale turbulence models. In fact, even in the case of Fourier-spectral numerics and a cutoff filter, using a constant eddy viscosity model that is designed solely to represent the correct dissipation rate a priori (as in equations (2.3) and (2.4)) will lead to a posteriori energy spectra with excess energy in the largest wavenumbers and deficient energy in the low-intermediate wavenumbers (see figure 4.1). This is a result of the well-known 'spectral-cusp' in the eddy viscosity near the cutoff wavenumber κ_c, first identified by Kraichnan [158]. Specifically, several statistical theories of turbulence, such as eddy-damped quasi-normal markovian (EDQNM) theory, predict that a wavenumber dependent eddy viscosity that is constant for $\kappa \ll \kappa_c$ but rises sharply near κ_c is required for an LES to represent a theoretical inertial range spectrum. This wavenumber dependent eddy viscosity has informed the development of several subgrid stress models in LES (see section 4.2.3). Further, EDQNM theory has been useful in understanding the energy transfer process between resolved and subgrid scales [159, 160, 131].

However, traditional applications of EDQNM to LES have been mainly limited to isotropic Fourier cutoff filters and Fourier-spectral numerics. Although this is theoretically interesting, it is not practically realistic. We are therefore interested in identifying how the complex-

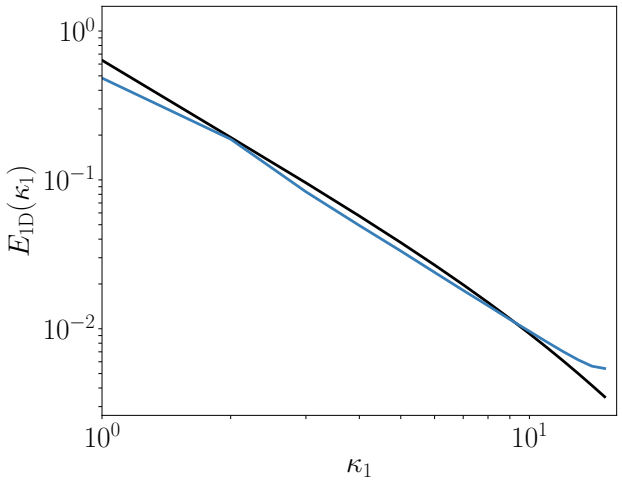

Figure 4.1: One-dimensional energy spectrum computed from an LES with Fourier-spectral numerics and a Fourier-cutoff filter in the same setup as section 3.2. A Kolmogorov eddy viscosity model $\nu_t = C\varepsilon^{1/3}\Delta^{4/3}$ is used with constant $C = 0.054$ chosen so that $\nu_t \sum_{\boldsymbol{\kappa}} C_{kol}\varepsilon^{-2/3}\kappa^{-5/3}/2\pi\kappa^2 = \varepsilon$ (——). A equivalently filtered Kolmogorov spectrum with $C_{kol} = 2.1$ is also shown (——).

ities of an LES enumerated above affect the wavenumber dependent behavior of the eddy viscosity. To do so, we develop a two-point closure model based on EDQNM theory that is applicable to the filtered turbulence in an LES. The techniques developed here may be a useful guide for developing better subgrid stress models for practical LES applications. Further, this theory is also useful to illuminate how numerical discretization and filtering affect the nonlinear energy transfer between Fourier-modes in an LES.

The remainder of this chapter is organized as follows. In section 4.1 EDQNM theory is reviewed, and in section 4.2 applications of EDQNM theory to LES represented with Fourier-cutoff filters and spectral numerics are revisited with some new insights. In section 4.3, the limitations of the traditional approach are discussed and a new EDQNM-type theory is developed for filtered turbulence LES. This is used to study nonlinear and linear dispersion in sections 4.3.3 and 4.3.4, respectively. A further discussion is offered in section 4.4.

4.1 EDQNM Theory

EDQNM theory arose as one of many approaches to an analytical statistical theory of turbulence. The resulting model for the two-point correlation can be obtained in several ways (see Figure 7.1 in [161] for example). The route taken here will be to first apply the quasi-normal (QN) approximation to the Navier-stokes equations, then to apply the eddy damped hypothesis (EDQN), and finally to use the Markovian assumption to arrive at the EDQNM closure. This is the sequence proposed by Orszag [162], and for completeness each of these hypotheses are reviewed briefly below. Although several other analytical theories of turbulence have been developed [161], the EDQNM formulation was chosen for use here because it has proven to be an excellent tool for predicting the energy transfer between modes in high Reynolds number turbulence [159, 160].

Quasi-normal approximation

Consider the evolution equation for a velocity Fourier-mode $\hat{u}_k(\boldsymbol{\kappa})$ for isotropic turbulence represented in a cubical periodic domain

$$\left(\frac{\partial}{\partial t} + \nu\kappa^2\right)\hat{u}_k(\boldsymbol{\kappa}) = -iP_{ki}(\boldsymbol{\kappa})\sum_{\kappa'}\kappa_\ell\hat{u}_i(\boldsymbol{\kappa}')\hat{u}_\ell(\boldsymbol{\kappa}-\boldsymbol{\kappa}'), \tag{4.1}$$

where $P_{ij}(\boldsymbol{\kappa}) = (\delta_{ij} - \kappa_i\kappa_j/|\boldsymbol{\kappa}|^2)$ is the projection tensor. Then the evolution of the velocity-spectrum tensor $\Phi_{kj}(\boldsymbol{\kappa}) = \langle\hat{u}_k(\boldsymbol{\kappa})\hat{u}_j^*(\boldsymbol{\kappa})\rangle$ is given by

$$\begin{aligned}\left(\frac{\partial}{\partial t} + 2\nu\kappa^2\right)\Phi_{kj}(\boldsymbol{\kappa}) = &- iP_{ki}(\boldsymbol{\kappa})\sum_{\boldsymbol{\kappa}'}\kappa_\ell\langle\hat{u}_j^*(\boldsymbol{\kappa})\hat{u}_i(\boldsymbol{\kappa}')\hat{u}_\ell(\boldsymbol{\kappa}-\boldsymbol{\kappa}')\rangle \\ &+ iP_{ji}(\boldsymbol{\kappa})\sum_{\boldsymbol{\kappa}'}\kappa_\ell\langle\hat{u}_k(\boldsymbol{\kappa})\hat{u}_i^*(\boldsymbol{\kappa}')\hat{u}_\ell^*(\boldsymbol{\kappa}-\boldsymbol{\kappa}')\rangle.\end{aligned} \tag{4.2}$$

Continuing, the evolution of the third-order correlation $\langle \hat{u}_k(\boldsymbol{\kappa})\hat{u}_i^*(\boldsymbol{\kappa}')\hat{u}_\ell^*(\boldsymbol{\kappa}-\boldsymbol{\kappa}')\rangle$ is

$$\begin{aligned}\left(\frac{\partial}{\partial t}+\nu(|\boldsymbol{\kappa}|^2+|\boldsymbol{\kappa}'|^2+|\boldsymbol{\kappa}'-\boldsymbol{\kappa}|^2)\right)\langle \hat{u}_k(\boldsymbol{\kappa})\hat{u}_i(-\boldsymbol{\kappa}')\hat{u}_\ell(-\boldsymbol{\kappa}+\boldsymbol{\kappa}')\rangle = \\ -iP_{km}(\boldsymbol{\kappa})\sum_{\boldsymbol{\kappa}''}\kappa_s\langle \hat{u}_m(\boldsymbol{\kappa}'')\hat{u}_s(\boldsymbol{\kappa}-\boldsymbol{\kappa}'')\hat{u}_i(-\boldsymbol{\kappa}')\hat{u}_\ell(-\boldsymbol{\kappa}+\boldsymbol{\kappa}')\rangle \\ -iP_{im}(\boldsymbol{\kappa}')\sum_{\boldsymbol{\kappa}''}-\kappa_s'\langle \hat{u}_m(\boldsymbol{\kappa}'')\hat{u}_s(-\boldsymbol{\kappa}'-\boldsymbol{\kappa}'')\hat{u}_k(\boldsymbol{\kappa})\hat{u}_\ell(-\boldsymbol{\kappa}+\boldsymbol{\kappa}')\rangle \\ -iP_{\ell m}(-\boldsymbol{\kappa}+\boldsymbol{\kappa}')\sum_{\boldsymbol{\kappa}''}(-\kappa+\kappa')_s\langle \hat{u}_m(\boldsymbol{\kappa}'')\hat{u}_s(-\boldsymbol{\kappa}+\boldsymbol{\kappa}'-\boldsymbol{\kappa}'')\hat{u}_k(\boldsymbol{\kappa})\hat{u}_i(-\boldsymbol{\kappa}')\rangle\end{aligned} \quad . \tag{4.3}$$

Clearly a closure problem is manifesting. An additional relationship between the velocity moments is needed to close this hierarchy of moments. Millionshchikov [163] and Chou [164] introduced the quasi-normal approximation, which was extended to isotropic turbulence by Proudman and Reid [165] and Tatsumi et al. [166] to close equation (4.3). The key observation is that, for a Gaussian random variable, even-order moments can be expressed in terms of the second-order moments. It is unrealistic to approximate the velocity by a Gaussian random field (there would be no energy transfer between wavenumbers as odd order moments are then zero), so instead the quasi-normal approximation assumes that the fourth order cummulants are zero as for a Gaussian process, without any assumptions on the third-order moments. Lesieur [161] argues that Gaussianity may not be totally unphysical, if turbulence is considered to be the result of independent Brownian-like chaotic motions to which the central limit theorem applies. Orszag [130] argues that a Gaussian initial state is as plausible as any other. In any case, under this modeling assumption the fourth-order moments in equation (4.3) can be expressed as

$$\sum_{\boldsymbol{\kappa}''}\langle u_m(\boldsymbol{\kappa}'')u_s(\boldsymbol{\kappa}-\boldsymbol{\kappa}'')u_i(-\boldsymbol{\kappa}')u_\ell(-\boldsymbol{\kappa}+\boldsymbol{\kappa}')\rangle = \Phi_{mi}(\boldsymbol{\kappa}')\Phi_{\ell s}(-\boldsymbol{\kappa}+\boldsymbol{\kappa}')+\Phi_{\ell m}(-\boldsymbol{\kappa}+\boldsymbol{\kappa}')\Phi_{si}(\boldsymbol{\kappa}'), \tag{4.4}$$

$$\sum_{\boldsymbol{\kappa}''}\langle u_m(\boldsymbol{\kappa}'')u_s(-\boldsymbol{\kappa}'-\boldsymbol{\kappa}'')u_k(\boldsymbol{\kappa})u_\ell(-\boldsymbol{\kappa}+\boldsymbol{\kappa}')\rangle = \Phi_{km}(\boldsymbol{\kappa})\Phi_{\ell s}(-\boldsymbol{\kappa}+\boldsymbol{\kappa}') + \Phi_{\ell m}(-\boldsymbol{\kappa}+\boldsymbol{\kappa}')\Phi_{ks}(\boldsymbol{\kappa}), \tag{4.5}$$

and,

$$\sum_{\boldsymbol{\kappa}''}\langle u_m(\boldsymbol{\kappa}'')u_s(-\boldsymbol{\kappa}+\boldsymbol{\kappa}'-\boldsymbol{\kappa}'')u_k(\boldsymbol{\kappa})u_i(-\boldsymbol{\kappa}')\rangle = \Phi_{km}(\boldsymbol{\kappa})\Phi_{si}(\boldsymbol{\kappa}') + \Phi_{mi}(\boldsymbol{\kappa}')\Phi_{ks}(\boldsymbol{\kappa}). \tag{4.6}$$

so that the Q.N. equations for the third order moments are

$$\begin{aligned}\left(\frac{\partial}{\partial t} + \nu(|\boldsymbol{\kappa}|^2 + |\boldsymbol{\kappa}'|^2 + |\boldsymbol{\kappa}'-\boldsymbol{\kappa}|^2)\right)\langle \hat{u}_k(\boldsymbol{\kappa})\hat{u}_i(-\boldsymbol{\kappa}')\hat{u}_\ell(-\boldsymbol{\kappa}+\boldsymbol{\kappa}')\rangle = \\ - iP_{km}(\boldsymbol{\kappa})\left[\kappa_s\left(\Phi_{mi}(\boldsymbol{\kappa}')\Phi_{\ell s}(-\boldsymbol{\kappa}+\boldsymbol{\kappa}') + \Phi_{\ell m}(-\boldsymbol{\kappa}+\boldsymbol{\kappa}')\Phi_{si}(\boldsymbol{\kappa}')\right)\right] \\ - iP_{im}(\boldsymbol{\kappa}')\left[-\kappa'_s\left(\Phi_{km}(\boldsymbol{\kappa})\Phi_{\ell s}(-\boldsymbol{\kappa}+\boldsymbol{\kappa}') + \Phi_{\ell m}(-\boldsymbol{\kappa}+\boldsymbol{\kappa}')\Phi_{ks}(\boldsymbol{\kappa})\right)\right] \\ - iP_{\ell m}(-\boldsymbol{\kappa}+\boldsymbol{\kappa}')\left[(-\kappa+\kappa')_s\left(\Phi_{km}(\boldsymbol{\kappa})\Phi_{si}(\boldsymbol{\kappa}') + \Phi_{mi}(\boldsymbol{\kappa}')\Phi_{ks}(\boldsymbol{\kappa})\right)\right]\end{aligned}. \tag{4.7}$$

Eddy-damped approximation

Equations (4.2) and (4.7) form a closed set of equations for the velocity spectrum tensor. However, when the spectrum tensor is allowed to evolve according to this model, negative values of the energy spectrum develop [167, 168]. Orszag [162] argued that this deficiency of the quasi-normal approximation is a result of improper treatment of relaxation effects. In particular, correlations between velocity Fourier modes are weakened by two processes in high Reynolds number flows. First, turbulent convection leads to a decoherence of the phase correlations between Fourier-modes through nonlinear scrambling. Second, viscous dissipation damps the velocity Fourier-modes. However, the quasi-normal approximation only represents this latter effect. Orszag [162] proposed to model the effects of nonlinear convection through a linear damping term η that reduces the third-order correlations. This

leads to the eddy-damped quasi-normal equations

$$\begin{aligned}\left(\frac{\partial}{\partial t}+\mu(\boldsymbol{\kappa})+\mu(\boldsymbol{\kappa}')+\mu(\boldsymbol{\kappa}'-\boldsymbol{\kappa})\right)\langle\hat{u}_k(\boldsymbol{\kappa})\hat{u}_i(-\boldsymbol{\kappa}')\hat{u}_\ell(-\boldsymbol{\kappa}+\boldsymbol{\kappa}')\rangle = \\ -iP_{km}(\boldsymbol{\kappa})\left[\kappa_s\left(\Phi_{mi}(\boldsymbol{\kappa}')\Phi_{\ell s}(-\boldsymbol{\kappa}+\boldsymbol{\kappa}')+\Phi_{\ell m}(-\boldsymbol{\kappa}+\boldsymbol{\kappa}')\Phi_{si}(\boldsymbol{\kappa}')\right)\right] \\ -iP_{im}(\boldsymbol{\kappa}')\left[-\kappa'_s\left(\Phi_{km}(\boldsymbol{\kappa})\Phi_{\ell s}(-\boldsymbol{\kappa}+\boldsymbol{\kappa}')+\Phi_{\ell m}(-\boldsymbol{\kappa}+\boldsymbol{\kappa}')\Phi_{ks}(\boldsymbol{\kappa})\right)\right] \\ -iP_{\ell m}(-\boldsymbol{\kappa}+\boldsymbol{\kappa}')\left[(-\kappa+\kappa')_s\left(\Phi_{km}(\boldsymbol{\kappa})\Phi_{si}(\boldsymbol{\kappa}')+\Phi_{mi}(\boldsymbol{\kappa}')\Phi_{ks}(\boldsymbol{\kappa})\right)\right]\end{aligned} . \tag{4.8}$$

where $\mu(\boldsymbol{\kappa})=\eta(\boldsymbol{\kappa})+\nu|\boldsymbol{\kappa}|^2$ and $\eta(\boldsymbol{\kappa})$ must be modeled and represents a relaxation rate.

Markovian Approximation

The EDQN approximation does not guarantee positiveness of the energy spectrum in all situations. Orszag [162] showed that this can be ensured by assuming that the right hand side of equation (4.8) varies on a timescale that is long compared to $(\mu(\boldsymbol{\kappa})+\mu(\boldsymbol{\kappa}')+\mu(\boldsymbol{\kappa}'-\boldsymbol{\kappa}))^{-1}$. In this case, the solution for the triple correlation is quasi-steady and can therefore be approximated as

$$\begin{aligned}\langle\hat{u}_k(\boldsymbol{\kappa})\hat{u}_i(-\boldsymbol{\kappa}')\hat{u}_\ell(-\boldsymbol{\kappa}+\boldsymbol{\kappa}')\rangle = \Theta(\boldsymbol{\kappa},\boldsymbol{\kappa}',\boldsymbol{\kappa}'-\boldsymbol{\kappa})\Big[\\ -iP_{km}(\boldsymbol{\kappa})\left[\kappa_s\left(\Phi_{mi}(\boldsymbol{\kappa}')\Phi_{\ell s}(-\boldsymbol{\kappa}+\boldsymbol{\kappa}')+\Phi_{\ell m}(-\boldsymbol{\kappa}+\boldsymbol{\kappa}')\Phi_{si}(\boldsymbol{\kappa}')\right)\right] \\ -iP_{im}(\boldsymbol{\kappa}')\left[-\kappa'_s\left(\Phi_{km}(\boldsymbol{\kappa})\Phi_{\ell s}(-\boldsymbol{\kappa}+\boldsymbol{\kappa}')+\Phi_{\ell m}(-\boldsymbol{\kappa}+\boldsymbol{\kappa}')\Phi_{ks}(\boldsymbol{\kappa})\right)\right] \\ -iP_{\ell m}(-\boldsymbol{\kappa}+\boldsymbol{\kappa}')\left[(-\kappa+\kappa')_s\left(\Phi_{km}(\boldsymbol{\kappa})\Phi_{si}(\boldsymbol{\kappa}')+\Phi_{mi}(\boldsymbol{\kappa}')\Phi_{ks}(\boldsymbol{\kappa})\right)\right]\Big]\end{aligned} \tag{4.9}$$

where

$$\Theta(\boldsymbol{\kappa},\boldsymbol{\kappa}',\boldsymbol{\kappa}'-\boldsymbol{\kappa})=\left[\frac{1}{(\mu(\boldsymbol{\kappa})+\mu(\boldsymbol{\kappa}')+\mu(\boldsymbol{\kappa}'-\boldsymbol{\kappa}))}\right]. \tag{4.10}$$

This is commonly referred to as a Markovian assumption (putting the "M" in EDQNM) because the approximation involves neglecting the history effects of Φ_{ij} so that the evolution of the triple correlation at any time depends only on the solution for Φ_{ij} at that time. All

that is needed to close these equations is a model for $\eta(\boldsymbol{\kappa})$, which is discussed in section 4.2.1.

4.2 Applications to LES and the spectral eddy viscosity

EDQNM theory is largely successfully in predicting the inertial range energy transfers in three dimensional turbulence [159, 169]. This has motivated its use to formulate an LES model. As Kraichnan [158] notes, equations (4.2) and (4.10) form a closed set of equations for $\Phi_{ij}(\boldsymbol{\kappa})$ and is therefore applicable to anisotropric, inhomogeneous turbulence. However, applications of EDQNM to LES have mainly been limited to isotropic turbulence represented with a Fourier-cutoff filter and spectral numerics. As we will see, EDQNM predicts that a wavenumber dependent eddy viscosity $\nu_t(\boldsymbol{\kappa})$ can be specified in this case to produce any given energy spectrum, such as a Kolmogorov spectrum. In this section we review the formulation of $\nu_t(\boldsymbol{\kappa})$ via EDQNM for spectral cutoff filters and spectral numerics, providing some new insight in the process. Moreover, the ability of the eddy viscosity to produce a theoretical Kolmogorov spectrum in an LES a posteriori is demonstrated. The application of EDQNM to non-cutoff filters and non-spectral numerics is pursued in section 4.3.

There is an important subtlety to the formulation here that differs from standard approaches that should be discussed. In isotropic turbulence the spectrum tensor is fully determined by the three-dimensional energy spectrum ($\Phi_{ij}(\boldsymbol{\kappa}) = P_{ij}(\boldsymbol{\kappa})E(\kappa)/4\pi\kappa^2$), and the evolution of the spectrum is governed by the energy transfer between scales. The same is true for the filtered spectrum $\overline{\Phi}_{ij}(\boldsymbol{\kappa}) = G(\boldsymbol{\kappa})^2\Phi_{ij}(\boldsymbol{\kappa})$ in an LES when an isotropic Fourier-cutoff filter and spectral numerics are used. This is the setting in which EDQNM has commonly been applied to LES and so the primary interest has been on isotropic inertial range energy transfers. However, we will be interested in including the anisotropies induced by discretization and filtering. Therefore, we will generally let the filter $G(\boldsymbol{\kappa})$ be anisotropic. The focus in this chapter will remain on the anisotropic scalar energy spectrum equation, determined through the trace of the filtered spectrum tensor $\overline{E}(\boldsymbol{\kappa}) \equiv \frac{1}{2}\overline{\Phi}_{kk}(\boldsymbol{\kappa})$, and the effects of nu-

merical discretization and filtering on the energy transfer process. In this case, a scalar wavenumber dependent eddy viscosity $\nu_t(\boldsymbol{\kappa})$ that is allowed to varying anisotropically with $\boldsymbol{\kappa}$ is sufficient for an LES to produce a given energy spectrum. This is contrary to typical formulations of the spectral eddy viscosity in which ν_t is taken to be isotropic. The EDQNM theory formulated here would also be useful for analyzing the anisotropies of the full spectrum tensor $\overline{\Phi}_{ij}(\boldsymbol{\kappa})$ as discussed further in section 4.4.

Consider for instance the formulation of the spectral eddy viscosity for an LES of statistically stationary forced infinite Reynolds number isotropic turbulence in a cubical domain of size $L = 2\pi$ represented with Fourier-spectral numerics and a Cartesian Fourier cutoff filter $G(\boldsymbol{\kappa}) = \Pi_{\alpha=1}^{3} H(\kappa_c - \kappa_\alpha)$ where H is the heavyside function. This G is anisotropic as opposed to its spherical counterpart $H(\kappa_c - |\boldsymbol{\kappa}|)$. The equation for the filtered energy spectrum can be written

$$\frac{\partial \overline{E}(\boldsymbol{\kappa})}{\partial t} = T^{<}(\boldsymbol{\kappa}) + T^{>}(\boldsymbol{\kappa}) + 2F(\boldsymbol{\kappa})\overline{E}(\boldsymbol{\kappa}) \tag{4.11}$$

where $T^{<}$ and $T^{>}$ are the resolved and subgrid energy transfers, respectively, and $F(\boldsymbol{\kappa})$ is the spectrum of the forcing which injects energy at a rate of ε (taken to be 1). A negative viscosity forcing is used so that $F(\boldsymbol{\kappa}) = -\alpha|\boldsymbol{\kappa}|^2 \mathcal{I}_{\{0<|\boldsymbol{\kappa}|\leq 2\}}$ where $\mathcal{I}$ is the indicator function. In this setup,

$$T^{<}(\boldsymbol{\kappa}) = -\mathrm{Im}\left[\sum_{\boldsymbol{\kappa}'} G(\boldsymbol{\kappa})^2 G(\boldsymbol{\kappa}') G(\boldsymbol{\kappa}' - \boldsymbol{\kappa}) \kappa_\ell \langle \hat{u}_k(\boldsymbol{\kappa}) \hat{u}_k^*(\boldsymbol{\kappa}') \hat{u}_\ell^*(\boldsymbol{\kappa} - \boldsymbol{\kappa}') \rangle\right] \tag{4.12}$$

$$T^{>}(\boldsymbol{\kappa}) = -\mathrm{Im}\left[\sum_{\boldsymbol{\kappa}'} G(\boldsymbol{\kappa})^2 (1 - G(\boldsymbol{\kappa}') G(\boldsymbol{\kappa}' - \boldsymbol{\kappa})) \kappa_\ell \langle \hat{u}_k(\boldsymbol{\kappa}) \hat{u}_k^*(\boldsymbol{\kappa}') \hat{u}_\ell^*(\boldsymbol{\kappa} - \boldsymbol{\kappa}') \rangle\right], \tag{4.13}$$

so that $T^{<}$ only involves triad interactions between resolved wavenumbers, and $T^{>}$ involves triad interactions that cross the cutoff wavenumber κ_c. EDQNM provides a closure for the triple correlation $\langle \hat{u}_k(\boldsymbol{\kappa}) \hat{u}_k^*(\boldsymbol{\kappa}') \hat{u}_\ell^*(\boldsymbol{\kappa} - \boldsymbol{\kappa}') \rangle$ in equation (4.13) for a given spectrum $\overline{\Phi}_{ij}(\boldsymbol{\kappa})$.

Therefore, we can determine the eddy viscosity needed to produce a given energy spectrum as

$$-2\nu_t(\boldsymbol{\kappa})|\boldsymbol{\kappa}|^2\overline{E}(\boldsymbol{\kappa}) = T^{>}(\boldsymbol{\kappa}) \implies \nu_t(\boldsymbol{\kappa}) = -\frac{T^{>}(\boldsymbol{\kappa})}{2|\boldsymbol{\kappa}|^2\overline{E}(\boldsymbol{\kappa})}. \tag{4.14}$$

In particular, we can take $\overline{\Phi}_{ij}(\boldsymbol{\kappa}) = G(\boldsymbol{\kappa})^2 P_{ij}(\boldsymbol{\kappa})E(\kappa)/4\pi\kappa^2$ with $E(\kappa) = C_{kol}\varepsilon^{2/3}\kappa^{-5/3}$ to determine the eddy viscosity required to produce an equivalently filtered Kolmogorov spectrum. A Kolmogorov constant of $C_{kol} = 2.1$ will be used here as this was found to lead to good agreement between the a priori EDQNM approximations and a posteriori LES calculations. All that is needed to formulate $\nu_t(\boldsymbol{\kappa})$ is a model for the relaxation rate η in equation (4.10), which is pursued in the following subsection.

4.2.1 The relaxation timescale η

Typically η is modeled as depending on ε and κ through dimensional analysis consistent with inertial range assumptions, i.e., $\eta = D\varepsilon^{1/3}\kappa^{-2/3}$ for some constant D. Kraichnan [159] set $D = 0.1904C_{kol}^2$ so that the EDQNM approximation of the energy transfer agree with that from direct interaction approximation (DIA) theory, which was used in several subsequent EDQNM studies [131, 170, 160]. However, this value did not necessarily lead to a statistically stationary LES a posteriori as it does not guarantee that $\sum_{\boldsymbol{\kappa}} T^{>}(\boldsymbol{\kappa}) = -\varepsilon$. Further, DIA is often a poor approximation of high Reynolds number flows [161], so there is reason to doubt this value of D. In fact, Kraichnan [171] showed that DIA predicts $\eta \sim (\kappa u_{rms})^{-1}$, although this scaling is found to perform poorly in high Reynolds number turbulence [131]. Thus, we propose an alternative calculation for the constant D here.

The parameter D can be determined so that the relaxation rate of the turbulence leads to the correct dissipation rate, i.e., $\sum_{\boldsymbol{\kappa}} T^{>}(\boldsymbol{\kappa}) = -\varepsilon$. This guarantees the eddy viscosity will provide the correct rate of mean kinetic energy dissipation a priori. This is a necessary condition to produce correct LES statistics a posteriori [1]. However, there is a further subtlety here. Numerically approximating $T^{>}(\boldsymbol{\kappa})$ via equation (4.13) involves computing

triad interactions up to some $\kappa_{\max} > \kappa_c$. For infinite Reynolds number turbulence, $\kappa_{\max}$ is formally infinite, so we are interested in the convergence of the estimates as $\kappa_{\max} \to \infty$. We consider the steady state solution of equation (4.11) and examine the balance between $T^{>}$ and $T^{<} + 2F\overline{E}$ as $\kappa_{\max}$ increases. In this case, the spectral eddy viscosity can be determined either through equation (4.14) or equivalently as

$$2\nu_t(\boldsymbol{\kappa})|\boldsymbol{\kappa}|^2\overline{E}(\boldsymbol{\kappa}) = T^{<}(\boldsymbol{\kappa}) + 2F(\boldsymbol{\kappa})\overline{E}(\boldsymbol{\kappa}) \implies \nu_t(\boldsymbol{\kappa}) = \frac{T^{<}(\boldsymbol{\kappa}) + 2F(\boldsymbol{\kappa})\overline{E}(\boldsymbol{\kappa})}{2|\boldsymbol{\kappa}|^2\overline{E}(\boldsymbol{\kappa})}. \tag{4.15}$$

For instance, consider a resolution of $\Delta = 2\pi/32$ so that the LES can represent wavenumber components up to $\kappa_c = 16$. We compute the spectral eddy viscosity via equation (4.14) for triad interactions up to $\kappa_{\max} = 32$, 64, and 128. In all cases, there is a constant D such that $\sum_{\boldsymbol{\kappa}} T^{>}(\boldsymbol{\kappa}) = -\varepsilon$, all leading to spectral eddy viscosity with approximately the same one-dimensional spectra (see figure 4.2a). However, equation (4.15) only leads to an equivalent eddy viscosity for $\kappa_{\max} \geq 128$ (see figure 4.2b). Notice that there is a discrepancy between these two eddy viscosities in the lowest wavenumbers due to the forcing, which is not surprising since the forcing is not representative of realistic turbulence in these scales. For $\kappa_{\max} = 8\kappa_c$, $D \approx 0.772$, which was found to hold regardless of κ_c and is used for the remainder of this chapter.

These results suggest that important nonlocal triad interactions occur between the resolved wavenumbers and wavenumbers up to (at least) $8\kappa_c$. Domaradzki and Rogallo [169] emphasize that one must be careful to distinguish between local/nonlocal energy transfers and local/nonlocal triad interactions. In particular, both DNS data and EDQNM theory suggest that local energy transfers (which dominate nonlocal energy transfers) arise primarily from nonlocal triad interactions, typically where two legs of the triad are much longer than the remaining one [169]. This may explain why large values of $\kappa_{\max}$ are needed here to recover the correct local relaxation timescale of the turbulence.

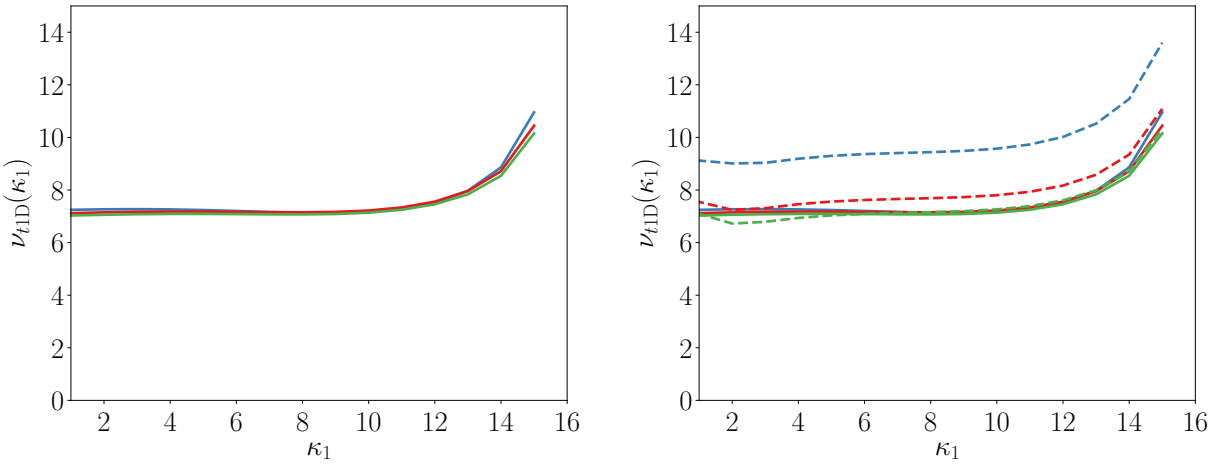

Figure 4.2: (a) One-dimensional spectral eddy viscosity $\sum_{\kappa_2,\kappa_3} \nu_{1D}(\boldsymbol{\kappa})$ computed from equation (4.14) with $\kappa_c = 16$ and $\kappa_{\max} = 32$ (——), 64 (——) and 128 (——). In each case the relaxation time scale $\eta(\boldsymbol{\kappa}) = D\varepsilon^{1/3}\kappa^{2/3}$ is determined so that $\sum_{\boldsymbol{\kappa}} T^{>}(\boldsymbol{\kappa}) = -\varepsilon$, leading to $D = 0.587$, 0.719, and 0.772, respectively. (b) One-dimensional eddy viscosity computed from equation (4.15) with the same values of $\eta(\boldsymbol{\kappa})$ from (a), i.e., $D = 0.587$ (– – –), $D = 0.719$ (– – –), $D = 0.772$ (– – –).

4.2.2 A posteriori LES calculation

The EDQNM approximation to the energy transfer developed in the previous subsection led to the well-known spectral-cusp behavior of the eddy viscosity. Recall, the EDQNM approximation was for a Cartesian cutoff filter, spectral numerics, and an equivalently filtered Kolmogorov spectrum. The behavior of the eddy viscosity spectra here are consistent with the three dimensional isotropic eddy viscosity spectra reported in the literature for a spherical cutoff filter [158, 131, 170]. The one-dimensional eddy viscosity spectra are constant for $\kappa_1 \ll \kappa_c$ and rise sharply near κ_c (see figure 4.2). This behavior has also been verified using filtered DNS data of isotropic turbulence by Chasnov [160]. Additionally, Chollet and Lesieur [92] showed that the EDQNM equations lead to a Kolmogorov spectrum given this parameterization of the eddy viscosity. However, a posteriori LES calculations of high Reynolds number turbulence with this spectral-eddy viscosity model are scarce in the literature and

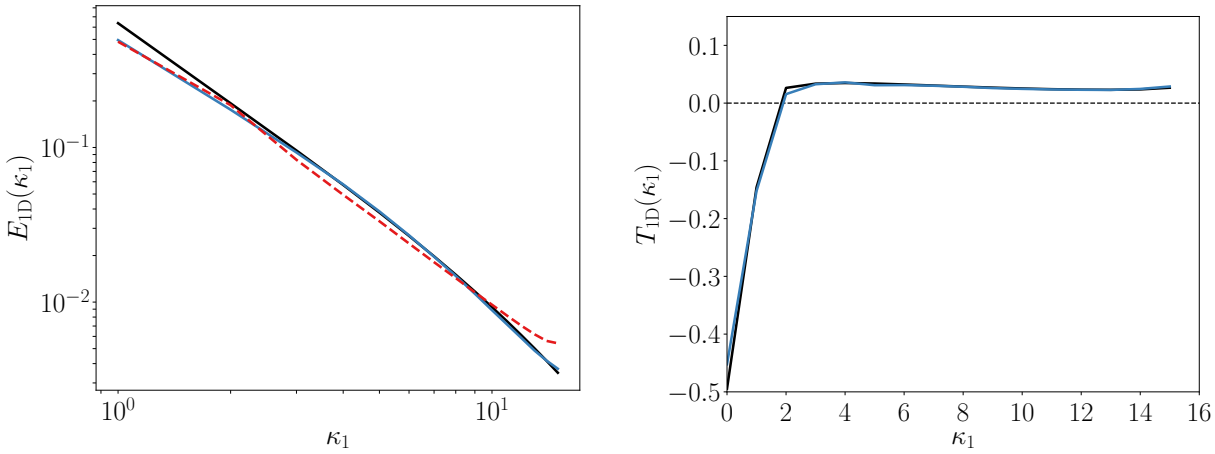

(a) (b)

Figure 4.3: One-dimensional energy and energy transfer spectra computed from an LES with Fourier-spectral numerics, a cutoff filter, and the spectral EDQNM eddy viscosity model as shown in figure 4.2 (———). Theoretical energy and energy transfer spectra are also shown based on a Kolmogorov model with $C_{kol} = 2.1$ and the EDQNM approximation for $T^<$ (———). The energy spectrum computed from an LES with a Kolmogorov eddy viscosity model $\nu_t = C\varepsilon^{1/3}\Delta^{4/3}$ with constant $C = 0.054$ chosen so that $\nu_t \sum_{\boldsymbol{\kappa}} 2.1\varepsilon^{-2/3}\kappa^{-5/3}/2\pi\kappa^2 = \varepsilon$ is also shown in (a) (– – –).

so they are pursued here.

An LES of infinite Reynolds number turbulence with a Cartesian cutoff filter, Fourier-spectral numerics, and a resolution of $\Delta = 2\pi/32$ is performed. The same setup described in section 3.2 is used here with the wavenumber dependent model for the eddy viscosity predicted by EDQNM theory with a Kolmogorov spectrum. This LES leads to energy spectra that are in excellent agreement with an equivalently filtered Kolmogorov spectrum throughout the entire inertial range (see figure 4.3a). Further, the a posteriori energy transfer spectra agree with the a priori estimates from EDQNM theory with a Kolmogorov spectrum (see figure 4.3b), suggesting that the theoretically determined LES model not only leads to correct second-order statistics (for which it was developed) but also third-order statistics.

4.2.3 Impact on LES modeling

The existence of a spectral cusp in the eddy viscosity has had a large impact on the field of LES modeling. Based on the analysis of Kraichnan [47], Chollet and Lesieur [92] introduced a parameterization of the spectral eddy viscosity in wavespace that depends on the value of the energy spectrum at the cutoff wavenumber, $E(\kappa_c)$, and the constant value of the spectral eddy viscosity for $\kappa \ll \kappa_c$. Lesieur and Metais [48] then proposed a constant eddy viscosity model based on the average value of the parameterization in [92]. This is similar to the constant eddy viscosity discussed in sections 2.1.1 and 3.5 which was constructed solely to represent the correct dissipation rate. As shown above, an LES with a constant eddy viscosity model cannot exactly reproduce a Kolmogorov spectrum throughout the entire inertial range. An average eddy viscosity will be over-dissipative for scales $\kappa \ll \kappa_c$ and under-dissipative for scales near κ_c (see figure 4.3a). Alternatively, one may view a constant eddy viscosity model as consistent with a Kolmogorov spectrum for a slightly different value of C_{kol} except near the cutoff (as in section 3.3 and [17]). However, a constant eddy viscosity may be largely acceptable in practice, and several realspace eddy viscosity models can be interpreted as approximating this spectral average [34, 1]. To include the effects of the spectral cusp in realspace, several authors have introduced hyperviscosity models that will have a strong effect on wavenumbers near κ_c [92, 48, 172, 173, 174, 175, 46, 176, 177, 94, 178, 179]. The parameterization of the eddy viscosity based on $E(\kappa_c)$ also motivated the structure function models of Métais and Lesieur [54], which can be viewed as a way to approximate $E(\kappa_c)$ in realspace based on the second-order structure function. Lastly, we note that EDQNM has informed the development of stochastic subgrid models aimed at representing back-scatter effects [180, 181].

4.3 EDQNMLES

EDQNM theory provides a good model of the energy transfer process in turbulent flows. It is reasonable then to suspect that EDQNM may also be useful for modeling the dynamics represented in an LES when including the practical considerations that are introduced by the underlying numerics and discretization. This may further inform the requirements of SGS models in practical LES applications.

At first it may seem that a straightforward introduction of effective wavenumbers and filters into the formulations of $T^{>}$ and $T^{<}$ in equations (4.12) and (4.13), along with the EDQNM approximation for $\langle \hat{u}_k(\boldsymbol{\kappa})\hat{u}_k^*(\boldsymbol{\kappa}')\hat{u}_\ell^*(\boldsymbol{\kappa}-\boldsymbol{\kappa}')\rangle$, would be sufficient for this purpose. In fact, Leslie and Quarini [131] first introduced such a formulation to represent general filters in an LES and showed that the eddy viscosity analysis of Kraichnan [47] could be extended to a Gaussian and Box filter. However, their formulation cannot be extended in a consistent way to account for numerical discretization. The reason is that (1) the effect of numerical discretization in an LES cannot be represented by an effective three-dimensional filter operator acting on the velocity field [140]; (2) numerical discretization and explicit filtering impact the EDQNM hypotheses; and (3) the numerical approximation to the continuity constraint can lead to an ill-posed formulation in equation (4.13) because the effective wavenumbers are not defined for wavenumbers beyond the Nyquist wavenumber. Therefore, although EDQNM theory provides a good approximation for the unfiltered triple correlations $\langle \hat{u}_k(\boldsymbol{\kappa})\hat{u}_k^*(\boldsymbol{\kappa}')\hat{u}_\ell^*(\boldsymbol{\kappa}-\boldsymbol{\kappa}')\rangle$, in an LES a model for the filtered triple correlations $\langle \widehat{\overline{u}}_k(\boldsymbol{\kappa})\widehat{\overline{u}}_k^*(\boldsymbol{\kappa}')\widehat{\overline{u}}_\ell^*(\boldsymbol{\kappa}-\boldsymbol{\kappa}')\rangle$ is needed. An extension of the theory, denoted here as EDQNMLES, is developed in this section for this purpose.

4.3.1 Formulation

The EDQNMLES approximation is derived for an LES of statistically stationary infinite Reynolds number turbulence represented with uniform resolution Δ, an explicit filter $\tilde{G}(\boldsymbol{\kappa})$ applied to the nonlinear terms, and numerical approximations to the first derivative operator $\tilde{\kappa}_j$ and Laplacian operator $-\widetilde{\kappa_j\kappa_j}$. The derivation for the skew-symmetric form of the nonlinear terms $\frac{1}{2}\left(\delta_j\widetilde{\overline{u}_i\overline{u}_j} + \overline{u}_j\delta_j\tilde{\overline{u}}_i\right)$ is presented here. The corresponding conservative and convective forms follow immediately. The filter $\bar{\cdot}$ is defined through a Cartesian Fourier cutoff filter as in the previous section. However, recall from chapter 3 that although the explicit filter is only directly applied to the nonlinear terms, the frequency content of the filter velocity field $\overline{\mathbf{u}}$ is dictated by the properties of filter $\tilde{G}(\boldsymbol{\kappa})$ because the nonlinear terms are responsible for transferring energy to higher wavenumbers. Therefore, the filtered velocity spectrum tensor is defined as $\overline{\Phi}_{ij}(\boldsymbol{\kappa}) = \tilde{G}(\boldsymbol{\kappa})^2\Phi_{ij}(\boldsymbol{\kappa})$.

The evolution of a filtered Fourier-mode $\widehat{\overline{u}}_k(\boldsymbol{\kappa})$ with a spectral eddy viscosity subgrid model $\nu_t(\boldsymbol{\kappa})$ is

$$\left(\frac{\partial}{\partial t} + \nu_t(\boldsymbol{\kappa})\widetilde{\kappa_j\kappa_j} - F(\boldsymbol{\kappa})\right)\widehat{\overline{u}}_k(\boldsymbol{\kappa}) = -iP_{km}(\widetilde{\boldsymbol{\kappa}})\sum_{\boldsymbol{\kappa}'}\frac{1}{2}\left(\tilde{\kappa}_\ell\tilde{G}(\boldsymbol{\kappa}) + \tilde{\kappa}'_\ell\tilde{G}(\boldsymbol{\kappa}')\right)\widehat{\overline{u}}_m(\boldsymbol{\kappa}')\widehat{\overline{u}}_\ell(\boldsymbol{\kappa}-\boldsymbol{\kappa}'). \tag{4.16}$$

The projection tensor is evaluated at the effective wavenumber as $P_{km}(\widetilde{\boldsymbol{\kappa}}) = \delta_{km} - \tilde{\kappa}_k\tilde{\kappa}_m/\tilde{\kappa}_j\tilde{\kappa}_j$. The equation for the filtered velocity spectrum tensor $\overline{\Phi}_{kp}(\boldsymbol{\kappa})$ is then

$$\begin{aligned}\left(\frac{\partial}{\partial t} + 2\nu_t(\boldsymbol{\kappa})\widetilde{\kappa_j\kappa_j} - 2F(\boldsymbol{\kappa})\right)\overline{\Phi}_{kp}(\boldsymbol{\kappa}) = &- iP_{ki}(\widetilde{\boldsymbol{\kappa}})\sum_{\boldsymbol{\kappa}'}\frac{1}{2}(\tilde{\kappa}_\ell\tilde{G}(\boldsymbol{\kappa}) + \tilde{\kappa}'_\ell\tilde{G}(\boldsymbol{\kappa}'))\langle\widehat{\overline{u}}^*_j(\boldsymbol{\kappa})\widehat{\overline{u}}_i(\boldsymbol{\kappa}')\widehat{\overline{u}}_\ell(\boldsymbol{\kappa}-\boldsymbol{\kappa}')\rangle \\ &+ iP_{pi}(\widetilde{\boldsymbol{\kappa}})\sum_{\boldsymbol{\kappa}'}\frac{1}{2}(\tilde{\kappa}_\ell\tilde{G}(\boldsymbol{\kappa}) + \tilde{\kappa}'_\ell\tilde{G}(\boldsymbol{\kappa}'))\langle\widehat{\overline{u}}_k(\boldsymbol{\kappa})\widehat{\overline{u}}^*_i(\boldsymbol{\kappa}')\widehat{\overline{u}}^*_\ell(\boldsymbol{\kappa}-\boldsymbol{\kappa}')\rangle.\end{aligned} \tag{4.17}$$

Lastly, the evolution equation for the triple correlation $\langle \widehat{\overline{u}}_k(\boldsymbol{\kappa})\widehat{\overline{u}}_i^*(\boldsymbol{\kappa}')\widehat{\overline{u}}_\ell^*(\boldsymbol{\kappa}-\boldsymbol{\kappa}')\rangle$ is

$$\begin{aligned}
&\Bigg(\frac{\partial}{\partial t}+\nu_t(\boldsymbol{\kappa})\widetilde{\kappa_j\kappa_j}+\nu_t(\boldsymbol{\kappa}')\widetilde{\kappa_j'\kappa_j'}+\nu_t(\boldsymbol{\kappa}'-\boldsymbol{\kappa})\widetilde{(\kappa_j'-\kappa_j)(\kappa_j'-\kappa_j)}- \\
&\qquad F(\boldsymbol{\kappa})-F(\boldsymbol{\kappa}')-F(\boldsymbol{\kappa}'-\boldsymbol{\kappa})\Bigg)\langle\widehat{\overline{u}}_k(\boldsymbol{\kappa})\widehat{\overline{u}}_i(-\boldsymbol{\kappa}')\widehat{\overline{u}}_\ell(\boldsymbol{\kappa}'-\boldsymbol{\kappa})\rangle = \\
&-iP_{km}(\widetilde{\boldsymbol{\kappa}})\sum_{\boldsymbol{\kappa}''}\frac{1}{2}(\tilde{\kappa}_s\tilde{G}(\boldsymbol{\kappa})+\tilde{\kappa''}_s\tilde{G}(\boldsymbol{\kappa}''))\langle\widehat{\overline{u}}_m(\boldsymbol{\kappa}'')\widehat{\overline{u}}_s(\boldsymbol{\kappa}-\boldsymbol{\kappa}'')\widehat{\overline{u}}_i(-\boldsymbol{\kappa}')\widehat{\overline{u}}_\ell(\boldsymbol{\kappa}'-\boldsymbol{\kappa})\rangle \\
&-iP_{im}(\widetilde{\boldsymbol{\kappa}}')\sum_{\boldsymbol{\kappa}''}\frac{1}{2}(-\tilde{\kappa}'_s\tilde{G}(\boldsymbol{\kappa}')+\tilde{\kappa''}_s\tilde{G}(\boldsymbol{\kappa}''))\langle\widehat{\overline{u}}_m(\boldsymbol{\kappa}'')\widehat{\overline{u}}_s(-\boldsymbol{\kappa}'-\boldsymbol{\kappa}'')\widehat{\overline{u}}_k(\boldsymbol{\kappa})\widehat{\overline{u}}_\ell(\boldsymbol{\kappa}'-\boldsymbol{\kappa})\rangle \\
&-iP_{\ell m}(\widetilde{\boldsymbol{\kappa}'-\boldsymbol{\kappa}})\sum_{\boldsymbol{\kappa}''}\frac{1}{2}((\widetilde{\kappa'-\kappa})_s\tilde{G}(\boldsymbol{\kappa}'-\boldsymbol{\kappa})+\tilde{\kappa''}_s\tilde{G}(\boldsymbol{\kappa}''))\langle\widehat{\overline{u}}_m(\boldsymbol{\kappa}'')\widehat{\overline{u}}_s(-\boldsymbol{\kappa}+\boldsymbol{\kappa}'-\boldsymbol{\kappa}'')\widehat{\overline{u}}_k(\boldsymbol{\kappa})\widehat{\overline{u}}_i(-\boldsymbol{\kappa}')\rangle
\end{aligned} \tag{4.18}$$

The EDQNM hypotheses can be applied to approximate the solution of equation (4.18) as

$$\begin{aligned}
&\langle\widehat{\overline{u}}_k(\boldsymbol{\kappa})\widehat{\overline{u}}_i(-\boldsymbol{\kappa}')\widehat{\overline{u}}_\ell(\boldsymbol{\kappa}'-\boldsymbol{\kappa})\rangle = \overline{\Theta}(\boldsymbol{\kappa},\boldsymbol{\kappa}',\boldsymbol{\kappa}'-\boldsymbol{\kappa})\Bigg[\\
&-iP_{km}(\widetilde{\boldsymbol{\kappa}})\Bigg[\frac{1}{2}(\tilde{\kappa}_s\tilde{G}(\boldsymbol{\kappa})+\tilde{\kappa}'_s\tilde{G}(\boldsymbol{\kappa}'))\overline{\Phi}_{mi}(\boldsymbol{\kappa}')\overline{\Phi}_{\ell s}(\boldsymbol{\kappa}'-\boldsymbol{\kappa}) \\
&\qquad+\frac{1}{2}(\tilde{\kappa}_s\tilde{G}(\boldsymbol{\kappa})-(\widetilde{\kappa'-\kappa})_s\tilde{G}(\boldsymbol{\kappa}'-\boldsymbol{\kappa}))\overline{\Phi}_{\ell m}(-\boldsymbol{\kappa}+\boldsymbol{\kappa}')\overline{\Phi}_{si}(\boldsymbol{\kappa}')\Bigg] \\
&-iP_{im}(\widetilde{\boldsymbol{\kappa}}')\Bigg[\frac{1}{2}(-\tilde{\kappa}'_s\tilde{G}(\boldsymbol{\kappa}')-\tilde{\kappa}_s\tilde{G}(\boldsymbol{\kappa}))\overline{\Phi}_{km}(\boldsymbol{\kappa})\overline{\Phi}_{\ell s}(\boldsymbol{\kappa}'-\boldsymbol{\kappa}) \\
&\qquad+\frac{1}{2}(-\tilde{\kappa}'_s\tilde{G}(\boldsymbol{\kappa}')-(\widetilde{\kappa'-\kappa})_s\tilde{G}(\boldsymbol{\kappa}-\boldsymbol{\kappa}'))\overline{\Phi}_{\ell m}(\boldsymbol{\kappa}'-\boldsymbol{\kappa})\overline{\Phi}_{ks}(\boldsymbol{\kappa})\Bigg] \\
&-iP_{\ell m}(\widetilde{\boldsymbol{\kappa}'-\boldsymbol{\kappa}})\Bigg[\frac{1}{2}((\widetilde{-\kappa+\kappa'})_s\tilde{G}(\boldsymbol{\kappa}'-\boldsymbol{\kappa})-\tilde{\kappa}_s\tilde{G}(\boldsymbol{\kappa}))\overline{\Phi}_{km}(\boldsymbol{\kappa})\overline{\Phi}_{si}(\boldsymbol{\kappa}') \\
&\qquad+\frac{1}{2}((\widetilde{-\kappa+\kappa'})_s\tilde{G}(\boldsymbol{\kappa}'-\boldsymbol{\kappa})+\tilde{\kappa}'_s\tilde{G}(\boldsymbol{\kappa}'))\overline{\Phi}_{mi}(\boldsymbol{\kappa}')\overline{\Phi}_{ks}(\boldsymbol{\kappa})\Bigg]\Bigg]
\end{aligned} \tag{4.19}$$

where the long-time relaxation timescale is $\overline{\Theta}(\boldsymbol{\kappa},\boldsymbol{\kappa}',\boldsymbol{\kappa}'-\boldsymbol{\kappa})=[\overline{\mu}(\boldsymbol{\kappa})+\overline{\mu}(\boldsymbol{\kappa}')+\overline{\mu}(\boldsymbol{\kappa}'-\boldsymbol{\kappa})]^{-1}$ and $\overline{\mu}(\boldsymbol{\kappa})$ must be modeled. The EDQNMLES model provides a closure for the filtered spectrum tensor $\overline{\Phi}_{ij}(\boldsymbol{\kappa})$ in equation (4.17). As before, the focus here will be on the energy spectrum

$\overline{E}(\boldsymbol{\kappa}) = \frac{1}{2}\overline{\Phi}_{kk}(\boldsymbol{\kappa})$ and the EDQNMLES approximation of the filtered energy transfer rate

$$T^{<}_{\text{skew}}(\boldsymbol{\kappa}) = -\text{Im}\left[\sum_{\boldsymbol{\kappa}'} \frac{1}{2}\left(\kappa_\ell \tilde{G}(\boldsymbol{\kappa}) + \kappa'_\ell \tilde{G}(\boldsymbol{\kappa}')\right) \langle \widehat{\overline{u}}_k(\boldsymbol{\kappa}) \widehat{\overline{u}}^*_k(\boldsymbol{\kappa}') \widehat{\overline{u}}^*_\ell(\boldsymbol{\kappa} - \boldsymbol{\kappa}') \rangle\right]. \tag{4.20}$$

The eddy damping hypothesis suggests that $\overline{\mu}(\boldsymbol{\kappa}) = \overline{\eta}(\boldsymbol{\kappa}) + \nu_t(\boldsymbol{\kappa})\widetilde{\kappa_j \kappa_j} + F(\boldsymbol{\kappa})$. In particular, $\nu_t(\boldsymbol{\kappa})\widetilde{\kappa_j \kappa_j}$ is the relaxation rate introduced by the eddy viscosity and accounts for phase scrambling effects due to nonlinear interactions between the resolved and subgrid scales. The eddy-damping term $\overline{\eta}$ represent the decorrelation rate of Fourier modes as a result of nonlinear interactions between resolved modes. The scaling of $\overline{\eta}$ is more complicated than η because of interactions with the subgrid stress. However, we can ensure the EDQNM and EDQNMLES approximations of the energy transfer agree for the case of Fourier spectral numerics and a Fourier cutoff filter by equating equations (4.9) and (4.19). This implies $\overline{\Theta} = \Theta$, i.e.,

$$\overline{\eta}(\boldsymbol{\kappa}) + \nu_t(\boldsymbol{\kappa})\widetilde{\kappa_j \kappa_j} = \eta(\boldsymbol{\kappa}). \tag{4.21}$$

Thus, at least in the idealized case, this theory will provide a good approximation to the filtered energy transfer rate $T^{<}_{\text{skew}}$. As before, we can determine the spectral eddy viscosity needed to reproduce a filtered Kolmogorov spectrum by substituting $\overline{\Phi}_{ij}(\boldsymbol{\kappa}) = \tilde{G}(\boldsymbol{\kappa})^2 P_{ij}(\tilde{\boldsymbol{\kappa}}) E(\kappa)/4\pi\kappa^2$ with Kolmogorov $E(\kappa)$ into equation (4.19) to approximate $T^{<}_{\text{skew}}(\boldsymbol{\kappa})$ a priori, and solve for spectral eddy viscosity via the steady state equation for the energy spectrum as $\nu_t(\boldsymbol{\kappa}) = \left(T^{<}_{\text{skew}}(\boldsymbol{\kappa}) + 2F(\boldsymbol{\kappa})\overline{E}(\boldsymbol{\kappa})\right)/2|\boldsymbol{\kappa}|^2\overline{E}(\boldsymbol{\kappa})$. This leads to the same eddy viscosity as in figure 4.2 and therefore the same a posteriori energy and energy transfer spectra as in figure 4.3. This model is extended to non-spectral numerics and graded explicit filters below.

4.3.2 Numerical dispersion error

The key observation in developing a statistical theory for the resolved nonlinear terms in an LES is that non-spectral numerics and non-cutoff filters lead to a phase decoherence between velocity Fourier modes that disrupts the energy transfer rate in the dispersive wavenumbers. This behavior was first identified by Yalla et al. [126] for the case of dispersion error introduced by a large mean convection velocity and lower-order numerics (linear dispersion error). They presumed that a similar phenomena may occur for nonlinear dispersion error that arises due to convection through the grid by turbulent fluctuations. Further, the analysis of Yalla et al. [126] indicates that the inverse timescale, ω, on which phase-scrambling due to dispersion error occurs is related to a characteristic velocity scale $\mathcal{U}$ and the error in the effective wavenumber and non-cutoff filter, i.e., $\omega(\boldsymbol{\kappa}) \sim \mathcal{U} \cdot (\boldsymbol{\kappa} - \tilde{G}(\boldsymbol{\kappa})\tilde{\boldsymbol{\kappa}})$.

The phase scrambling effects introduced by dispersion error therefore influence the eddy-damping hypothesis and must be accounted for in the corresponding eddy-damping model. There are at least two ways an appropriate model may be formulated. First, we propose to model $\overline{\Theta} = (\overline{\mu}(\boldsymbol{\kappa}) + \overline{\mu}(\boldsymbol{\kappa}') + \overline{\mu}(\boldsymbol{\kappa}' - \boldsymbol{\kappa}))^{-1}$ through

$$\overline{\mu}(\boldsymbol{\kappa}) \equiv \overline{\eta}(\boldsymbol{\kappa}) + \nu_t(\boldsymbol{\kappa})\widetilde{\kappa_j \kappa_j} + F(\boldsymbol{\kappa}) = \eta(\boldsymbol{\kappa}) + \omega(\boldsymbol{\kappa}) + F(\boldsymbol{\kappa}), \tag{4.22}$$

where $\omega(\boldsymbol{\kappa}) \sim \mathcal{U} \cdot (\boldsymbol{\kappa} - \tilde{G}(\boldsymbol{\kappa})\tilde{\boldsymbol{\kappa}})$ as above. In this case, the linear damping term $\omega(\boldsymbol{\kappa})$ appears in the evolution equation for each wavenumber in the triad interaction. Second, it would also be reasonable to instead introduce $\omega(\boldsymbol{\kappa}, \boldsymbol{\kappa}', \boldsymbol{\kappa}' - \boldsymbol{\kappa}) \sim \mathcal{U} \cdot (\tilde{G}(\boldsymbol{\kappa}')\tilde{\boldsymbol{\kappa}}' - \tilde{G}(\boldsymbol{\kappa})\tilde{\boldsymbol{\kappa}} - \tilde{G}(\boldsymbol{\kappa}' - \boldsymbol{\kappa})\widetilde{(\boldsymbol{\kappa}' - \boldsymbol{\kappa})})$ to the denominator of $\overline{\Theta}$. Based on the analysis in [126], this may more directly represent the dispersive characteristics of the triad interactions. However, we found that these two models performed identically for the tests reported in this chapter. Thus, we will generally consider $\omega(\boldsymbol{\kappa}) \sim \mathcal{U} \cdot (\boldsymbol{\kappa} - \tilde{G}(\boldsymbol{\kappa})\tilde{\boldsymbol{\kappa}})$ here.

The EDQNMLES approximation exposes the relaxation timescale of the filtered turbu-

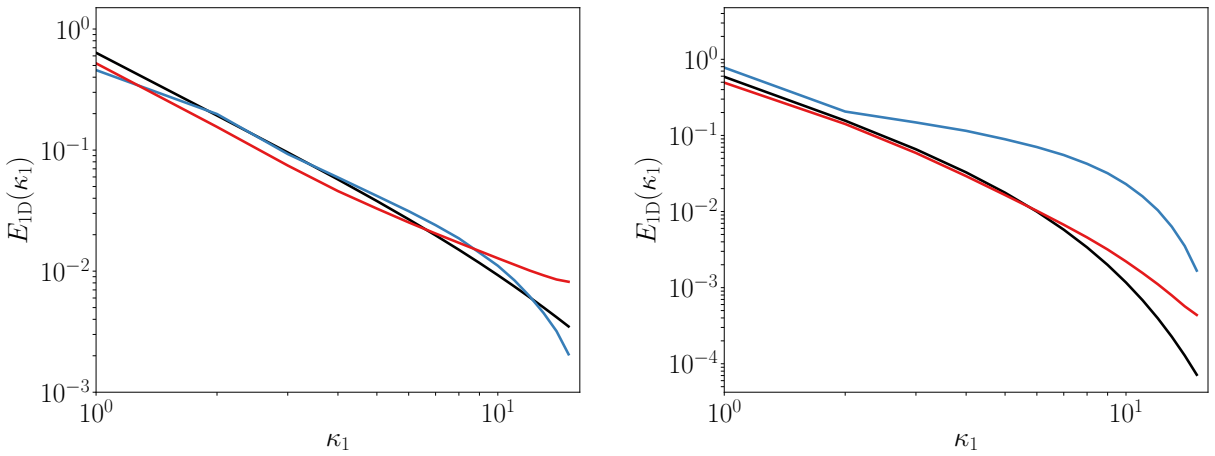

Figure 4.4: One-dimensional energy spectra computed from an LES with (a) second-order centered difference first derivative operators, Fourier-spectral second derivative operators, the skew symmetric form of the nonlinear terms, and a Fourier-cutoff filter and (b) Fourier-spectral numerics, the skew symmetric form of the nonlinear terms, and a Gaussian filter with filter width $\tilde{\Delta} = 2\Delta$. The eddy viscosity models in (a) and (b) are derived from the a priori EDQNM approximation for Fourier-spectral numerics and a cutoff filter (——) and the EDQNMLES approximation corresponding to each formulation with the Fourier-spectral model for $\overline{\Theta}$ (i.e., $\omega_N = 0$) (——). The equivalently filtered theoretical spectra are shown in both cases (——).

lence and is therefore well-positioned for directly investigating the effects of both nonlinear and linear dispersion error on the evolution of the third-order correlation. This is unlike the analysis in [126] which was only applicable to linear dispersion error in the regime of Taylor's hypothesis. An ω model is needed for each of these phenomena as they operate on different velocity scales. In the following subsection, we explore nonlinear dispersion error and its effect on the wavenumber dependent behavior of the eddy viscosity. Linear dispersion is considered in section 4.3.4.

4.3.3 Nonlinear dispersion error

Yalla et al. [126] demonstrated the effects of linear dispersion error on the energy and energy transfer spectra in LES. We pursue a similar investigation for the effects of nonlinear

dispersion error here. In particular, we are interested in how nonlinear dispersion error effects the energy spectrum when compared to an equivalently filtered Kolmogorov spectrum. This can be demonstrated in two ways. First, the EDQNMLES model of the eddy viscosity for the case of Fourier spectral numerics, a cutoff filter, and a Kolmogorov spectrum (see figure 4.2) can be applied to an LES computed with a lower-order numerical approximation to the convective derivative. For instance, consider an LES computed with second-order centered difference first derivatives operators, Fourier-spectral second derivatives, the skew-symmetric form of the nonlinear terms, and a mean velocity of $U = 0$. The 'spectral cusp' eddy viscosity model is not appropriate in this case. Excess energy is observed in the middle of the spectrum and the largest wavenumbers are overly damped (see figure 4.4a). This is not unlike the effects of linear dispersion error, which shut down the energy transfer for higher wavenumbers and led to an energy pile up in lower wavenumbers [126]. Second, we can compute the EDQNMLES eddy viscosity model for second-order centered difference numerics, the skew-symmetric form, a Kolmogorov spectrum, and the Fourier-spectral model for $\overline{\Theta}$, i.e., not modifying the eddy-damping hypothesis to account for dispersive phase scrambling. Applying this eddy viscosity to the same LES calculation leads to a posteriori energy spectra that are deficient for lower wavenumbers and increased near the cutoff (see figure 4.4a). Similar behaviors are also observed for non-cutoff explicit filters. For instance, consider an LES defined with an isotropic Gaussian explicit filter $\tilde{G}(\boldsymbol{\kappa}) = \exp(-|\boldsymbol{\kappa}|^2\tilde{\Delta}^2/24)$ with filter width $\tilde{\Delta} = 2\Delta$ and computed with Fourier-spectral numerics. As expected from [131], the spectral-cusp eddy viscosity is clearly not appropriate in this case (see figure 4.4b), however, neither is the EDQNMLES approximation of the eddy viscosity with the standard model of Θ (see figure 4.4b). Thus, when accounting for implicit and explicit filtering, the formulation of Leslie and Quarini [131] for the eddy viscosity will generally not lead to the correct a posteriori energy spectra.

This discussion indicates that nonlinear dispersion error has a meaningful impact on

the relaxation time of the filtered turbulence. To account for these effects, we introduce an additional relaxation rate ω_N into the eddy damping model as in equation (4.22). We are interested in determining ω_N so that the a priori EDQNMLES approximation of the energy transfer with a Kolmogorov model for $\overline{\Phi}_{ij}(\boldsymbol{\kappa})$ lead to a posteriori LES energy spectra that agree with a filtered Kolmogorov spectrum. This will determine the requirements of the spectral eddy viscosity needed to produce a Kolmogorov spectrum in the presence of nonlinear dispersion error. The model $\omega_N(\boldsymbol{\kappa}) = C_{\omega_N} u_{rms}(\kappa - \tilde{\kappa}\tilde{G}(\boldsymbol{\kappa}))$ for some constant C_{ω_N} was found to be sufficient for this purpose. The constant C_{ω_N} was determined by fitting the energy spectrum computed from an LES with the EDQNMLES model of the spectral eddy viscosity to a theoretical spectrum. The constant was found depend on κ_c for this model, with $C_{\omega_N} = -0.185$ for $\kappa_c = 16$ and $C_{\omega_N} = -0.275$ for $\kappa_c = 8$, although we anticipate a limiting value for large κ_c in the inertial range. Part of the κ_c dependence comes from the a priori estimate of $u_{rms} = \sqrt{2k/3}$ used, which was determined from $k = \sum_{\boldsymbol{\kappa}} \frac{1}{2}\Phi_{ii}(\boldsymbol{\kappa})$ based on a Kolmogorov spectrum, yielding $u_{rms} = 1.49$ for $\kappa_c = 16$ and $u_{rms} = 1.43$ for $\kappa_c = 8$.

The a priori EDQNMLES approximation of the spectral eddy viscosity needed to reproduce a Kolmogorov spectrum is evaluated a posteriori in four different LES. In each case the eddy viscosity is determined via $\nu_t(\boldsymbol{\kappa}) = \left(T^<(\boldsymbol{\kappa}) + 2F(\boldsymbol{\kappa})\overline{E}(\boldsymbol{\kappa})\right)/2|\boldsymbol{\kappa}|^2\overline{E}(\boldsymbol{\kappa})$ given the EDQNMLES approximation of $T^<_{\text{skew}}$ with an equivalently filtered Kolmogorov spectrum and nonlinear dispersion model ω_N. In each LES, the skew symmetric form of the nonlinear terms is used. In the first two LES, a Fourier-cutoff filter is used and the convective derivative is approximated with a second-order centered difference method and a second-order B-spline method. In the other two LES, Fourier-spectral numerics are used, but a Gaussian explicit filter is applied with filter width $\tilde{\Delta} = \Delta$ and $\tilde{\Delta} = 2\Delta$. These cases were chosen because they are expected to introduce significant dispersion error, either through the lower order numerics or the graded explicit filters. In each simulation, EDQNMLES approximates the eddy viscosity needed to represent an equivalently filtered Kolmogorov spectrum, which deviate

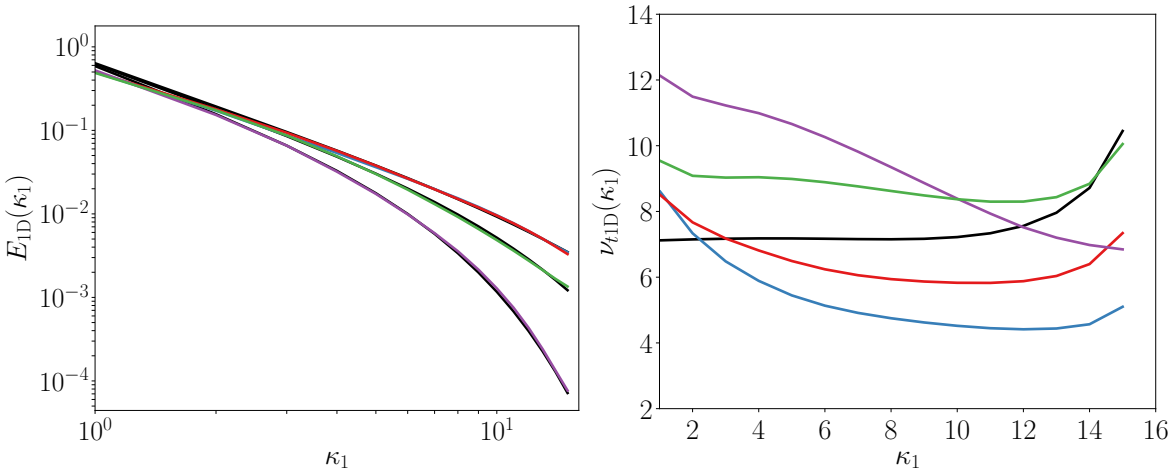

(a) (b)

Figure 4.5: (a) One-dimensional energy spectra of an LES computed with the EDQNMLES approximation of the eddy viscosities whose one-dimensional spectra are shown in (b). All cases correspond to the skew-symmetric form of the nonlinear term, a mean velocity of $U = 0$, a resolution of $\Delta = 2\pi/32$, and Fourier-spectral second derivative operators. The following four cases of explicit filters and first derivative approximations are shown: A Fourier cutoff filter with filter width $\tilde{\Delta} = \Delta$ and second-order centered difference numerics (——), and second-order B-spline numerics (——); Fourier-spectral numerics and a Gaussian explicit filter with filter width $\tilde{\Delta} = \Delta$ (——) and $\tilde{\Delta} = 2\Delta$ (——). The corresponding equivalently filtered Kolmogorov spectra for each case are also shown in (a) (——) and the spectral-cusp eddy viscosity spectra from figure 4.2 is shown in (b) (——).

significantly from the spectral-cusp eddy viscosity model (see figure 4.5b). The a posteriori spectra in all LES using these eddy viscosity models match remarkable well with the theoretical spectra (see figure 4.5a).

This can be extended to non-conservative formulations as well. Consider the second-order B-spline case for the skew-symmetric, convective, and conservative form of the nonlinear terms. EDQNMLES provides an a priori estimate of the energy injection rate introduced by the non-energy conserving resolved nonlinear interactions in each case ($\sum_{|\boldsymbol{\kappa}|\leq 8} T^{<}_{\text{cons}} = 0.47$, $\sum_{|\boldsymbol{\kappa}|\leq 8} T^{<}_{\text{conv}} = 0.55$, $\sum_{|\boldsymbol{\kappa}|\leq 8} T^{<}_{\text{skew}} = 0$), and adjusts the eddy viscosities accordingly (see figure 4.6c). Again, the a posteriori energy spectra match very well with a theoretical Kolmogorov spectrum for all nonlinear forms (see figure 4.6a) as do the energy transfer spectra

(see figure 4.6b). This result is particularly impressive since LES in this setting with either of the non-conservative nonlinear forms and standard subgrid stress models (such as a Kolmogorov or Smagorinsky model) are numerically unstable. However, we note that the EDQNMLES eddy viscosity model cannot correct these numerical instabilities in all cases. For instance, in the same setup but with second-order centered difference numerics, the a posteriori LES are numerically unstable. This is perhaps not surprising as EDQNMLES indicates that $\sum_{|\boldsymbol{\kappa}|\leq 8} T^{<}_{\text{conv}} = 0.85$ in this case, i.e., the convective formulation injects energy at a rate that is 85% of the total dissipation rate. Lastly, we note that EDQNMLES theory predicts that both the convective and conservative forms add energy into the system, despite the skew-symmetric form being energy conserving. This behavior was observed experimentally in section 3.5, and it was hypothesized that the turbulence was adjusting in both cases so that the convective and conservative forms added energy to the resolved scales. However, such an adjustment is clearly not possible in the theoretical analysis, so it is inherent to the numerical formulation of the nonlinear terms. Further, this behavior is contrary to explicit filters in non-energy conserving formulations where the conservative form is found to remove energy from the system, while the convective form adds energy, which is observed in both a priori EDQNMLES approximations and a posteriori LES calculations.

4.3.4 Linear dispersion error

The EDQNMLES model of the energy transfer can also be extended to include the effects of linear dispersion error introduced by a nonzero mean velocity $\mathbf{U}$ and non-spectral numerics or non-cutoff explicit filters. For the study of nonlinear dispersion error in the previous section, EDQNMLES approximated the eddy viscosity needed to reproduce a Kolmogorov spectrum, which was evaluated a posteriori in an LES. Although important, nonlinear dispersion effects are small enough that a good approximation to a Kolmogorov spectrum is attainable a posteriori with the right wavenumber dependent eddy viscosity. However, for $U \gg u_{rms}$, the

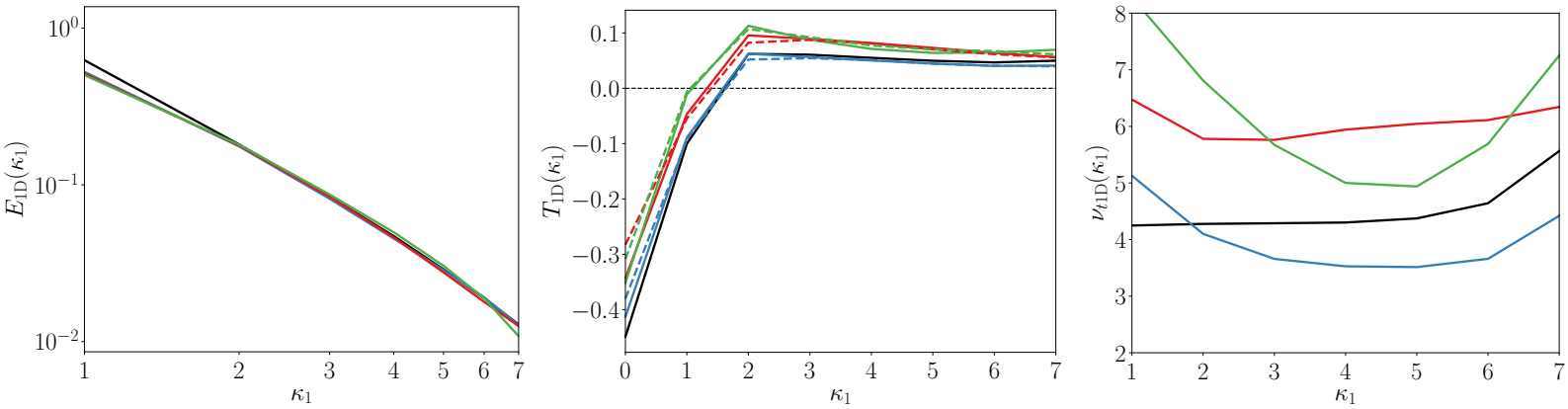

(a) (b) (c)

Figure 4.6: One-dimensional energy (a) and energy transfer (b) spectra from an LES computed with the EDQNMLES approximation of the eddy viscosities whose one-dimensional spectra are shown in (c). Each case corresponds to second-order B-spline first derivative operators, a mean velocity of $U = 0$, a resolution of $\Delta = 2\pi/16$, Fourier-spectral second derivative operators, and a Fourier-cutoff filter. The skew-symmetric (———), conservative (———), and convective (———) form of the nonlinear terms are shown. In (b) the a priori EDQNMLES approximations of the energy transfer are given by the solid lines, and the corresponding a posteriori LES energy transfer spectra are given by the dashed lines. The equivalently filtered Kolmogorov spectrum is also shown in (a) (———), and the EDQNMLES approximation of the energy transfer and energy viscosity spectra for Fourier spectral numerics and filtering are shown (b) and (c) (———).

results in [126] suggest that a Kolmogorov spectrum is not attainable when considering linear dispersion error. This is because the shut down of energy transfer rate $T^<$ is so strong for the dispersive wavenumbers that no dynamic balance resembling a Kolmogorov spectrum can be obtained. Therefore, we instead ask if EDQNMLES can predict the energy and energy transfer spectra that arise in an LES of turbulence being convected through a grid with a given mean velocity.

To answer this question, first consider the EDQNMLES approximation of the energy transfer $T^<_{\text{skew}}$ given a filtered energy spectrum $\overline{\Phi}_{ij}$ computed from an LES. Specifically, we follow Yalla et al. [126] and consider an LES computed with a Cartesian Fourier-cutoff filter, a mean velocity of $U = 35$, the skew-symmetric form of the nonlinear terms, Fourier-spectral second derivative approximations, and third-order B-spline collocation first derivative ap-

proximations. The eddy viscosity model used in this LES is determined from EDQNMLES with nonlinear dispersion model ω_N so that the energy spectra match a Kolmogorov spectrum for $U = 0$ (as in section 4.3.3). The energy spectra in this case exhibit the same behavior as reported in section 3.3. The energy transfer rate in the direction of mean convection shuts down around $\kappa_1 = 8$ (see figure 4.7b), leading to an energy spectrum that is increased for intermediate wavenumbers and depleted in the largest wavenumbers (see figure 4.7a). In directions orthogonal to mean convection, the energy transfer rate remains consistent with the theoretical result throughout the inertial range (see figure 4.7d), and a slight energy-pile up is observed in the mid-to-largest wavenumbers of the energy spectrum because of the deficiency in the x-direction (see figure 4.7c). Given $\Phi_{ij}(\boldsymbol{\kappa})$ from the LES, the EDQNMLES closure of the energy transfer (via equations (4.19) and (4.20)) is then computed.

First suppose that the relaxation timescale of the EDQNMLES approximation is not adjusted to account for linear dispersion error. In this case, the approximation of the energy transfer in the direction of mean convection is highly inaccurate. There seems to be a type of inflection point at the wavenumber where the true energy transfer shuts down ($\kappa_1 = 8$), with the approximated transfer spectra going negative for $\kappa_1 < 8$ and rising sharply for $\kappa_1 > 8$ (see figure 4.7b). This behavior is difficult to interpret physically. However, an additional damping term ω_L is clearly needed to account for the relaxation rate introduced by linear dispersion error. We take $\omega_L(\boldsymbol{\kappa}) = C_{\omega_L}\mathbf{U}\cdot(\boldsymbol{\kappa} - \tilde{\boldsymbol{\kappa}}\tilde{G}(\boldsymbol{\kappa}))$ so that $\overline{\Theta}(\boldsymbol{\kappa}, \boldsymbol{\kappa}', \boldsymbol{\kappa}' - \boldsymbol{\kappa}) = [\overline{\mu}(\boldsymbol{\kappa}) + \overline{\mu}(\boldsymbol{\kappa}') + \overline{\mu}(\boldsymbol{\kappa}' - \boldsymbol{\kappa})]^{-1}$ is modeled through

$$\overline{\mu}(\boldsymbol{\kappa}) \equiv \overline{\eta}(\boldsymbol{\kappa}) + \nu_t(\boldsymbol{\kappa})\widetilde{\kappa_j\kappa_j} + F(\boldsymbol{\kappa}) = \eta(\boldsymbol{\kappa}) + \omega_N(\boldsymbol{\kappa}) + \omega_L(\boldsymbol{\kappa}) + F(\boldsymbol{\kappa}). \tag{4.23}$$

The constant C_{ω_L} is determined so that the EDQNMLES approximation of the energy transfer agree with the a posteriori LES computation of the energy transfer (a value of $C_{\omega_L} = -2.0$ is used here).

The EDQNMLES approximation with this model for ω_L yields a much more physically meaningful approximation to the energy transfer. The energy transfer spectra agree roughly the calculation from an LES for low wavenumbers and tends to zero over the range of dispersive wavenumbers (see figure 4.7b). Although the shut down of the energy transfer is captured well for $\kappa_1 > 8$, the model does not quite capture the increase in the energy transfer observed in the low-to-mid wavenumbers in the LES (see figure 4.7b). Additional refinements to the ω_L model may be needed to improve this behavior. Nonetheless, these results demonstrate that the relaxation timescale introduced by linear dispersion error is a significant component of the energy transfer process in an LES, as expected, and must therefore be represented by the eddy-damping model in EDQNMLES. Further, this model for ω_L is able to preserve the correct energy transfer in the directions orthogonal to mean convection (see figure 4.7d), which is particularly encouraging as it indicates that the EDQNMLES theory developed here is rich enough to represent such anisotropies in the turbulence. Lastly we note that the behavior reported here was found to be consistent across mean velocities U and numerical first derivative approximations. The seventh-order B-spline case is shown in figure 4.8 for completeness.

The EDQNMLES approximation of the energy spectrum for a given eddy viscosity and ω_L model could also be determined by solving equation (4.17) for $\overline{\Phi}_{ij}$ with the closure in equation (4.18). However, this would require the development of software capable of solving this highly non-linear three-dimensional systems. This is a much more challenging computational task than solving for the spectral eddy viscosity or energy transfer rate for a given spectrum because of the anisotropies introduced by numerical discretization and filtering. Such an EDQNMLES solver for the energy spectrum will be pursued in future work. This will serve as a further validation test for the ω_L model and provide further insight into the effects of dispersion error on the nonlinear dynamics of turbulence.

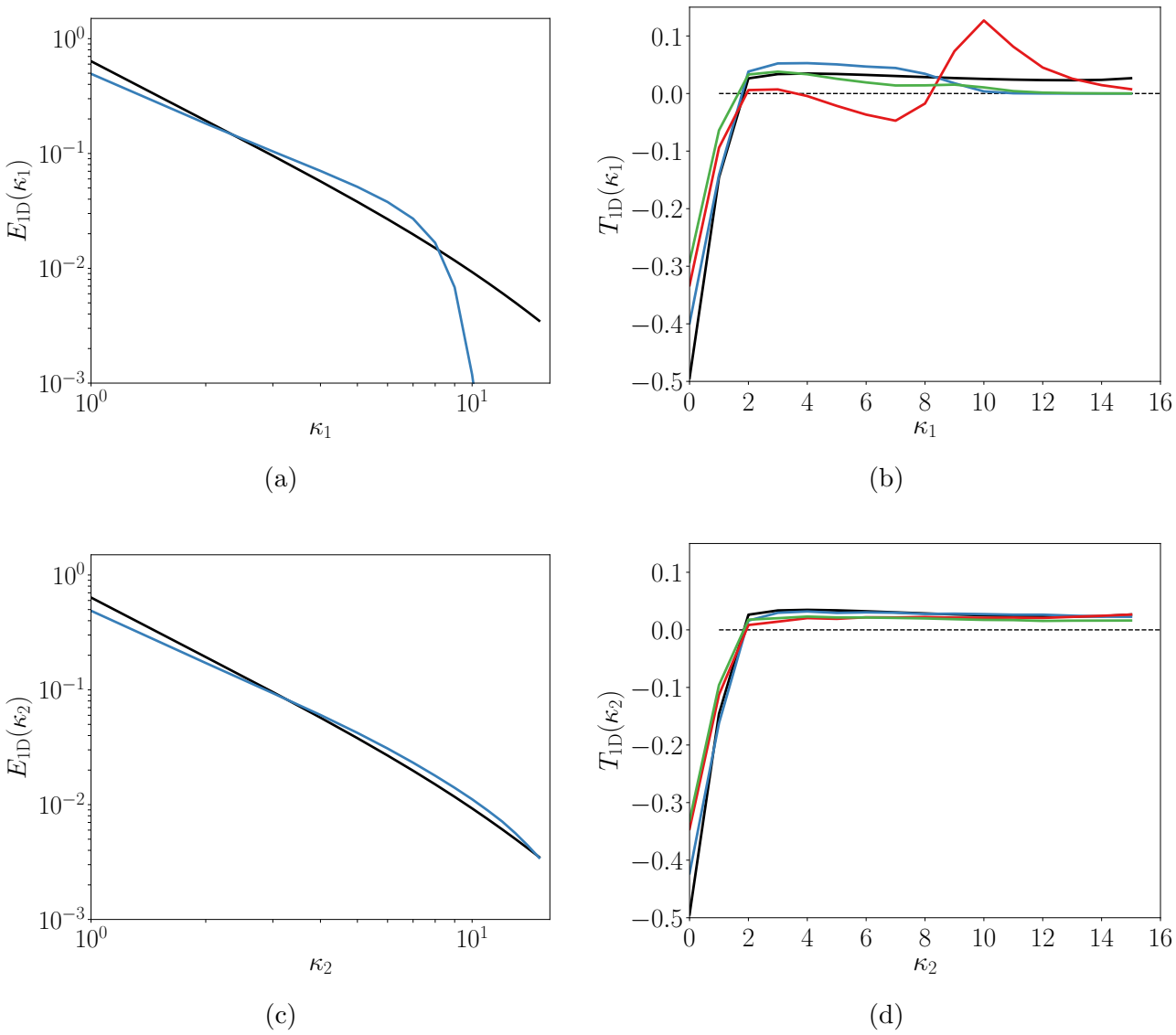

Figure 4.7: One-dimensional energy and energy transfer spectra corresponding to an implicitly filtered LES with 3rd-order B-spline collocation first derivative approximations, Fourier-spectral second derivatives, the skew-symmetric form of the nonlinear terms, and $U = 35$. The EDQNMLES eddy viscosity with nonlinear dispersion model ω_N is used. The spectra computed from an LES are shown (——), along with the EDQNMLES approximation to the energy transfer given the LES energy spectrum with $\omega_L = 0$ (——), and $\omega_L = C_{\omega_L}\mathbf{U} \cdot (\boldsymbol{\kappa} - \tilde{G}(\boldsymbol{\kappa})\tilde{\boldsymbol{\kappa}})$ (——). The theoretical case for a Kolmogorov spectrum is also shown (——). (a) and (b) are one-dimensional spectra in the direction of mean convection, while (c) and (d) are in a direction orthogonal to mean convection.

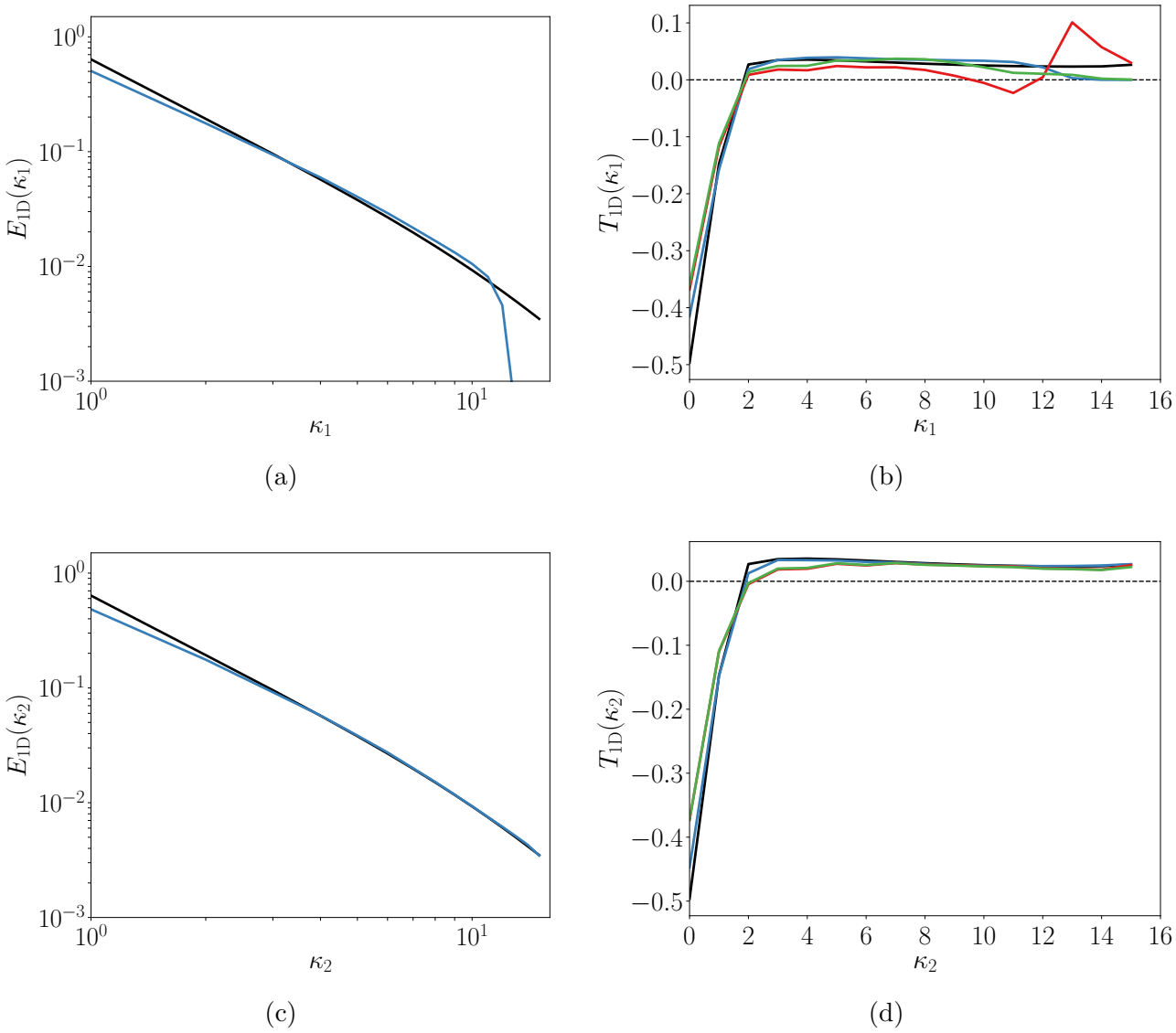

Figure 4.8: One-dimensional energy and energy transfer spectra corresponding to an implicitly filtered LES with 7th-order B-spline collocation first derivative approximations, Fourier-spectral second derivatives, the skew-symmetric form of the nonlinear terms, and $U = 35$. The EDQNMLES eddy viscosity with nonlinear dispersion model ω_N is used. The spectra computed from an LES are shown (——), along with the EDQNMLES approximation to the energy transfer given the LES energy spectrum with $\omega_L = 0$ (——), and $\omega_L = C_{\omega_L}\mathbf{U} \cdot (\boldsymbol{\kappa} - \tilde{G}(\boldsymbol{\kappa})\tilde{\boldsymbol{\kappa}})$ (——). The theoretical case for a Kolmogorov spectrum is also shown (——). (a) and (b) are one-dimensional spectra in the direction of mean convection, while (c) and (d) are in a direction orthogonal to mean convection.

4.4 Discussion

In this chapter we introduced an analytical statistical theory for the filtered turbulence represented in an LES based on EDQNM theory. Previous applications of EDQNM to LES were mainly restricted to the case of a Fourier-cutoff filter and Fourier-spectral numerics [47] or to graded filters with no regard for implicit filtering [131], because the underlying two-point closure ultimately applied to the unfiltered third-order correlations (see section 4.2). Here we extended EDQNM to represent the filtered third-order correlations (denote EDQNMLES), so the formulation extends naturally to implicit and explicit filtering, non-Fourier spectral numerics and other particulars of an LES formulation (see section 4.3). This theory is useful for exposing how these particulars of an LES influence the nonlinear energy transfer between Fourier modes and indicating the requirements of subgrid scale turbulence models for a given LES formulation.

Classical EDQNM theory informed the eddy-damping model in the LES case through η, however, it was necessary to further modify the eddy-damping hypothesis to account for the effects of filtering and numerics on the relaxation time of velocity correlations for both linear and nonlinear dispersion error (see section 4.3.2). Notably, the results here indicate that nonlinear dispersion error has a meaningful impact on the evolution of the third-order correlations and must therefore be accounted for in the formulation of subgrid scale turbulence models. In fact, this was important for recovering a Kolmogorov spectrum a posteriori for non-spectral numerics and non-cutoff filters (see section 4.3.3). As hypothesized by Yalla et al. [126], the underlying process through which nonlinear dispersion error affects the energy transfer is by increasing the relaxation rate of the correlation between velocity Fourier-modes for dispersive wavenumbers. This timescale is directly accessible in the EDQNMLES closure, unlike in the analytical approach in section 3.3, which only applies to the mean convection case in the regime of Taylor's hypothesis.

The techniques developed here may be useful for exploring several characteristics of an LES as discussed by Moser et al. [1]. Regarding dissipation, the results here may inform the requirements of SGS models for a given choice of numerics and filter. For instance, hyperviscosity models may not be appropriate for lower-order numerics, since the spectral-eddy viscosity do not exhibit as large of a cusp near the cutoff (see figure 4.5b). Similarly, the a priori estimates of the energy injection rate for different numerical formulations of the nonlinear terms could inform SGS constants (as in equation (3.20)) or even provide an a priori test of implicit LES models. The formulation here should also extend naturally to the case of resolution anisotropy. This may indicate the effect of anisotropic resolution on the energy transfer rate that lead to the energy spectra reported by Haering et al. [17]. It may also inform the requirements of anisotropic subgrid-stress models, which could lead to model improvements or explain why certain anisotropic models perform well despite not seemingly representing the dissipation anisotropy of the turbulence [17]. It would also be interesting to see if EDQNMLES could say something useful about very-coarse LES where modeling mean subgrid stress effects become important [37]. Perhaps these techniques could inform the requirements of split eddy viscosity formulations [38, 40, 99] for instance. The effects of resolution inhomogeneity in LES could be explored. In chapter 5 a spectral representation of the inhomogeneous commutator is developed. EDQNMLES would be useful for informing nonlinear commutation error in this case, computing an a priori estimate of the effects of commutation error on the energy spectrum, and perhaps informing the requirements of commutator models. Lastly, this analysis may be useful for analyzing aliasing errors a priori.

Lastly, we note that although the focus in this chapter was on the energy spectrum and energy transfer process, the EDQNMLES theory developed here would be useful in analyzing the anisotropies of the full filtered spectrum tensor $\overline{\Phi}_{ij}(\boldsymbol{\kappa})$ as well as the anisotropies of the corresponding spectral eddy viscosity. This may be particularly important because practical numerical discretizations and filtering induce anisotropies.

Chapter 5

Analysis of the inhomogeneous commutator

Note that much of the material in this chapter was published previously by Yalla, Oliver, Haering, Engquist, and Moser [139]

In this chapter we investigate the issues that arise from inhomogeneous filtering/resolution (note that by inhomogeneity of an LES filter or resolution, we mean that the filter or resolution characteristics vary in space; this should not be confused with homogeneity or inhomogeneity of the turbulence). The challenges posed by resolution inhomogeneity arise because, in this case, the filter that defines the resolved scales does not commute with spatial differentiation (see section 1.1). This effect is represented the commutation term $\mathcal{C}_j^I$, which should appear in the LES evolution equation. When this effect is neglected it gives rise to "commutation error", which was first analyzed in detail by Ghosal and Moin [22]. Since then, several investigators have acknowledged the significant impact commutation error can have on an LES solution [145, 146, 147, 151, 182, 34, 33, 183, 11, 184, 185]. Despite this, the commutation term is often neglected in practice.

Most of the previous work to address commutation error has been in the context of explicit filtering. As discussed in section 3.6, explicit filters, which may be employed in addition to the discrete projection that defines the implicit filter, are used to minimize the effects of numerical discretization errors by defining a filter width larger than the discretization scale [144, 140, 118, 120, 119, 141, 142, 149, 148]. Approximately commuting with differentiation

is then viewed as a desirable property of explicit filters to minimize commutation error. In this context, van der Ven [145] introduced a one-parameter family of analytical filters that commute with differentiation up to a given order in filter width. Vasilyev et al. [146] developed a set of constraints for constructing discrete filters that commute with differentiation up to a desired order. Marsden et al. [147] extended the work of [146] to unstructured meshes.

However, in an LES, the projection onto a finite dimensional LES solution space that is inherent in numerical discretization is ultimately responsible for discarding information about the small-scale turbulence [15, 16]. Therefore, the commutator between filtering and differentiation that arises due to spatially nonuniform numerical discretization and the commutation error that arises from neglecting it are the fundamental issues introduced by resolution inhomogeneity in LES. They are of particular importance in practical LES as many applications rely solely on implicit filtering. Further, the commutation analysis of Ghosal and Moin [22] only applies to smooth formally invertible filters, not filters that include a discrete projection. Similarly, the commutative property of an explicit filter (such as those mentioned above) would only reduce the additional commutation error introduced by the explicit filter applied in addition to the discrete projection. These explicit filters do not represent the commutator associated with the implicit filter and so, in general, do not reduce the corresponding commutation error. Neither the commutation error nor commutator models applicable to implicit filtering have been well investigated.

In this section we explore a multiscale asymptotic analysis of $\mathcal{C}^I$, with the goal of analytically identifying an *a priori* statistical requirement imposed by this commutator on the flow. The numerical effects of commutation error in LES are explored in chapter 6. For the purposes of analysis, it is useful to start by considering the effects of the resolution inhomogeneity on the filtered one-dimensional advection equation:

$$\overline{\frac{\partial u}{\partial t} + U\frac{\partial u}{\partial x}} = 0, \tag{5.1}$$

where U is the constant convection velocity. In many turbulent flows the mean velocity relative to the grid is much larger than the fluctuating velocity, so arguably the commutation error for the mean convection term is most important. As before, we can write equation (5.1) as

$$\frac{\partial \overline{u}}{\partial t} + U\frac{\delta \overline{u}}{\delta x} = -U\mathcal{C}(u), \tag{5.2}$$

where $\mathcal{C}(u) = \overline{\partial u/\partial x} - \delta\overline{u}/\delta x$ is the commutation term, which can can be further decomposed into an inhomogeneous and homogeneous part as $\mathcal{C}(u) = \mathcal{C}^I(u) + \mathcal{C}^H(u)$ where,

$$\mathcal{C}^I(u) = \overline{\frac{\partial u}{\partial x}} - \overline{\frac{\partial u}{\partial \xi}}\frac{d\xi}{dx} \qquad \mathcal{C}^H(u) = \overline{\frac{\partial u}{\partial \xi}}\frac{d\xi}{dx} - \frac{\delta \overline{u}}{\delta x}, \tag{5.3}$$

and ξ is the new spatial coordinate in which the grid or resolution is uniform as in [22].

In the seminal work of Ghosal and Moin [22], the commutator is estimated through Taylor series analysis allowing the commutator to be analyzed. However there were limitations of that work. First, the analysis uses an approximate inversion of the filter operator, and as such is formally only applicable to invertible filters, and thus not to filters including discrete projections as considered here. And second, in simplifying the expansions, an ad hoc ordering is employed which resulted in the neglect of terms that a more careful analysis would identify as important. Here we pursue a similar program using asymptotic analysis with the goals of placing the results of Ghosal and Moin [22] for invertible filters on firmer ground (section 5.4), and of developing statistical characterizations of the commutator applicable to non-invertible filters (section 5.2). The results for invertible filters are of interest here because they can provide guidance on appropriate forms and dependencies for a model of the commutator. This may be valuable because filters that include discrete projections can be considered to be limits of sequences of invertible filters. The multiscale analysis is presented in sections 5.1 to 5.3 with a general discussion section 5.4.

5.1 Series representation of the inhomogeneous commutator

As in Ghosal and Moin [22], any smoothly nonuniform grid x with spacing $\Delta(x)$ can be mapped to a uniform grid of spacing Δ_ξ through some invertible monotonic differentiable mapping function $\xi = f(x)$. Let $G(\xi)$ be a symmetric filter kernel normalized on ξ that decays sufficiently fast so that all moments of G exist. To define the filtering operation applied to an arbitrary function $\psi(x)$, we first make a change of variables to ξ ($\psi(\xi) \equiv \psi(f^{-1}(\xi))$) and then filter $\psi(\xi)$ with the homogeneous filter defined by $G(\xi)$:

$$\overline{\psi}(\xi) = \frac{1}{\Delta_\xi} \int G\left(\frac{\xi - \eta}{\Delta_\xi}\right) \psi(\eta) d\eta. \tag{5.4}$$

The result is then transformed back to x to obtain:

$$\overline{\psi}(x) \equiv \overline{\psi}(f(x)) = \frac{1}{\Delta_\xi} \int G\left(\frac{f(x) - f(y)}{\Delta_\xi}\right) \psi(y) f'(y) dy. \tag{5.5}$$

Therefore $\dfrac{d\overline{\psi}}{dx} \equiv \dfrac{d\overline{\psi}}{d\xi}\dfrac{d\xi}{dx}$, so that the inhomogeneous part of the commutator is

$$\mathcal{C}^I(\psi) = \overline{\frac{d\psi}{dx}} - \frac{d\overline{\psi}}{d\xi}\frac{d\xi}{dx} \tag{5.6}$$

as in equation (5.3).

Now, suppose that the resolution (filter width) is slowly varying in x, that is $\frac{d\Delta}{dx}$ is order $\epsilon \ll 1$. Notice that this limit can be approached in two ways. In particular, consider the length scale L_Δ defined as the inverse logarithmic derivative of the resolution ($\frac{1}{L_\Delta} \sim \frac{1}{\Delta}\frac{d\Delta}{dx}$). Then the ϵ limit can be approached by (1) allowing L_Δ to grow while Δ remains constant, or (2) letting L_Δ remain constant while Δ goes to zero. In either case, equation (5.5) is

asymptotically equivalent to

$$\overline{\psi}(x) = \frac{f'(x)}{\Delta_\xi} \int G\left(\frac{f'(x)(x-y)}{\Delta_\xi}\right) \psi(y) dy + \mathcal{O}(\epsilon). \tag{5.7}$$

Further, in the case of an inhomogeneous filter with slowly varying resolution, a filtered quantity will vary over a long and short length scale, the scale of filter variation and the scale of resolved turbulent fluctuations, respectively. As such, we use equation (5.7) to facilitate a multiscale asymptotic analysis of the commutator in terms of a slow variable $w = \epsilon x$ and fast variable $\tilde{x}$. In this case, Δ depends on w, but not $\tilde{x}$. Since $f'(x) = \Delta_\xi / \Delta(x)$, we have

$$\overline{\psi}(w, \tilde{x}) = \frac{1}{\Delta(w)} \int G\left(\frac{\tilde{x}-y}{\Delta(w)}\right) \psi(y) dy. \tag{5.8}$$

In what follows, the dependence of Δ on w is implied though no longer explicitly indicated. Using multiscale asymptotics, the derivative of $\overline{\psi}$ with respect to x is written

$$\frac{d\overline{\psi}}{dx} = \frac{\partial \overline{\psi}}{\partial \tilde{x}} + \epsilon \frac{\partial \overline{\psi}}{\partial w} + \mathcal{O}(\epsilon^2). \tag{5.9}$$

Since the filter is homogeneous in $\tilde{x}$, $\dfrac{\partial \overline{\psi}}{\partial \tilde{x}} = \overline{\dfrac{d\psi}{dx}}$. Therefore, to leading order the commutator is given by

$$\mathcal{C}^I(\psi) = \overline{\frac{d\psi}{dx}} - \frac{d\overline{\psi}}{\partial x} = -\epsilon \frac{\partial \overline{\psi}}{\partial w}, \tag{5.10}$$

which can be computed as

$$\mathcal{C}^I(\psi) = \frac{1}{\Delta^2} \frac{d\Delta}{dx} \int \left(\frac{\tilde{x}-y}{\Delta} G'\left(\frac{\tilde{x}-y}{\Delta}\right) + G\left(\frac{\tilde{x}-y}{\Delta}\right)\right) \psi(y)\, dy. \tag{5.11}$$

where G' is the derivative of G with respect to its argument. Introducing the variable

$\zeta = (y - \tilde{x})/\Delta$ and expanding $\psi(y)$ in a Taylor series about $\tilde{x}$ gives

$$\begin{aligned} \mathcal{C}^I(\psi) &= \frac{1}{\Delta}\frac{d\Delta}{dx}\int \left(\zeta G'(\zeta) + G(\zeta)\right)\left(\sum_{n=0}^{\infty}\frac{(\zeta\Delta)^n}{n!}\frac{d^n\psi}{dx^n}(\tilde{x})\right)d\zeta \\ &= \sum_{n=1}^{\infty}\left(\frac{-\Delta^{2n-1}}{(2n-1)!}\frac{d\Delta}{dx}\frac{d^{2n}\psi}{dx^{2n}}(\tilde{x})\int \zeta^{2n}G(\zeta)d\zeta\right) \end{aligned}, \tag{5.12}$$

where we have used the fact that odd order moments of G are zero. To express the commutator in terms of the filtered field $\overline{\psi}$, we first invert equation (5.8) using the same procedure to obtain

$$\psi(\tilde{x}) = \overline{\psi}(w,\tilde{x}) - \sum_{n=1}^{\infty}\frac{\Delta^{2n}}{(2n)!}\frac{d^{2n}\psi}{dx^{2n}}(\tilde{x})\int \zeta^{2n}G(\zeta)d\zeta. \tag{5.13}$$

Then we can recursively substitute equation (5.13) into equation (5.12) to obtain an expression for the commutator in terms of $\overline{\psi}$. However, to properly order this expansion, the way in which derivatives of $\overline{\psi}$ and Δ scale with ϵ must be considered. When $\epsilon \to 0$ at constant Δ, both $\overline{\psi}$ and Δ are order one in ϵ. However, when $\epsilon \to 0$ at constant L_Δ, $\Delta \sim \epsilon$ and, in general, the derivatives of $\overline{\psi}$ scale with powers of ϵ. In high Reynolds number turbulence that has been filtered at scale Δ in the inertial range, the Kolmogorov scale similarity hypotheses for the statistics of velocity differences imply that the statistics of the derivatives of the filtered velocity $\overline{u}$ depend only on Δ and the rate of kinetic energy dissipation ε_k. Dimensional analysis then requires that the standard deviation of $\partial^n\overline{u}/\partial x^n$ scales as $\varepsilon_k^{2/3}\Delta^{1/3-n}$. Thus, taking ψ to be u, the n^{th} derivative of $\overline{u}$ in the series expansion will scale as $\epsilon^{1/3-n}$.

Regardless of how the limit of small ϵ is approached, one obtains

$$\begin{aligned}\mathcal{C}^I(u) &= -M_2\Delta\frac{d\Delta}{dx}\frac{\partial^2\overline{u}}{\partial\tilde{x}^2} + \left(\frac{M_2^2}{2} - \frac{M_4}{6}\right)\Delta^3\frac{d\Delta}{dx}\frac{\partial^4\overline{u}}{\partial\tilde{x}^4} + \cdots + C_N\Delta^{N-1}\frac{d\Delta}{dx}\frac{\partial^N\overline{u}}{\partial\tilde{x}^N} + \cdots + \mathcal{O}(\epsilon^q) \\ &= \sum_{n=1}^{\infty}\left(C_{2n}\Delta^{2n-1}\frac{d\Delta}{dx}\frac{\partial^{2n}\overline{u}}{\partial\tilde{x}^{2n}}\right) + \mathcal{O}(\epsilon^q)\end{aligned}, \tag{5.14}$$

where $q = 2$ when the asymptotic limit is taken with constant Δ (the leading order series being order ϵ) and $q = 4/3$ when it is taken at constant L_Δ (the leading order series being order $\epsilon^{1/3}$). Here we let M_k denote the kth order moment of the filter kernel, N is even, and in general, the coefficient C_j on the j^{th} order term depends on the moments of the filter up to order j.

5.2 Spectral characteristics of the commutator

We turn our attention now to the spectral characteristics of the commutator. However, to make a connection to the statistical properties of the commutator in LES of turbulence, we consider instead a three-dimensional isotropic inhomogeneous filter, defined similarly to equation (5.7) as

$$\overline{\psi}(\mathbf{x}) = \frac{1}{\Delta(\mathbf{x})^3}\int G\left(\frac{|\mathbf{x}-\mathbf{y}|}{\Delta(\mathbf{x})}\right)\psi(\mathbf{y})d\mathbf{y}, \tag{5.15}$$

where G is now a scalar function on $[0,\infty)$ satisfying $4\pi\int_0^\infty G(r)r^2\,dr = 1$. The same multiscale expansion holds as above for the case where $\frac{\partial\Delta}{\partial x_i} \sim \mathcal{O}(\epsilon)$. The filtering operation can be expressed as

$$\overline{\psi}(\mathbf{w},\tilde{\mathbf{x}}) = \frac{1}{\Delta(\mathbf{w})^3}\int G\left(\frac{|\tilde{\mathbf{x}}-\mathbf{y}|}{\Delta(\mathbf{w})}\right)\psi(\mathbf{y})d\mathbf{y}, \tag{5.16}$$

where $\mathbf{w} = \epsilon\mathbf{x}$ is the slow variable and $\tilde{\mathbf{x}}$ is the fast variable, and the commutator, $\mathcal{C}_i^I(\psi) = \overline{\frac{\partial \psi}{\partial x_i}} - \frac{\partial \overline{\psi}}{\partial x_i} = -\epsilon \frac{\partial \overline{\psi}}{\partial w_i}$, can be computed as

$$\begin{aligned} \mathcal{C}_i^I(\psi) &= \frac{\epsilon}{\Delta^4} \frac{\partial \Delta}{\partial w_i} \int \left(\frac{|\tilde{\mathbf{x}} - \mathbf{y}|}{\Delta} G' \left(\frac{|\tilde{\mathbf{x}} - \mathbf{y}|}{\Delta} \right) + 3G \left(\frac{|\tilde{\mathbf{x}} - \mathbf{y}|}{\Delta} \right) \right) \psi(\mathbf{y})\, d\mathbf{y} \\ &\equiv \int \mathcal{C}_i(\mathbf{w}, \tilde{\mathbf{x}} - \mathbf{y}) \psi(\mathbf{y}) d\mathbf{y} \end{aligned}, \tag{5.17}$$

Furthermore, because the filter is homogeneous in the fast variable, it is useful to consider the Fourier transform of $\overline{\psi}$ in the fast variable:

$$\widehat{\overline{\psi}}(\mathbf{w}, \boldsymbol{\kappa}) = \frac{1}{(2\pi)^3} \int \overline{\psi}(\mathbf{w}, \tilde{\mathbf{x}}) e^{-i\boldsymbol{\kappa}\cdot\tilde{\mathbf{x}}}\, d\tilde{\mathbf{x}}. \tag{5.18}$$

Applying the convolution theorem to equation (5.16) yields $\widehat{\overline{\psi}}(\mathbf{w}, \boldsymbol{\kappa}) = \widehat{\psi}(\boldsymbol{\kappa}) \widehat{G}(\Delta|\boldsymbol{\kappa}|)$, where $\widehat{\psi}$ is the Fourier transform of ψ and $\widehat{G}(|\boldsymbol{\kappa}|) = \frac{1}{(2\pi)^3} \int G(|\mathbf{z}|) e^{-i\boldsymbol{\kappa}\cdot\mathbf{z}}\, d\mathbf{z}$ is the Fourier transform of the filter kernel, which depends only on $|\boldsymbol{\kappa}|$ because $G(|\mathbf{z}|)$ is isotropic. Note that because the unfiltered quantity ψ does not depend on Δ, it also does not depend on $\mathbf{w}$. The Fourier transform of the commutator is thus given by

$$\widehat{\mathcal{C}}_i^I(\psi) = -\epsilon \frac{\partial \widehat{\overline{\psi}}}{\partial w_i}(\mathbf{w}, \boldsymbol{\kappa}) = -\widehat{\psi}(\boldsymbol{\kappa}) \frac{\partial \widehat{G}(\Delta|\boldsymbol{\kappa}|)}{\partial x_i} = -\widehat{\psi}(\boldsymbol{\kappa}) \widehat{G}'(\Delta|\boldsymbol{\kappa}|) |\boldsymbol{\kappa}| \frac{\partial \Delta}{\partial x_i} \equiv -\widehat{\mathcal{C}}_i(\mathbf{w}, \boldsymbol{\kappa}) \widehat{\psi}(\boldsymbol{\kappa}). \tag{5.19}$$

where $\widehat{G}'$ is the derivative of $\widehat{G}$ with respect to its argument.

While equations (5.17) and (5.19)) provide explicit expressions for the commutator, they require knowledge of the unfiltered field ψ or its Fourier transform. If G were invertible, we could relate ψ and $\overline{\psi}$ as in equation (5.13), but this is not the case for non-invertible filters, such as those that include a finite dimensional projection. As such, this information is generally not available in an LES, however, we may have theory or models for the statistics of ψ, which could allow us to determine the statistics of the commutator.

Consider, for example, homogeneous, isotropic turbulence flowing through an inhomogeneous grid at a velocity U_i that is much greater than the fluctuations u_i so that Taylor's frozen field hypothesis holds. In this case, Kolmogorov theory provides a model for the spectrum tensor $\phi_{ij}(\boldsymbol{\kappa}) = \int \langle \widehat{u}_i(\boldsymbol{\kappa}')\widehat{u}_j^*(\boldsymbol{\kappa})\rangle \, d\boldsymbol{\kappa}'$, $*$ denotes complex conjugate, $\widehat{u}_i$ is the Fourier transform of the velocity, and ϕ_{ij} is also the Fourier transform of the two-point correlation tensor. The spectrum tensor of the filtered velocity is given by $\overline{\phi}_{ij}(\boldsymbol{\kappa}) = \widehat{G}^2(\Delta|\boldsymbol{\kappa}|)\phi_{ij}(\boldsymbol{\kappa})$. The commutator arising from the convection term in the filtered evolution equation is $U_k\mathcal{C}_k(u_j)$, and its contribution to the evolution of $\overline{\phi}_{ij}$ is given by

$$\tilde{\mathcal{C}}^I(\overline{\phi}_{ij}) = U_k \int \langle \widehat{\overline{u}}_i(\boldsymbol{\kappa}')\widehat{\mathcal{C}}_k^I(u_j)^*\rangle \, d\boldsymbol{\kappa}' + U_k \int \langle \widehat{\overline{u}}_j^*(\boldsymbol{\kappa})\widehat{\mathcal{C}}_k^I(u_i)\rangle \, d\boldsymbol{\kappa}' = -2U_k \frac{\partial \Delta}{\partial x_k} \widehat{G}(\Delta|\boldsymbol{\kappa}|)\widehat{G}'(\Delta|\boldsymbol{\kappa}|)|\boldsymbol{\kappa}|\phi_{ij}(\boldsymbol{\kappa}) \tag{5.20}$$

where the $\tilde{\mathcal{C}}$ nomenclature indicates the contribution of the commutator to the evolution equation for its argument. The contribution of the commutator to the evolution of the filtered three-dimensional energy spectrum $\overline{E}(|\boldsymbol{\kappa}|) = 2\pi|\boldsymbol{\kappa}|^2\overline{\phi}_{ii}(\boldsymbol{\kappa})$ and resolved turbulent kinetic energy $k^> = \int_0^\infty \overline{E}(\kappa)\, d\kappa$ can easily be obtained from equation (5.20) as:

$$\tilde{\mathcal{C}}^I(\overline{E}) = -2U_k \frac{\partial \Delta}{\partial x_k} \widehat{G}(\Delta\kappa)\widehat{G}'(\Delta\kappa)\kappa E(\kappa) \tag{5.21}$$

$$\tilde{\mathcal{C}}^I(k^>) = -2U_k \frac{\partial \Delta}{\partial x_k} \int_0^\infty \widehat{G}(\Delta\kappa)\widehat{G}'(\Delta\kappa)\kappa E(\kappa)\, d\kappa \tag{5.22}$$

Note that unlike the analysis in section 5.1, the analysis outlined here does not rely on deconvolution, and so is applicable to noninvertible filters that include implicit truncation. For example, if G is a Fourier cutoff and G' is interpreted in the sense of distributions, then equation (5.22) simplifies to

$$\tilde{\mathcal{C}}^I(k^>) = -U_k \frac{\partial \kappa_c}{\partial x_k} E(\kappa_c), \tag{5.23}$$

where κ_c is the cutoff wavenumber.

5.3 Generalizing the analysis of Ghosal and Moin

Ghosal and Moin [22] did not employ a multiscale asymptotic analysis such as that above, however, their analysis can be interpreted asymptotically. In this section, we explore the relationship between the series analysis of section 5.1 and that of Ghosal and Moin, and extend the latter to characterize the asymptotically higher order terms.

Recall, the filtering of an arbitrary function $\psi(x)$ was defined in equation (5.5) as

$$\overline{\psi}(x) = \frac{1}{\Delta_\xi} \int G\left(\frac{f(x) - f(y)}{\Delta_\xi}\right) \psi(y) f'(y) dy. \tag{5.24}$$

As in Ghosal and Moin [22], we work directly with equation (5.24) and obtain

$$\mathcal{C}^I(\psi) = \int G(\zeta) \psi'(y) \left[1 - \frac{f'(x)}{f'(y)}\right] d\zeta \tag{5.25}$$

for the inhomogeneous part of the commutator, where we have introduced the variable $\zeta = (f(y) - f(x))/\Delta_\xi$.

To expand equation (5.25) in a series of explicit powers of Δ_ξ, we follow [22] but consider the general case including terms up to Δ_ξ^N for some N. By inverting the definition of ζ, we can express y as

$$y = \sum_{i=0}^{\infty} \Delta_\xi^i \zeta^i y_i, \tag{5.26}$$

where $y_0 = x$, $y_1 = 1/f'(x)$ and y_i is given by

$$y_i = -\sum_{n=2}^{i} \frac{\beta_{n,i-n}}{n! f'(x)} \frac{d^n f}{dx^n}, \tag{5.27}$$

where

$$\beta_{n,0} = y_1^n, \qquad \beta_{n,m} = \frac{1}{m y_1} \sum_{k=1}^{m} (kn - m + k) y_{k+1} \beta_{n,m-k}. \tag{5.28}$$

Then $(y-x)$ can be expressed as

$$(y-x)^n = \left(\sum_{m=1}^{\infty} \Delta_\xi^m \zeta^m y_m \right)^n = \sum_{j=0}^{N-n} \Delta_\xi^{j+n} \zeta^{j+n} \beta_{n,j} + \dots \ , \tag{5.29}$$

for $n > 0$, which includes all terms with explicit powers of Δ_ξ up to some power N. Substitution of equation (5.29) into a general Taylor series expansion of $\psi(y)$ about x gives:

$$\psi(y) = \psi(x) + \sum_{n=1}^{N} \left(\frac{\psi^{(n)}(x)}{n!} \sum_{j=0}^{N-n} \Delta_\xi^{j+n} \zeta^{j+n} \beta_{n,j} \right) + \dots \ . \tag{5.30}$$

Equation (5.30) can be used to expand each term in equation (5.25) about x so that all the terms of the commutator with explicit powers of Δ_ξ up to some order N is given by:

$$\begin{aligned} \mathcal{C}^I(\psi) = & \sum_{m=1}^{N} \left[\frac{1}{m!} \left[\psi' \left(\frac{1}{f'} \right)^{(m)} f' \right] (x) \sum_{\substack{k=0 \\ k+m \in 2\mathbb{Z}}}^{N-m} \Delta_\xi^{k+m} \beta_{m,k} \int \zeta^{k+m} G(\zeta) d\zeta \right] \\ & + \sum_{n=1}^{N} \sum_{m=1}^{N} \left[\frac{1}{n!m!} \left[\psi^{(n+1)} \left(\frac{1}{f'} \right)^{(m)} f' \right] (x) \sum_{\substack{j=0 \\ j+k+n+m \leq N \\ j+k+n+m \in 2\mathbb{Z}}}^{N-n} \sum_{k=0}^{N-m} \Delta_\xi^{j+k+n+m} \beta_{n,j} \beta_{m,k} \int \zeta^{j+k+n+m} G(\zeta) d\zeta \right]. \end{aligned} \tag{5.31}$$

For example, for $N = 2$ we obtain,

$$\mathcal{C}^I(\psi) = \left(\frac{f''}{f'^3} \frac{d^2\psi}{dx^2} + \left(\frac{f'''}{2f'^3} - \frac{3f''^2}{2f'^4} \right) \frac{d\psi}{dx} \right) \Delta_\xi^2 \int \zeta^2 G(\zeta) d\zeta \ , \tag{5.32}$$

which agrees with equation (3.9) in [22].

To express the commutator in terms of $\overline{\psi}$, we follow the same procedure as equation (5.13).

Inverting equation (5.24) gives

$$\psi(x) = \overline{\psi}(x) - \sum_{n=1}^{N} \left(\frac{\psi^{(n)}(x)}{n!} \sum_{\substack{j=0 \\ j+n \in 2\mathbb{Z}}}^{N-n} \Delta_\xi^{j+n} \beta_{n,j} \int \zeta^{j+n} G(\zeta) d\zeta \right) + \dots \,. \tag{5.33}$$

Equation (5.33) can be recursively substituted into equation (5.31) to obtain the commutator in terms of the filtered velocity field. Moreover, the commutator can be expressed in terms of the local grid spacing $\Delta(x)$ using the relationship $f' = \Delta_\xi / \Delta$. The terms with explicit powers of Δ_ξ up to $N = 2$ are

$$\mathcal{C}^I(\psi) = \left(- \left[\frac{1}{2} \left(\Delta'^2 + \Delta\Delta'' \right) \right] \frac{d\overline{\psi}}{dx} - \left[\Delta\Delta' \right] \frac{d^2\overline{\psi}}{dx^2} \right) \int \zeta^2 G(\zeta) d\zeta. \tag{5.34}$$

For $N = 4$ we obtain,

$$\begin{aligned}
\mathcal{C}^I(\psi) = & - \left[\frac{1}{2} \left(\Delta'^2 + \Delta\Delta'' \right) \right] \frac{d\overline{\psi}}{dx} \int \zeta^2 G(\zeta) d\zeta - \left[\Delta\Delta' \right] \frac{d^2\overline{\psi}}{dx^2} \int \zeta^2 G(\zeta) d\zeta \\
& + \left[\frac{-\Delta'^4 - 11\Delta\Delta'^2\Delta'' - 7\Delta^2\Delta'\Delta''' - 4\Delta^2\Delta''^2 - \Delta^3\Delta''''}{24} \right] \frac{d\overline{\psi}}{dx} \int \zeta^4 G(\zeta) d\zeta \\
& + \left[\frac{\Delta'^4 + 8\Delta\Delta'^2\Delta'' + \Delta^2\Delta''^2 + 2\Delta^2\Delta'\Delta'''}{4} \right] \frac{d\overline{\psi}}{dx} \left(\int \zeta^2 G(\zeta) d\zeta \right)^2 \\
& + \left[\frac{-7\Delta\Delta'^3 - 13\Delta^2\Delta'\Delta'' - 2\Delta^3\Delta'''}{12} \right] \frac{d^2\overline{\psi}}{dx^2} \int \zeta^4 G(\zeta) d\zeta \\
& + \left[\frac{11\Delta\Delta'^3 + 11\Delta^2\Delta'\Delta''}{4} \right] \frac{d^2\overline{\psi}}{dx^2} \left(\int \zeta^2 G(\zeta) d\zeta \right)^2 \\
& + \left[\frac{-3\Delta^2\Delta'^2 - \Delta^3\Delta''}{4} \right] \frac{d^3\overline{\psi}}{dx^3} \int \zeta^4 G(\zeta) d\zeta + \left[\frac{11\Delta^2\Delta'^2 + \Delta^3\Delta''}{4} \right] \frac{d^3\overline{\psi}}{dx^3} \left(\int \zeta^2 G(\zeta) d\zeta \right)^2 \\
& + \left[\frac{-\Delta^3\Delta'}{6} \right] \frac{d^4\overline{\psi}}{dx^4} \int \zeta^4 G(\zeta) d\zeta + \left[\frac{\Delta^3\Delta'}{2} \right] \frac{d^4\overline{\psi}}{dx^4} \left(\int \zeta^2 G(\zeta) d\zeta \right)^2
\end{aligned} \tag{5.35}$$

Unlike the analysis in section 5.1, no ordering has been given to the commutation terms.

They are simply expressed in explicit powers of Δ_ξ to show the structure of the higher order terms neglected in equation (5.14). To get back to this result, take the limit $\Delta_\xi \to 0$ and recall that in high Reynolds number turbulence it makes sense to consider the scaling $d^n\overline{\psi}/dx^n \sim \Delta_\xi^{1/3-n}$. In this case one obtains

$$\mathcal{C}^I(\psi) = \sum_{n=1}^{\infty}\left(C_{2n}\frac{f''}{f'^{2n+1}}\Delta_\xi^{2n}\frac{\partial^{2n}\overline{\psi}}{\partial x^{2n}}\right) + \mathcal{O}(\Delta_\xi^{4/3}) = \sum_{n=1}^{\infty}\left(C_{2n}\Delta^{2n-1}\frac{d\Delta}{dx}\frac{\partial^{2n}\overline{\psi}}{\partial x^{2n}}\right) + \mathcal{O}(\Delta_\xi^{4/3}), \tag{5.36}$$

which is the same as equation (5.14). Each term in the sum in equation (5.36) is of order $\Delta_\xi^{1/3}$, and is proportional to $d\Delta/dx$ and an even derivative of $\overline{\psi}$. However, the asymptotically higher order terms (order $\Delta_\xi^{4/3}$ and higher), such as those in equation (5.34) and equation (5.35), include higher order derivatives of Δ, higher powers of $d\Delta/dx$ and odd-order derivatives of $\overline{\psi}$.

To arrive at (5.8) and (5.9) in Ghosal and Moin [22], which are the analog of equation (5.36), the authors consider $\Delta_\xi \ll 1$, which we interpret in the sense of an asymptotic analysis for $\Delta_\xi \to 0$. They also introduce the ansatz $\psi = \exp(i\kappa x)$, along with the assumption that $\kappa\Delta_\xi \gg \Delta_\xi$, which while dimensionally inconsistent, arose from the assertion that $\kappa\Delta_\xi$ could be as large as order one. In the context of the current analysis, this implies a scaling for the derivatives of $\overline{\psi}$. Equations (5.8) and (5.9) in Ghosal and Moin [22] include only the first term in equation (5.36) because the remaining terms would be higher order in $\kappa\Delta_\xi$. The authors do, however, point out that the series can be extended to higher order in $\kappa\Delta_\xi$, which would then include more of the terms in equation (5.36). We interpret these arguments from [22] to be asymptotic for $\kappa\Delta_\xi \to 0$, while $\kappa \to \infty$, which would be consistent with $\kappa \sim \Delta_\xi^{-p}$ for $0 < p < 1$. However, the introduction of the $\psi = \exp(i\kappa x)$ ansatz is essentially ad hoc, and is inconsistent with the scaling of the derivatives of the filtered velocity for high Reynolds number turbulence.

5.4 Recap of analysis and further discussion

To recap the analysis in sections 5.1 and 5.3, Ghosal and Moin [22] employ an ad hoc ordering of the commutator terms, however, their results can be consistently interpreted asymptotically. The analysis in [22] employs a mapping of the physical space x to a mapped space ξ in which the resolution is uniform to define the filtering operator. A Taylor series expansion yields a series representations for $\mathcal{C}^I$ that is valid asymptotically for $\Delta_\xi \to 0$, where Δ_ξ is the uniform resolution in ξ space. This expansion is in terms of the derivatives of the unfiltered field u. To express the commutator in terms of the derivatives of $\overline{u}$, the filter is inverted through another asymptotic expansion in Δ_ξ. But, to properly order the expansion, the way in which the derivatives of $\overline{u}$ scale with Δ_ξ must be determined. In Ghosal and Moin [22], it is assumed that $u = e^{i\kappa x}$ and their analysis is consistent with the assumption that $\kappa \sim \Delta_\xi^{-p}$ for $0 < p < 1$. However, this is not necessarily consistent with the way the derivatives of $\overline{u}$ scale when u is the turbulent velocity.

Assuming the resolution in physical space $\Delta(x)$ is in the inertial range of a high Reynolds number turbulence, the Kolmogorov hypotheses imply that

$$\frac{\partial^n \overline{u}}{\partial x^n} \sim \Delta_\xi^{1/3-n}. \tag{5.37}$$

With this ordering, the lowest order expansion for the commutator is given by

$$\begin{aligned}\mathcal{C}^I(u) &= -M_2 \Delta \frac{d\Delta}{dx}\frac{\partial^2 \overline{u}}{\partial x^2} + \left(\frac{M_2^2}{2} - \frac{M_4}{6}\right)\Delta^3 \frac{d\Delta}{dx}\frac{\partial^4 \overline{u}}{\partial x^4} + \cdots + C_N \Delta^{N-1}\frac{d\Delta}{dx}\frac{\partial^N \overline{u}}{\partial x^N} + \cdots + \mathcal{O}(\Delta_\xi^{4/3}) \\ &= \frac{d\Delta}{dx}\sum_{n=1}^{\infty} C_{2n}\Delta^{2n-1}\frac{\partial^{2n}\overline{u}}{\partial x^{2n}} + \mathcal{O}(\Delta_\xi^{4/3})\end{aligned}, \tag{5.38}$$

where M_k is the k^{th} order moment of the filter kernel, N is even, and in general, the coefficient

C_j on the j^{th} order term depends on the moments of the filter up to order j. In Ghosal and Moin [22], only the first term in this series is retained because the other terms are higher order in $\kappa\Delta \sim \Delta_\xi^{1-p}$, but clearly this would not be consistent with filtering turbulence in a Kolmogorov inertial range as equation (5.38) is.

An alternative approach to developing a series representation of $\mathcal{C}^I$ is formulated for a different, though related asymptotic limit. Consider the situation in which the derivative $d\Delta/dx$ is order ϵ, where ϵ is asymptotically small. In this case, a multiscale asymptotic analysis of $\overline{u}$ in terms of a fast variable $\tilde{x}$ and slow variable $w = \epsilon x$ yields the simple result $\mathcal{C}^I = -\epsilon\partial\overline{u}/\partial w + \mathcal{O}(\epsilon^2)$, which can be expressed directly as a convolution operator applied to the unfiltered field, where the kernel is in terms of the filter kernel and its derivative in equation (5.11). As with the analysis discussed above, a Taylor series representation of the filter inverse can be applied to produce a series representation of the commutator in terms of the filtered field and its derivatives. However, the asymptotic interpretation may be different. In particular, the $\epsilon \to 0$ limit can be approached by allowing the length scale L_Δ over which the resolution changes ($\frac{1}{L_\Delta} \sim \frac{1}{\Delta}\frac{d\Delta}{dx}$) to grow while Δ remains constant. In this case derivatives of $\overline{u}$ as well as Δ are order one in ϵ. Alternatively, L_Δ can remain constant while Δ goes to zero, which is equivalent to the previous analysis. In this case, $\Delta \sim \epsilon$ and for inertial range turbulence, the n^{th} derivative of $\overline{u}$ scales as $\epsilon^{1/3-n}$. In either case, one obtains

$$\mathcal{C}^I(u) = \frac{d\Delta}{dx}\sum_{n=1}^{\infty} C_{2n}\Delta^{2n-1}\frac{\partial^{2n}\overline{u}}{\partial\tilde{x}^{2n}} + \mathcal{O}(\epsilon^q), \tag{5.39}$$

where $q = 2$ when the asymptotic limit is taken with constant Δ while $q = 4/3$ when it is taken at constant L_Δ. This is the same series as in equation (5.38).

Despite the fact that the above analyses are predicated on the use of an invertible filter and we are concerned with filters that include a discrete projection, the characteristics of the commutator expression provide insights relevant to modeling of the commutation term.

First, note that to leading order this approximation is proportional to $d\Delta/dx$, and is a series in the even x derivatives of $\overline{u}$. The lowest order term appears as a viscous term, which is dissipative when $d\Delta/dx > 0$ (i.e. convecting from fine to coarse resolution), and the higher order terms are hyperviscous. Similarly, these terms would be anti-dissipative when convecting from coarse to fine resolution, and thus will create resolved energy in this case. Clearly this commutator expression is characterizing the transfer of energy between resolved and unresolved scales as a consequence of the resolution inhomogeneity. In addition, since each of the terms in equations (5.38) and (5.39) are of the same asymptotic order, they are all equally important, and indeed, depending on the characteristics of the filter, the higher order derivative terms could dominate. This suggests that a model of the commutator formulated as a differential operator should include as high-order derivatives as possible. It is also interesting to observe that the asymptotically higher order terms include dispersive terms in addition to dissipative ones, and that higher order derivatives of Δ appear (see section 5.3).

Finally, this analysis may provide clarity on some of the existing literature surrounding commutation error. In particular, the deconvolution analysis in [22] has often been used to motivate the development of smooth explicit filters whose first $N-1$ moments are zero so that the commutation error is of explicit order Δ^N (e.g, [146, 147, 145, 151]). However, this is only meaningful if the derivatives of $\overline{u}$ scale sufficiently weakly with Δ, as discussed above, so that the first terms in equation (5.38) dominate asymptotically. Unfortunately, for high Reynolds number turbulence, each term in equation (5.38) is of the same asymptotic order. Therefore, this analysis suggests that constructing filters so that the coefficients C_j for $j < N-1$ in equation (5.38) vanish would likely not render the commutator negligible. The commutator will thus need to be modeled.

Further, as discussed in section 1.2, an LES filter always includes a projection to the finite-dimensional numerical solution space, either explicitly or implicitly, and so the information in a filtered turbulent field is not sufficient to determine the evolution of that filtered

turbulence [15, 143, 141, 186]. As a consequence, one can only expect LES models, including models of the commutator, to match statistical characteristics of the quantity being modeled [1, 187]. Therefore, in section 5.2, we analyzed *a priori* statistical properties of the commutator in terms of statistical characteristics of the unfiltered turbulence, to inform potential commutator models.

The finite-dimensional projection inherent to LES filters determines the information available in an LES upon which to base a model, and so a deconvolution analysis is ill-suited to determining statistical properties. Instead, we apply a multiscale asymptotic analysis to characterize the statistics of the commutator for an inhomogeneous three-dimensional isotropic filter characterized by a slowly varying filter width Δ. After performing a Fourier transform in the fast variable for which the filter is homogeneous, the commutator between filtering and differentiation applied to turbulent velocity fluctuations u_j can be written explicitly as

$$\widehat{\mathcal{C}}_i^I(u_j) = -\frac{\partial \Delta}{\partial x_i}\widehat{G}'(\Delta|\boldsymbol{\kappa}|)|\boldsymbol{\kappa}|\widehat{u}_j(\boldsymbol{\kappa}), \tag{5.40}$$

where $\boldsymbol{\kappa}$ is the wavenumber vector, $\widehat{G}$ is the Fourier transform of the isotropic filter kernel G, and $\widehat{G}'$ is the derivative of $\widehat{G}$ with respect to its argument. Note that the "local Fourier transform" analysis in [188] holds in this multiscale asymptotic sense.

The commutator is a linear operator, and equation (5.40) shows that it is proportional to the gradient of Δ and its spectrum is proportional to $\widehat{G}'$. The commutator thus acts on the wavenumbers over which the filter spectrum rolls off from order one to zero. These are generally the smallest resolved scales of the LES. For a Fourier cutoff filter in which $\widehat{G}$ is discontinuous at the cutoff wavenumber κ_c, $\widehat{G}'$ is a Dirac delta function at κ_c, so in this case the commutator acts only at the slowly varying cutoff.

While equation (5.40) is an explicit expression for the commutator, it requires knowledge of the unfiltered quantity, which is generally not available. If the turbulence is being convected by a mean velocity U_i, then the commutator $\mathcal{C}_i^I(u_j)$ arising from the mean convection

term enters the u_j evolution equation as $U_i \mathcal{C}_i^I(u_j)$, and equation (5.40) can be used to determine the contribution of the commutator to the evolution of the filtered spectrum tensor, and in particular the three-dimensional filtered energy spectrum $\overline{E}(\mathbf{w}, \kappa)$, to obtain

$$\tilde{\mathcal{C}}^I(\overline{E}) = -U_k \frac{\partial \Delta}{\partial x_k} \widehat{G}(\Delta\kappa)\widehat{G}'(\Delta\kappa)\kappa E(\kappa) \tag{5.41}$$

where $\tilde{\mathcal{C}}$ indicates the contribution of the commutator to the evolution equation for its argument. This contribution still requires knowledge of the unfiltered turbulence, in this case the unfiltered spectrum, but at least in high Reynolds number isotropic turbulence, Kolmogorov inertial range theory provides a good model for E. This is useful because *a priori* consistency of a commutator model with equation (5.41) is a necessary condition for LES prediction of the energy spectrum [187, 1]. Similarly, integrating equation (5.41) over κ yields the contribution of the commutator to the evolution of the resolved turbulent kinetic energy $k^>$, and a necessary condition for LES prediction of $k^>$. For the special case of a Fourier cutoff filter, the result simplifies to

$$\tilde{\mathcal{C}}^I(k^>) = -U_k \frac{\partial \kappa_c}{\partial x_k} E(\kappa_c), \tag{5.42}$$

which is consistent with the result obtained by Moser et al. [1] by other means.

Further, when this spectral analysis is applied to the full nonlinear terms in the filtered Navier-Stokes equations, an additional commutator contributes to the evolution of the spectrum tensor, which can be determined in terms of $\widehat{S}_{ijk}(\boldsymbol{\kappa})$, the Fourier transform of the two-point third-order correlation tensor. For isotropic turbulence with uniform resolution, this term shows up in the $\overline{E}$ equation as

$$\tilde{C}^I(\overline{E}) = \widehat{G}(\Delta\kappa)\widehat{G}'(\Delta\kappa)\Delta\kappa \frac{\partial \Delta}{\partial x_\ell} \mathrm{Re}\left\{ \sum_{\kappa'} \langle \hat{u}_k(\boldsymbol{\kappa}) \hat{u}_k^*(\boldsymbol{\kappa}') \hat{u}_\ell^*(\boldsymbol{\kappa} - \boldsymbol{\kappa}') \rangle \right\}. \tag{5.43}$$

Interestingly, the standard EDQNM closure for isotropic turbulence (see section chapter 4) suggests

$$\begin{aligned}\langle \hat{u}_k(\boldsymbol{\kappa})\hat{u}_k(-\boldsymbol{\kappa}')\hat{u}_\ell(-\boldsymbol{\kappa}+\boldsymbol{\kappa}')\rangle = \Theta\Big[& \\ & - iP_{km}(\boldsymbol{\kappa})\left[\kappa_s\left(\Phi_{mk}(\boldsymbol{\kappa}')\Phi_{\ell s}(-\boldsymbol{\kappa}+\boldsymbol{\kappa}')+\Phi_{\ell m}(-\boldsymbol{\kappa}+\boldsymbol{\kappa}')\Phi_{sk}(\boldsymbol{\kappa}')\right)\right] \\ & - iP_{km}(\boldsymbol{\kappa}')\left[-\kappa'_s\left(\Phi_{km}(\boldsymbol{\kappa})\Phi_{\ell s}(-\boldsymbol{\kappa}+\boldsymbol{\kappa}')+\Phi_{\ell m}(-\boldsymbol{\kappa}+\boldsymbol{\kappa}')\Phi_{ks}(\boldsymbol{\kappa})\right)\right] \\ & - iP_{\ell m}(-\boldsymbol{\kappa}+\boldsymbol{\kappa}')\left[(-\kappa+\kappa')_s\left(\Phi_{km}(\boldsymbol{\kappa})\Phi_{sk}(\boldsymbol{\kappa}')+\Phi_{mk}(\boldsymbol{\kappa}')\Phi_{ks}(\boldsymbol{\kappa})\right)\right]\Big]\end{aligned} \tag{5.44}$$

which is a purely imaginary function. Therefore, the commutator arising from the nonlinear terms is zero to leading order (the higher order term may be non-zero). Thus to leading order the commutator related to mean convection dominates, which agrees with our intuition at the beginning of this section. For a Kolmogorov spectrum and cutoff filter the convective time derivative of the kinetic energy to leading order is then

$$\frac{Dk^{>}}{Dt} = C_k\varepsilon^{2/3}\kappa_c^{-5/3}U_k\frac{\partial\kappa_c}{\partial x_k} - \varepsilon. \tag{5.45}$$

For coarsening resolution ($U_k\partial\kappa_c/\partial x_k < 0$), the commutator transfers energy to unresolved scales with the dissipation occurring only at the cutoff wavenumber. Similarly, for refining resolution ($U_k\partial\kappa_c/\partial x_k > 0$), the commutator transfers energy from the subgrid to the resolved turbulence at the cutoff wavenumber. Further, it is clear from equation (5.45) that depending on strength of the mean convection velocity or gradient of the grid resolution the dissipation rate from the commutator may significantly outweigh that of the subgrid stress and a model is clearly needed to maintain the correct energy balance.

5.5 Extensions to three dimensional anisotropic inhomogeneous resolution

The analyses in sections 5.1 and 5.2 can be extended to the general case of three dimensional anisotropic inhomogeneous resolution. To support the development of anisotropic resolution, we consider the resolution tensor $\mathcal{M}_{ij}$ [17], which is the symmetric part of the Jacobian defining the mapping of a unit cube to a resolution cell. The eigenvalues of $\mathcal{M}_{ij}$ represent the size of the resolution cell in the principal directions defined by the corresponding eigenvectors. In the isotropic resolution case considered above $\mathcal{M}_{ij} = \Delta\delta_{ij}$.

In the three-dimensional anisotropic case, the definition of the filter considered in equation (5.7) can written

$$\overline{\psi}(\mathbf{x}) = \frac{1}{\det(\mathcal{M})} \int G\left(|\mathcal{M}^{-1}(\mathbf{x})(\mathbf{x}-\mathbf{y})|\right) \psi(\mathbf{y}) d\mathbf{y}. \tag{5.46}$$

As before, suppose that $\partial_k M_{ij}$ is order ε and let $\mathbf{w} = \varepsilon\mathbf{x}$ and $\mathbf{x}$ be slow and fast variables so that

$$\overline{\psi}(\mathbf{x}, \mathbf{w}) = \frac{1}{\det(\mathcal{M}(\mathbf{w}))} \int G\left(|\mathcal{M}^{-1}(\mathbf{w})(\mathbf{x}-\mathbf{y})|\right) \psi(\mathbf{y}) d\mathbf{y}. \tag{5.47}$$

The inhomogeneous commutator is then $\mathcal{C}_i^I(\psi) = -\varepsilon\partial\overline{\psi}/dw_i$ which can be computed as

$$\mathcal{C}_i^I(\psi) = \frac{1}{\det(\mathcal{M})} \frac{\partial \mathcal{M}_{\ell j}}{\partial x_i} \int \left[\mathcal{M}_{\ell t}^{-1} \mathcal{M}_{js}^{-1} z_t z_s \frac{G'(|\mathcal{M}^{-1}\mathbf{z}|)}{|\mathcal{M}^{-1}\mathbf{z}|} + \mathcal{M}_{\ell j}^{-1} G(|\mathcal{M}^{-1}\mathbf{z}|) \right] \psi(\mathbf{y}) d\mathbf{y}, \tag{5.48}$$

where $\mathbf{z} = (\mathbf{x} - \mathbf{y})$.

The generalized series representation of the inhomogeneous commutator can be derived by introducing the variable $\zeta_i = \mathcal{M}_{ij}^{-1}(y-x)_j$. Then $y_k = \mathcal{M}_{ki}\zeta_i + x_k$ and equation (5.48)

becomes

$$\mathcal{C}_i^I(\psi) = \frac{\partial \mathcal{M}_{\ell j}}{\partial x_i} \int \left[\mathcal{M}_{\ell r}^{-1} \zeta_r \zeta_j \frac{G'(|\boldsymbol{\zeta}|)}{|\boldsymbol{\zeta}|} + \mathcal{M}_{\ell j}^{-1} G(|\boldsymbol{\zeta}|) \right] \psi(\mathcal{M}_{ki}\zeta_i + x_k) d\boldsymbol{\zeta}. \tag{5.49}$$

Taylor expanding ψ about $\mathbf{x}$ gives

$$\begin{aligned} \mathcal{C}_i^I(\psi) = \frac{\partial \mathcal{M}_{\ell j}}{\partial x_i} \int & \left[\mathcal{M}_{\ell r}^{-1} \zeta_r \zeta_j \frac{G'(|\boldsymbol{\zeta}|)}{|\boldsymbol{\zeta}|} + \mathcal{M}_{\ell j}^{-1} G(|\boldsymbol{\zeta}|) \right] \times \\ & \left[\psi(\mathbf{x}) + \partial_k \psi(\mathbf{x}) \mathcal{M}_{ki} \zeta_i + \frac{1}{2} \partial_k \partial_j \psi(\mathbf{x}) \mathcal{M}_{ki} \zeta_i \mathcal{M}_{js} \zeta_s + \cdots \right] d\boldsymbol{\zeta}. \end{aligned} \tag{5.50}$$

Let $\mathcal{C}_i^{I-k}$ denote the kth term in this Taylor expansion. Since, $\int \zeta_r \zeta_j \frac{G'(|\boldsymbol{\zeta}|)}{|\boldsymbol{\zeta}|} d\boldsymbol{\zeta} = -\int \delta_{rj} G(|\boldsymbol{\zeta}|) d\boldsymbol{\zeta}$, the first term in equation (5.50), $\mathcal{C}_i^{I-1}$, is identically 0, i.e.,

$$\begin{aligned} \mathcal{C}_i^{I-1} &= \frac{\partial \mathcal{M}_{\ell j}}{\partial x_i} \int \left[\mathcal{M}_{\ell r}^{-1} \zeta_r \zeta_j \frac{G'(|\boldsymbol{\zeta}|)}{|\boldsymbol{\zeta}|} + \mathcal{M}_{\ell j}^{-1} G(|\boldsymbol{\zeta}|) \right] \psi(\mathbf{x}) d\boldsymbol{\zeta} \\ &= \frac{\partial \mathcal{M}_{\ell j}}{\partial x_i} \int \mathcal{M}_{\ell j}^{-1} (G(|\boldsymbol{\zeta}|) - G(|\boldsymbol{\zeta}|)) \psi(\mathbf{x}) d\boldsymbol{\zeta} \\ &= 0, \end{aligned} \tag{5.51}$$

as expected. Isotropy of $G(|\boldsymbol{\zeta}|)$ implies the odd order moments of G are zero and the even order moments can be computed as:

$$\int \zeta_i \zeta_j G(|\boldsymbol{\zeta}|) d\boldsymbol{\zeta} = M_2 \delta_{ij}, \qquad \int \zeta_s \zeta_k \zeta_i \zeta_j G(|\boldsymbol{\zeta}|) d\boldsymbol{\zeta} = M_4 \left[\delta_{sk}\delta_{ij} + \delta_{si}\delta_{kj} + \delta_{sj}\delta_{ki} \right], \qquad \text{etc.} \tag{5.52}$$

where M_i is the i-th moment of the filter as above (not to be confused with the resolution tensor $\mathcal{M}$ here). Therefore, the second term $\mathcal{C}_i^{I-2}$ in equation (5.50) is

$$\mathcal{C}_i^{I-2} = -\frac{\partial \mathcal{M}_{\ell j}}{\partial x_i} \int \mathcal{M}_{\ell r}^{-1} \mathcal{M}_{kj} \zeta_r G(|\boldsymbol{\zeta}|) \frac{\partial \psi}{\partial x_k} d\boldsymbol{\zeta} = 0. \tag{5.53}$$

The first nonzero term is $\mathcal{C}_i^{I-3}$ which can be computed as

$$\begin{aligned}
\mathcal{C}_i^{I-3} &= \frac{\partial \mathcal{M}_{\ell j}}{\partial x_i} \int \mathcal{M}_{\ell r}^{-1} \mathcal{M}_{kp} \mathcal{M}_{qb} \zeta_r \zeta_p \zeta_b \frac{\xi_j}{|\boldsymbol{\zeta}|} G'(|\boldsymbol{\zeta}|) \partial_k \frac{1}{2} \partial_p \psi(\mathbf{x}) d\boldsymbol{\zeta} \\
&\quad + \frac{\partial \mathcal{M}_{\ell j}}{\partial x_i} \int \mathcal{M}_{\ell j}^{-1} \mathcal{M}_{kp} \mathcal{M}_{qb} \zeta_p \zeta_b G(|\boldsymbol{\zeta}|) \partial_k \frac{1}{2} \partial_p \psi(\mathbf{x}) d\boldsymbol{\zeta} \\
&= \frac{\partial \mathcal{M}_{\ell j}}{\partial x_i} \int \mathcal{M}_{\ell r}^{-1} \mathcal{M}_{kp} \mathcal{M}_{qb} \left(\delta_{rp}\delta_{bj} + \delta_{rb}\delta_{pj} + \delta_{pb}\delta_{rj}\right) G(|\boldsymbol{\zeta}|) \partial_k \frac{1}{2} \partial_p \psi(\mathbf{x}) d\boldsymbol{\zeta}. \qquad (5.54) \\
&\quad + \frac{\partial \mathcal{M}_{\ell j}}{\partial x_i} \int \mathcal{M}_{\ell j}^{-1} \mathcal{M}_{kp} \mathcal{M}_{qb} \zeta_p \zeta_b G(|\boldsymbol{\zeta}|) \partial_k \frac{1}{2} \partial_p \psi(\mathbf{x}) d\boldsymbol{\zeta} \\
&= -M_2 \frac{\partial \mathcal{M}_{\ell j}}{\partial x_i} \mathcal{M}_{qj} \partial_\ell \partial_q \psi(\mathbf{x})
\end{aligned}$$

Similarly, the fifth term $\mathcal{C}_i^{I-5}$ will be

$$\mathcal{C}_i^{I-5}(\psi) = -\frac{12}{4!} M_4 \frac{\partial \mathcal{M}_{\ell j}}{\partial x_i} \mathcal{M}_{pq} \mathcal{M}_{qs} \mathcal{M}_{tj} \partial_\ell \partial_p \partial_s \partial_t \psi(\mathbf{x}), \qquad (5.55)$$

and so on. Notice that the multiplicity of the moments changes the constants from the one-dimensional case. Similarly, replacing ψ with $\overline{\psi}$ as in section 5.1 will introduce additional constants so that the structure of the commutator is generally

$$\mathcal{C}_i^I(\psi) = C_2 \frac{\partial \mathcal{M}_{\ell j}}{\partial x_i} \mathcal{M}_{qj} \frac{\partial^2 \overline{\psi}}{\partial x_\ell \partial x_q}(\mathbf{x}) + C_4 \frac{\partial \mathcal{M}_{\ell j}}{\partial x_i} \mathcal{M}_{pq} \mathcal{M}_{qs} \mathcal{M}_{tj} \frac{\partial^4 \overline{\psi}}{\partial x_\ell \partial x_p \partial x_s \partial x_t}(\mathbf{x}) + \dots \qquad (5.56)$$

for constants C_k that depend on the moments of G up to order k.

To further explore the structure of these commutators, consider equation (5.56) in three different settings: a homogeneous, isotropic grid (see figure 5.1a), an inhomogeneous anisotropic grid (see figure 5.1b), and an isotropic inhomogeneous grid (see figure 5.1c), with resolution

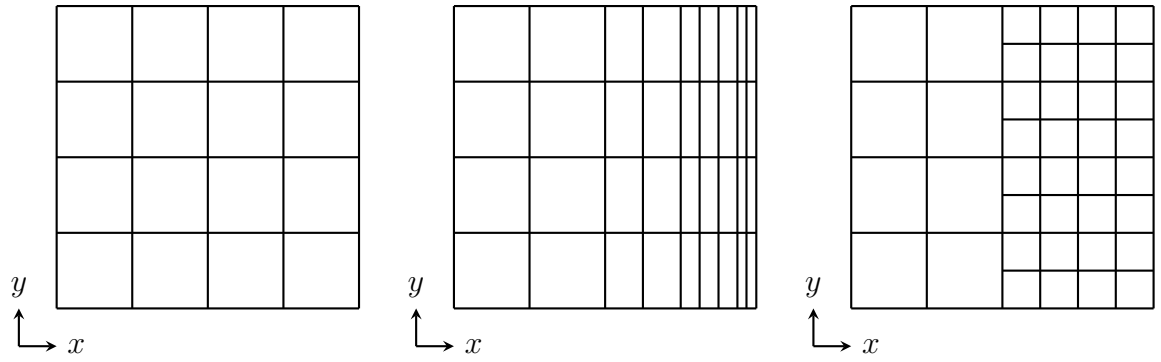

(a) (b) (c)

Figure 5.1: Two-dimensional schematics of (a) a homogeneous, isotropic grid, (b) an inhomogeneous, anisotropic grid, and (c) an isotropic, inhomogeneous grid.

tensors

$$\mathcal{M}_{ij}^{(a)} = \begin{bmatrix} \Delta & & \\ & \Delta & \\ & & \Delta \end{bmatrix}, \qquad \mathcal{M}_{ij}^{(b)} = \begin{bmatrix} \Delta_x(x) & & \\ & \Delta_y & \\ & & \Delta_z \end{bmatrix}, \qquad \mathcal{M}_{ij}^{(c)} = \begin{bmatrix} \Delta(x) & & \\ & \Delta(x) & \\ & & \Delta(x) \end{bmatrix}, \tag{5.57}$$

respectively. In the homogeneous isotropic case, the commutator, $\mathcal{C}_i^{I-(a)}(\psi)$, is clearly zero as expected. In the inhomogeneous anisotropic case, the commutator $\mathcal{C}_i^{I-(b)}(\psi)$ is

$$\mathcal{C}_1^{I-(b)}(\psi) = C_2 \frac{\partial \Delta_x}{\partial x} \Delta_x \frac{\partial^2 \overline{\psi}}{\partial x^2} + C_4 \frac{\partial \Delta_x}{\partial x} \Delta_x \left[\Delta_x^2 \frac{\partial^4 \overline{\psi}}{\partial x^4} + \Delta_y^2 \frac{\partial^4 \overline{\psi}}{\partial y^2 \partial x^2} + \Delta_z^2 \frac{\partial^4 \overline{\psi}}{\partial z^2 \partial x^2} \right] + \ldots. \tag{5.58}$$

Lastly, in the isotropic inhomogeneous grid case, the commutator $\mathcal{C}_i^{I-(c)}(\psi)$ is

$$\mathcal{C}_2^{I-(c)}(\psi) = C_2 \frac{\partial \Delta}{\partial x} \Delta \frac{\partial^2 \overline{\psi}}{\partial x_j \partial x_j} + C_4 \frac{\partial \Delta}{\partial x} \Delta^3 \frac{\partial^4 \overline{\psi}}{\partial x_j \partial x_j \partial x_i \partial x_i} + \ldots. \tag{5.59}$$

It is interesting to compare the structure of these commutators to the numerical propagation of a wave packet through each of these grids as explored in section 6.4.1.

The spectral characteristics of the inhomogeneous commutator can be extended to the

anisotropic case in a similar way. Fourier transforming equation (5.47) in the fast variable gives

$$\widehat{\overline{\psi}}(\mathbf{w},\boldsymbol{\kappa}) = \widehat{\psi}(\boldsymbol{\kappa})\widehat{G}(|\mathcal{M}(\mathbf{w})\boldsymbol{\kappa}|). \tag{5.60}$$

The Fourier-transform of the inhomogeneous commutator $\widehat{\mathcal{C}_i^I}$ is then

$$\widehat{\mathcal{C}_i^I}(\psi) = -\varepsilon\frac{\partial\widehat{\overline{\psi}}}{\partial w_i} = -\varepsilon\widehat{\psi}\frac{\partial\widehat{G}(|\mathcal{M}(\mathbf{w})\boldsymbol{\kappa}|)}{\partial w_i} = -\frac{\widehat{G}'(|\mathcal{M}(\mathbf{w})\boldsymbol{\kappa}|)}{|\mathcal{M}(\mathbf{w})\boldsymbol{\kappa}|}\mathcal{M}_{sj}\kappa_j\kappa_\ell\frac{\partial\mathcal{M}_{s\ell}}{\partial x_i}\widehat{\psi}(\boldsymbol{\kappa}). \tag{5.61}$$

The spectral form of the commutator for the three cases considered in figure 5.1 are:

$$\widehat{\mathcal{C}}_i^{I-(a)}(\psi) = 0 \tag{5.62}$$

$$\widehat{\mathcal{C}}_1^{I-(b)}(\psi) = \frac{\widehat{G}'(|\Delta_x\kappa_x + \Delta_y\kappa_y + \Delta_z\kappa_z|)}{(|\Delta_x\kappa_x + \Delta_y\kappa_y + \Delta_z\kappa_z|)}\Delta_x\kappa_x^2\frac{\partial\Delta_x}{\partial x}\widehat{\psi}(\boldsymbol{\kappa}) \tag{5.63}$$

$$\widehat{\mathcal{C}}_1^{I-(c)}(\psi) = \widehat{G}'(\Delta|\boldsymbol{\kappa}|)|\boldsymbol{\kappa}|\frac{\partial\Delta}{\partial x}\widehat{\psi}(\boldsymbol{\kappa}). \tag{5.64}$$

Further, the full three dimensional velocity spectrum equations with anisotropic, inhomogeneous resolution/filtering can be derived as

$$\frac{1}{2}\frac{\partial\overline{\phi}_{ii}(\boldsymbol{\kappa})}{\partial t} = \overline{T}(\boldsymbol{\kappa}) - \mathcal{C}^I\left(\frac{1}{2}\phi_{ii}\right) + \nu|\boldsymbol{\kappa}|^2\overline{\phi}_{ii}(\boldsymbol{\kappa}), \tag{5.65}$$

where

$$\hat{\overline{T}}(\boldsymbol{\kappa}) = \frac{1}{2}i\kappa_\ell P_{jk}(\boldsymbol{\kappa})\hat{G}(|\mathcal{M}\boldsymbol{\kappa}|)^2\hat{S}_{jk\ell}(\boldsymbol{\kappa}) - \frac{1}{2}i\kappa_\ell P_{jk}(\boldsymbol{\kappa})\hat{G}(|\mathcal{M}\boldsymbol{\kappa}|)^2\hat{S}^*_{jk\ell}(\boldsymbol{\kappa}) \tag{5.66}$$

and

$$\begin{aligned}\hat{\mathcal{C}}^I = &\frac{1}{2}P_{jk}(\boldsymbol{\kappa})\frac{G'(|\mathcal{M}\boldsymbol{\kappa}|)}{|\mathcal{M}\boldsymbol{\kappa}|}\mathcal{M}_{st}\kappa_t\kappa_q\frac{\partial\mathcal{M}_{sq}}{\partial x_\ell}\hat{G}(|\mathcal{M}\boldsymbol{\kappa}|)\hat{S}_{jk\ell}(\boldsymbol{\kappa})\\ &+\frac{1}{2}P_{jk}(\boldsymbol{\kappa})\frac{G'(|\mathcal{M}\boldsymbol{\kappa}|)}{|\mathcal{M}\boldsymbol{\kappa}|}\mathcal{M}_{st}\kappa_t\kappa_q\frac{\partial\mathcal{M}_{sq}}{\partial x_\ell}\hat{G}(|\mathcal{M}\boldsymbol{\kappa}|)\hat{S}^*_{jk\ell}(\boldsymbol{\kappa})\end{aligned}. \tag{5.67}$$

Chapter 6

Commutation error and modeling in LES

Note that much of the material in sections 6.1 to 6.3 was published previously by Yalla, Oliver, Haering, Engquist, and Moser [139]

In the previous chapter we analyzed the properties of the inhomogeneous commutator through a multiscale analysis. When the inhomogeneous commutator is ignored, as is typical in an LES, it gives rise to commmutation error. In this chapter we investigate the numerical issues of commutation error that arise from the convection of turbulence through inhomogeneous resolution.

When convecting through a coarsening grid, the resolved fluctuations in a fine region will be moving into a coarse region in which not all the resolved scales can be represented. Similarly, solution scales that cannot be resolved in a coarse region will become resolvable as the solution convects into a finer resolution region. The previous subsections show how the inhomogeneous commutator $\mathcal{C}^I$ is responsible for transferring energy between the subgrid and resolved turbulence in both these cases. However, notice that the injection of energy into the resolved scales is required for the refining resolution case to maintain consistency with the definition of the filter, but that neglecting this effect will not lead to numerical inconsistencies since the coarse region solution is perfectly well represented in the fine region. This is not true for flow through a coarsening grid. For this reason, our investigation of commutation error (neglect of $\mathcal{C}$) in this chapter is particularly focused on flow through coarsening grids

because of the numerical consistency issues inherent to this case. Flow through refining grids will be examined in chapter 7.

6.1 Numerical analysis of resolution inhomogeneity in one dimension

The impact of the commutator and specifically its neglect is affected by the characteristics of the discrete derivative operator, which is accounted for in the homogeneous commutator $\mathcal{C}^H$. Here, by recalling results from numerical analysis [189, 190, 191, 192, 45, 193, 194, 195], we consider the impact of neglecting both commutators, as is typical in LES, in the case of a filter consisting of just the projection to the finite-dimensional discrete solution space (i.e. only an implicit filter). As in chapter 5, we will start by considering the effects of the resolution inhomogeneity on the filtered one-dimensional advection equation. Neglecting the commutator in equation (5.2) gives:

$$\frac{\partial \overline{u}}{\partial t} + U\frac{\delta \overline{u}}{\delta x} = 0. \tag{6.1}$$

We begin by recalling, as an example, the solution of equation (6.1) using a second-order centered finite difference scheme on a uniform mesh with mesh size Δ. The numerical first derivative is then given by $\delta u_j/\delta x = \frac{1}{2\Delta}(u_{j+1} - u_{j-1})$.

It is well recognized that, for initial conditions of the form $e^{i\kappa x}$, solutions of equation (6.1) take the form $e^{i(\kappa x - \omega t)}$ and propagate at a phase velocity that depends on their wavenumber [189]. The relation $\omega = \omega(\kappa)$ is called the *dispersion relation*. Individual waves propagate at a phase speed given by $c(\kappa) = \omega(\kappa)/\kappa$; however, the evolution of a wave packet, which can be decomposed into Fourier modes with wavenumbers ranging over a relatively narrow

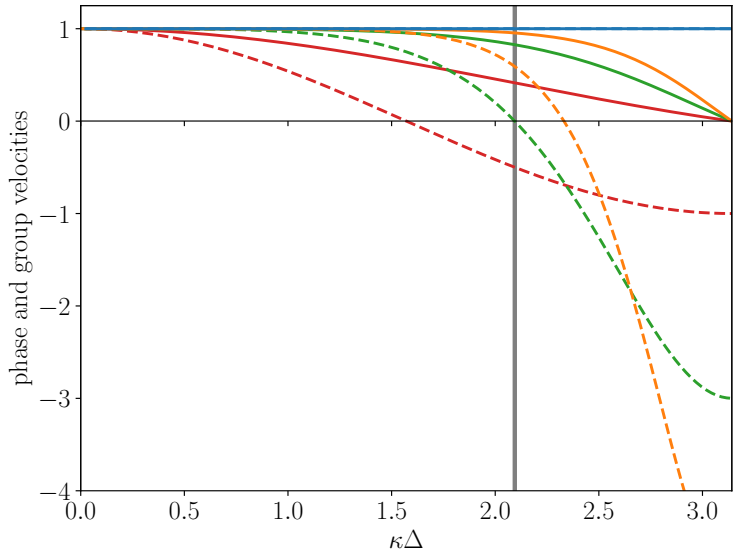

Figure 6.1: The phase and group velocities for second-order centered difference (——), third-order B-spline collocation (——), fifth-order B-spline collocation (——) and exact (——). Note, the vertical line as $\kappa\Delta = 2\pi/3$ and marks the lower bound of wavenumbers affected by aliasing.

band, is governed by the *group velocity* (see figure 6.1):

$$\mathcal{G}(\kappa) = \frac{d\omega}{d\kappa}(\kappa). \tag{6.2}$$

The group velocity is of particular important in LES because it is the velocity at which energy propagates and we have been concerned with the statistical effects of the commutators.

Substituting the form $u_j = e^{i(\kappa x_j - \omega t)}$ into equation (6.1) with the second order centered difference scheme yields the dispersion relation and group velocity:

$$\omega(\kappa) = U\kappa'(\kappa) = U\frac{\sin(\kappa\Delta)}{\Delta} \qquad \text{and} \qquad \mathcal{G}(\kappa) = U\cos(\kappa\Delta), \tag{6.3}$$

where κ' is the spectrum of the numerical derivative operator (previously denoted $\tilde{\kappa}$), which is often referred to as the effective or modified wavenumber (see section 3.1). Notice that at the Nyquist wavenumber for the grid, $\kappa_c = \pi/\Delta$, both κ' and ω are zero. As a consequence

there is a wavenumber $\kappa_a \in (0, \kappa_c)$ at which ω is maximized with value $\omega_{\max}(\Delta) = \omega(\kappa_a)$ ($\kappa_a = \kappa_c/2$ for second order central difference) so that the group velocity is zero. Therefore, for $\kappa \in (\kappa_a, \kappa_c)$ the group velocity is negative so that wave packets with wavenumbers in this range will propagate upstream against the convection velocity. Also note that for any frequency $\omega < \omega_{\max}(\Delta)$, there are two wavenumbers that will evolve with that frequency, one with positive and one with negative group velocity. The wavenumber with positive group velocity ($\kappa < \kappa_a$) is a consistent approximation to a solution of the advection equation while the other ($\kappa > \kappa_a$) is spurious. As pointed out by Vichnevetsky [190], a general solution to (equation (6.1)) can therefore be decomposed as $u = p+q$, where p has a forward propagation and is a consistent approximation, and q propagates backwards and is spurious.

Consider next a grid for a domain of length $L = 4\pi$ with a sharp change in resolution from $\Delta_f = 2\pi/128$ to $\Delta_c = 2\pi/32$ as shown in figure 6.2, and two different initial conditions given by

$$u_i(x, t = 0) = \cos(\eta_i x) e^{-5(x-3\pi/2)^2}, \tag{6.4}$$

with $\eta_1 = 4$ and $\eta_2 = 18$, which we refer to as wave packets P_1 and P_2, respectively. The energy spectrum of these wave packets is the sum of three Gaussian functions of wavenumber, with standard deviation of $\sqrt{5}$. They are centered around $\kappa = \pm\eta_i$ and 0. As a consequence, more than 99% of the energy resides in wavenumbers with $|\kappa| < \eta + 5.8$. In the fine region, $\kappa_a^f = 32$, so both wave packets have virtually all of their energy in wavenumbers $|\kappa| < \kappa_a^f$. Both wave packets are thus well resolved in the fine region and propagate as expected with approximately the convection velocity (figures 6.2b and 6.2d). The packet P_1 is centered around the wavenumber $\kappa = 4$ which can be supported on the coarse as well as the fine grid (figure 6.2a), with more than 90% of the energy residing in wavenumbers with $|\kappa| < \kappa_a^c = 8$. The packet therefore mostly propagates into the coarse region (figure 6.2c) in a wave packet centered around a slightly larger wavenumber with a slightly lower group velocity (T_1 in figure 6.2a). But because of the resolution change, some of P_1 is also reflected

back into the fine region in a wave packet centered around a much higher wavenumber (R_1 in figure 6.2a) which has negative group velocity. Since equation (6.1) with a central difference derivative scheme is an energy preserving approximation of the advection equation, the energy from the incident wave is split between the reflected wave and the transmitted wave [190, 191, 192, 45]. The P_2 packet is centered around the wavenumber $\kappa = 18$ on the fine grid, which cannot be supported on the coarse grid (P_2 in figure 6.2a), and indeed virtually none of the energy resides in wavenumbers with $|\kappa| < \kappa_a^c$. It therefore cannot propagate into the coarse region and instead is entirely reflected back into the fine region (figure 6.2e) in a packet centered around a much larger wavenumber (R_2 in figure 6.2a). In both cases, it is effective wavenumbers that are preserved through the resolution change (figure 6.2a). The reflected waves R_1 and R_2 are entirely spurious.

Because the system is linear, the above results can be extended to grids with gradually changing resolution. In this case, a local wavenumber κ_j and a local group velocity $\mathcal{G}_j$ can be defined by substituting a given frequency ω (or κ') and the local grid spacing $\Delta(x_j)$ into equation (6.3). As above, there will be two possible values of κ_j, $\kappa_j^{(1)}$ and $\kappa_j^{(2)}$, satisfying $\kappa_j^{(1)} < \kappa_j^{(2)}$ and $(\kappa_j^{(2)}\Delta(x_j)) = \pi - (\kappa_j^{(1)}\Delta(x_j))$, with group velocities $\mathcal{G}_j$ and $-\mathcal{G}_j$, respectively. There are three main results of such an analysis [193, 45] that will be relevant for our purposes. First, no reflections occur if the local group velocity is uniform and nonzero, as expected. Second, a total reflection occurs for all wavenumbers that become unresolvable on the grid (i.e., exceed the Nyquist wavenumber), and the reflection occurs at the point where the local group velocity vanishes ($\mathcal{G}_j = 0$). Thirdly, no reflections occur for wavenumbers that can be resolved throughout the domain if $\Delta(x_j)$ varies over length scales that are long compared to the wavelength $\lambda = 2\pi/\kappa_j$ ($\frac{\lambda}{\Delta}\frac{d\Delta}{dx} \ll 1$). Thus, wave packets analogous to P_1 will be completely transmitted through a sufficiently smooth resolution change.

The behavior described here is representative of all energy-conserving numerical schemes with two wavenumbers per effective wavenumber. These are among the most common nu-

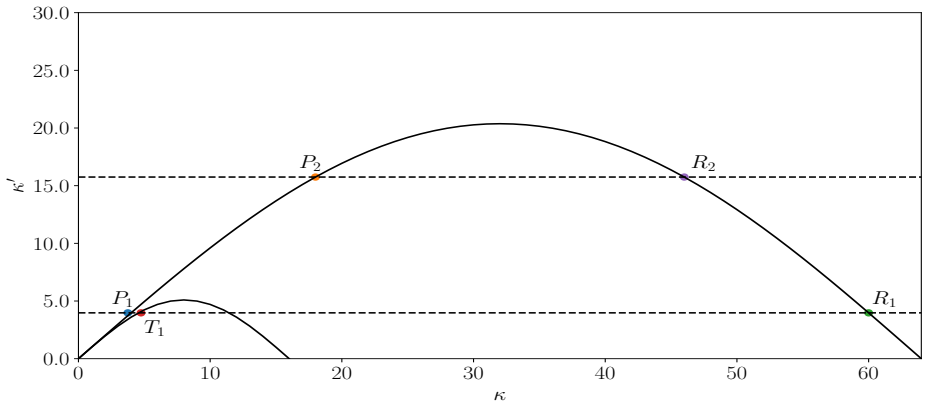

(a)

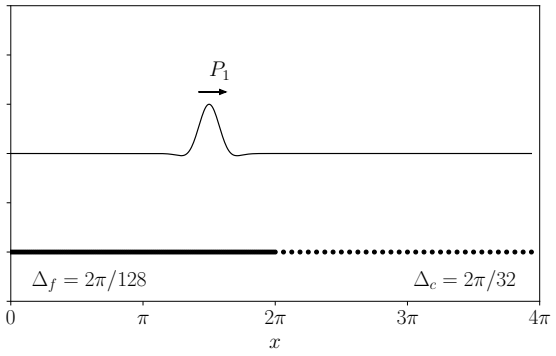

(b)

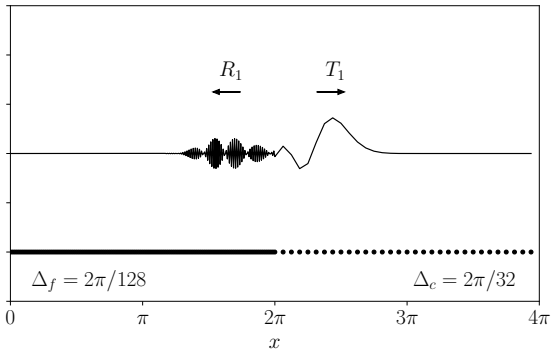

(c)

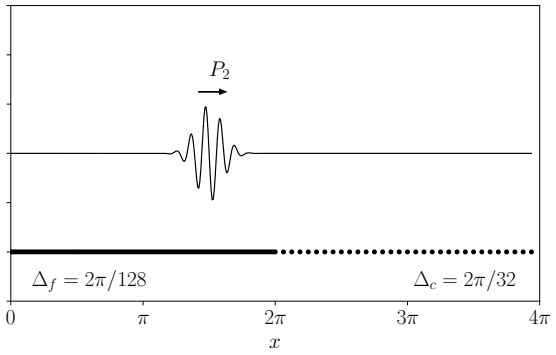

(d)

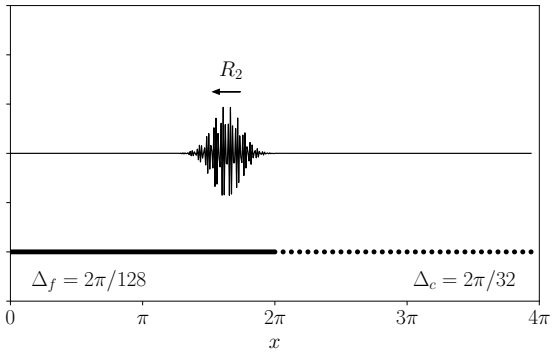

(e)

Figure 6.2: (a) The second order centered difference dispersion relation for both the fine ($\Delta_f = 2\pi/128$) and coarse ($\Delta_c = 2\pi/32$) regions of the grid, (b) An incident wave P_1 (●) that can be resolved in both the fine and coarse regions. (c) The subsequent reflected wave R_1 (●) and transmitted wave T_1 (●) after the P_1 wave has propagated through the resolution change. (d) An incident wave P_2 (●) that can only be resolved in the fine region. (e) The subsequent reflected wave R_2 (●) after the P_2 wave has propagated through the resolution change.

merical schemes used in turbulence applications (e.g., centered difference, B-splines, finite volume), however, other numerics with different propagation properties are possible. For instance, consider the box scheme whose semi-discretization of equation (6.1) is given by

$$\frac{\partial}{\partial t}\left(\frac{u_j + u_{j+1}}{2}\right) + U\frac{u_{j+1} - u_j}{x_{j+1} - x_j} = 0, \tag{6.5}$$

which is also energy preserving. Instead of reflecting unresolvable scales of motion at higher wavenumbers into the fine region, the box scheme transmits unresolvable scales at lower wavenumbers through the coarse region (similar to an aliasing effect) [194, 195]. The result is still spurious numerical oscillations.

These results from numerical analysis have profound consequences for LES. When LES turbulence convects into a more coarsely resolved region, the spectral characteristics of the numerical derivative operator $\delta/\delta x$ dictate that neglecting the inhomogeneous commutator can produce non-physical fine-scale noise propagating upstream, spoiling the solution far from the resolution change. This is explored in the next section.

6.2 Impacts of resolution inhomogeneity on LES

The commutator analysis of chapter 5 indicates that the combined effects of neglecting the inhomogeneous commutator and the dispersion characteristics of the numerical derivative operator could have a profound impact on an LES of turbulence flowing through a domain with varying spatial resolution. To characterize this impact, we consider a simple case of such a flow, making two simplifications to clearly expose the effects. As discussed in chapter 5, we consider commutation error for mean convection since this is commonly the dominant effect. This is consistent with the Taylor frozen field hypothesis. Moreover, a localized packet of turbulent fluctuations is used to expose the non-local effects of commutation error. Again we consider filters that consist of only an implicit projection to the discrete solution space.

6.2.1 A numerical experiment

Under the frozen field hypothesis and neglecting commutators, the LES equations for turbulence flowing at constant velocity U_x in the x direction simplify to:

$$\frac{\partial \overline{\mathbf{u}'}}{\partial t} + U_x \frac{\delta \overline{\mathbf{u}'}}{\delta x} = 0. \tag{6.6}$$

The resolution in the x direction is made to vary with x, while the resolution in the other directions is constant, and periodic boundary conditions are imposed in all three directions.

The filter is defined as a projection onto a periodic B-spline representation in the x-direction and Fourier spectral representations in the y- and z-directions. The $\delta/\delta x$ operator in equation (6.6) is defined as B-spline collocation. As in section 3.1, let B_n^k denote the nth derivative B-spline operator of order k, and B_n^{CD} denote the nth derivative second-order centered difference operator. The spectra of the B_1^k operators (figure 6.3) have similar propagation properties as the B_1^{CD} operator discussed in section 6.1, in that there are generally two wavenumbers κ that have the same effective wavenumber κ', one with positive group velocity and the other with negative group velocity. Further, with increasing κ, the negative group velocities get larger in magnitude (larger negative slopes on the right side of figure 6.3a).

For the results presented here, a third-order low storage Runge-Kutta method is used for time advancement [127]. Note that the spurious reflection/transmission phenomena described in section 6.1 depend only on spatial discretization [196].

A two dimensional slice of the numerical grid is shown in figure 6.4a. The domain in the propagation direction is divided into a uniform fine region of size 2π, a uniform coarse region of size 6π, and two transition regions of approximate size 2π in which the resolution is inhomogeneous. The fine resolution spacing between B-spline knot points is $\Delta_f = 2\pi/128$, and the coarse knot spacing is $\Delta_c = 2\pi/32$. In the transition regions, the knot spacing is

designed to vary as a Sigmoid function between Δ_f and Δ_c over a distance in x of order $1/\alpha$. To this end, the mapping function $g(\xi) : [0,1] \to [x_{\text{start}}, x_{\text{end}}]$ is defined implicitly through the differential equation:

$$\Delta(x) \equiv \frac{dg(\xi)}{d\xi}\Delta_\xi = \frac{\Delta_f}{1+e^{\alpha g(\xi)}} + \frac{\Delta_c}{1+e^{-\alpha g(\xi)}}, \tag{6.7}$$

where, $\Delta_\xi = 1/N_\xi$ is the uniform resolution in $\xi \in [0,1]$, with N_ξ the number of knot intervals in the transition region. The knot points x_j are then defined as $x_j = g(j\Delta_\xi)$ for $j = 0, 1, \ldots N_\xi$. The parameter α controls the sharpness of the grid change, with the transition thickness defined by $(\Delta_c - \Delta_f)/(d\Delta/dx) = 4/\alpha$. To generate the knot points used here, equation (6.7) was solved numerically for $g(\xi)$ using a standard Runge–Kutta–Fehlberg method and $g(0) = x_{\text{start}} = -\pi$, $\alpha = 4$ and $N_\xi = 75$. With these parameters, $g(1) \approx 3.1996$, defining a transition region grid on an interval slightly larger than 2π.

The domain in the two spectral directions is $[0, 2\pi]$ and with an effective uniform grid spacing of Δ_f. Thus, LES turbulence will be convected through an *anisotropic*, inhomogeneous grid — a common scenario in practice for structured grids. Moreover, in this configuration the three dimensional commutation error simplifies to the one dimensional case, which will expose the implications of the numerical analysis in section 6.1 for commutation error in LES.

The initial condition is taken to be a 'packet' of well-resolved, homogeneous, isotropic turbulence. This packet is analogous to the wave packets studied in the one-dimensional examples in section 6.1. To create this packet, a spectral LES of infinite Reynolds number homogeneous, isotropic turbulence was performed in a $2\pi \times 2\pi \times 2\pi$ domain with 64 Fourier modes in each direction. A Smagorinsky model was used to represent the subgrid stress in this simulation and a negative viscosity forcing that isotropically injects energy over a wavenumber shell of radius $0 < |\boldsymbol{\kappa}| \leq 2$ was introduced to allow the turbulence to become

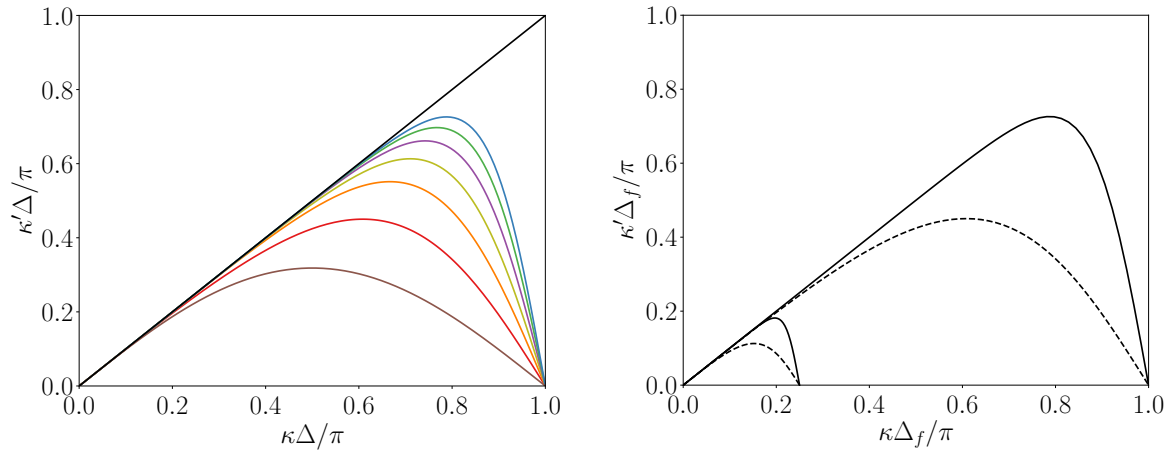

Figure 6.3: (a) The spectrum of the first derivative operators for a B-spline collocation method of several orders, a second-order centered difference method, and a spectral method; —— (B_1^2), —— (B_1^3), —— (B_1^4), —— (B_1^5), —— (B_1^6), —— (B_1^7), —— (B_1^{CD}), —— (Spectral). (b) The consistently normalized spectrum of the B_1^2 and B_1^7 operators for the fine region of the domain with spacing Δ_f and the coarse region of the domain with spacing $\Delta_c = 4\Delta_f$; —— (B_1^7), - - - (B_1^2).

statistically stationary. The energy injection rate and therefore, the equilibrium dissipation rate was set to 1. A representative instantaneous velocity field from the LES was then introduced into the fine region of the the B-spline/spectral simulation and modulated with a Gaussian so that the fluctuations go smoothly to zero. Note that this procedure does not produce a divergence free velocity, however, this is not an issue for the linear problem solved here; in fact, a divergence free projection would distort the desirable properties of the packet. The resolution used in the spectral simulation ensures that the modulated packet is well-resolved by the B-splines in the fine resolution region. Specifically, an isotropic grid spacing of $2\pi/64$ in the fully spectral simulation corresponds to $\kappa_{max}\Delta_f \approx 1.5$ in the B-spline simulation, where $\kappa_{max} = 32$ is the largest nonzero wavenumber in the turbulence packet. As seen in figure 6.3a, $(\kappa\Delta) = 1.5$ is in the positive group velocity regime.

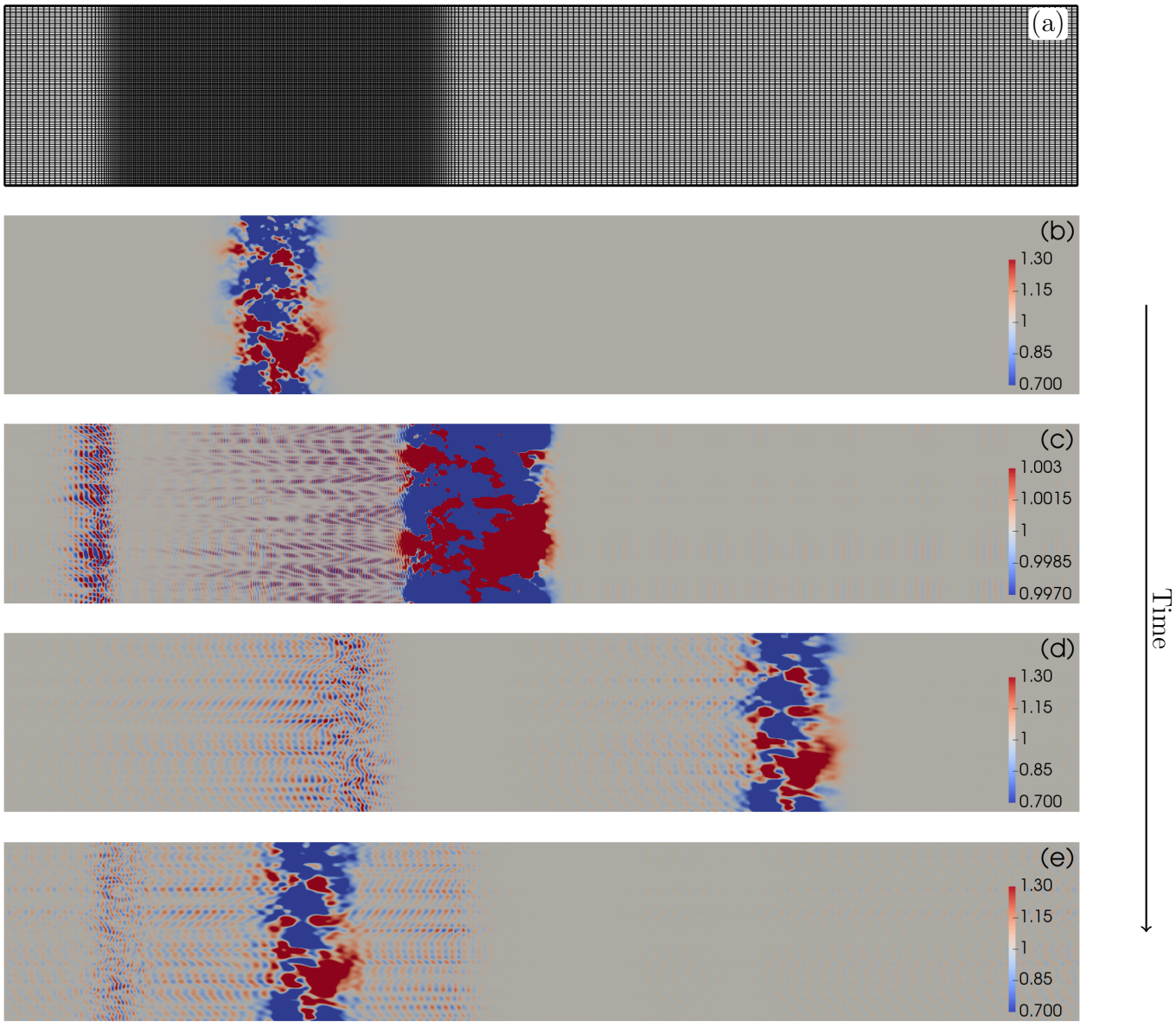

Figure 6.4: Convection of a packet of homogeneous, isotropic turbulence through an anisotropic, inhomogeneous grid with seventh-order B-splines and a convection velocity of 1. The packet is moving through the resolution change to the right. (a) A slice of the numerical grid. (b), (c), (d), and (e) show the streamwise velocity field at times 0.00, 7.03, 11.72, and 39.06, respectively. In part (c) the color scale is different to emphasize small amplitude fluctuations to highlight the spurious high wavenumber reflections moving to the left through the fine region of the grid. The results for the second-order B-spline case are qualitatively similar to those shown here albeit with more dispersion in the higher wavenumbers and a wider range of reflected scales.

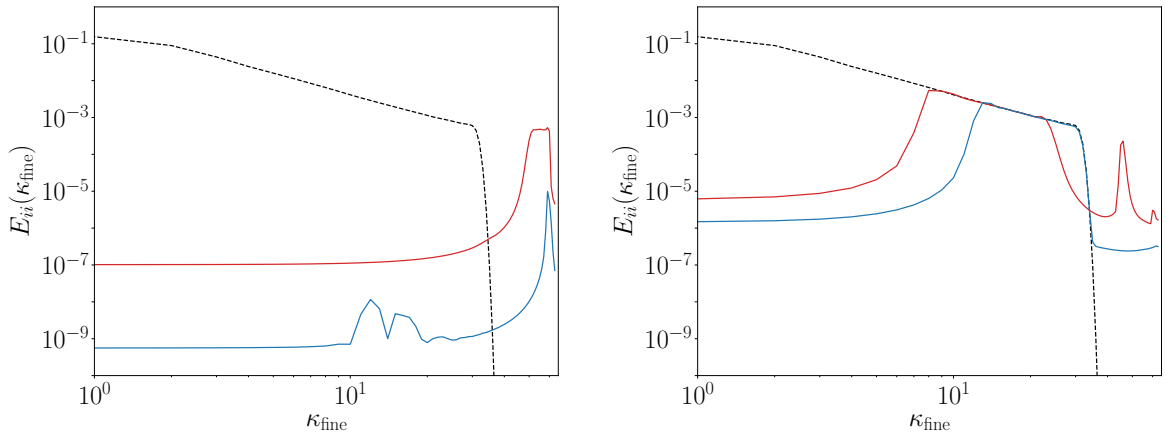

(a) $t = 7.03$(—), 11.72 (—)

(b) $t = 15.63$(—), 23.44 (—)

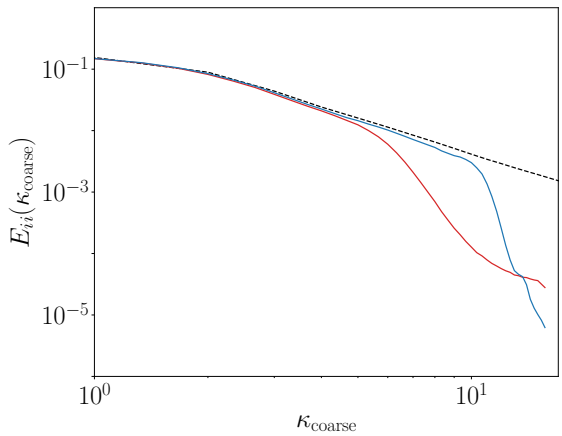

(c) $t = 18.75$(—), 11.72 (—)

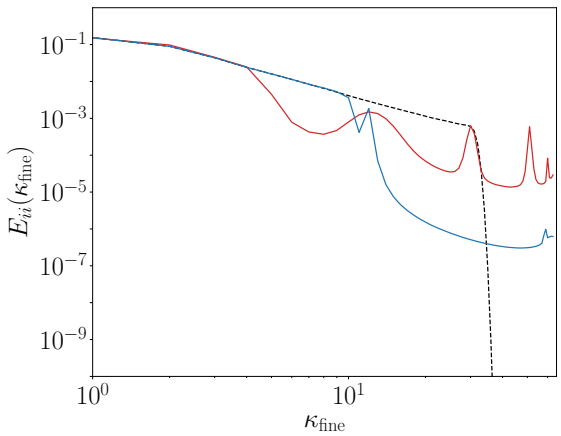

(d) $t = 39.06$(—), 39.84 (—)

Figure 6.5: One dimensional energy spectra, E_{ii}, in the direction of inhomogeneity at different times t; κ_{fine} and κ_{coarse} represent the wavenumbers in the fine and coarse regions of the domain, respectively. (a) High wavenumber reflections propagating backward through the fine region corresponding to the energy in the fine region in figure 6.4c. (b) The subsequent reflections propagating forward through the fine region corresponding to the energy in the fine region in figure 6.4d. (c) The spectra of the resolved turbulence packet in the coarse region corresponding to the energy in the coarse region in figure 6.4d. (d) The spectra of the turbulence packet after one flow through corresponding to the energy in the fine region in figure 6.4e. ——— (7th order B-splines), ——— (2nd order B-splines), – – – (Initial spectra of the turbulence packet shown in figure 6.4b).

6.2.2 Results

The effects of resolution inhomogeneity on the spatial structure (see figure 6.4) and on the one dimensional energy spectra (see figure 6.5) of the turbulence packet are examined at several

stages of the simulation for a single flow-through. Seventh-order B-splines and second-order B-splines are used to illustrate the behavior of higher- and lower-order methods. Based on the numerical analysis in section 6.1, the consistently normalized spectra of the B_1^2 and B_1^7 operators in the fine and coarse regions of the domain are sufficient to predict the behavior of the commutation error (see figure 6.3b). To see this, let the wavenumbers $|\kappa| \in [0, 16]$ be referred to as the *coarse wavenumbers*, wavenumbers $|\kappa| \in (16, 32]$ be the *fine wavenumbers*, and wavenumber $|\kappa| \in (32, 64]$ be the *spurious wavenumbers*, and recall that the fine region of the domain is capable of representing the fine, coarse, and spurious wavenumbers, while the coarse region is only capable of representing the coarse wavenumbers. The initial packet of turbulence only contains fine and coarse wavenumbers, so any energy transferred to higher wavenumbers by the resolution inhomogeneity is indeed spurious.

As the turbulence packet convects into the coarse region of the domain, all of the energy in the fine wavenumbers is transferred to scales with negative group velocity in the spurious wavenumber regime (see figure 6.4c). As in section 6.1, this energy transfer occurs between wavenumbers that share an effective wavenumber. The corresponding energy spectra at this stage of the simulation show a pile up of energy in the largest wavenumbers in the fine region of the domain (see figure 6.5a). Notice that, for each numerical scheme, the energy is concentrated in a narrow band of wavenumbers that corresponds to the region with negative slope in the effective wavenumbers shown in figure 6.3b. The reflections in the second order B-spline case occur over a wider range of wavenumbers and are collectively more intense than for seventh-order case, as more energy is being reflected (see figure 6.5a). Furthermore, the propagation speed of the reflections is much greater for seventh-order B-splines than second-order B-splines, as indicated by the slopes of the effective wavenumbers. Interestingly, we observed that, for a B-spline collocation method, the ratio of the group velocity to the convection velocity of the highest wavenumber reflections for each B-spline order matches the order of the B-spline (e.g., the Nyquist wavenumber propagates at negative N times

the convection velocity for Nth order B-splines). This appears to be a special property of B-spline collocation that deserves proof and is consistent with the work of Vichnevetsky and Scheidegger [197], who demonstrated that an infinite speed of reflection occurs for spectral numerics.

Once the reflected fluctuations reach the resolution change on the left side of the fine region, they are reflected back into the fine region with positive group velocity with their initial wavenumbers. This re-reflection can be tracked from figure 6.4c in which the reflected wavepacket consisting of spurious wavenumbers is visible on the left-hand side as it propagates upstream (to the left), to figure 6.4d in which the re-reflected wavepacket consisting now of fine wavenumbers is visible propagating down-stream. These secondary reflections occur in the fine wavenumber regime but are as erroneous as the spurious reflections that created them. For both B-spline orders, the energy spectra in the fine resolution region for the initial turbulence packet and the reflected scales of motion match for all fine wavenumbers (see figure 6.5b). This indicates a total reflection occurs for all scales that are only representable on the fine grid, which agrees with the analysis of the P_2-type waves discussed in section 6.1. Without the commutator $\mathcal{C}^I$, this cycle of reflection between fine and spurious wavenumbers repeats. The energy initially contained in the fine wavenumber regime gets trapped in the fine resolution region.

The only fluctuation scales that make it through to the coarse region of the domain are those that can be represented on the coarse grid, i.e., the coarse wavenumbers (see figure 6.4d). The energy spectra at the initial time, and after the packet has convected into the coarse region, match *almost* identically for all coarse wavenumbers (see figure 6.5c). A relatively small fraction of the energy in the coarse wavenumbers also gets trapped in the fine region, as shown in figure 6.5b. This behavior is also predicted by the numerical analysis of the P_1-type waves discussed in section 6.1, and would vanish in the limit of a smoothly varying grid.

The numerical experiment described here focuses on the idealized case of frozen turbulence consistent with Taylor's hypothesis to emphasize the impact of commutation error. The scales trapped in the fine region of the domain are physically incorrect and numerically problematic. An increase in high wavenumber energy can lead to numerical instabilities, and the trapped low wavenumber energy can corrupt otherwise meaningful statistics. Moreover, it is reasonable to expect that in an LES nonlinear effects would magnify these problems as erroneous fluctuations would interact with and contaminate incoming turbulence. Consider, for instance, the turbulence packet after one flow through (see figure 6.4e). As the coarsely resolved packet re-enters the fine region (without any active forcing), the spectrum gets corrupted by the trapped energy (see figure 6.5d). Furthermore, a shift in energy from lower wavenumbers to higher wavenumbers would be particularly damaging in real turbulence as the former are more responsible for momentum transport while the latter are more responsible for dissipation. The nonlocal wavenumber interactions introduced by resolution inhomogeneity may corrupt the energy cascade, which, in homogeneous isotropic turbulence, is known to be dominated by interactions local in wavespace [91]. Lastly, notice that unlike the effects of discretization error, the effects of resolution inhomogeneity do not improve with higher-order numerics. Further study of these effects in an actual LES is warranted, but is out of scope for this paper. However, it is clear that a model for the inhomogeneous part of the commutator is needed to mitigate the effects of the commutation error.

6.3 Commutator Modeling

In this section we propose an approach to modeling the inhomogeneous commutator based on the characteristics of the commutator and the commutation error explored above. As previously discussed, a model for the commutator is responsible for transferring energy between resolved and unresolved scales as a consequence of the resolution inhomogeneity. In the coarsening grid case, a commutation model must transfer the energy in newly unresolvable

scales to the subgrid scales. In the refining grid case, a model for $\mathcal{C}^I$ would have to transfer energy from the subgrid to the resolved turbulence, presumably through some type of forcing. Notice that the requirements of a commutation model in the coarsening and refining cases are fundamentally different. It has been suggested that a "good" commutation model should handle both of these scenarios (e.g., [183]), however, because of these different requirements, this may not be appropriate. A commutation model for the coarsening and refining grid cases may need to be developed independently. We pursue this modeling approach here for the case of flow through coarsening grids to address the issues discussed in section 6.2.

A common mechanism for providing the transfer of energy from resolved to subgrid scales is a viscosity-based model, as suggested by the second order term in equation (5.38), which is equipped with the viscosity $\nu_{comm} = U\Delta\partial\Delta/\partial x$. However, as indicated by equation (5.40), a commutation model should ideally only affect wavenumbers near the cutoff wavenumber. This property preserves wavenumbers that are well resolved throughout the resolution change while removing those that are not. As such, a hyperviscosity is a more appropriate model for the commutator, as also indicated by the leading order terms in equation (5.38). Specifically, the leading order terms in equation (5.38) suggest the following form for a general one dimensional hyperviscosity commutation model:

$$U\mathcal{C}^I(u) \simeq (-1)^{N/2} C U \Delta \frac{d\Delta}{dx}\left(\Delta^{N-2}\frac{\partial^N \overline{u}}{\partial x^N}\right), \tag{6.8}$$

for some coefficient C and even order N (N is assumed to be a positive even integer for the remainder of this paper).

For any finite value of N in equation (6.8), there is a trade-off between removing high wavenumber scales in fine regions of the grid that are approaching unresolvability, and preserving the well-resolved scales in coarse regions of the grid. Larger values of N lead to sharper filters, which perform better in the context of this trade-off than smaller values of

N. Accordingly, it is desirable to make N as large as possible. Again, this is consistent with equation (5.40). However, the number of available derivatives of the filtered field limits how large N can be, i.e., the underlying numerics constrain N based on the number of accessible derivative operators. For example, CFD codes typically only have access to second derivative operators so that N would be limited to 2. Furthermore, larger values of N require not only higher order numerics but also additional boundary conditions, which are often mentioned as a problem with hyperviscosity models [153, 146].

Let $F_N(u) \approx \partial^N u/\partial x^N$ be some numerical operator that approximates the Nth derivative. The commutation model (6.8) can then be written as:

$$\mathcal{C}^I(u) = (-1)^{N/2} C\Delta \frac{d\Delta}{dx} \left(\Delta^{N-2} F_N(\overline{u})\right). \tag{6.9}$$

As mentioned above, it is desirable to take N large, but the underlying numerics often limit N. However, we saw earlier how lower-order numerical operators can be designed to mimic higher-order filters without increasing the order of the differential equation. In particular, it was shown in section 3.8 that $(-1)^{N/2+1}(B_2 - B_1 B_1) \sim \Delta^{N-2} F_N$ for some value of N (and positive constant of proportionality), which corresponds exactly to the form of (6.9); i.e.,

$$\mathcal{C}^I(u) = -C\Delta \frac{d\Delta}{dx} \left(B_2 - B_1 B_1\right) \overline{u}. \tag{6.10}$$

This is equivalent to filtering via a hyperviscosity (as opposed an explicit filter — see section 3.6) and is appropriate here since the time and length scales dependencies of the model are determined from the analyses in chapter 5. Further, notice that the $B_2 - B_1 B_1$ operator is particularly well suited to reduce commutation error as it will significantly damp wavenumbers with negative group velocity, which is where the commutation error manifests for many typical numerical schemes (see figure 3.10).

The constant C in equation (6.10) must also be specified. In an LES, the statistical

analysis in section 5.2 can be used to set the model coefficient C to produce the correct rate of energy transfer to the subgrid scales (e.g., evaluating equation (5.41) or (5.42) for a Kolmogorov spectrum). However, for the simple case of linear convection considered here, it is useful to examine how the behavior of the model changes as the coefficient varies. Momentarily, let $\varepsilon \in (0,1)$ be the maximum allowed fraction of energy at any wavenumber to be reflected due to resolution variation. Now, consider the action of the commutation model defined in equation (6.9) on the Fourier coefficient $\widehat{u}(\kappa,t)$, which is given by

$$\frac{\partial \hat{u}(\kappa,t)}{\partial t} = (-1)^{\frac{N-2}{2}} CU \frac{\partial \Delta}{\partial x} \Delta^{N-1} \hat{F}_N(\kappa) \hat{u}(\kappa,t), \tag{6.11}$$

where $\hat{F}_N(\kappa)$ is the spectrum of F_N evaluated at wavenumber κ. After a time t, the amplification of $\hat{u}(\kappa)$ is:

$$\frac{\hat{u}(\kappa,t)}{\hat{u}(\kappa,0)} = \exp\left((-1)^{\frac{N-2}{2}} CU \frac{\partial \Delta}{\partial x} \Delta^{N-1} \hat{F}_N(\kappa) t \right). \tag{6.12}$$

As the resolved turbulence convects through a coarsening grid, we insist that $\hat{u}^2(\kappa,t)/\hat{u}^2(\kappa,0) \leq \varepsilon$ for all reflected wavenumbers. This requires that C satisfy

$$C \geq \frac{(-1)^{\frac{N-2}{2}} \log(\varepsilon)}{2U \frac{\partial \Delta}{\partial x} \Delta^{N-1} \hat{F}_N(\kappa) t}, \tag{6.13}$$

for all reflected wavenumbers. If we assume for simplicity that $d\Delta/dx \approx (\max(\Delta) - \min(\Delta))/L$ and that $t = L/U$, for some length of gradual coarsening L, equation (6.13) simplifies to

$$C \geq \frac{(-1)^{\frac{N-2}{2}} \log(\varepsilon)}{2 \left(\frac{\max(\Delta) - \min(\Delta)}{\Delta} \right) \left(\Delta^N \hat{F}_N(\kappa) \right)}. \tag{6.14}$$

Notice that the lower the wavenumber with positive group velocity, the higher the wavenumber of the reflection with negative group velocity. Accordingly, the smallest wavenumber

with nonpositive group velocity is dissipated the least by the model. Therefore, evaluating $\hat{F}_N$ at κ_a associated with the numerical first derivative operator B_1, as defined in section 6.1 will ensure equation (6.14) is satisfied for all reflected wavenumbers. Furthermore, because for any numerical approximations, $\kappa_a \sim 1/\Delta$ and $\hat{F}_N(\kappa\Delta) \sim 1/\Delta^N$, $\Delta^N \hat{F}_N(\kappa_a)$ depends only on the numerical schemes, and is independent of Δ. Finally, by replacing the remaining Δ with $\max(\Delta)$ in equation (6.14) when evaluating C, we ensure that the inequality is satisfied, and obtain an expression that depend only on the numerical schemes involved and the extreme values of Δ:

$$C = \frac{(-1)^{\frac{N-2}{2}} \log(\varepsilon)}{2\left(\frac{(\max(\Delta)-\min(\Delta)}{\max(\Delta)}\right)\left(\Delta^N \hat{F}_N(\kappa_a)\right)}. \tag{6.15}$$

Note that when using the $B_2 - B_1 B_1$ model, one can simply substitute $(-1)^{\frac{N-2}{2}} \Delta^2 (\hat{B}_2 - \hat{B}_1 \hat{B}_1)$ for $\Delta^N F_N$ in equation (6.15) to obtain the coefficient in (6.10).

This choice of coefficient may indicate how the numerical properties of the commutation error discussed in section 6.1 can be exploited to improve the model. To elaborate, notice that we use the value of $\hat{F}_N$ at the apex wavenumber κ_a. This choice is made to take advantage of how the commutation error manifests numerically. Specifically, the coefficient is designed to quickly damp high wavenumbers *after* they have been reflected. Targeting reflections yields a larger separation between the scales that must be filtered out, and those that need to be preserved. This approach is especially advantageous for low values of N for which the filters produced from equation (6.8) are not particularly sharp. In essence, it is more advantageous to use a model to correct for the absence of $\mathcal{C}^I$ (commutation error) in this problem, than to model $\mathcal{C}^I$ directly. This strategy works particularly well with the $B_2 - B_1 B_1$ filters described in the previous section, which target the poorly resolved wavenumbers. In LES, more work is needed to see if a similar exploit can be performed. For example, nonlinear interactions may require scales to be removed before reflection, but this would lead to more dissipation of the resolved turbulence.

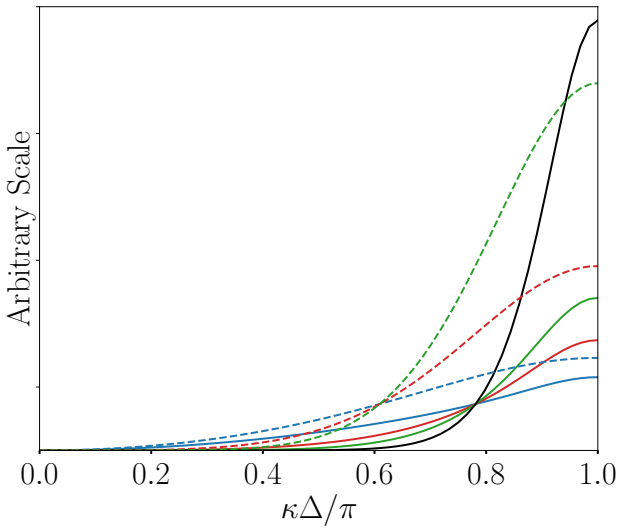

Figure 6.6: Spectra of the operator CF_N for various forms of F_N and the coefficient C determined by (6.15). The scale is arbitrary and depends on ε and the resolution Δ. —— $(F_2 = B_2^7)$, —— $(F_4 = B_4^7)$, —— $(F_6 = B_6^7)$, —— $(\Delta^8 F_{10} \sim B_2^7 - B_1^7 B_1^7)$, - - - $(F_2 = B_2^2)$, - - - $(\Delta^2 F_4 \sim B_2^2 - B_1^2 B_1^2)$, - - - $(F_6 = (B_2^2)^3)$.

The spectrum of the operator CF_N for second- and seventh-order B-splines with this choice of coefficient and several different choices of N is shown is shown in figure 6.6. For an arbitrary tolerance value of ε, the model coefficient creates an intersection point at κ_a between different values of N. This intersection point shifts depending on the order of the underlying numerics. figure 6.6 shows how as N increases, the poorly resolved scales are dissipated more rapidly and the well resolvable scales are better preserved.

6.3.1 Model results

The ability of the model to correct for the issues related to resolution inhomogeneity is tested in the same setting described in section 6.2. The commutation model is introduced into equation (6.6) as

$$\frac{\partial \overline{\mathbf{u}'}}{\partial t} + U_x \frac{\delta \overline{\mathbf{u}'}}{\delta x} = (-1)^{\frac{N}{2}+1} C \Delta_x \left(U_x \frac{\partial \Delta_x}{\partial x} \right) \left(\Delta_x^{N-2} F_N(\overline{\mathbf{u}'}) \right), \tag{6.16}$$

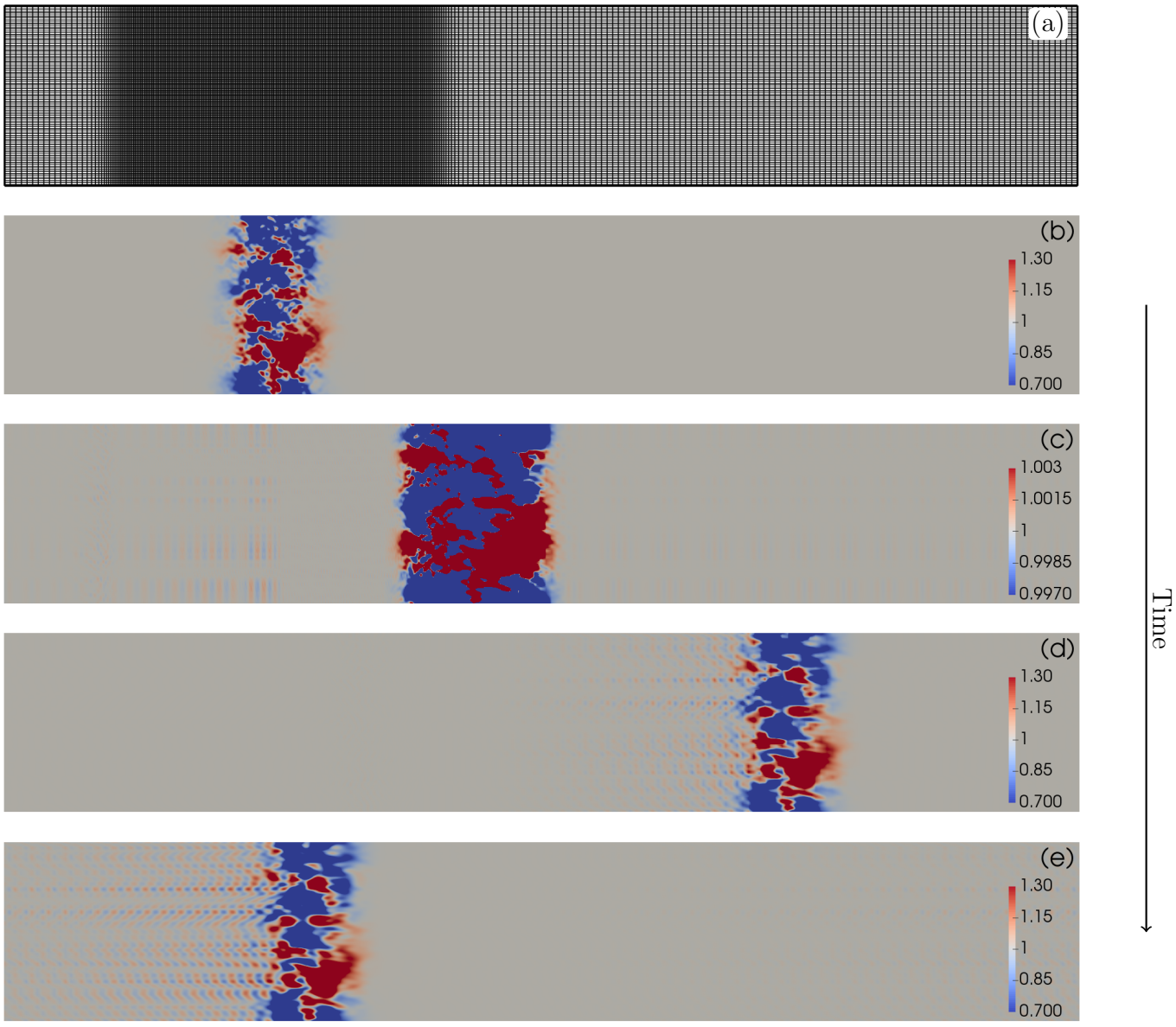

Figure 6.7: Convection of a packet of homogeneous, isotropic turbulence through an anisotropic, inhomogeneous grid with seventh-order B-splines, a convection velocity of 1, and a commutation model with $\Delta^8 F_{10} \sim (B_2^7 - B_1^7 B_1^7)$ and $\varepsilon = 0.001$. The packet is moving through the resolution change to the right. (a) A slice of the numerical grid. (b), (c), (d), and (e) show the streamwise velocity field at times 0.00, 7.03, 11.72, and 39.06, respectively. Figure (c) is scaled to highlight the absence of the spurious high wavenumber reflections, as in figure 6.4c.

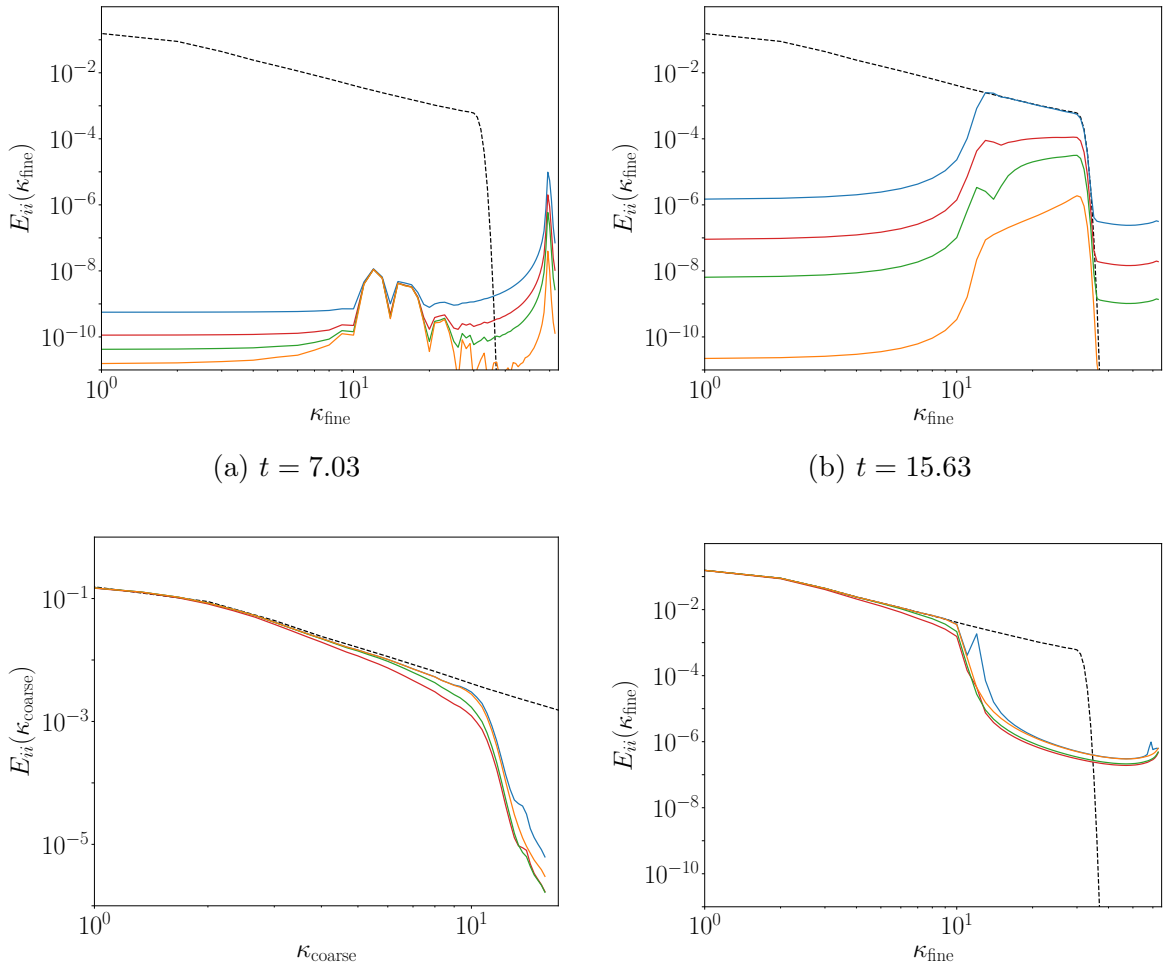

(a) $t = 7.03$ (b) $t = 15.63$

(c) $t = 11.72$ (d) $t = 39.06$

Figure 6.8: Energy spectra, E_{ii}, in the direction of convection at different times t for 7th order B-splines; κ_{fine} and κ_{coarse} represent the wavenumbers in the fine and coarse regions of the domain, respectively. (a) High wavenumber reflections propagating backward through the fine region. (b) The subsequent reflections propagating forward through the fine region. (c) The spectra of the resolved turbulence packet in the coarse region. (d) The spectra of the turbulence packet after one flow through. —— (No model), —— ($F_2 = B_2^7$, $\varepsilon = 0.1$), —— ($F_4 = B_4^7$, $\varepsilon = 0.01$), —— ($\Delta^8 F_{10} \sim (B_2^7 - B_1^7 B_1^7)$, $\varepsilon = 0.001$), – – – (Initial Packet)

where the coefficient C is given by equation (6.15), and the operator F_N is an approximation of the Nth derivative in the x-direction ($F_N \approx \partial^N / \partial_x^N$). Recall that in this setting the local grid spacing is $\boldsymbol{\Delta}(x) = (\Delta_x(x), \Delta_y, \Delta_z)$ and the dependence on x in equation (6.16) arises because the resolution inhomogeneity is only in the x-direction.

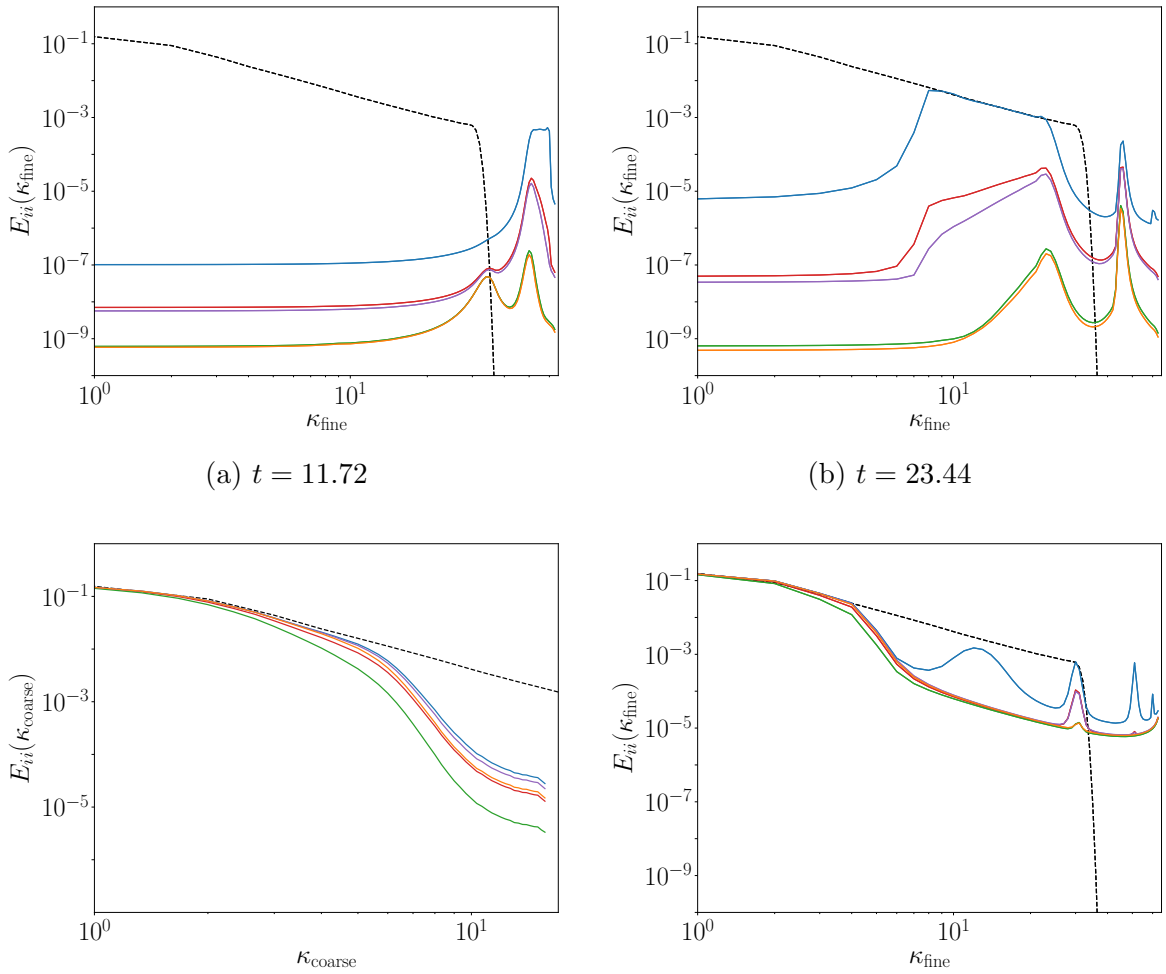

(a) $t = 11.72$

(b) $t = 23.44$

(c) $t = 11.72$

(d) $t = 39.84$

Figure 6.9: Energy spectra, E_{ii}, in the direction of convection at different times t for 2nd order B-splines; κ_{fine} and κ_{coarse} represent the wavenumbers in the fine and coarse regions of the domain, respectively. (a) High wavenumber reflections propagating backward through the fine region. (b) The subsequent reflections propagating forward through the fine region. (c) The spectra of the resolved turbulence packet in the coarse region. (d) The spectra of the turbulence packet after one flow through. —— (No model), —— ($\Delta^2 F_4 \sim -(B_2^2 - B_1^2 B_1^2)$, $\varepsilon = 0.1$), —— ($\Delta^2 F_4 \sim -(B_2^2 - B_1^2 B_1^2)$, $\varepsilon = 0.001$), —— ($F_2 = B_2^2$, $\varepsilon = 0.001$), —— ($F_2 = B_2^2$, $\varepsilon = 0.1$), - - - (Initial Packet)

For the seventh-order B-spline results, three different choices of N and ε are tested: $N = 2$ corresponding to the second derivative operator $F_2 = B_2^7$ with $\varepsilon = 0.1$, $N = 4$ corresponding to the fourth derivative operator $F_4 = B_4^7$ with $\varepsilon = 0.01$, and $N = 10$ corresponding to the $\Delta^8 F_{10} \sim B_2^7 - B_1^7 B_1^7$ operator with $\varepsilon = 0.001$. For the second-order B-spline results, two

choices of N are tested for both $\varepsilon = 0.1$ and $\varepsilon = 0.001$: $N = 2$ corresponding to the $F_2 = B_2^2$ operator, and $N = 4$ corresponding to the $\Delta^2 F_4 \sim -(B_2^2 - B_1^2 B_1^2)$ operator. These values, along with the model coefficients, are listed in table 6.1. The one-dimensional energy spectra in the fine and coarse regions of the domain are shown in figures 6.8 and 6.9 for seventh- and second-order B-splines, respectively. The results of the model in physical space for the seventh order B-spline case with $\Delta^8 F_{10} \sim (B_2^7 - B_1^7 B_1^7)$ and $\varepsilon = 0.001$ are shown in figure 6.7.

Compare these results with the pure convection case (i.e., the no model case) examined in section 6.2. The model significantly corrects the spatial structure and the energy distribution of the turbulence packet as it flows through the inhomogeneous grid. In all cases, the model reduces the spurious high wavenumber reflections by (at least) a factor around ε, as desired (see figures 6.8b and 6.9b). Recall that the largest initial wavenumber with positive group velocity has the smallest reflected wavenumber and is dissipated the least by the model, so the value of ε should be validated at these wavenumbers in the spectra results. Moreover, the model preserves the resolvable turbulence in the coarse region as much as possible. The seventh-order results show that higher order filters (i.e., larger values of N) preserve the resolvable turbulence while dissipating the reflections more strongly. In particular, the $B_2^7 - B_1^7 B_1^7$ model matches the ideal spectra in the coarse region almost exactly and is still

Table 6.1: Model Coefficients.

N	F_N	ε	C
2	B_2^7	0.1	0.24
4	B_4^7	0.01	0.07
10	$\Delta^{-8}(B_2^7 - B_1^7 B_1^7)$	0.001	4.31
2	B_2^2	0.1	0.38
2	B_2^2	0.001	1.15
4	$-\Delta^{-2}(B_2^2 - B_1^2 B_1^2)$	0.1	0.76
4	$-\Delta^{-2}(B_2^2 - B_1^2 B_1^2)$	0.001	2.28

able to reduce reflections by at least three orders of magnitude (see figure 6.8c). Similarly, in the second-order B-spline results, the $N = 4$ cases match the original spectra in the coarse region more closely than the $N = 2$ cases for the same value of ε (see figure 6.9c). Finally, the model mitigates the effect of erroneous reflections on incoming turbulence, as demonstrated by examining the turbulence packet after one flow through (see figures 6.8d and 6.9d). Even a modest reduction in the reflections — such as that from the low N and ε cases — yields much better spectra than the pure convection case. The spectra after one flow through match quite well with the initial packet's spectrum for all coarse wavenumbers.

6.4 Commutation error and modeling in isotropic turbulence

The results in sections 6.2 and 6.3 expose the issues of commutation error in the simple case of a convecting packet of homogeneous isotropic turbulence, and suggest a promising approach to correcting commutation error in terms of the analysis discussed in chapter 5 and the filtering techniques discussed in chapter 3. In this section we extend those results to the three dimensional isotropic turbulence case.

6.4.1 Multi-dimensional wave propagation

Based on the success in one dimension, we expect the multi-dimensional wave propagation characteristics of spatial discretization schemes to be useful in describing resolution inhomogeneity effects in three dimensional evolving turbulence. However, to the authors knowledge, the numerical analysis in [190, 191, 192, 45, 193] has not been extended to the multi-dimensional case. To explore this, we consider the two-dimensional propagation of a wave packet through two different grids — an anisotropic inhomogeneous grid and an isotropic inhomogeneous grids — analogous to the example studied in the one dimensional case (see figure 6.2).

Specifically, consider a two dimensional Cartesian grid with domain lengths $L_x = 4\pi$

and $L_y = 2\pi$ and a sharp change in the x-directional resolution, Δ_x, from $\Delta_{x_f} = 2\pi/128$ to $\Delta_{x_c} = 2\pi/32$ at the location $x = 2\pi$. In the anisotropic, inhomogeneous grid $\Delta_y = \Delta_{x_f}$ throughout the entire domain, and in the isotropic inhomogeneous grid $\Delta_y = \Delta_x$. The initial condition is taken to be

$$u(x, y, t = 0) = \cos(4x)\cos(25y)e^{-\left[(x-\pi)^2+(y-\pi)^2\right]}, \tag{6.17}$$

which is well resolved in the x- and y-directions of both grids in the fine region of the domain (see figures 6.10a and 6.11a). We consider the convection of this two dimensional wave packet in the x direction towards the resolution change with a mean velocity of $U = 1$. A second order centered difference scheme is used in the x-direction and a Fourier-spectral representation is used in the y-direction. The isotropic grid is constructed in the Fourier spectral case by setting the Fourier coefficients of wavenumbers greater than $\kappa_c(x) = \lfloor \pi/\Delta_x(x) \rceil$ to zero.

In the anisotropic inhomogeneous grid case, the initial wave packet is resolvable in both the fine and coarse regions of the domain. The wave packet is therefore transmitted through the resolution change (see figure 6.10b) at wavenumber pair $(\kappa_x, \kappa_y) \approx (4, 25)$ (see figure 6.10d). The sharp resolution change also generates a reflected wave that propagates upstream through the fine region of the domain and is centered around the wavenumber pair $(\kappa_x, \kappa_y) = (60, 25)$ since $\sin(4\Delta_{x_f})/\Delta_{x_f} = \sin(60\Delta_{x_f})/\Delta_{x_f}$ (see figure 6.10c). This is analogous to the R_1-type wave examined in figure 6.2 and would vanish in the limit of a smooth grid change. Notice that only the wavenumber in the direction of convection is affected through the resolution change. Since wavenumbers $|\kappa_y| < \pi/\Delta_{x_f}$ can be resolved throughout the entire domain, totally reflected waves only occur for wavepackets for which $|\kappa_x| > \pi/\Delta_{x_c}$. This is the sense in which commutation effects were limited to one-dimension in section 6.2.

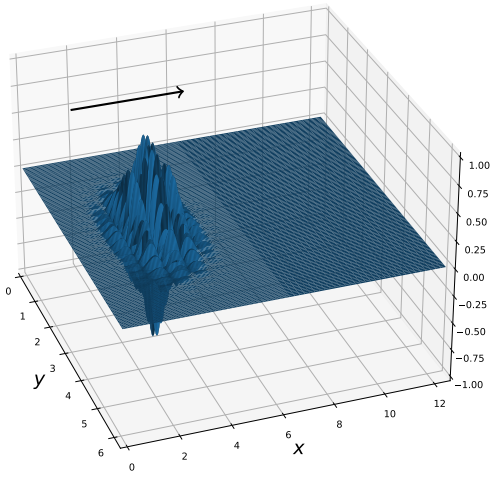

(a) $t = 0$

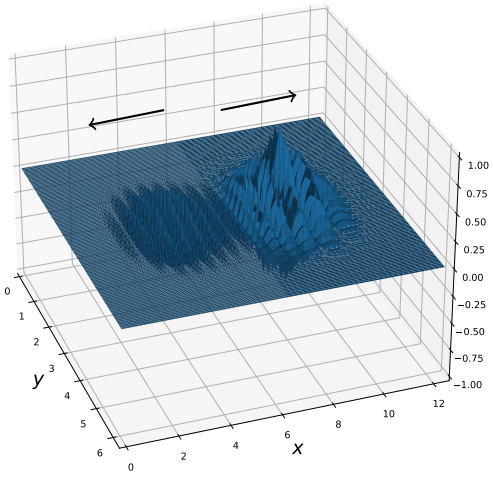

(b) $t = 6.38$

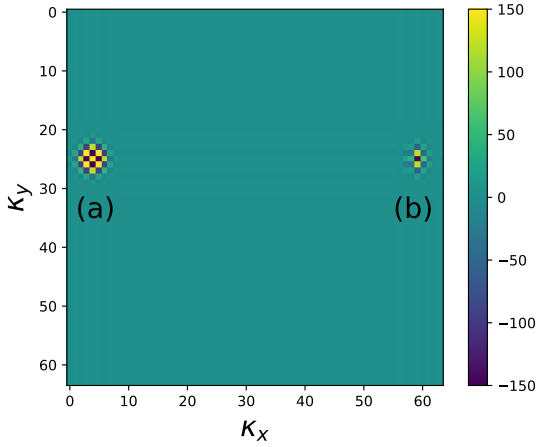

(c) Fine region ($x < 2\pi$)

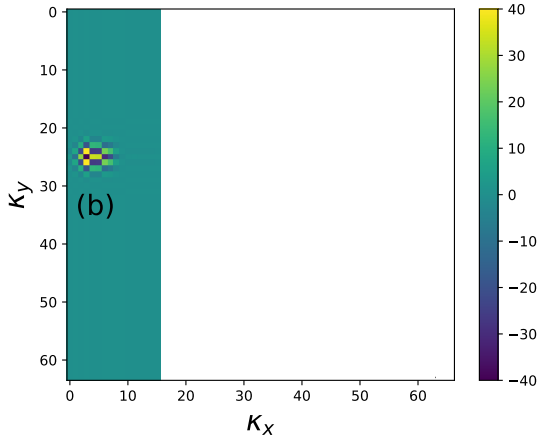

(d) Coarse region ($x > 2\pi$)

Figure 6.10: Two dimensional wave propagation example through an anisotropic inhomogeneous grid with a mean velocity of $U = 1$. (a) The initial wave packet at $t = 0$ given by equation (6.17) propagating to the right towards the resolution change. (b) The transmitted and reflected wave generated through the resolution change at $t = 6.38$ propagating to the right and left, respectively. (c) Two dimensional Fourier transform of the wave packet in the fine region of the domain. The Fourier coefficient for the wave in part (a) and (b) are shown. (d) Two dimensional Fourier transform of the wave packet in the coarse region of the domain for the transmitted wave in part (b).

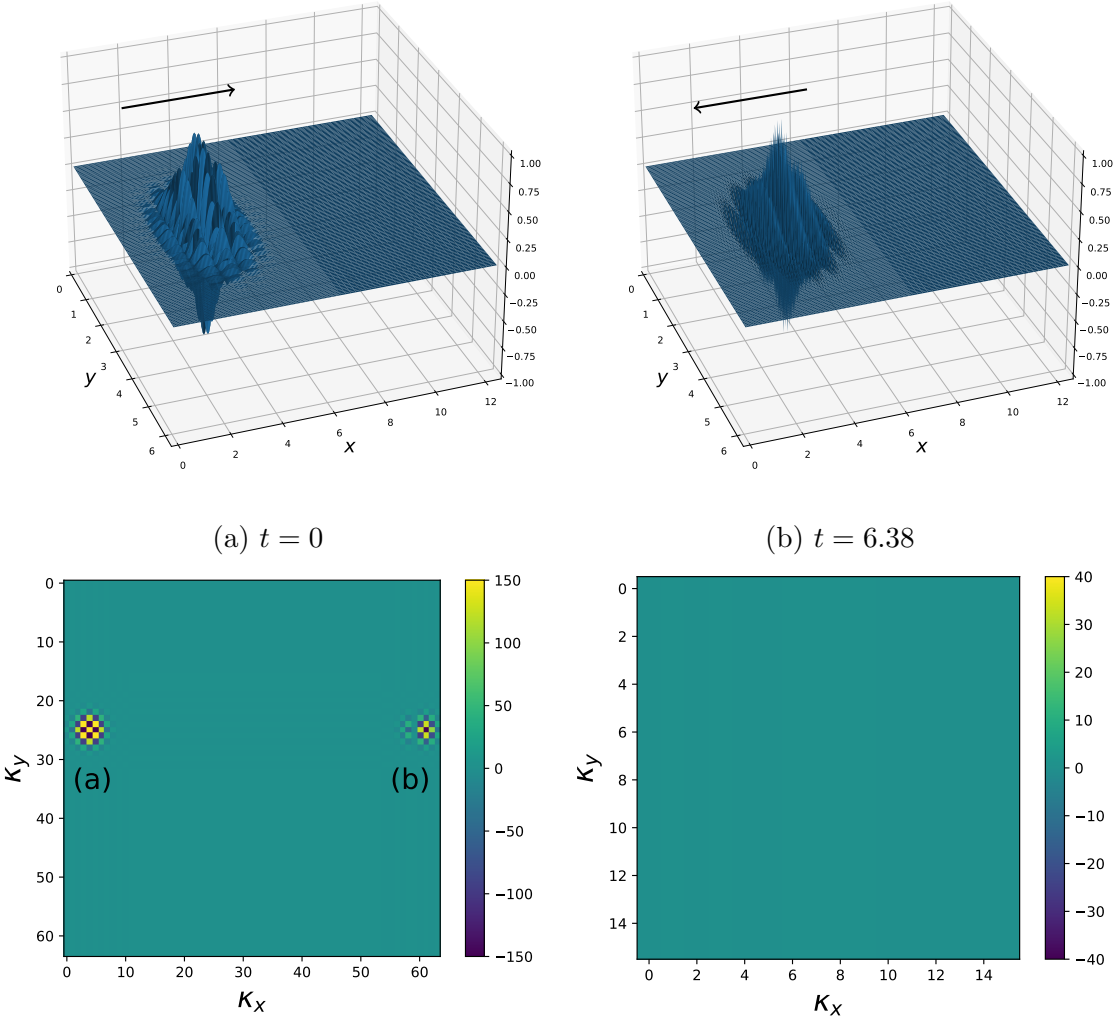

(a) $t = 0$

(b) $t = 6.38$

(c) Fine region ($x < 2\pi$)

(d) Coarse region ($x > 2\pi$)

Figure 6.11: Two dimensional wave propagation example through an isotropic inhomogeneous grid with a mean velocity of $U = 1$. (a) The initial wave packet at $t = 0$ given by equation (6.17) propagating to the right towards the resolution change. (b) The reflected wave generated through the resolution change at $t = 6.38$ propagating to the left. (c) Two dimensional Fourier transform of the wave packet in the fine region of the domain before and after the reflection before and after the reflection. (d) Two dimensional Fourier transform of the wave packet in the coarse region of the domain, showing no energy is transmitted to the coarse region in this case.

In the isotropic inhomogeneous grid, the wavepacket in equation (6.17) cannot be resolved in the coarse region of the domain so a total reflection occurs as the packet convects towards the resolution change (see figure 6.11b). However, notice in this case that it is the wavenumber $\kappa_y = 25$ that cannot be represented in the coarse region, while the wavenumber in the direction of convection $\kappa_x = 4$ can be represented in the coarse region. Nonetheless, the energy in the initial packet is also transferred to the wave packet centered around $(\kappa_x, \kappa_y) = (60, 25)$ (see figure 6.11c) as before, which has negative group velocity in the x-direction and therefore propagates upstream. No energy is transmitted to the coarse region in this case (see figure 6.11d). This simple example illustrates the energy exchange that can occur between resolved turbulent modes in an LES due to resolution inhomogeneity. Regardless of which wavenumber component causes a mode to become unresolvable in a certain region of the grid, that energy is transferred to a mode whose wavenumber in the direction of mean convection is larger (with the same effective wavenumber as the original mode), but the wavenumber components in directions orthogonal to mean convection remain the same as the original mode.

Further, it is useful to compare the analytical commutator to the numerical wave propagation results in these cases. In section 5.5 the form of the inhomogeneous commutator was analyzed in both the anisotropic and isotropic inhomogeneous grid case considered here. For the isotropic inhomogeneous grid in particular, it was found that

$$U\mathcal{C}^I(\psi) = C_2 U \frac{\partial \Delta}{\partial x} \Delta \frac{\partial^2 \overline{\psi}}{\partial x_j \partial x_j} + C_4 U \frac{\partial \Delta}{\partial x} \Delta^3 \frac{\partial^4 \overline{\psi}}{\partial x_j \partial x_j \partial x_i \partial x_i} + \ldots, \tag{6.18}$$

and

$$U\widehat{\mathcal{C}}^I(\psi) = \widehat{G}'(\Delta|\boldsymbol{\kappa}|)|\boldsymbol{\kappa}| U \frac{\partial \Delta}{\partial x} \widehat{\psi}(\boldsymbol{\kappa}). \tag{6.19}$$

As turbulence convects through a coarsening grid, the commutator affects the variation in all directions to transfer energy in any wavenumber that cannot be represented in the coarse

region of the grid to the subgrid scales. We can clearly see this in the wave packet cases considered above; for the isotropic inhomogeneous grid, equation (6.19) simplifies to

$$U\widehat{\mathcal{C}}^I(\psi) = U\delta(\pi - \Delta_{x_c}|\boldsymbol{\kappa}|)\delta(x - 2\pi)\Delta_{x_c}|\boldsymbol{\kappa}|\widehat{\psi}(\boldsymbol{\kappa}), \tag{6.20}$$

so that modes with $|\boldsymbol{\kappa}| > \pi/\Delta_{x_c}$ are removed at the resolution change. For a smooth grid change, we may expect a similar behavior in the transition region between a fine and coarse grid, namely $U\widehat{\mathcal{C}}^I(\psi) \approx U\delta(\pi - \Delta(x)|\boldsymbol{\kappa}|)\frac{\partial\Delta}{\partial x}|\boldsymbol{\kappa}|\widehat{\psi}(\boldsymbol{\kappa})$. Thus, a model for the commutator would need to have a similar behavior, presumably constructed through a Laplacian or bi-harmonic operator as in equation (6.18). On the other hand, the wave propagation characteristics discussed here suggest commutation error may be reduced by an operator targeted at wavenumbers with negative group velocity in the direction of convection. For instance, explicit filters aimed at reducing discretization error would also aid in reducing commutation error, despite not modeling the actual commutator. Similarly, the subgrid stress may be successful in reducing commutation error despite not representing the actual commutator as it acts strongly on wavenumbers near the cutoff. Resolution inhomogeneity effects in evolving turbulence are explored in the following sections.

6.4.2 Setup

We consider an LES of isotropic turbulence represented on a non-uniform grid in a similar setup to the numerical experiments in sections 3.3 and 6.2.1. To handle the inhomogeneous resolution in this setup, a (significant) modification of the code POONGBACK [124], originally designed for turbulent channel flow, was implemented.

The filtered Navier-Stokes equations are solved using the vorticity-velocity formulation of Kim et al. [128] with periodic boundary conditions and the lower-order numerical implementation described in appendix A. A periodic Bspline collocation representation is used in the

x-direction (allowing for inhomogeneous resolution) and a dealiased Fourier spectral method is used in the y- and z-directions. To separate the issues of resolution anisotropy [17] and inhomogeneity, we consider the convection of turbulence through an inhomogeneous isotropic grid. The Fourier spectral numerics can represent wavenumbers up to $\pi/\max(\Delta_x)$, however, the isotropic grid is constructed in the y- and z-directions by setting the Fourier coefficients of wavenumbers greater than $\kappa_c(x) = \lfloor \pi/\Delta(x) \rceil$ to zero. Further, an isotropic numerical representation is considered by using effective wavenumbers in the y- and z-directions that correspond to the numerics used in the x-direction for the effective resolution of $\Delta(x) = \pi/\kappa_c(x)$ at each x-location. As before, a third-order low storage Runge-Kutta method [127] is used for time advancement.

A negative viscosity forcing f_i is formulated to inject energy at a constant rate of ε, which is active only in the wavenumber range $0 < |\boldsymbol{\kappa}| \leq 2$. To ensure energy is only injected at these low wavenumbers in the x-direction, we compute

$$\hat{u}_i(\kappa_x, \kappa_y, \kappa_z) = \frac{1}{L_x} \int_x \hat{u}_i(x, \kappa_y, \kappa_z) e^{-i\kappa_x x} dx = \sum_j c_j \frac{1}{L_x} \int_x B_{0_j}(x) e^{-i\kappa_x x} dx \tag{6.21}$$

for wavenumbers $|\kappa_x| \leq 2$, where c_j are the B-spline coefficients ($c_j = B_0^{-1} u$), and the integral in equation (6.21) is computed using Gaussian quadrature. The forcing is then computed as $f_i(x, \kappa_y, \kappa_z) = \sum_{\boldsymbol{\kappa}} \hat{f}_i(\boldsymbol{\kappa}) e^{i\kappa_x x}$ and added to the right hand side of the KMM formulation along with the nonlinear terms and the subgrid stress model. For statistically stationary turbulence, ε is also the mean rate of kinetic energy dissipation, which is taken to be $\varepsilon = 1$ here.

The domain length in the y- and z-directions is fixed to 2π. The isotropic resolution is designed to vary as a Sigmoid function between Δ_f and Δ_c over a distance in x of order $1/\alpha$ as in section 6.2.1. The parameters in equation (6.7) will be specified below (see figure 6.13 for example). The same mapping function $g(x)$ is used to define the refining and coarsening

regions of the grid so that there are a total of $2N_\xi$ points in the x direction. The fine region of the grid is generally centered in the domain with the two coarse regions at the ends which are connected through the periodic boundary condition (see figure 6.14).

Two different statistics are reported here. First are one-dimensional energy spectra in y for a fixed x location, defined generally as $E_{1\mathrm{D}}(\kappa_2; x) = \sum_{\kappa_3} \frac{1}{2}\langle \hat{\overline{u}}_i(x, \kappa_2, \kappa_3)\hat{\overline{u}}_i^*(x, \kappa_2, \kappa_3)\rangle$. These one-dimensional spectra provide information about second order statistics through the resolution change, but only in directions orthogonal to the resolution change. Because of the change in resolution, energy spectra in the x-direction are generally unavailable. Therefore, also reported are the time-averaged one-point turbulence structure tensors of Kassinos et al. [198] as a function of x and averaged in the y- and z-directions. In particular, for stream function vectors Ψ'_i defined as $\overline{u}'_i = \epsilon_{its}\partial\Psi'_s/\partial x_t$, we consider the structure tensors

$$R_{ij} = \epsilon_{ipq}\epsilon_{jts}\left\langle \frac{\partial\Psi'_q}{\partial x_p}\frac{\partial\Psi'_s}{\partial x_t}\right\rangle, \qquad D_{ij} = \left\langle \frac{\partial\Psi'_n}{\partial x_i}\frac{\partial\Psi'_n}{\partial x_j}\right\rangle, \qquad F_{ij} = \left\langle \frac{\partial\Psi'_i}{\partial x_n}\frac{\partial\Psi'_j}{\partial x_n}\right\rangle, \qquad C_{ij} = \left\langle \frac{\partial\Psi'_i}{\partial x_n}\frac{\partial\Psi'_n}{\partial x_j}\right\rangle, \tag{6.22}$$

which represent the resolved Reynolds stress tensor, dimensionality tensor, circulicity tensor, and inhomogeneity tensor, respectively. Generally, R_{ij} provides information about the componentality of the turbulence, or anisotropy of the velocity components; D_{ij} provides information about the directionality of the turbulence, or the scale anisotropy; F_{ij} provides information about rotational anisotropy; and C_{ij} provides information about the inhomogeneity of the turbulence[198]. In homogeneous isotropic turbulence, $R_{ij} = D_{ij} = F_{ij} = u'^2\delta_{ij}$ and $C_{ii} = 0$ so we are generally interested in the anisotropy of the structure tensors induced by the resolution inhomogeneity. In the results reported here, the structure tensors are averaged over the same number of eddy-turn over times as the energy spectra. However, there is still a noticeable amount of statistical noise in the y- and z-averaged structure tensors in x-direction. This indicates that more samples may be needed in time to compute the time-average, which will be explored in future work. The general behavior of the structure

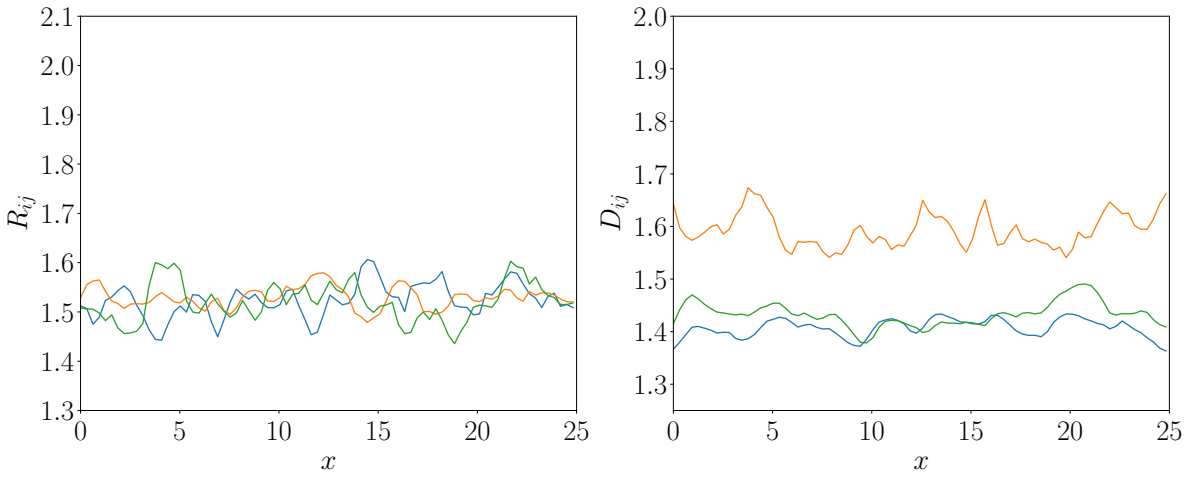

(a) (b)

Figure 6.12: Diagonal components of the one-point structure tensors R_{ij} and D_{ij} averaged in the y- and z-directions as a function of x. Shown are the 11-component (——), the 22-component (——), and the 33-component (——). Both figures correspond to LES of isotropic turbulence computed with a 7th order B-spline collocation method and a mean convection velocity of $U = 0$ on a uniform grid with resolution $\Delta = 2\pi/16$. A Kolmogorov subgrid stress model is used along with the skew symmetric form of the nonlinear terms.

tensors are discussed below. Further, the elongated domain size in the streamwise direction L_x induces an anisotropy in the structure tensors computed here. For instance, consider the one-point structure tensors for turbulence evolving in a uniform grid of resolution of $\Delta = 2\pi/16$ with $L_x = 8\pi$ and $L_y = L_z = 2\pi$ (see figure 6.12). Notably, the anisotropic domain size leads to an increase in the 11-component of D_{ij} (see figure 6.12b). There is a similar decrease in the 11-component of F_{ij} (not shown). Further, note that the velocity components remain isotropic in this setting (see figure 6.12a).

6.4.3 Nonlinear commutation error

The work on the inhomogeneous commutator up to this point has been focused on the effects of mean convection through a change in resolution. It was argued that, since the mean velocity relative to the grid is much larger than the fluctuating velocity in many turbulent flows, it is expected that the commutator for the mean convection term is most important.

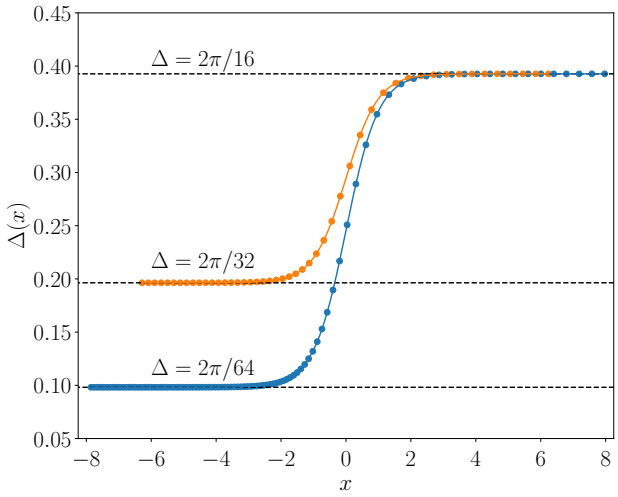

Figure 6.13: Nonuniform grid resolution defined through equation (6.7) with the following parameters: For the —— grid, $\Delta_f = 2\pi/32$, $\Delta_c = 2\pi/16$, $\alpha = 2$, $N_\xi = 48$ and initial condition $g(0) = -2\pi$. This leads to $g(1) = 6.23$, defining a transition region on an interval slightly smaller than 4π with $\max(d\Delta/dx) = 0.09$. See figure 6.14a for a two-dimensional slice of the domain for this grid spacing. For the —— grid, $\Delta_f = 2\pi/364$, $\Delta_c = 2\pi/16$, $\alpha = 2$, $N_\xi = 96$ and initial condition $g(0) = -2.5\pi$. This leads to $g(1) = 7.96$, defining a transition region on an interval slightly larger than 5π with $\max(d\Delta/dx) = 0.14$.

The analysis in chapter 5 seems to support this argument. In the asymptotic limit where $\partial_j\Delta/\partial x_j$ is order $\epsilon \ll 1$, the leading order term of the inhomogeneous commutator for the nonlinear convection term is identically zero (see section 5.4). This result seems intuitively reasonable — for an asymptotically smooth change in resolution, the turbulence evolves slowly enough through the resolution change that no extra forcing (through refining grids) or dissipation (through coarsening grids) is needed, i.e., the commutator is negligible. However, outside of this asymptotic regime, nonlinear commutation error may have a significant effect on the evolution of the turbulence. These effects are explored in this subsection.

Consider first an isotropic inhomogeneous grid with a resolution change from $\Delta_f = 2\pi/32$ to $\Delta_c = 2\pi/16$ defined through equation (6.7) with parameters $\alpha = 2$, $N_\xi = 48$, and initial condition $g(0) = -2\pi$. This leads to $g(1) = 6.23$, defining a coarsening grid on an interval slightly smaller than 4π with $\max(d\Delta/dx) = 0.09$ (see figure 6.13). An LES of isotropic turbulence is computed on this grid with a 7th order B-spline collocation method and the

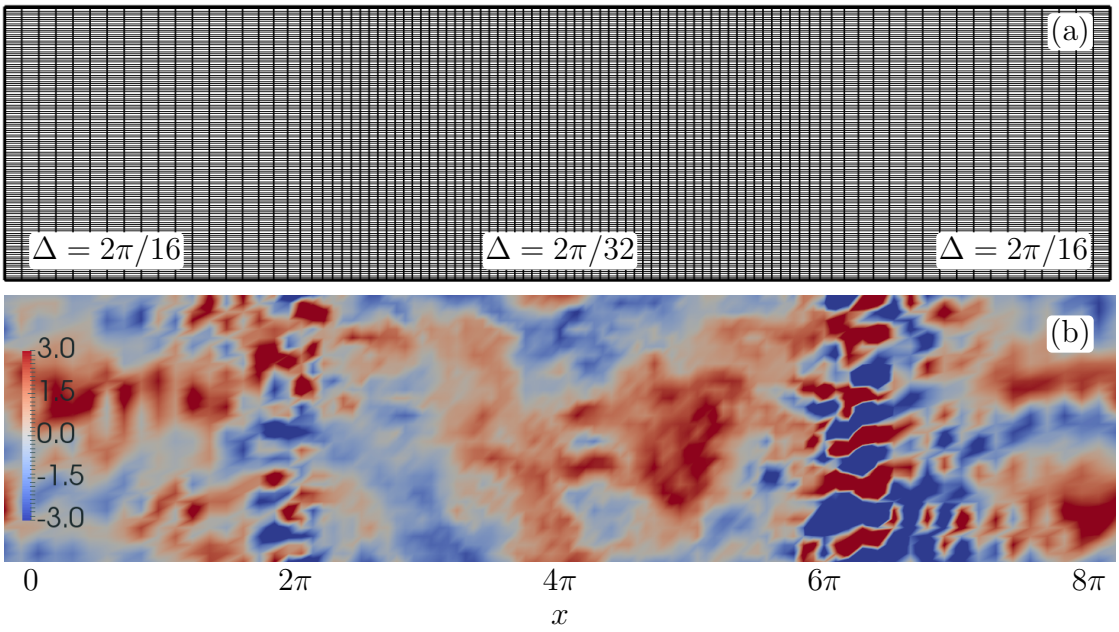

Figure 6.14: Example of the large eddy simulations used to explore commutation error and modeling in homogeneous isotropic turbulence. (a) A two dimensional slice of the numerical grid with resolution varying from $\Delta_f = 2\pi/32$ to $\Delta_c = 2\pi/16$ as defined in figure 6.13. (b) The streamwise velocity for isotropic turbulence computed with a 7th order B-spline collocation method, a mean convection velocity of $U = 0$, the skew-symmetric form of the nonlinear terms, a Kolmogorov subgrid stress model with constant $C = 0.065$, and no explicit filtering or commutation model. The resolution change leads to a numerically instability as shown in the snapshot here, eventually causing the simulation to blow-up.

skew symmetric form of the nonlinear terms. The mean convection velocity is taken to be zero so that turbulent interactions across the resolution change occur only due to nonlinear convection. An LES in this setting with a Kolmogorov SGS model is numerically unstable (see figure 6.14). The resolution change leads to non-physical large scale velocity fluctuations that eventually cause the simulation to blow up (see figure 6.14). However, the same LES with a Smagorinsky SGS model is numerically stable and statistically stationary. This result may highlight an important distinction between fluctuating and non-fluctuating SGS models, namely the ability of former to respond to numerical errors even though the latter is sufficient for producing the correct dissipation rate to the subgrid scales. However note that the response of the Smagorinsky model to numerical errors may be generally incorrect,

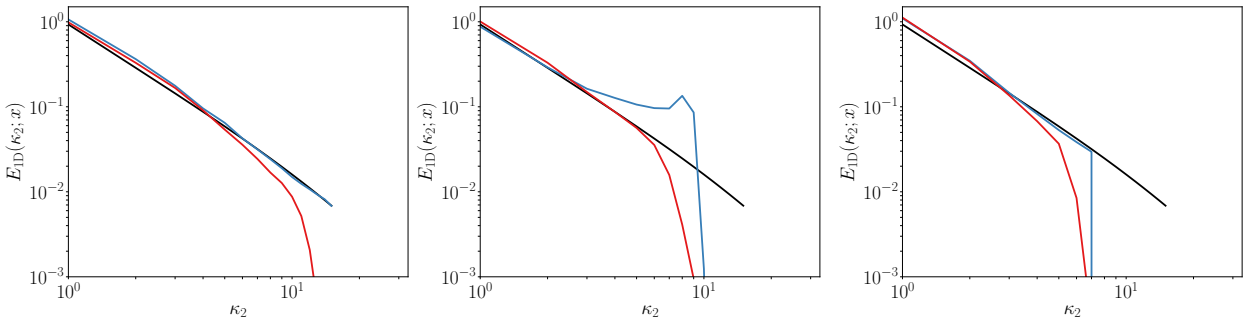

(a) $x = 4\pi$ (b) $x = 6\pi$ (c) $x = 8\pi$

Figure 6.15: One dimensional energy spectra for fixed x locations for the LES of isotropic turbulence computed with a 7th order B-spline collocation method and a mean convection velocity of $U = 0$ on a grid with resolution varying from $\Delta_f = 2\pi/32$ to $\Delta_c = 2\pi/16$ (see figures 6.13 and 6.14). The theoretical spectrum (——); Spectrum computed with a Smagorinsky SGS model with constant $C = 0.14$ and no explicit filtering or commutation model (——); Spectrum computed with a Kolmogorov SGS model with constant $C = 0.065$ and a $B_2 - B_1 B_1$ differential explicit filter (——).

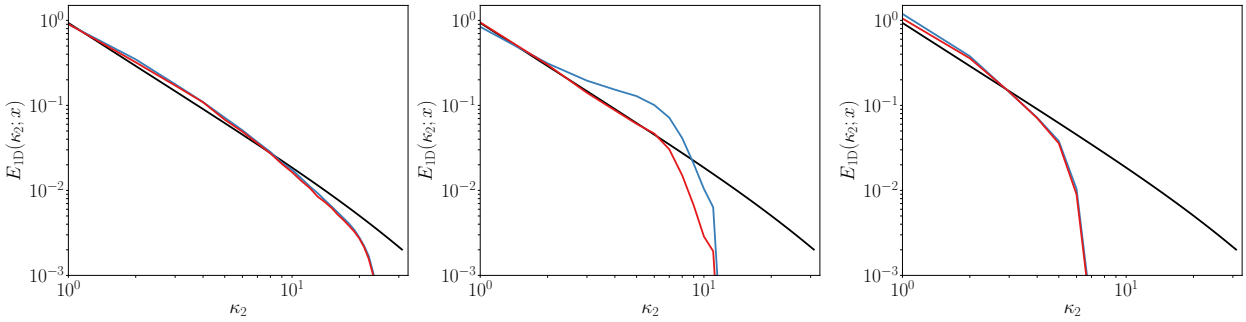

(a) $x = 5\pi$ (b) $x = 7.5\pi$ (c) $x = 10\pi$

Figure 6.16: One dimensional energy spectra at fixed x locations for the LES of isotropic turbulence computed with a 7th order B-spline collocation method and a mean convection velocity of $U = 0$ on a grid with resolution varying from $\Delta_f = 2\pi/64$ to $\Delta_c = 2\pi/16$ (see figure 6.13). The theoretical spectrum (——); Spectrum computed with a Kolmogorov SGS model with constant $C = 0.065$ and a $B_2 - B_1 B_1$ differential explicit filter (——). Spectrum computed with a Kolmogorov SGS model with constant $C = 0.065$, a $B_2 - B_1 B_1$ differential explicit filter, and nonlinear commutation model equation (6.23). (——).

as is the case here. As the sole subgrid scale model in this setting, the Smagorinsky model is essentially overburdened with statistical properties of the flow to represent. We find that a constant eddy viscosity model (for the dissipation rate) paired with appropriate explicit filters and models (for addressing numerical effects) perform well in the LES here (see below),

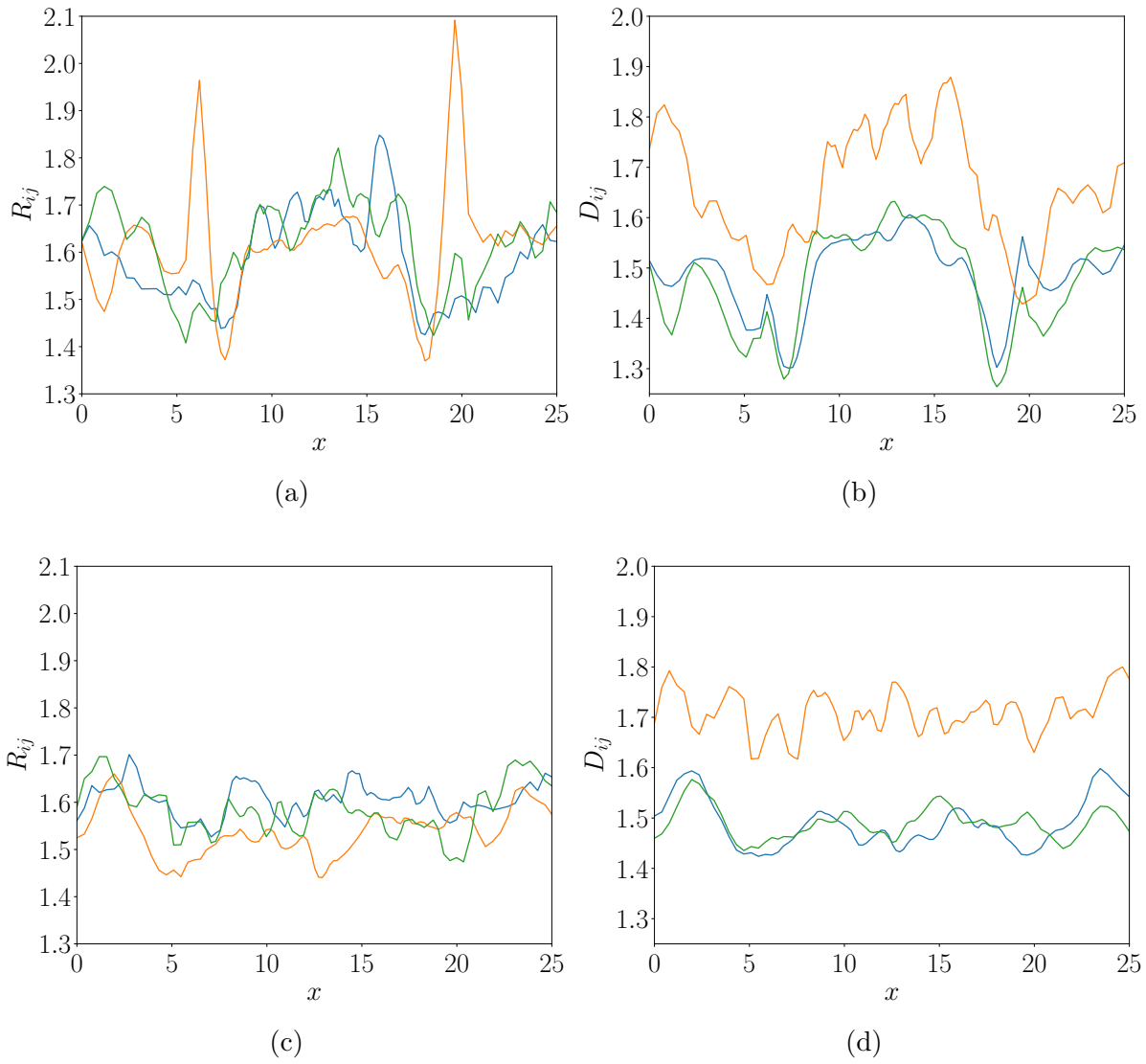

Figure 6.17: Diagonal components of the one-point structure tensors R_{ij} and D_{ij} averaged in the y- and z-directions as a function of x. Shown are the 11-component (——), the 22-component (——), and the 33-component (——). All figures correspond LES of isotropic turbulence computed with a 7th order B-spline collocation method and a mean convection velocity of $U = 0$ on a grid with resolution varying from $\Delta_f = 2\pi/32$ to $\Delta_c = 2\pi/16$ (see figures 6.13 and 6.14). Figures (a) and (b) are the structure tensors for LES computed with a Smagorinsky SGS model with constant $C = 0.14$ and no explicit filtering or commutation model, corresponding to the spectra in figures 6.17a and 6.17b. Further, the trace of the structure tensors in this case are $R_{ii} = 1.6110$, $D_{ii} = 1.5502$, $F_{ii} = 1.5502$ and $C_{ii} = 0.0007$. Figures (c) and (d) are the structure tensors for LES computed with a Kolmogorov SGS model with constant $C = 0.065$ and a $B_2 - B_1 B_1$ differential explicit filter, corresponding to the spectra in figures 6.17c and 6.17d). Further, the trace of the structure tensors in this case are $R_{ii} = 1.5734$, $D_{ii} = 1.5692$, $F_{ii} = 1.5692$ and $C_{ii} = 0.0001$.

although a more thorough investigation of fluctuating eddy viscosities is worthwhile.

The Smagorinsky model results allow us to investigate the statistical effects of nonlinear commutation error. In both the fine and coarse regions of the domain, the LES successfully reproduces a theoretical $\kappa^{-5/3}$ spectrum (see figures 6.15a and 6.15c). However, in the region of resolution change, a significant pile up of energy occurs in all y- and z-modes outside of the forcing regime (see figure 6.15b). The most significant increase in energy occurs in the streamwise velocity component where $d\Delta/dx$ is largest (see figure 6.17a). There is a similar increase in energy in the large x-directional wavenumbers near the resolution change (see figure 6.17b near $x = 20$ for example). The inhomogeneous resolution is introducing nonlocal wavenumber interactions, similar to those in mean convection case, resulting in a nonphysical transfer of energy between small and large scales near the resolution change. In general, the effects of nonlinear convection through a nonuniform grid can be particularly damaging in LES of turbulent flows and must be addressed. Presumably, the same type of energy pile up observed here was more severe for the Kolmogorov model simulation mentioned above leading to the numerical instability.

The highly dispersive modes are particularly damaging in this setting because of their interaction with the large scales through the resolution change. Recall that these dispersive scales were not markedly harmful in the uniform resolution $U = 0$ cases, but we noted their potential danger in more complex flows. Therefore, it may be useful to use an explicit filter to remove the small-scale velocity fluctuations. Consider a $B_2 - B_1 B_1$ differential filter aimed at removing scales past the apex wavenumber κ_a ($\alpha = 2$ in equation (3.36)) applied to the nonlinear terms in the LES described above. A Kolmogorov SGS model is used now with characteristics length scale π/κ_a. For the 7th order B-spline collocation method used here, $\kappa_a \Delta/\pi \approx 0.8$ (see figure 3.1). The explicit filter avoids any numerical instabilities and successfully reduces large scale energy pile ups throughout the domain (see figure 6.15). The energy spectrum follows a theoretical $\kappa^{-5/3}$ spectrum as scales populate from the coarse to

fine resolution regions and vise-versa (see figures 6.15a to 6.15c). Moreover, the explicit filter significantly reduces wavenumbers passed κ_a throughout the entire domain (see figure 6.15). Notably, the velocity components are isotropic in this case, avoiding the large energy spikes in the streamwise velocity seen before (see figure 6.17c). Similarly, the model leads to the correct behavior of the dimensionality tensor D_{ij} (see figure 6.17d), avoiding large-scale energy pile-ups near the resolution change.

In addition to dispersive errors, nonlinear convection may also result in well-resolved turbulent fluctuations convecting into a region of the grid in which they can no longer be represented. In certain cases a model for the inhomogeneous commutator may be needed for these commutation effects as well as an explicit filter for the dispersive modes. For instance, suppose we increase the resolution change by a factor of 2 from the previous simulation. Now, the inhomogeneous grid transitions from $\Delta_f = 2\pi/64$ to $\Delta_c = 2\pi/16$, defined through equation (6.7) with parameters $\alpha = 2$, $N_\xi = 96$, and initial condition $g(0) = -2.5\pi$. This leads to a coarsening grid on an interval slightly larger than 5π with $\max(d\Delta/dx) = 0.14$ (see figure 6.13). In this case, an LES with either a Kolmogorov or Smagorinsky SGS model is numerically unstable without an explicit filter. Further, using the $B_2 - B_1 B_1$ explicit filter from above without a model for the commutator leads to excess energy in the spectrum through the transition region (see figure 6.16). Since the leading order term of the nonlinear inhomogeneous commutator is zero in the multiscale analysis, we base the model for the commutator on the linear term with a characteristic velocity u_{rms} instead of U, e.g.,

$$\mathcal{C}_i^I(u_i u_j) = C u_{rms} \Delta \left| \frac{d\Delta}{dx} \right| \frac{\partial^2 \overline{u}_i}{\partial x_j \partial x_j}. \tag{6.23}$$

Hyperviscosity models may also be considered as in section 6.3. Interestingly, the statistical analysis of the commutator in the linear case provides a good constant for the model in equation (6.23). Specifically, by applying equation (5.42) to a Kolmogorov spectrum, the

constant can be set so that the commutation model provides the correct dissipation rate through a coarsening grid a priori, i.e.,

$$\begin{aligned} C_{kol}\varepsilon^{-2/3}\kappa_c^{-5/3}U\frac{\partial \kappa_c}{\partial x_j} &= C\pi^2\kappa_c^{-3}U\frac{\partial \kappa_c}{\partial x_j}\int_{\mathcal{D}}\widetilde{\kappa_j\kappa_j}\frac{1}{2}\Phi_{ii}(\boldsymbol{\kappa})d\boldsymbol{\kappa} \\ &= \frac{1}{4}C_{kol}\varepsilon^{2/3}C\pi\kappa_c^{-3}U\frac{\partial \kappa_c}{\partial x_j}\int_{\mathcal{D}}\widetilde{\kappa_j\kappa_j}|\boldsymbol{\kappa}|^{-11/3}d\boldsymbol{\kappa}. \end{aligned} \tag{6.24}$$

Solving for C in equation (6.24) gives $C \approx 0.14$, which leads to an energy spectrum that follows a theoretical $\kappa^{-5/3}$ spectrum as scales populate from the coarse to fine resolution regions and vise-versa (see figure 6.16). The behavior of the structure tensors in these two cases are similar to those in figure 6.17 (not shown). Further, we note that using the local velocity fluctuations instead of u_{rms} in equation (6.23) leads to a similar spectrum as in figure 6.16.

Lastly, we note that the nonlinear commutation errors reported here seem to worsen as the order of the underlying numerical scheme increases. For instance, there are no observed commutation errors in the $\Delta = 2\pi/32 \rightarrow 2\pi/16$ LES considered above for a 2nd order B-spline representation, even with a constant eddy viscosity model and no explicit filters. However, as $d\Delta/dx$ increases, similar types of errors are observed in the spectrum. One reason for this may be that the nonlinear convection of the dispersive modes occurs on velocity-scales that are much faster than, say, the characteristic velocity-scale of the turbulence (e.g., the rms-velocity), because of large negative group velocities in the higher order numerics cases. This results in a faster energy transfer rate from small to large scales through the resolution change. For lower order numerics, the SGS model and/or explicit filters therefore have more time to dissipate the small scale fluctuations before they convect through the resolution change, reducing commutation effects and avoiding energy piles up in the larger scales. This behavior was confirmed experimentally through a frozen-field study of a 'packet' of dispersive modes convecting in a stationary turbulent field through a coarsening grid.

6.4.4 Linear commutation error

Commutation error arising from linear convection was studied in section 6.2 for the case of a localized packet of turbulent fluctuations under the Taylor frozen field hypothesis. This was useful for exposing effects of commutation error in absence of other turbulence processes. However, equally important is to characterize these commutation effects in evolving three-dimensional turbulence. To do so, consider an LES computed on an isotropic inhomogeneous grid with a resolution change from $\Delta_f = 2\pi/64$ to $\Delta_c = 2\pi/16$ defined through equation (6.7) with parameters $\alpha = 4$, $N_\xi = 72$, and initial condition $g(0) = -1.875\pi$. This leads to $g(1) = 5.75$, defining a coarsening grid on an interval slightly smaller than 3.75π with $\max(d\Delta/dx) = 0.27$ (see figure 6.18a and figure 6.19f). The differential operators are represented with a second-order centered difference method and the skew-symmetric form of the nonlinear terms are computed. A Kolmogorov SGS model is used with $C = 0.065$. Lastly, the mean convection velocity is taken to be $U = 5$, which is roughly four-times larger than the rms-velocity.

As resolved turbulent fluctuations convect through the downstream resolution change, the energy in modes that cannot be represented in the coarse resolution region is transferred to modes that propagate upstream through the fine resolution region. These erroneous reflections are clearly visible in the streamwise velocity near the downstream resolution change (see figure 6.18b). Further, the discussion in section 6.4.1 indicates that this energy transfer occurs between modes $(\kappa_{x_1}, \kappa_y, \kappa_z)$ and $(\kappa_{x_2}, \kappa_y, \kappa_z)$ where $\tilde{\kappa}_{x_1} = \tilde{\kappa}_{x_2}$ and $\kappa_{x_2} > \pi/2\Delta_f$. This result is crucial for interpreting the flow statistics here. The large increase in the dimensionality tensor in the fine region is indicative of the erroneous reflections propagating backwards through the fine region (see figure 6.20b). Further, the energy spectra for all wavenumbers in the y- and z-directions experience a vertical shift upwards throughout the fine region, which increases towards the downstream resolution change (see figures 6.19c to 6.19e). This behav-

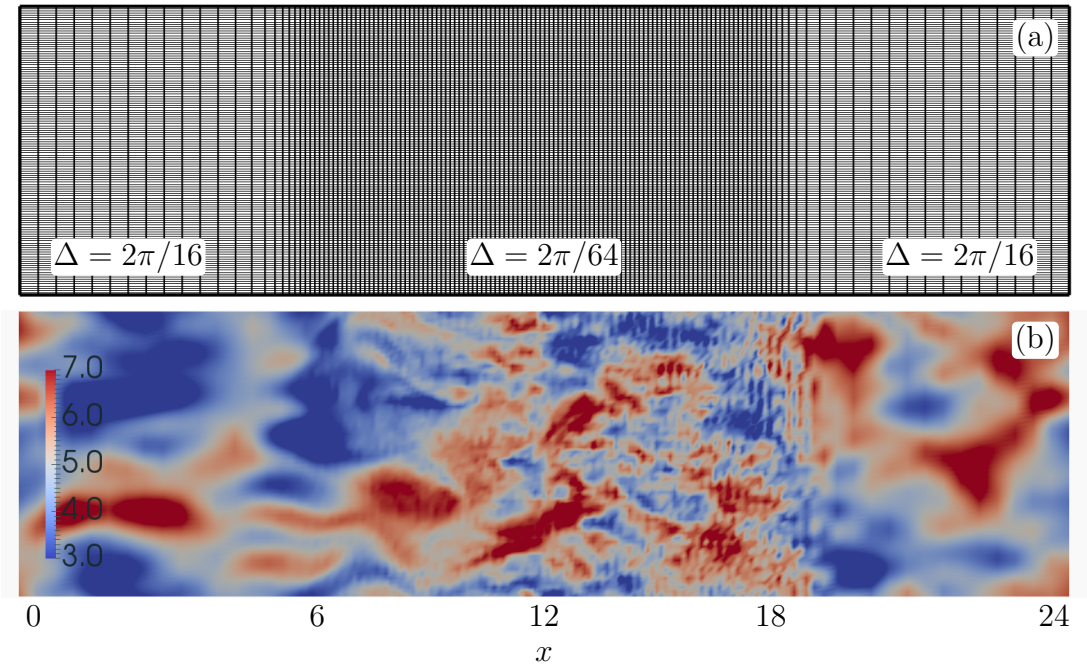

Figure 6.18: Two-dimensional slice of the large eddy simulation computed with a second-order centered difference method, the skew-symmetric form of the nonlinear terms, a Kolmogorov SGS model, and a mean convection velocity of $U = 5$. (a) The numerical grid with resolution varying from $\Delta_f = 2\pi/64$ to $\Delta_c = 2\pi/16$ (see figure 6.19f). (b) The streamwise velocity.

ior is consistent with the observation that y- and z-directional wavenumbers remain constant through the energy transfer process induced by resolution inhomogeneity. In other words, the energy spectra and dimensionality tensor indicate that large x-directional wavenumbers are carrying energy backwards through the fine region in scales with the same y- and z-wavenumber components as before the interaction with the downstream resolution change. Similarly, the energy in all velocity components significantly increases near the downstream resolution change (see figure 6.20a). Only far from downstream resolution change is the LES able to reproduce a theoretical $\kappa^{-5/3}$ spectrum (see figures 6.19a and 6.19b).

There are more considerations in designing an LES to expose linear commutation effects than the nonlinear case. First, for large U, mean dispersion effects will shut down the energy transfer in the direction of convection from large to small scales (see section 3.3). This can

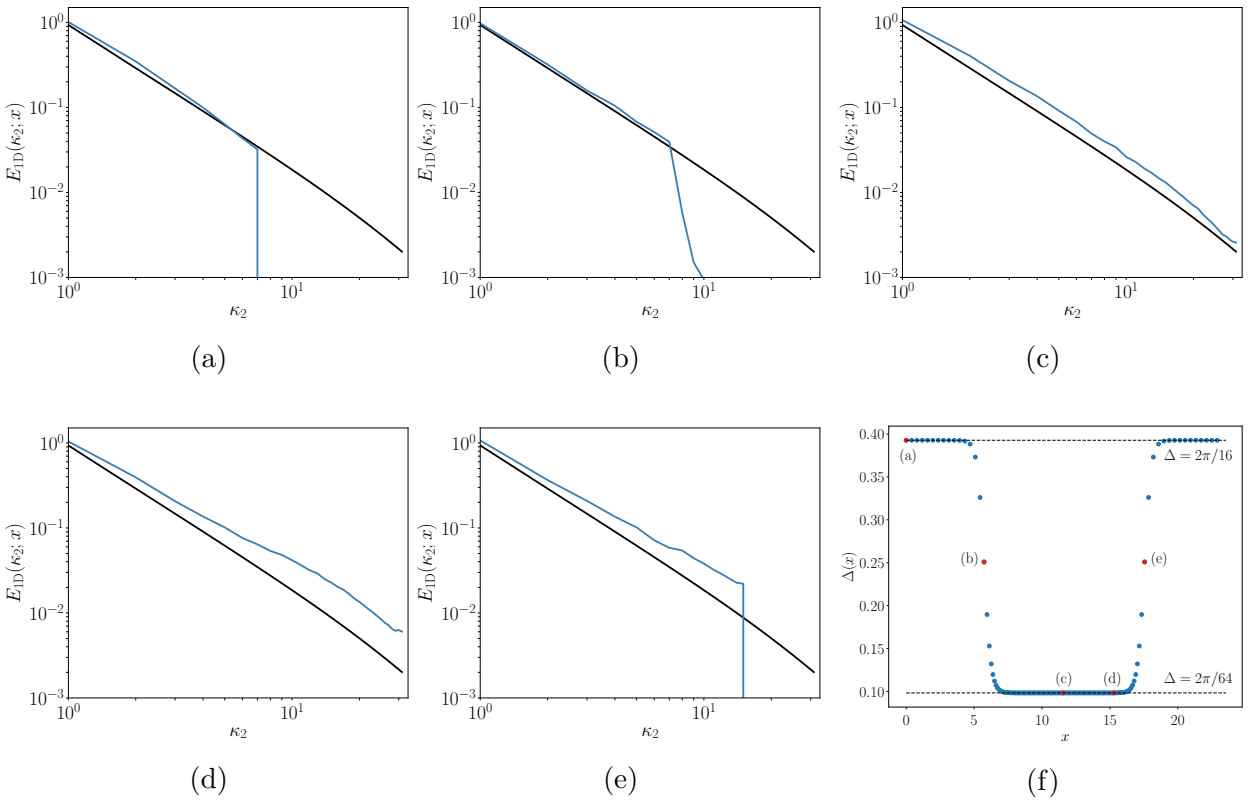

Figure 6.19: One dimensional energy spectra at fixed x locations for the LES of isotropic turbulence computed with 2nd-order centered difference numerics and a mean convection velocity of $U = 5$. In (a)-(e) —— are the computed spectra, and —— are the theoretical spectra. The resolution varies from $\Delta_f = 2\pi/64$ to $\Delta_c = 2\pi/16$ as shown in (f). Also shown in (f) are the x-locations for the energy spectra in (a)-(e).

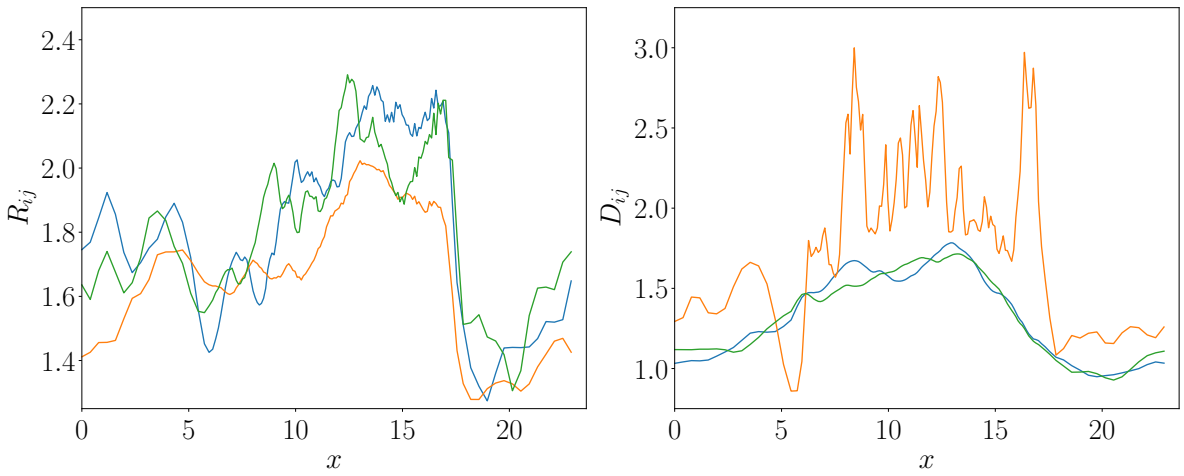

(a) (b)

Figure 6.20: Diagonal components of the one-point structure tensors R_{ij} and D_{ij} averaged in the y- and z-directions as a function of x. Shown are the 11-component (——), the 22-component (——), and the 33-component (——). Both figures correspond to LES of isotropic turbulence shown in figure 6.18.

significantly reduce commutation error because not all the scales that can be represented in the fine region will be populated upon interaction with the resolution change. Thus, U was chosen here to be larger than u_{rms} so that linear commutation error dominated nonlinear commutation error, but small enough so that mean dispersion error had little effect on the energy cascade. Second, since there is no active forcing as the turbulence convects through the refining resolution (see chapter 7), the length of the fine region must be long enough to allow the energy cascade to populate the small scales in the fine region. Presumably, this length is related to the scaling

$$L \sim U \int_{\kappa_c^{\text{coarse}}}^{\kappa_c^{\text{fine}}} E(\kappa) d\kappa \Big/ \varepsilon = U \frac{3}{2} C_{kol} \varepsilon^{-1/3} \left(\kappa_c^{\text{coarse}} - \kappa_c^{\text{fine}} \right), \tag{6.25}$$

where $\kappa_c^{\text{coarse}} = \pi/\Delta_c$ and $\kappa_c^{\text{fine}} = \pi/\Delta_f$. This was roughly used to inform the parameters for equation (6.7) listed above. Lastly, the effects of the order of the numerics are important. For the second-order centered difference case, the 'reflections' occur at relatively large scales,

(up to $\kappa_c^{\text{fine}}/2$) and propagate at a speed equal to or less than the mean convection velocity. Thus, the reflections are particularly damaging near the downstream boundary — interacting with and contaminating the well-resolved turbulence in the fine region. However, for higher order numerics, the reflections propagate at a speed much larger than U (up to $7U$ for 7th-order B-splines for example) and occur at much smaller scales in the x-direction than the lower order numerics cases. Thus, the linear commutation error for these higher order numerics cases are also particularly damaging at the upstream resolution change (notice this was not the case above as shown in figure 6.19b). The small scale reflections reach the upstream resolution extremely quickly when compared to the mean velocity, at which point the energy is transferred to the large scales in the coarse region, often resulting in a numerical instability similar to figure 6.14b. For these reasons, second-order numerics were chosen here to investigate the statistical properties of commutation error in stationary turbulence.

Although the setup in this section is useful for demonstrating the effects of commutation error and dispersion error in LES, it is not well-suited to explore LES modeling. This is because second-order centered difference numerics cannot accurately represent the dynamics of enough resolved scales for the LES to be meaningful. Either much finer resolution or higher order numerics are needed instead. Higher order numerics can introduce additional modeling challenges, as indicated above, because the reflections propagate at a velocity scale that is much larger than the mean velocity. Moreover, particularly sharp grid changes, such as the one used here, combined with large mean velocities may not give commutator models based on the resolution gradient enough time to remove the energy in scales that cannot be resolved in the coarse region. We expect the developments in explicit filtering and commutation modeling in this thesis will be useful for addressing linear commutation error, however, more work is needed to formulate a robust commutation model applicable to a wide range of LES scenarios.

6.5 Conclusion

Practical LES of high Reynolds number turbulent flows often requires inhomogeneous resolution. The inhomogeneous part of the commutator $\mathcal{C}^I$ is responsible for transferring energy between resolved and unresolved scales as a consequence of the resolution inhomogeneity, and so it must be modeled. However, $\mathcal{C}^I$ is often ignored in practice leading to commutation error. In chapters 5 and 6, we investigate the commutator and corresponding commutation error as related to filters that include a discrete projection.

The impact of the commutation error that occurs as turbulence convects through coarsening grids is governed by the propagation properties of the underlying numerics (see section 6.1). For many conservative numerical schemes such as those considered here, the energy in newly unresolvable scales is unphysically transferred to higher wavenumbers in the fine region of the grid, instead of to the subgrid scales in the coarse region of the grid. The result is a non-physical reflection of unresolvable scales back into the fine region of the grid at higher wavenumbers with negative group velocities. The nonlocal energy exchange in wavespace introduced by resolution inhomogeneity is especially problematic in LES of turbulence where the energy cascade occurs primarily between local wavenumbers [169]. This was demonstrated for both nonlinear and linear commutation error in LES of isotropic turbulence.

The statistical analysis of the commutation term $\mathcal{C}^I$ developed in chapter 5 yields a quantitative measure of the magnitude of $\mathcal{C}^I$ and therefore how important it is to model, as a function of the resolution gradient and the convection velocity. Furthermore, a commutator model can be formulated to match important statistical features of the commutator *a priori*, such as its spectrum. For example, the dependence of the commutator spectrum on the derivative of the Fourier transformed filter kernel shows that a commutator model should act at the high wavenumbers over which the filter rolls off. Similarly, the parameters in

a model of the commutator can be calibrated to match known statistical characteristics *a priori* (e.g., evaluating (5.41) for a Kolmogorov spectrum). This was found to be effective in modeling the nonlinear part of the inhomogeneous commutator (see section 6.4.3). It is important to consider the statistical characteristics of the commutation term because *a priori* consistency of certain statistical characteristics of an LES model is a necessary condition for accurate *a posteriori* statistics of an LES solution [187, 1].

The series approximation of $\mathcal{C}^I$ from section 5.4, is also useful for informing commutation models, despite the fact that this analysis is formally only applicable to invertible filters. In particular, (5.39) shows that asymptotically, the commutator is expressible in terms of even derivatives of the filtered field, is proportional to the resolution gradient and proportional to the convection velocity. This places significant constraints on any operator intended to model the commutator. Furthermore, when applied to inertial range turbulence, the fact that all the terms in the series (5.39) are of the same asymptotic order implies that high order derivatives of the filtered field are as important as low order derivatives, suggesting that practical models expressed in terms of derivatives of the filtered field should include derivatives of as high an order as feasible. Indeed, this observation motivated the formulation of the model proposed in section 6.3. The asymptotic ordering of the terms in (5.39) also suggests that using "commuting filters" whose low-order moments vanish, which has often been proposed based on the analysis of [22], is not sufficient to make the commutator negligible. This is not to say that explicit filters are not useful for other purposes, such as eliminating energy in scales with negative group velocity due to numerical dispersion, which will also mitigate the effects of commutation error.

Finally, the commutator modeling pursued here has focused on the case when the turbulence flows from fine resolution to coarse resolution. However, the other situation (flowing from coarse to fine resolution) is also of interest. Modeling $\mathcal{C}^I$ in this case is challenging because resolved fluctuations must be created. Models based on negative dissipation [22] and

forcing [99], have been proposed, but more work is required. As in the coarsening resolution case, the analysis in chapter 5 may be useful in developing an appropriate model. This is explored in the following chapter.

Chapter 7

Wavelet-based forcing of turbulence through refining grids

The previous chapter was focused on commutation errors that arise as turbulence convects through coarsening grids because of the inherent numerical inconsistency issues. However, as indicated by the analysis in chapter 5, the inhomogeneous commutator is also responsible for injecting energy into the turbulence as it convects through refining grids. A model for the commutator must therefore force the resolved scales that become newly-representable as turbulence convects from a coarse to fine resolution region.

It is clear that injecting energy into the resolved scales is required for the refining resolution case to maintain consistency with the definition of the filter in an LES, however, the effect of neglecting the commutator in this case, i.e., commutation error, is less obvious than for coarsening grids. This is in part due to the fact that the energy cascade will naturally populate additional finer scales of motion as they become representable. To motivate the need for forcing in this case, we briefly mention a result from Haering et al. [99], who were interested in hybrid RANS/LES turbulence models. Hybrid RANS/LES modeling exhibits several unique complications — in addition to inheriting the challenges of both LES and RANS — many of which are beyond the scope of the work here. However, hybrid RANS/LES applications provide a particularly useful setting for examining the effects of resolution inhomogeneity as there are often sharp transitions to/from RANS and LES regions in the domain. For instance, we expect the numerical issues discussed in chapter 6 to be especially damaging in hybrid RANS/LES as turbulence convects from an LES to

RANS region, since no turbulence fluctuations can be resolved in the RANS regions of the domain. For refining grids, Haering et al. [99] showed that reliance on the passive generation of resolved turbulence results in the well-known phenomenon of model stress depletion [199, 200, 201], which causes several common errors such as log-layer mismatch, reduced body forces, premature flow separation, and delayed flow reattachment [99]. Further, Haering et al. [99] demonstrated that explicitly introducing resolved fluctuations through refining grids avoids many of these issues. Thus, we may expect that even in LES, the coarse-to-fine transition will require forcing to accurately represent the flow statistics. In this chapter we explore the properties of a forcing formulation and propose an approach based on the use of divergence-free wavelets to circumvent some of the issues with the forcing scheme in [99].

7.1 The active-model-split forcing formulation for isotropic turbulence

The active-model-split (AMS) forcing formulation proposed by Haering et al. [99] relied on three ingredients, which they describe as: 1) the identification of regions where more turbulence can be resolved, 2) determination of the rate at which resolved fluctuations should be introduced, and 3) specification of the structure of the generated velocity fluctuations. Each of these components are recalled briefly here for the simple case of isotropic turbulence with periodic boundary conditions.

First, the resolution capacity of the grid is described by the resolution tensor $\mathcal{M}_{ij}$, which in the simple case considered here is simply $\Delta\delta_{ij}$. It is worth noting that the resolution properties of lower-order numerics are not taken into account here, which would characterize an effective resolution capacity of the discretization. To separate the issues of forcing and numerical discretization error, we will therefore only consider Fourier-spectral numerics, although the results in [99] generally relied on a 2nd-order finite volume method. More

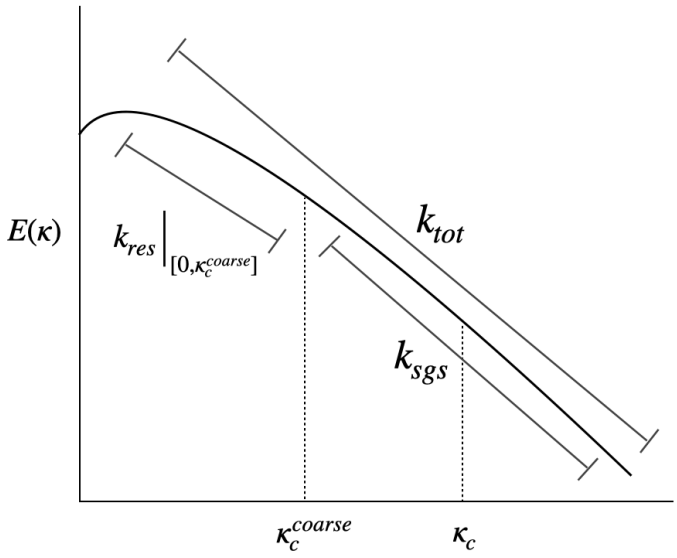

Figure 7.1: Estimates of k_{res}, k_{tot} and k_{sgs} based on a known energy spectrum $E(\kappa)$ for a refining grid.

turbulence can be resolved when the largest unresolved scale is larger than the scales that can be represented on the grid. A length scale measure for the largest unresolved scale of the turbulence is given by $\mathcal{L}_{sgs} = k_{sgs}^{3/2}/\varepsilon$, where k_{sgs} is the subgrid kinetic energy, analogous to the expression for the usual integral length scale of turbulence. Therefore, when the resolution indicator $\rho = \Delta/\mathcal{L}_{sgs} < 1$, the grid is locally capable of resolving smaller scale fluctuations. There are several ways in which k_{sgs} can be computed. In [99], a transport equation for the total turbulent kinetic energy k_{tot} appears as part of the RANS equations, so k_{sgs} can be estimated through k_{tot} and k_{res}, where k_{res} is the resolved turbulent kinetic energy. In the simple case of isotropic turbulence considered here, k_{sgs} can be estimated by integrating the energy spectrum. In particular, we compute

$$k_{tot} = k_{res}\big|_{[0,\kappa_c^{coarse}]} + \int_{\kappa_c^{coarse}}^{\infty} E(\kappa)d\kappa \tag{7.1}$$

where $k_{res}\big|_{[0,\kappa_c^{coarse}]}$ is the resolved kinetic energy up to the coarse wavenumber cutoff (see figure 7.1) and $E(\kappa)$ is a Kolmogorov spectrum. Then $k_{sgs} = k_{tot} - k_{res}$.

Second, the spatial structure of the acceleration field used to force the turbulence must be specified. In [99], an "artificial turbulence-like vortex field is defined based on the structure of a Taylor-Green vortex field with variable length scale", i.e.,

$$h_i(\mathbf{x},t) = \begin{cases} A\cos(\kappa_1 x_1^p)\sin(\kappa_2 x_2^p)\sin(\kappa_3 x_3^p) \\ B\sin(\kappa_1 x_1^p)\cos(\kappa_2 x_2^p)\sin(\kappa_3 x_3^p) \\ C\sin(\kappa_1 x_1^p)\sin(\kappa_2 x_2^p)\cos(\kappa_3 x_3^p) \end{cases} \tag{7.2}$$

where the magnitudes are chosen arbitrarily as $A = 1$, $B = -1/3$, and $C = -2/3$. The vortex scale is taken to mimic the local length scale where extra turbulence fluctuations are needed, i.e., $\kappa_i \sim \pi/L_{SGS}$ (with proportionality constant empirically set to 8). The Taylor-Green vortices are specified to translate with the mean flow as $x_i^p(x,t) = x_i - U_i t$.

Lastly, the magnitude of the forcing acceleration must be specified, which is related to the timescale that added turbulent fluctuations are "healed" into realistic turbulence. Dimensional analysis based on the eddy turnover time of the smallest resolved scales gives $F_{mag} = C_F\sqrt{k_{sgs}}/T_{sgs}$ where $T_{sgs} = k_{sgs}/\varepsilon$. Gradual attenuation of the forcing is prescribed through the resolution indicator via $F_\rho = -\tanh(1 - \min(\rho,1)^{-1/2})$ so that the forcing is activated when $\rho < 1$ and F_ρ goes to zero near $\rho \approx 1$. Finally, a clipping procedure is used so that the forcing always adds energy to the system so that the forcing field is generally

$$F_i^{\text{AMS}} = \begin{cases} F_{mag}F_\rho h_i & h_i u_i \geq 0 \\ 0 & \text{otherwise} \end{cases}. \tag{7.3}$$

The AMS formulation for the forcing described here was motivated by several desirable properties for a forcing field F_i. First, the forcing should add energy to the system, at least on average. This is enforced in the AMS formulation by clipping points with negative energy injection rate. Second, for incompressible turbulence, the forcing should be divergence free.

This was the *motivation* for using a forcing structure based on divergence free Taylor-Green vortices. Third, the energy injection rate $F_i u_i$ should be specifiable. And fourth, the forcing should ideally only force turbulence at scales near a specified length scale (L_{sgs} for example), as to not corrupt any meaningful resolved turbulence in the process.

All four of these considerations were appreciated in formulating the AMS forcing; however, its current form is rather rudimentary leading to several drawbacks. The most obvious issue is that the forcing field F_i is not in fact divergence free. The Taylor-Green structure is only divergence free when constructed using a uniform overall scaling and vortex length scale. The energy injection rate is therefore uncontrollable, as the divergence free projection will distort the properties of the forcing. Additionally, the forcing structure is not actually localized in wavespace in any sense, so it may effect the entire range of resolved scales. The clipping procedure worsens both of these issues as it introduces discontinuities in the forcing field.

7.2 A divergence-free wavelet construction for the forcing field

As Haering et al. [99] note, developing a better forcing formulation should allow one to force the turbulence more strongly, better preserve the well-resolved turbulence, and allow for sharper grid transitions to finer resolved LES regions. The most fundamental issue with the AMS forcing formulation lies in its structure. The forcing must be divergence free and also provide a degree of localization in both realspace and wavespace. Without satisfying these criteria, one cannot hope to control the energy injection rate or maintain the well-resolved turbulence. To provide a degree of localization in both realspace and wavespace, we propose the use of a divergence free wavelet basis for the construction of the forcing field.

Wavelets are functions ψ that are localized in both realspace and wavespace that satisfy

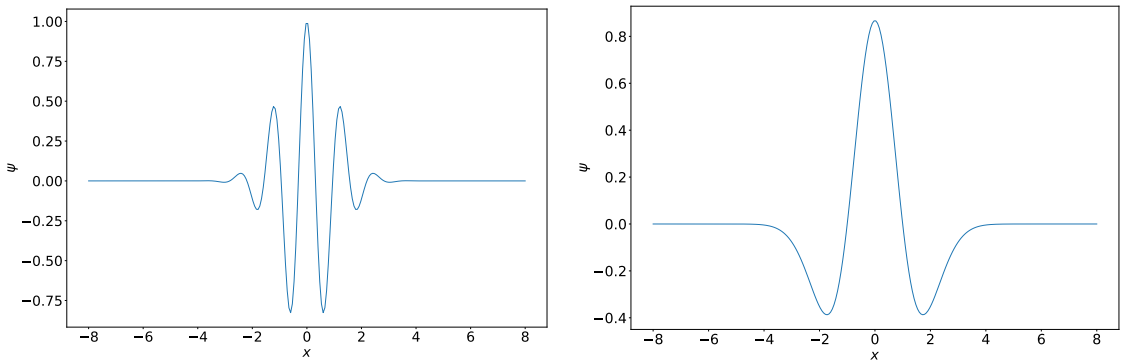

(a) Real morlet wavelet

(b) Mexican hat wavelet

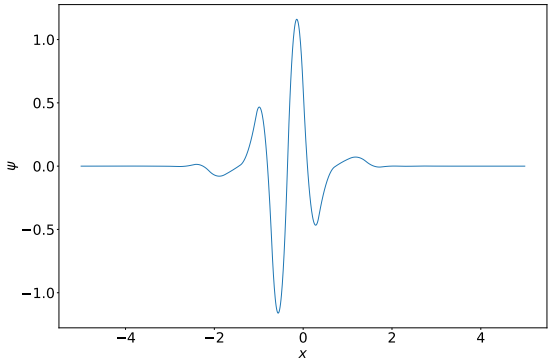

(c) Battle-Lemarie wavelet

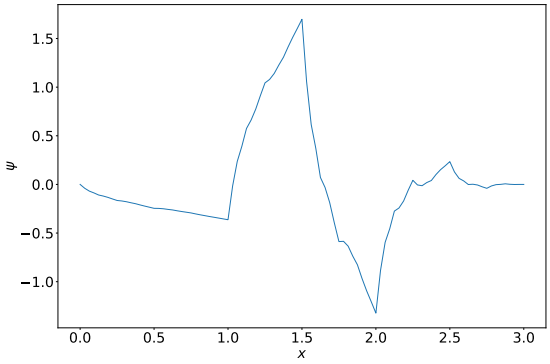

(d) Daubechies wavelet

Figure 7.2: Example of a real morlet wavelet, a Mexican hat wavelet, a Battle-Lemarie wavelet constructed with second order B-splines, and a Daubechies wavelet of order 2.

the admissibility condition

$$C_\psi = \int |\boldsymbol{\kappa}|^{-1} |\hat{\psi}(\boldsymbol{\kappa})|^2 d\boldsymbol{\kappa} < \infty. \tag{7.4}$$

Common wavelet functions include: *Mexican hat wavelets*, which are related to the second derivative of a Gaussian function; *Morlet wavelets*, which are simply a complex exponential function multiplied by a Gaussian window; *Battle-Lemarie wavelets*, which are constructed from varying orders of B-spline functions; and *Daubechies wavelets*, which are defined in terms of functions with a maximal number of vanishing moments for a given support (see figure 7.2). The choice of wavelet function is often dependent on the particulars of an application, as they

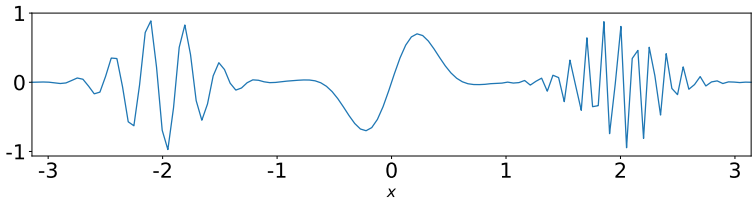

(a) Original signal in realspace

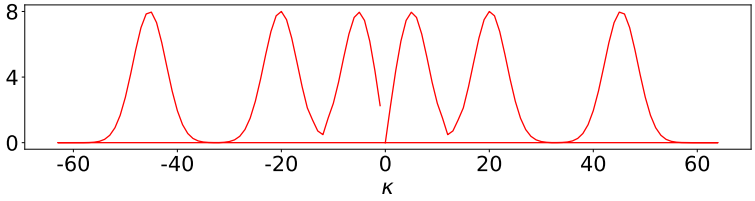

(b) Fourier transform of signal

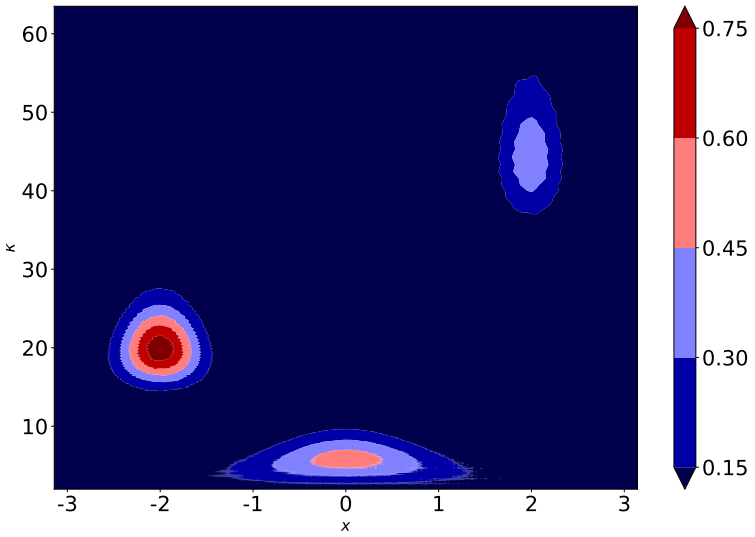

(c) Wavelet transform of signal

Figure 7.3: (a) The original signal in wavespace given by $f(x) = \sin(45x)e^{(-5(x-2)^2)} + \sin(5x)e^{(-5x^2)} + \sin(20x)e^{(-5(x+2)^2)}$. (b) The Fourier-transform of the signal. (c) The power spectrum of the wavelet transform of $f(x)$ generated with complex morlet wavelets.

each have different properties that may be more or less desirable. The continuous wavelet transform (CWT) represents a function $f(x)$ at *scale* $a \in \mathbb{R}^+$ and translational value $b \in \mathbb{R}$ by

$$W_f(a,b) = C_\psi^{-1/2} a^{-1/2} \int_{-\infty}^{\infty} f(x)\psi^* \left(\frac{x-b}{a}\right) dx. \tag{7.5}$$

For example, consider the function $f(x) = \sin(45x)e^{(-5(x-2)^2)} + \sin(5x)e^{(-5x^2)} + \sin(20x)e^{(-5(x+2)^2)}$ (see figure 7.3a). This function is clearly localized around three wavenumbers ($\kappa = 45, 5, 20$) at three spatial locations ($x = 2, 0, -2$). A Fourier-transform is able to identify each of these three wavenumber components (see figure 7.3b), however, all spatial information is lost. On the other hand, the wavelet transform of the signal captures both the wavenumber and spatial information about the signal (see figure 7.3c). Similarly, a general function f can also be represented through the superposition of wavelets as

$$f(x) = C_\psi^{-1/2} \int_0^{\infty} \int_{-\infty}^{\infty} a^{-1/2} \psi \left(\frac{x-b}{a}\right) W_f(a,b) \frac{db\, da}{a^2}. \tag{7.6}$$

There is a discrete analog of equation (7.6) that represents a discretely-sampled function as discrete translations and scalings of wavelets, as well as procedures for efficiently generating orthonormal wavelet bases (see [202] for a review).

However, for the forcing field we interested in forcing at a particular scale and spatial location. Thus, there is considerable freedom in constructing the divergence-free wavelet functions to represent the forcing field. For instance, given *any* wavelet $\psi(x)$, multi-dimensional divergence free wavelets can be constructed as tensor products of the one-dimensional wavelet ψ, e.g., in two-dimensions

$$\Psi^{2D}_{div}(x_1, x_2) = \begin{cases} \psi(x_1)\psi'(x_2) \\ -\psi'(x_1)\psi(x_2) \end{cases} . \tag{7.7}$$

For example, consider the simple case of a real morlet

$$\psi(\kappa(x-w)) = e^{-\sigma(\kappa(x-w))^2}\cos(\kappa(x-w)) \tag{7.8}$$

centered around the point $w = 0$ and wavenumber $\kappa = 5$ with $\sigma = 0.05$ (see figure 7.4a). Then equation (7.7) clearly generates a localized divergence-free vector field around the point $(0, 0)$ (see figure 7.4b). The parameters σ and κ control the number and magnitude of the vortices in figure 7.4b.

This example extends naturally to three-dimension and can be used to improve several of the drawbacks with the AMS forcing. We consider the forcing field

$$F_i^{\text{AMS-DIV}}(\mathbf{x}) = F_{mag}F_\rho \sum_{n=1}^{N} h_i^{div}(\kappa_n(\mathbf{x} - \mathbf{w}_n)) \tag{7.9}$$

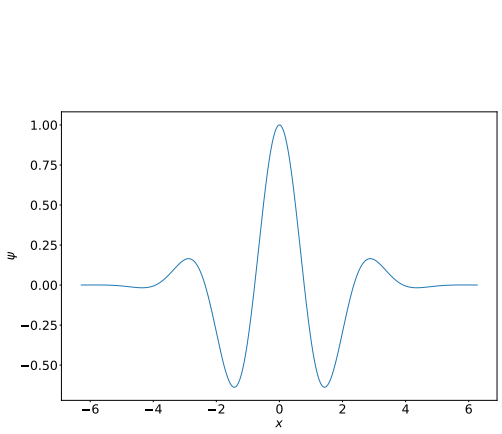

(a)

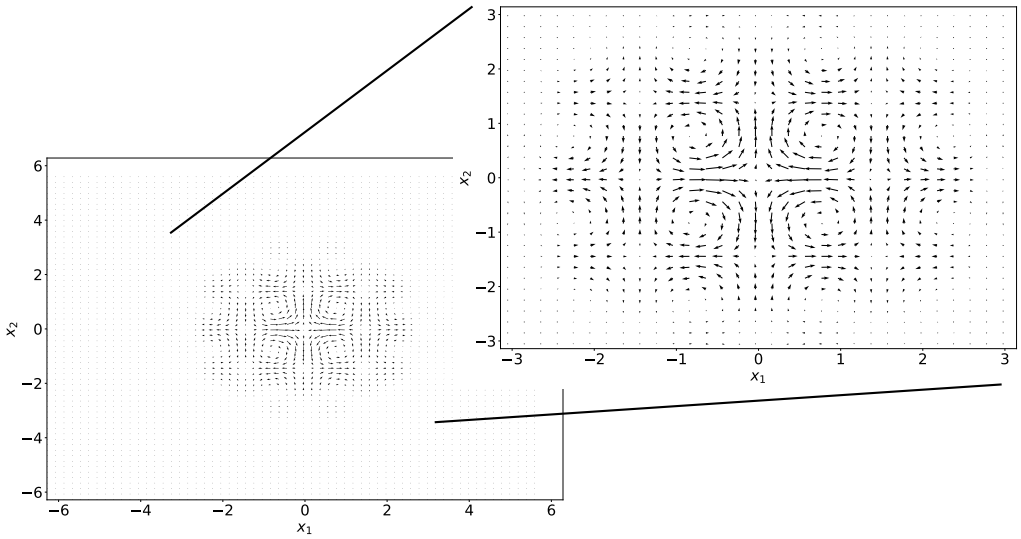

(b)

Figure 7.4: (a) A one dimensional real morlet wavelet with $\sigma = 0.05$, centered around the point $w = 0$ and wavenumber $\kappa = 2$ (see equation (7.8)). (b) The two-dimensional divergence free wavelet vector field generated from tensor products of the morlet wavelet (see equation (7.7)).

where the vector field $h_i^{div}(\mathbf{x})$ evaluated at $\kappa(\mathbf{x} - \mathbf{w})$ is

$$h_i^{div}(\kappa(\mathbf{x} - \mathbf{w})) = \begin{cases} \psi(\kappa(x_1 - w_1))\psi'(\kappa(x_2 - w_2))\psi'(\kappa(x_3 - w_3)) \\ -1/3\psi'(\kappa(x_1 - w_1))\psi(\kappa(x_2 - w_2))\psi'(\kappa(x_3 - w_3)) \\ -2/3\psi'(\kappa(x_1 - w_1))\psi'(\kappa(x_2 - w_2))\psi(\kappa(x_3 - w_3)) \end{cases} \tag{7.10}$$

and the summation in equation (7.9) is over N divergence free wavelet vector fields centered around the point $\mathbf{w}_n$ and scale κ_n.

In the following section we pursue a direct comparison between F_i^{AMS} and $F_i^{\text{AMS-DIV}}$ to highlight the importance of the structure of the forcing field. Therefore, all the same estimates from the AMS forcing are used to evaluate the wavelet-based forcing field including the forcing magnitude, forcing wavenumber, the resolution indicator function, and the estimates of k_{sgs} (see section 7.1). However, to preserve the divergence-free and localization

properties of $F_i^{\text{AMS-DIV}}$, no clipping procedure is used for the wavelet-based forcing.

7.2.1 A numerical experiment

The two forcing fields F_i^{AMS} and $F_i^{\text{AMS-DIV}}$ are examined in a refining LES of homogeneous isotropic turbulence. Specifically, a coarse LES of infinite Reynolds number turbulence is first computed with Fourier spectral numerics on a cubical domain of size $L = 2\pi$ with resolution scale $\Delta_c = 2\pi/8$. A negative viscosity forcing is active in the wavenumber range $0 < |\boldsymbol{\kappa}| \leq 2$ and injects energy at a constant rate of $\varepsilon = 1$. A Kolmogorov SGS model is used with constant tuned to provide a mean rate of kinetic energy dissipation of ε (see section 3.5). An instantaneous sample from the statistically stationary solution is then used as an initial condition in a finer LES with the same setup except now with a resolution scale of $\Delta_f = 2\pi/32$ (see figure 7.5a). The energy spectrum of this initial condition is representative of an equivalently filtered five-third spectrum up to $\kappa_c = 4$ (see figure 7.5d), however, the fine LES is capable of resolving scales up to $\kappa_c = 16$. The energy spectrum of the solution is then tracked in time as the scales populated from $\kappa_c = 4$ to $\kappa_c = 16$ (see figures 7.5b and 7.5c). Without any active forcing, the energy spectrum populates in roughly two large eddy turnover times, based on the value $T_L \approx 0.9$ as reported by Yalla et al. [126] (see figures 7.5e and 7.5f).

The ability of the forcing fields F_i^{AMS} and $F_i^{\text{AMS-DIV}}$ to more quickly populate scales $4 \leq |\boldsymbol{\kappa}| < 16$ is tested in this setting. Three different values of F_{mag} are used in both cases, which control the energy injection rate. For F_i^{AMS}, we take $C_F = 8$, 16, and 32, and for $F_i^{\text{AMS-DIV}}$, we take $C_F = 1$, 2, and 4. Note that because the wavelets in the formulation of $F_i^{\text{AMS-DIV}}$ overlap, the values of C_F should not be compared directly, and lead to very different energy characteristics between the two formulations. For instance, the max energy injection over time for F_i^{AMS} is roughly half that of $F_i^{\text{AMS-DIV}}$ for each value of C_F respectively (see table 7.1). The forcing field $F_i^{\text{AMS-DIV}}$ is computed with a real morlet wavelet centered at

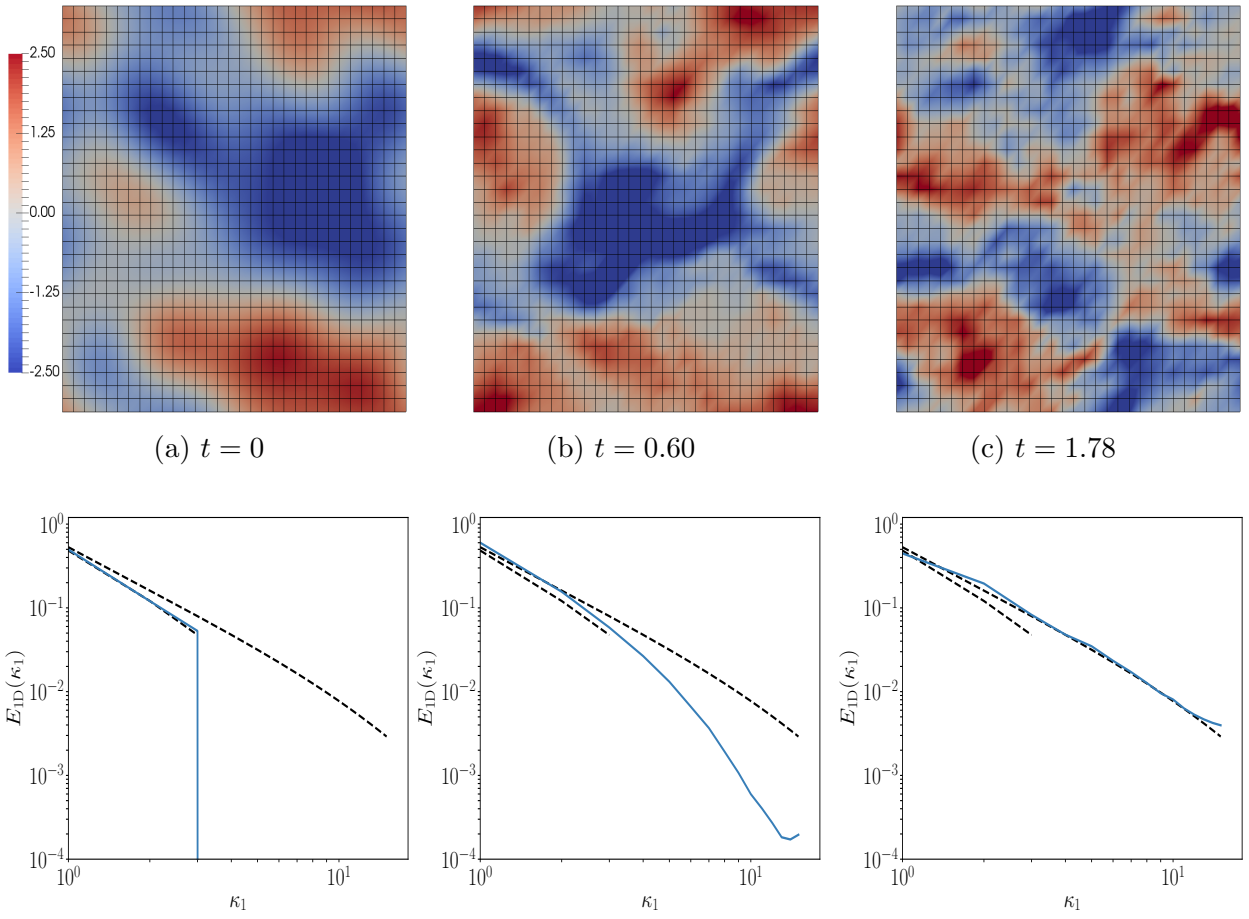

(a) $t = 0$ (b) $t = 0.60$ (c) $t = 1.78$

(d) $t = 0$ (e) $t = 0.60$ (f) $t = 1.78$

Figure 7.5: Time snapshots of the coarse-to-fine LES used to explore the forcing formulations. (a), (b), and (c) show a two-dimensional slice of the velocity field, u, at times $t = 0$, $t = 0.6$, and $t = 1.78$, respectively. The corresponding one-dimensional energy spectra are shown in (d), (e), and (f), respectively (———). The equivalently filtered five-thirds spectra for a resolution of $\Delta_c = 2\pi/8$ and $\Delta_f = 2\pi/32$ are also shown (– – –). All figures here are for the LES without active forcing.

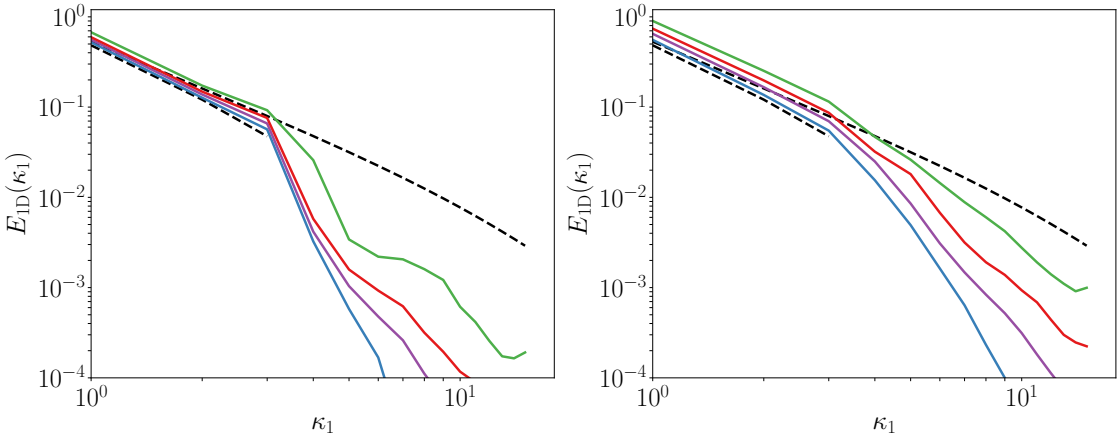

(a) $t = 0.11$ (b) $t = 0.30$

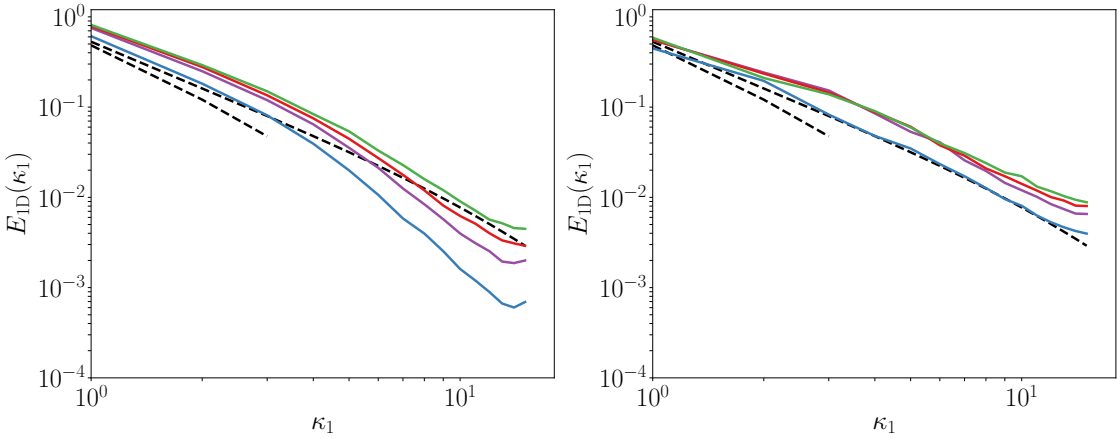

(c) $t = 0.90$ (d) $t = 1.78$

Figure 7.6: One dimensional energy spectra for the coarse-to-fine LES at four different times with the AMS forcing field F_i^{AMS} and values $C_F = 8$ (——), $C_F = 16$ (——), $C_F = 32$ (——), and $C_F = 0$ (——). The equivalently filtered five-thirds spectra for a resolution of $\Delta_c = 2\pi/8$ and $\Delta_f = 2\pi/32$ are also shown (– – –).

each grid point (see equation (7.8)) with a value of σ chosen so that the support of the wavelets span five grid cells in each coordinate direction. This value of σ was set empirically to provide a reasonable trade-off between the support in realspace and wavespace, although similar results were obtained for nearby values of σ. A more thorough discussion of the σ parameter is given in section 7.2.2.

The AMS forcing leads to a more rapid production of the turbulence across the entire range of resolved scales, which generally corrupts the energy characteristics throughout the $2T_L$ time period (see figure 7.6). By one eddy turnover time there is a clear excess of energy in the low wavenumbers for all cases (see figure 7.6c), which is noticeable even around $t = 1/3T_L$ (see figure 7.6b). Although the scales $4 \leq |\boldsymbol{\kappa}| < 16$ populate faster than the LES without active forcing, the excess energy in the low wavenumbers cascades down to these high wavenumbers leading to an energy pile-up in the entire spectrum by $t = 2T_L$ (see figure 7.6d). Note, the active forcing shuts off by $t = T_L$ for all C_F values (since $\rho > 1$), so the excess energy in these higher modes observed at $t = 2T_L$ is indeed a results of nonlinear turbulent processes.

The behavior of AMS forcing formulation is not particularly surprising. The Taylor-Green-like vortex field is generally not localized in wavespace. In fact, h_i may be interpreted as a wavelet with zero support in physical space, i.e., infinite support in wavespace. Additionally, the clipping procedure introduces sharp discontinuities into the forcing field, further affecting all wavenumbers. The field $F_i^{\text{AMS-DIV}}$ is free of these issues and thus leads to a better evolution of the energy spectrum in this test (see figure 7.7). The wavelet based forcing roughly halves the time it takes for the wavenumbers $4 \leq |\boldsymbol{\kappa}| < 16$ to reach a five-thirds spectra from the LES without active forcing (see figure 7.7). Moreover, it does so without affecting the low wavenumber band $0 \leq |\boldsymbol{\kappa}| < 4$.

The forcing field $F_i^{\text{AMS-DIV}}$ supports quite a large energy injection rate. For the $C_F = 4$ case, $\langle F_i^{\text{AMS-DIV}} u_i \rangle$ is nearly fifteen times larger than dissipation rate in the early stages of

	$C_f = 8$	$C_f = 16$	$C_f = 32$
$\max_t \langle F_i^{\text{AMS}} u_i \rangle$	1.4	3.3	7.2

	$C_f = 1$	$C_f = 2$	$C_f = 4$
$\max_t \langle F_i^{\text{AMS-DIV}} u_i \rangle$	3.3	6.7	15.5

Table 7.1: The maximum average energy injection rate from the forcing fields F_i^{AMS} and $F_i^{\text{AMS-DIV}}$over time from the LES in

the LES (see table 7.1), which decreases to around ε by the time $t = 0.11$. If we view this simulation as turbulence convecting through a sharp grid change, then the spectral characteristics of the inhomogeneous commutator suggest an infinite energy injection rate is required instantaneously over the wavenumbers $4 \leq |\boldsymbol{\kappa}| < 16$ (see equation (5.42)), which supports the behavior of the forcing seen here. However, because of the way the forcing-wavenumber is formulated ($\kappa_i = \pi / L_{sgs}$), when $\langle F_i u_i \rangle \gg \varepsilon$ higher wavenumbers may be targeted by the forcing before lower wavenumbers have been properly 'healed' into resolved turbulence and there is no way to retroactively force intermediate scales. This is apparent in the $C_F = 4$ simulation — wavenumbers $|\boldsymbol{\kappa}| \geq 7$ follow a five-third spectrum by $t = 0.11$ (see figure 7.7a), while wavenumbers $4 \leq |\boldsymbol{\kappa}| < 7$ match the theoretical case after $t = 0.9$ (see figure 7.7c). This behavior is not particularly problematic here, but may inform ways the estimate for the forcing-wavenumber could be improved.

The experiment here clearly indicates better forcing formulations allows one to force the turbulence more strongly, better preserve the well-resolved turbulence, and allows for sharper grid transitions to finer resolved LES regions.

7.2.2 Potential improvements to the wavelet-based forcing formulation

The results in the previous section suggest that the wavelet-based approach may be useful for developing a more robust forcing formulation. Possible improvements to this approach are discussed here.

Increasing the representation power of the underlying wavelet-basis may allow for more control over the properties of the forcing, such as the energy injection rate. For instance, sup-

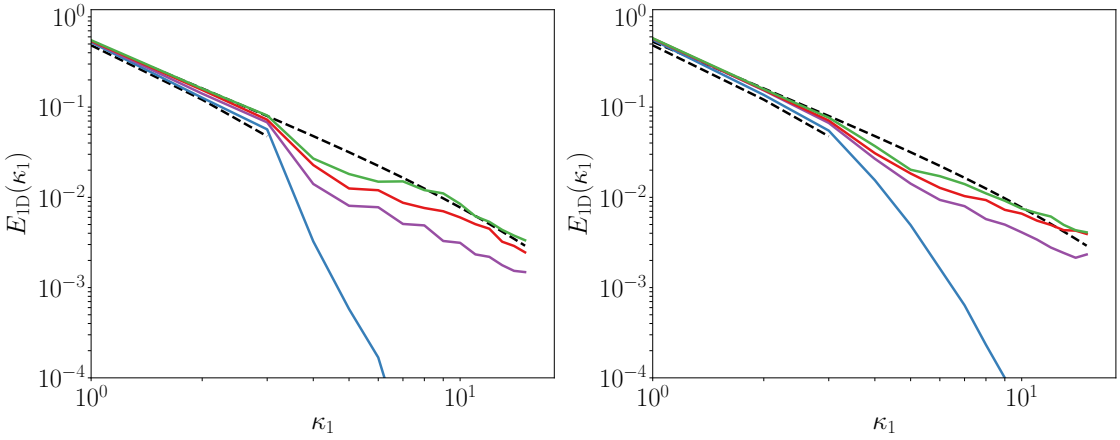

(a) $t = 0.11$

(b) $t = 0.30$

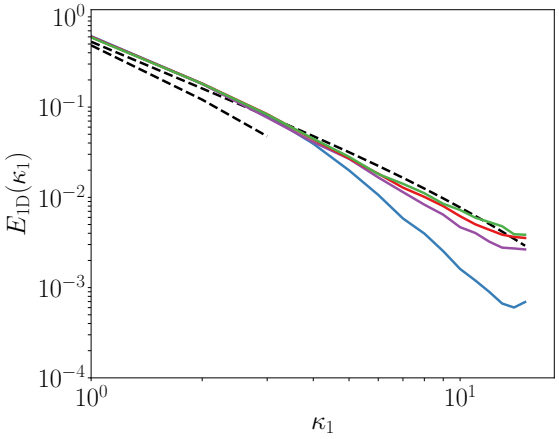

(c) $t = 0.90$

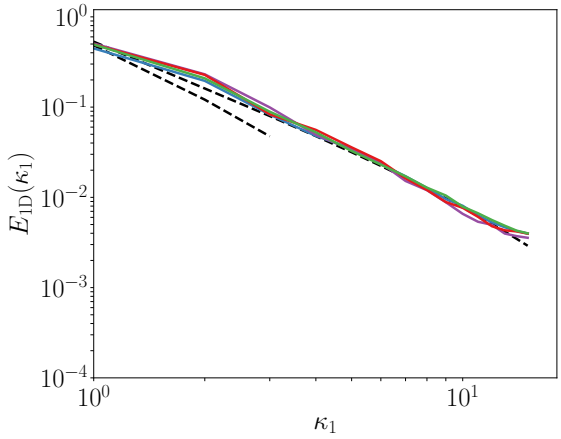

(d) $t = 1.78$

Figure 7.7: One dimensional energy spectra for the coarse-to-fine LES at four different times with the wavelet-based AMS forcing field $F_i^{\text{AMS-DIV}}$ and values $C_F = 1$ (——), $C_F = 2$ (——), $C_F = 4$ (——), and $C_F = 0$ (——). The equivalently filtered five-thirds spectra for a resolution of $\Delta_c = 2\pi/8$ and $\Delta_f = 2\pi/32$ are also shown (– – –).

pose the wavelets are isotropic in scale and consider the following two orthogonal divergence-free wavelet basis functions evaluated at the point $\kappa(\mathbf{x}-\mathbf{w})$:

$$\Psi^1_{div}(\kappa(\mathbf{x}-\mathbf{w})) = \begin{cases} \psi(\kappa(x_1-w_1))\psi'(\kappa(x_2-w_2))\psi'(\kappa(x_3-w_3)) \\ 0 \\ -\psi'(\kappa(x_1-w_1))\psi'(\kappa(x_2-w_2))\psi(\kappa(x_3-w_3)) \end{cases}, \tag{7.11}$$

$$\Psi^2_{div}(\kappa(\mathbf{x}-\mathbf{w})) = \begin{cases} \psi(\kappa(x_1-w_1))\psi'(\kappa(x_2-w_2))\psi'(\kappa(x_3-w_3)) \\ -2\psi'(\kappa(x_1-w_1))\psi(\kappa(x_2-w_2))\psi'(\kappa(x_3-w_3)) \\ \psi'(\kappa(x_1-w_1))\psi'(\kappa(x_2-w_2))\psi(\kappa(x_3-w_3)) \end{cases}. \tag{7.12}$$

The forcing field $\mathbf{F}(\mathbf{x})$ could then be represented as

$$\mathbf{F}(\mathbf{x}) = \sum_{n=1}^{N} C_{n,1}\Psi^1_{div}(\kappa_n(\mathbf{x}-\mathbf{w}_n)) + C_{n,2}\Psi^2_{div}(\kappa_n(\mathbf{x}-\mathbf{w}_n)), \tag{7.13}$$

where $C_{n,1}$ and $C_{n,2}$ are general constants and the sum is over N wavelets centered at the point $\mathbf{w}_n$ and scale κ_n. This basis is representative of any divergence-free function at a particular scale, unlike that in equation (7.10). The constants $C_{n,1}$ and $C_{n,2}$ could be determined through a target energy injection rate E_{inj}, which may be based on the energy characteristics of the inhomogeneous commutator (see equation (5.41)) for instance. If a wavelet is centered at each point in the domain, then equation (7.13) leads to an under-determined system when solving for $C_{n,1}$ and $C_{n,2}$. The minimal norm solution can be determined via an SVD, however, this is an expensive calculation, especially for the forcing field which is by necessity ad hoc. The authors attempted to reduce this computational cost through a low-rank approximation to the solution via a randomized SVD method [203], however, this proved infeasible. Instead, preliminary results suggest it may be reasonable to approximate this computation locally based solely on the value of the nth wavelet at the point

$\mathbf{w}_n$. This may be reasonable since the wavelets are localized around $\mathbf{w}_n$. The representation power of the basis could be improved even further by considering a divergence-free wavelet multi-resolution analysis [202]. Such a basis was constructed by Lemarié-Rieusset [204] and has been used as a computational technique to simulate turbulence in two- and three-dimensions [205, 206]. This basis and its associated wavelets may therefore be a natural candidate for the forcing field.

Turbulence has also been a popular application for wavelet-based analyses, because of its inherent multiscale and spatially varying nature. As Farge [207] notes, we generally have two different pictures of turbulence depending on the side of the Fourier transform from which we perceive it. On one hand, turbulence theory predicts the existence of an energy cascade between triad-interacting wavenumbers that lie within the inertial range. On the other hand, experimental and numerical results suggest the presence of coherent structures in turbulent flows that correspond to organized patterns in the vorticity field, which seem to play an important role in the underlying dynamics of the flow. Wavelet analyses have helped unify these two descriptions, and these insights may be useful for developing a more realistic forcing field.

For instance, the coherent vortex extraction (CVE) method [208] allows the flow to be split into two parts: active coherent vortices represented by a few wavelet coefficients, and incoherent vortices of the background flow, which largely resemble noise. Okamoto et al. [209] applied this to DNS of isotropic turbulence and found that the spectrum of coherent vortices is identical to the one of the total flow in the inertial range, implying that vortex turbulence leads to a five-thirds energy spectrum. The incoherent part of the flows led to a κ^2 energy spectrum which corresponds to an equipartitioning of the energy between wavenumbers and suggests that incoherent vortices are spatially decorrelated and indeed structureless [209, 210, 211]. Thus, with just a few wavelet coefficient one may be able to construct a more realistic forcing field similar to these coherent vortices, which should reduce the time

for added turbulent fluctuations to be "healed" into realistic turbulence. Further, Meneveau [212] derived the wavelet-transformed Navier-Stokes equations and defined quantities such as the local kinetic energy spectrum, energy transfer spectrum, and energy flux to provide spatial information to the usual energy spectrum dynamics. This may also be useful for informing the properties of the forcing field.

Each wavelet used to construct the forcing field has unique parameter σ controlling the support of the wavelet, which may depend on the local properties of the flow as well as the discretization. For instance, smaller values of σ allow the forcing to target particular wavenumbers more precisely. However, the wavelets should ideally not extend into coarser resolution regions where the forcing-wavenumber may not be representable. The computational cost of the wavelet approach should also be considered here. Equation (7.13) is not a pointwise computation like the AMS forcing field h_i, so it may introduce a significant computational expense depending on the number and support of the wavelets (especially when considering parallelized computations). Larger σ_n values aid in reducing this computational cost. It may therefore be reasonable to center the wavelets around the wavenumber $\kappa^{\text{force}} = \frac{1}{2}(\pi/\Delta + \pi/L_{SGS})$, allowing for a maximal support in wavespace that does not affect the well-resolved scales and thus a minimal support in realspace. It also may not be necessary to have a wavelet centered at every grid point to take advantage of the support in realspace. This would reduce the cost of forming $\mathbf{F}$ as well. The existence of a fast algorithm with near linear complexity for computing wavelet decompositions [213] is encouraging that a forcing field of this form may be constructed without introducing significant computation cost.

Several of the complications in formulating $\mathbf{F}$ stems from the wavelets support in physical space. However, if the forcing field is to be divergence free and localized in wavespace, then these issues may be unavoidable. A possible alternative is to base the forcing field on a high pass filter of the velocity field. For instance, De Laage de Meux et al. [152] use a second-

order differential filter (see section 3.7) applied to the velocity field as a basis for the forcing field. However, this requires the velocity field to already have turbulent fluctuations at the scales where the forcing is needed. In a coarse-to-fine LES, this may be reasonable, however, in cases such as the RANS-to-LES regions of a hybrid RANS/LES simulation, it is not. It may therefore be possible to combine these approaches by using a wavelet-based forcing scheme near RANS-to-LES transitions and a velocity field-based forcing for coarse-to-fine LES regions. Note that the velocity field-based forcing requires access to an appropriate high pass filter, which may be difficult to construct and may also have a wide support around any given point in physical space. Further, multi-resolution analysis essentially views wavelet constructions as a band-pass filter, which could suggest a natural connection to the filtered velocity field-based forcing approach.

Chapter 8

Conclusions

The largest scales of turbulence in many complex flows of interest have a wide range of scales themselves (e.g., the wake behind a wind turbine [138], turbulent boundary layers [137]). For LES to become a widely applicable engineering tool, it must therefore accommodate a wide range of large scales. This requires that LES and corresponding subgrid models tolerate very coarse and often highly inhomogeneous and anisotropic resolutions. The overarching challenge of current LES progress is therefore to move past the "well-resolved" barrier where the majority of the turbulent energy is resolved. In this case, subgrid models must do more than dissipate energy, which has been the primary focus of LES modeling since its inception (see chapter 2). In particular, the effects of numerical discretization cannot be ignored since the smallest resolved scales will be important energy-containing scales.

The dispersion error introduced by the numerical approximation of the convection term has a profound impact on the turbulence represented in an LES. These errors can be particularly problematic in convecting flows where the mean velocity is large compared to the turbulence fluctuations. By analyzing LES of isotropic turbulence convecting through a uniform grid with a mean velocity $U \gg u_{rms}$, we determined that linear dispersion error causes a decoherence of the phase relationship among interacting Fourier modes, which results in a reduction of the energy transfer rate from large to small scales (see section 3.3). This can corrupt LES statistics throughout the entire range of resolved scales. Nonlinear dispersion error from turbulence convecting through a uniform grid due to turbulent fluctuations was

also explored through the development of an EDQNM-type analysis that is applicable to the filtered turbulence in an LES. EDQNM is a particularly useful tool for exploring dispersion effects because it exposes the relaxation rate of the third-order velocity correlations. Numerical dispersion error effectively decreases this relaxation timescale, reducing velocity correlations at a faster rate than that introduced by the standard dissipation rate, and must therefore be account for by the eddy-damping modeling in the EDQNM analysis (see section 4.3.2).

The convection of turbulence through inhomogeneous resolution introduces additional challenges in LES due to so-called commutation-error, or neglect of the commutator of the filtering and differentiation operators. If this commutator is ignored as turbulence convects through coarsening grids, the energy in newly unresolvable scales is transferred to higher wavenumbers in the fine resolution region, instead of to the subgrid scales in the coarse region. The result is a non-physical reflection of unresolvable scales back into the fine region of the grid at higher wavenumbers with negative group velocities (see section 6.2). These nonlocal energy exchanges between wavenumbers introduced by resolution inhomogeneity are especially problematic in LES of turbulence where the energy cascade occurs primarily between local wavenumbers [169]. Both nonlinear commutation error (due to the convection of turbulence through a nonuniform grid by turbulent fluctuations), and linear commutation error (due to turbulence convecting through a nonuniform grid in the regime of Taylor's hypothesis) were shown to be particularly damaging to the energy spectrum in LES of isotropic turbulence (see section 6.4).

LES models must take the characteristics of the underlying numerics into account and, ideally, the resolved scales in an LES should be defined to exclude the highly dispersive modes. One approach to doing so is to define the large scales to be simulated through an explicit filter, acting in addition to the implicit filter defined by the numerical discretization, to ensure that the scales with significant dispersion error are not energized. However, an

explicit filter can introduce the same type of dispersive errors as numerics if not properly constructed (see section 3.6). An operator that is useful for this purpose was developed in section 3.8 and is based on the difference between the numerical second derivative operator and repeated application of the numerical first derivative operator. This operator naturally acts on scales with significant dispersion error and can therefore be used to design explicit filters or model terms that remove energy in the dispersive modes. Further, whether an explicit filter is used or not, the subgrid stress model must be formulated to account for the underlying numerics and filters. The EDQNMLES theory developed in section 4.3 was used to determine the properties of the subgrid stress needed to recover an inertial range spectrum in the presence of non-spectral numerics and non-cutoff explicit filters. The behavior of the wavenumber-dependent eddy viscosity varied significantly for lower-order numerics or graded filters from the 'spectral-cusp' behavior of the eddy viscosity found for spectral methods and truncations (see section 4.3.3).

Modeling of the inhomogeneous commutator $\mathcal{C}^I$ was also explored. A statistical analysis $\mathcal{C}^I$ yielded a quantitative measure of the magnitude of $\mathcal{C}^I$ and therefore how important it is to the energy balance as a function of the resolution gradient and the convection velocity (see section 5.2). The statistical characteristics of the commutator are important because *a priori* consistency of certain statistical characteristics of an LES model is a necessary condition for accurate *a posteriori* statistics of an LES solution [187, 1]. Further, a series approximation of $\mathcal{C}^I$ was developed in section 5.1, which was not only useful for informing commutation models, but also for interpreting previous work on commutation error in the literature [22, 146, 147, 145, 151]. A framework for modeling the inhomogeneous commutator was proposed in section 6.3, and was shown to perform well for correcting both nonlinear commutation error and commutation error in the regime of Taylor's hypothesis (see sections 6.3.1 and 6.4.3). However, further model developments are still required, especially for turbulence convecting through rapid grid changes with a large mean velocity.

Lastly, the forcing of newly resolvable scales as turbulence convects through refining grids was explored in chapter 7. Such a forcing scheme is needed to maintain consistency with the definition of the filter in an LES and for accurately represented flow statistics [99]. An improvement to the forcing scheme of Haering et al. [99] was proposed based on divergence-free wavelets. This formulation of the forcing provides a degree of localization in both wavespace and realspace and ensures the forcing field is divergence-free. More work is needed to make this formulation robust, however, a simple test of the forcing in isotropic turbulence suggests it may be effective at energizing newly resolvable scales faster than the natural turbulent energy cascade while maintaining the existing scales. It also appears to provide more efficient control of the energy injection rate (see section 7.2.1). Moreover, these results suggest that an improved forcing formulation should allow one to force the turbulence more strongly, allowing for sharper grid transitions to finer resolved regions.

In this thesis we have developed several computational and analytical tools for exploring the effects of numerical discretization in large eddy simulation. These techniques have been used to identify several a priori statistical characteristics that are important for subgrid models to satisfy in complex scenarios and have informed the development of LES models that directly account for the properties of the underlying numerics. We have successfully moved beyond analyzing LES in term of isotropic turbulence represented on a uniform grid with Fourier-spectral numerics and cutoff filters. By incorporating the practical requirements of LES into analytical and computational techniques and probing isotropic turbulence in a variety of different computational regimes, we have greatly enhanced our understanding of the flow physics represented in an LES and the requirements of practical LES model for complex scenarios. There are several additional challenges to formulating more broadly applicable subgrid models for LES, some of which were discussed in section 2.2, and we expect that the techniques developed here will also be useful for addressing these wide range of issues in LES.

Appendix A

Numerical representation of the vorticity-velocity formulation

The vorticity-velocity formulation introduced by Kim et al. [128] (referred to as KMM below) is a convenient way to solve the filtered or unfiltered Navier-Stokes equations when boundary conditions in two spatial directions (say x_1 and x_3) are periodic, and the numerical resolution in those directions is uniform. However, there is a subtlety to the formulation that arises when the discrete second derivative operator is not equivalent to the discrete first derivative applied twice.

In the KMM formulation, the curl and the double curl operators are applied to the momentum equations, to obtain equations for the vorticity and the Laplacian of the velocity. The 2-component is then solved for, and a complete representation of the velocity is obtained from continuity. This formulation relies on three identities from vector calculus, which must also be satisfied by the discrete operators. Let $\tilde{\nabla}\cdot$, $\tilde{\nabla}$, $\tilde{\nabla}\times$ and $\tilde{\Delta}$ be the discrete divergence, gradient, curl and Laplacian operators, respectively. To recover the property of the KMM formulation that the pressure is eliminated, we must have

$$\tilde{\nabla} \times \tilde{\nabla}\psi = 0 \tag{A.1}$$

for any scalar field ψ. Further, to obtain the simple form used in KMM for the double curl

of the momentum equation, and to reconstruct the full velocity,

$$\tilde{\nabla} \times \tilde{\nabla} \times \mathbf{A} = -\tilde{\nabla} \cdot \tilde{\nabla}\mathbf{A} + \tilde{\nabla}\tilde{\nabla} \cdot \mathbf{A} \tag{A.2}$$

must hold for any vector field $\mathbf{A}$, which ensures that the second term on the right will be zero when $\tilde{\nabla} \cdot \mathbf{A} = 0$. Both these discrete identities hold provided the same one-dimensional discrete derivatives are used to define the discrete divergence, gradient and curl operators. Finally, in KMM the 2-component of the double curl of the momentum equation yields an equation for ϕ, defined as the Laplacian of u_2, which requires that the discrete Laplacian obey $\tilde{\Delta} u_2 = \tilde{\nabla} \cdot \tilde{\nabla} u_2$, which is not generally true. So, instead, we define $\phi = \tilde{\nabla} \cdot \tilde{\nabla} u_2$.

Consider the discrete momentum and continuity equations:

$$\frac{\partial \mathbf{u}}{\partial t} = -\tilde{\nabla} p + \mathbf{H} \tag{A.3}$$

$$\tilde{\nabla} \cdot \mathbf{u} = 0 \tag{A.4}$$

which could be the Navier-Stokes equations (e.g. for a DNS) or the filtered Navier-Stokes equations (for an LES), in which case $\mathbf{u}$ is the filtered velocity. The $\mathbf{H}$ term includes the nonlinear, viscous and model (for LES) terms. Let $\tilde{\nabla}_p \cdot$ and $\tilde{\nabla}_p$ be the divergence and gradient operators restricted to the (1,3) plane, and let $\omega_2 = (\tilde{\nabla} \times \mathbf{u})_2$. Then the discrete version of

the KMM formulation is given by

$$\frac{\partial \phi}{\partial t} = -\tilde{\nabla} \times \tilde{\nabla} \times \mathbf{H} \tag{A.5}$$

$$\frac{\partial \omega_2}{\partial t} = \tilde{\nabla} \times \mathbf{H} \tag{A.6}$$

$$\tilde{\nabla} \cdot \tilde{\nabla} u_2 = \phi \tag{A.7}$$

$$\tilde{\nabla}_p \cdot \tilde{\nabla}_p u_1 = \left(\frac{\delta \omega_2}{\delta x_3} - \frac{\delta}{\delta x_1} \frac{\delta u_2}{\delta y} \right) \tag{A.8}$$

$$\tilde{\nabla}_p \cdot \tilde{\nabla}_p u_3 = \left(\frac{\delta \omega_2}{\delta x_1} - \frac{\delta}{\delta x_3} \frac{\delta u_2}{\delta y} \right). \tag{A.9}$$

With periodic boundary conditions and uniform resolution in the x_1 and x_3 directions, the discrete derivative operators in those directions are circulant matrices, so that given ϕ and ω_2, (A.7-A.9) can be easily solved using discrete Fourier transforms, which is what makes the KMM formulation efficient. This also allows one to show that the solution for $\mathbf{u}$ does indeed satisfy $\tilde{\nabla} \cdot \mathbf{u} = 0$. The operators $\tilde{\nabla} \cdot \tilde{\nabla}$ and $\tilde{\nabla}_p \cdot \tilde{\nabla}_p$ that must be solved to recover the velocities using (A.7-A.9) are in general rank deficient because eigenvalues associated with the Nyquist modes are zero. This is the property that leads to checkerboard instabilities in projection methods [214]. Here, the resulting singularity of the equations is resolved by insisting that all the Nyquist modes are zero, consistent with the Fourier cutoff filters used in the LES. Finally, note that for spatial directions with periodic boundary conditions and uniform resolution, there is generally no motivation to use other than Fourier spectral representations. Non-spectral methods are used here only to allow the impacts of dispersion errors to be assessed, since often an LES must be conducted for boundary conditions and resolutions for which Fourier spectral methods are not practical.

The modified KMM formulation described here is designed to ensure that the solutions obtained satisfy the discrete filtered or unfiltered Navier-Stokes equations (A.3)-(A.4). This is important in the current study because we are interested in the effects of dispersion error in

these equations, which are usually solved in practical simulations. However, it is also possible to derive the ϕ and ω_2 equations from the momentum and mass conservation equations before discretization, and then discretize them [128, 124]. In this case, the results are still numerical approximations to solutions of the conservation equations, but the numerical errors are different from those obtained by solving the discrete conservation equations.

Bibliography

[1] Robert D Moser, Sigfried W Haering, and Gopal R Yalla. Statistical properties of subgrid-scale turbulence models. *Annual Review of Fluid Mechanics*, 53:255–286, 2021.

[2] Osborne Reynolds. An experimental investigation of the circumstances which determine whether the motion of water shall be direct or sinuous, and of the law of resistance in parallel channels. *Philosophical Transactions of the Royal society of London*, (174): 935–982, 1883.

[3] WP Jones and Brian Edward Launder. The prediction of laminarization with a two-equation model of turbulence. *International Journal of Heat and Mass Transfer*, 15 (2):301–314, 1972.

[4] Brian Edward Launder and BI Sharma. Application of the energy-dissipation model of turbulence to the calculation of flow near a spinning disc. *Letters in Heat and Mass Transfer*, 1(2):131–137, 1974.

[5] Philippe Spalart and Steven Allmaras. A one-equation turbulence model for aerodynamic flows. In *30th aerospace sciences meeting and exhibit*, page 439, 1992.

[6] P Godin, DW Zingg, and TE Nelson. High-lift aerodynamic computations with one- and two-equation turbulence models. *AIAA Journal*, 35(2):237–243, 1997.

[7] Paul A Durbin. Near-wall turbulence closure modeling without "damping functions". *Theoretical and Computational Fluid Dynamics*, 3(1):1–13, 1991.

[8] Philippe R Spalart. Detached-eddy simulation. *Annual Review of Fluid Mechanics*, 41:181–202, 2009.

[9] Alan Celic and Ernst H Hirschel. Comparison of eddy-viscosity turbulence models in flows with adverse pressure gradient. *AIAA Journal*, 44(10):2156–2169, 2006.

[10] MA Leschziner and D Drikakis. Turbulence modelling and turbulent-flow computation in aeronautics. *The Aeronautical Journal*, 106(1061):349–384, 2002.

[11] Sigfried William Haering et al. *Anisotropic hybrid turbulence modeling with specific application to the simulation of pulse-actuated dynamic stall control*. PhD thesis, 2015.

[12] Joseph Smagorinsky. General circulation experiments with the primitive equations: I. the basic experiment. *Monthly Weather Review*, 91(3):99–164, 1963.

[13] Douglas G Fox and Douglas K Lilly. Numerical simulation of turbulent flows. *Reviews of Geophysics*, 10(1):51–72, 1972.

[14] Stephen B Pope. Ten questions concerning the large-eddy simulation of turbulent flows. *New Journal of Physics*, 6(35):1–24, 2004.

[15] Jacob A Langford and Robert D Moser. Optimal LES formulations for isotropic turbulence. *Journal of Fluid Mechanics*, 398:321–346, 1999.

[16] Thomas JR Hughes, Luca Mazzei, and Kenneth E Jansen. Large eddy simulation and the variational multiscale method. *Computing and Visualization in Science*, 3(1-2): 47–59, 2000.

[17] Sigfried W Haering, Myoungkyu Lee, and Robert D Moser. Resolution-induced anisotropy in large-eddy simulations. *Physical Review Fluids*, 4(11):114605, 2019.

[18] Athony Leonard. Energy cascade in large-eddy simulations of turbulent fluid flows. *Advances in Geophysics*, 18:237–248, 1974.

[19] Douglas G Fox and Steven A Orszag. Pseudospectral approximation to two-dimensional turbulence. *Journal of Computational Physics*, 11(4):612–619, 1973.

[20] Wai Yip Kwok, Robert D Moser, and Javier Jiménez. A critical evaluation of the resolution properties of b-spline and compact finite difference methods. *Journal of Computational Physics*, 174(2):510–551, 2001.

[21] John A Evans and Thomas JR Hughes. Isogeometric divergence-conforming b-splines for the steady navier–stokes equations. *Mathematical Models and Methods in Applied Sciences*, 23(08):1421–1478, 2013.

[22] Sandip Ghosal and Parviz Moin. The basic equations for the large eddy simulation of turbulent flows in complex geometry. *Journal of Computational Physics*, 118(1):24–37, 1995.

[23] Dochan Kwak, William C Reynolds, and Joel H Ferziger. Three-dimensional time dependent computation of turbulent flow. Technical Report NASA-CR-166408, SU-TF-5, Department of Mechanical Engineering, Stanford University, 1975.

[24] S Shaanan, JH Ferziger, and WC Reynolds. Numerical simulation of turbulence in the presence of shear. Technical Report TF-6, Department of Mechanical Engineering, Stanford University, 1975.

[25] JH Ferziger, UB Mehta, and WC Reynolds. Large eddy simulation of homogeneous isotropic turbulence. In *Symposium on Turbulent Shear Flows*, volume 1, pages 14.31–14.39, 1977.

[26] M Antonopoulos-Domis. Large-eddy simulation of a passive scalar in isotropic turbulence. *Journal of Fluid Mechanics*, 104:55–79, 1981.

[27] Robert A Clark, Joel H Ferziger, and William Craig Reynolds. Evaluation of subgrid-scale models using an accurately simulated turbulent flow. *Journal of Fluid Mechanics*, 91(1):1–16, 1979.

[28] Oden J McMillan and Joel H Ferziger. Direct testing of subgrid-scale models. *Aiaa Journal*, 17(12):1340–1346, 1979.

[29] Jorge Bardina, J Ferziger, and W Reynolds. Improved subgrid-scale models for large-eddy simulation. In *13th Fluid and PlasmaDynamics Conference*, page 1357, 1980.

[30] Oden J McMillan, Joel H Ferziger, and Robert S Rogallo. Tests of new subgrid-scale models in strained turbulence. Technical Report AIAA-80-1339, AIAA, 1980.

[31] Charles Meneveau. Statistics of turbulence subgrid-scale stresses: Necessary conditions and experimental tests. *Physics of Fluids*, 6(2):815–833, 1994.

[32] John Dennis Schwarzkopf, Daniel Livescu, Jon Ronald Baltzer, Robert Allen Gore, and JR Ristorcelli. A two-length scale turbulence model for single-phase multi-fluid mixing. *Flow, Turbulence and Combustion*, 96(1):1–43, 2016.

[33] Charles Meneveau and Joseph Katz. Scale-invariance and turbulence models for large-eddy simulation. *Annual Review of Fluid Mechanics*, 32(1):1–32, 2000.

[34] Pierre Sagaut. *Large eddy simulation for incompressible flows: an introduction*. Springer Science & Business Media, 2006.

[35] Emmanuel Lévêque, Federico Toschi, Liang Shao, and J-P Bertoglio. Shear-improved Smagorinsky model for large-eddy simulation of wall-bounded turbulent flows. *Journal of Fluid Mechanics*, 570:491–502, 2007.

[36] Maurits H Silvis, Ronald A Remmerswaal, and Roel Verstappen. Physical conisistency of subgrid-scale models for large-eddy simulation of incompressible turbulent flows. *Physics of Fluids*, 29:1–16, 2016.

[37] Javier Jimenez and Robert D Moser. Large-eddy simulations: where are we and what can we expect? *AIAA Journal*, 38(4):605–612, 2000.

[38] Ulrich Schumann. Subgrid scale model for finite difference simulations of turbulent flows in plane channels and annuli. *Journal of Computational Physics*, 18:376–404, 1975.

[39] Parviz Moin and John Kim. Numerical investigation of turbulent channel flow. *Journal of Fluid Mechanics*, 118:341–377, 1982.

[40] Juan Camilo Uribe, Nicolas Jarrin, Robert Prosser, and Dominique Laurence. Development of a two-velocities hybrid RANS-LES model and its application to a trailing edge flow. *Flow Turbulence and Combustion*, 85:181–197, 2010.

[41] George Park. Wall-modeled large-eddy simulation of a high reynolds number separating and reattaching flow. *AIAA Journal*, 55(11):3709–3721, 2017.

[42] O Lehmkuhl, GI Park, ST Bose, and P Moin. Large-eddy simulation of practical aeronautical flows at stall conditions. *Proceedings of the 2018 Summer Program, Center for Turbulence Research, Stanford University*, pages 87–96, 2018.

[43] Luis A Martinez-Tossas, Matthew J Churchfield, Ali Emre Yilmaz, Hamid Sarlak, Perry L Johnson, Jens N Sørensen, Johan Meyers, and Charles Meneveau. Comparison of four large-eddy simulation research codes and effects of model coefficient and inflow turbulence in actuator-line-based wind turbine modeling. *Journal of Renewable and Sustainable Energy*, 10(3):033301, 2018.

[44] Antonio Posa, Riccardo Broglia, Mario Felli, Massimo Falchi, and Elias Balaras. Characterization of the wake of a submarine propeller via large-eddy simulation. *Computers & Fluids*, 184:138–152, 2019.

[45] David Long and John Thuburn. Numerical wave propagation on non-uniform one-dimensional staggered grids. *Journal of Computational Physics*, 230(7):2643–2659, 2011.

[46] G Dantinne, Hervé Jeanmart, GS Winckelmans, Vincent Legat, and Daniele Carati. Hyperviscosity and vorticity-based models for subgrid scale modeling. *Applied Scientific Research*, 59(4):409–420, 1997.

[47] Robert H Kraichnan. Eddy viscosity in two and three dimensions. *Journal of the Atmospheric Sciences*, 33(8):1521–1536, 1976.

[48] Marcel Lesieur and Olivier Metais. New trends in large-eddy simulations of turbulence. *Annual Review of Fluid Mechanics*, 28(1):45–82, 1996.

[49] Stephen B Pope. *Turbulent Flows*. Cambridge University Press, 2006.

[50] Johan Meyers and Pierre Sagaut. On the model coefficients for the standard and the variational multi-scale Smagorinsky model. *Journal of Fluid Mechanics*, 569:287–319, 2006.

[51] Daniele Carati, Kenneth Jansen, and Thomas Lund. A family of dynamic models for large-eddy simulation. *CTR Annual Research Briefs*, 1995.

[52] James W Deardorff. A numerical study of three-dimensional turbulent channel flow at large reynolds numbers. *Journal of Fluid Mechanics*, 41:453–480, 1970.

[53] Andrey Nikolaevich Kolmogorov. The local structure of turbulence in incompressible viscous fluid for very large reynolds numbers. *Doklady Akademii Nauk SSSR*, 30:301–305, 1941.

[54] Olivier Métais and Marcel Lesieur. Spectral large-eddy simulation of isotropic and stably stratified turbulence. *Journal of Fluid Mechanics*, 239, 1992.

[55] Douglas K Lilly. On the application of the eddy viscosity concept in the inertial subrange of turbulence. Technical Report 123, National Center for Atmospheric Research, 1966.

[56] Massimo Germano, Ugo Piomelli, Parviz Moin, and William H Cabot. A dynamic subgrid-scale eddy viscosity model. *Physics of Fluids A: Fluid Dynamics*, 3(7):1760–1765, 1991.

[57] Douglas K Lilly. A proposed modification of the germano subgrid-scale closure method. *Physics of Fluids A: Fluid Dynamics*, 4(3):633–635, 1992.

[58] Sandip Ghosal, Thomas S Lund, Parviz Moin, and K Akselvoll. A dynamic localization model for large-eddy simulation of turbulent flows. *Journal Fluid Mechanics*, 286:229–255, 1995.

[59] Charles Meneveau, Thomas S Lund, and William H Cabot. A lagrangian dynamic subgrid-scale model of turbulence. *Journal of Fluid Mechanics*, 319:353–385, 1996.

[60] Charles Meneveau. Lagrangian dynamics and models of the velocity gradient tensor in turbulent flows. *Annual Review of Fluid Mechanics*, 43:219–245, 2011.

[61] AW Vreman. An eddy-viscosity subgrid-scale model for turbulent shear flow. *Physics of Fluids*, 16(10):3670–3681, 2004.

[62] Donghyun You and Parviz Moin. A dynamic global-coefficient subgrid-scale eddy-viscosity model for large-eddy simulation in complex geometries. *Physics of Fluids*, 19 (6):065110, 2007.

[63] Takeo Kajishima and Takayuki Nomachi. One-equation subgrid scale model using dynamic procedure for the energy production. *Transactions of the ASME*, 73:368–373, 2006.

[64] Yipeng Shi, Zuoli Xiao, and Shiyi Chen. Constrained subgrid-scale stress model for large eddy simulation. *Physics of Fluids*, 20(1):011701, 2008.

[65] Yan Zang, Robert L Street, and Jeffrey R Koseff. A dynamic mixed subgrid-scale model and its application to turbulent recirculating flows. *Physics of Fluids A: Fluid Dynamics*, 5:3186–3196, 1993.

[66] Bert Vreman, Bernard Geurts, and Hans Kuerten. Large-eddy simulation of the temporal mixing layer using the clark model. *Theoretical and Computational Fluid Dynamics*, 8:309–324, 1996.

[67] Yannick Fabre and Guillaume Balarac. Development of a new dynamic procedure for the clark model of the subgrid-scale scalar flux using the concept of optimal estimator. *Physics of Fluids*, 23(11):115103, 2011.

[68] Shewen Liu, Charles Meneveau, and Joseph Katz. On the properties of similarity subgrid-scale models as deduced from measurements in a turbulent jet. *Journal of Fluid Mechanics*, 275:83–119, 1994.

[69] Vadim Borue and Steven A Orszag. Local energy flux and subgrid-scale statistics in three-dimensional turbulence. *Journal of Fluid Mechanics*, 366:1–31, 1998.

[70] Fernando Porté-Agel, Charles Meneveau, and Marc B Parlange. A scale-dependent dynamic model for large-eddy simulation: application to a neutral atmospheric boundary layer. *Journal of Fluid Mechanics*, 415:261–284, 2000.

[71] Franck Nicoud and Frédéric Ducros. Subgrid-scale stress modelling based on the square of the velocity gradient tensor. *Flow, turbulence and Combustion*, 62(3):183–200, 1999.

[72] Franck Nicoud, Hubert Baya Toda, Olivier Cabrit, Sanjeeb Bose, and Jungil Lee. Using singular values to build a subgrid-scale model for large eddy simulations. *Physics of Fluids*, 23(8):085106, 2011.

[73] Roel Verstappen. When does eddy viscosity damp subfilter scales sufficiently? *Journal of Scientific Computing*, 49(1):94, 2011.

[74] Wybe Rozema, Hyun J. Bae, Parviz Moin, and Roel Verstappen. Minimum-dissipation models for large-eddy simulation. *Physics of Fluids*, 27:085107, 2015.

[75] Roel Verstappen. How much eddy dissipation is needed to counterbalance the nonlinear production of small, unresolved scales in a large-eddy simulation of turbulence? *Computers & Fluids*, 176:276–284, 2018.

[76] Bernard J Geurts and Darryl D Holm. Leray and LANS-α modeling of turbulent mixing. *Journal of Turbulence*, 7:237–248, 2006.

[77] James W Deardorff. Three-dimensional numerical modeling of the planetary boundary layer. In *Workshop on Micrometeorogy, 1973*. Am. Meteorol. Soc., 1973.

[78] Akira Yoshizawa and Kiyosi Horiuti. A statistically-derived subgrid-scale kinetic energy model for the large-eddy simulation of turbulent flows. *Journal of the Physical Society of Japan*, 54(9):2834–2839, 1985.

[79] Sharath S Girimaji and Stefan Wallin. Closure modeling in bridging regions of variable-resolution (vr) turbulence computations. *Journal of Turbulence*, 14(1):72–98, 2013.

[80] Sharath S Girimaji. Partially-averaged navier-stokes model for turbulence: A reynolds-averaged navier-stokes to direct numerical simulation bridging method. *Journal of Applied Mechanics*, 73(3):413–421, 2006.

[81] Bruno Chaouat and Roland Schiestel. A new partially integrated transport model for subgrid-scale stresses and dissipation rate for turbulent developing flows. *Physics of Fluids*, 17(6):065106, 2005.

[82] Bruno Chaouat and Roland Schiestel. Hybrid RANS/LES simulations of the turbulent flow over periodic hills at high reynolds number using the pitm method. *Computers & Fluids*, 84:279–300, 2013.

[83] Pooyan Razi, Pedram Tazraei, and Sharath Girimaji. Partially-averaged Navier-Stokes (PANS) simulations of flow separation over smooth curved surfaces. *International Journal of Heat and Fluid Flow*, 66:157–171, 2017.

[84] Hans-Jakob Kaltenbach. Cell aspect ratio dependence of anisotropy measures for resolved and subgrid scale stresses. *Journal of Computational Physics*, 136(2):399–410, 1997.

[85] Christer Fureby and Fernando F Grinstein. Large eddy simulation of high-reynolds-number free and wall-bounded flows. *Journal of Computational Physics*, 181(1):68–97, 2002.

[86] Jay P Boris. On large eddy simulation using subgrid turbulence models comment 1. In *Whither turbulence? Turbulence at the crossroads*, pages 344–353. Springer, 1990.

[87] Fernando F Grinstein and Christer Fureby. Recent progress on miles for high reynolds number flows. *Journal of Fluids Engineering*, 124(4):848–861, 2002.

[88] Nikolaus A Adams. The role of deconvolution and numerical discretization in subgrid-scale modeling. In *Direct and Large-Eddy Simulation IV*, pages 311–320. Springer, 2001.

[89] Fernando F Grinstein, Len G Margolin, and William J Rider. *Implicit large eddy simulation: computing turbulent fluid dynamics*. Cambridge university press, 2007.

[90] Julian A Domaradzki, Ralph W Metcalfe, Robert S Rogallo, and James J Riley. Analysis of subgrid-scale eddy viscosity with use of results from direct numerical simulations. *Physical Review Letters*, 58(6):547, 1987.

[91] Fabian Waleffe. The nature of triad interactions in homogeneous turbulence. *Physics of Fluids A: Fluid Dynamics*, 4(2):350–363, 1992.

[92] Jean-Pierre Chollet and Marcel Lesieur. Parameterization of small scales of three-dimensional isotropic turbulence utilizing spectral closures. *Journal of the Atmospheric Sciences*, 38(12):2747–2757, 1981.

[93] Stefano Cerutti, Charles Meneveau, and Omar M Knio. Spectral and hyper eddy viscosity in high-reynolds-number turbulence. *Journal of Fluid Mechanics*, 421:307–338, 2000.

[94] Vadim Borue and Steven A Orszag. Forced three-dimensional homogeneous turbulence with hyperviscosity. *EPL (Europhysics Letters)*, 29(9):687, 1995.

[95] Kyle Spyksma, Moriah Magcalas, and Natalie Campbell. Quantifying effects of hyperviscosity on isotropic turbulence. *Physics of Fluids*, 24(12):125102, 2012.

[96] Rob JM Bastiaans, CCM Rindt, and AA Van Steenhoven. Experimental analysis of a confined transitional plume with respect to subgrid-scale modelling. *International Journal of Heat and Mass Transfer*, 41:3989–4007, 1998.

[97] Yi Li and Charles Meneveau. Analysis of mean momentum flux in subgrid models of turbulence. *Physics of Fluids: Brief Communications*, 16(9):3483–3486, 2004.

[98] Takashi Ishihara, Kyo Yoshida, and Yukio Kaneda. Anisotropic velocity correlation spectrum at small scales in a homogeneous turbulent shear flow. *Physical Review Letters*, 88(15):154501, 2002.

[99] Sigfried W Haering, Todd A Oliver, and Robert D Moser. Active model split hybrid rans/les. *arXiv preprint arXiv:2006.13118*, 2020.

[100] Shiyi Chen, Zhenhua Xia, Suyang Pei, Jianchun Wang, Yantao Yang, Zuoli Xiao, and Yipeng Shi. Reynolds-stress-constrained large-eddy simulation of wall-bounded turbulent flows. *Journal of Fluid Mechanics*, 703:1–28, 2012.

[101] Linus Marstorp, Geert Brethouwer, Olof Grundestam, and Arne V Johansson. Explicit algebraic subgrid stress models with application to rotating channel flow. *Journal of Fluid Mechanics*, 639:403–432, 2009.

[102] Ronald J Adrian. Conditional eddies in isotropic turbulence. *The Physics of Fluids*, 22(11):2065–2070, 1979.

[103] Ronald J Adrian and Parviz Moin. Stochastic estimation of organized turbulent structure: homogeneous shear flow. *Journal of Fluid Mechanics*, 190:531–559, 1988.

[104] Ronald J Adrian, BG Jones, MK Chung, Yassin Hassan, CK Nithianandan, and AT-C Tung. Approximation of turbulent conditional averages by stochastic estimation. *Physics of Fluids A: Fluid Dynamics*, 1(6):992–998, 1989.

[105] RJ Adrian. Stochastic estimation of sub-grid scale motions. *Applied Mechanics Reviews*, 43(5S):S214–218, 1990.

[106] Athanasios Papoulis. *Probability, Random Variables*. McGraw-Hill, 1965.

[107] Robert D Moser, Nicholas P Malaya, Henry Chang, Paulo S Zandonade, Prakash Vedula, Amitabh Bhattacharya, and Andreas Haselbacher. Theoretically based optimal large-eddy simulation. *Physics of Fluids*, 21(10):105104, 2009.

[108] Antoine Moreau, Olivier Teytaud, and Jean-Pierre Bertoglio. Optimal estimation for large-eddy simulation of turbulence and application to the analysis of subgrid models. *Physics of Fluids*, 18(10):105101, 2006.

[109] Antoine Vollant, Guillaume Balarac, and C Corre. Subgrid-scale scalar flux modelling based on optimal estimation theory and machine-learning procedures. *Journal of Turbulence*, 18(9):854–878, 2017.

[110] Andrea Beck, David Flad, and Claus-Dieter Munz. Deep neural networks for data-driven les closure models. *Journal of Computational Physics*, 398:108910, 2019.

[111] Marcel Lesieur and Robert Rogallo. Large-eddy simulation of passive scalar diffusion in isotropic turbulence. *Physics of Fluids A: Fluid Dynamics*, 1(4):718–722, 1989.

[112] Jacob A Langford and Robert D Moser. Optimal large-eddy simulation results for isotropic turbulence. *Journal of Fluid Mechanics*, 521:273–294, 2004.

[113] S Völker, Robert D Moser, and P Venugopal. Optimal large eddy simulation of turbulent channel flow based on direct numerical simulation statistical data. *Physics of Fluids*, 14(10):3675–3691, 2002.

[114] Paulo S Zandonade, Jacob A Langford, and Robert D Moser. Finite-volume optimal large-eddy simulation of isotropic turbulence. *Physics of Fluids*, 16(7):2255–2271, 2004.

[115] Henry Chang. *Modeling turbulence using optimal large eddy simulation*. PhD thesis, University of Texas at Austin, 2012.

[116] Ryan King, Peter E Hamlington, and Werner Dahm. Autonomic subgrid-scale closure for large eddy simulations. In *53rd AIAA Aerospace Sciences Meeting*, page 1285, 2015.

[117] Noma Park, Jung Yul Yoo, and Haecheon Choi. Toward improved consistency of a priori tests with a posteriori tests in large eddy simulation. *Physics of Fluids*, 17(1): 015103, 2005.

[118] Sandip Ghosal. An analysis of numerical errors in large-eddy simulations of turbulence. *Journal of Computational Physics*, 125(1):187–206, 1996.

[119] AG Kravchenko and Parviz Moin. On the effect of numerical errors in large eddy simulations of turbulent flows. *Journal of Computational Physics*, 131(2):310–322, 1997.

[120] Fotini Katopodes Chow and Parviz Moin. A further study of numerical errors in large-eddy simulations. *Journal of Computational Physics*, 184(2):366–380, 2003.

[121] A Kravchenko, Parviz Moin, Karim Shariff, A Kravchenko, P Moin, and K Shariff. B-spline method and zonal grids for simulations of complex turbulent flows. In *35th Aerospace Sciences Meeting and Exhibit*, page 433, 1999.

[122] Karim Shariff and Robert D Moser. Two-dimensional mesh embedding for b-spline methods. *Journal of Computational Physics*, 145(2):471–488, 1998.

[123] Y Bazilevs, VM Calo, JA Cottrell, TJR Hughes, A Reali, and G Scovazzi. Variational multiscale residual-based turbulence modeling for large eddy simulation of incompressible flows. *Computer Methods in Applied Mechanics and Engineering*, 197 (1-4):173–201, 2007.

[124] Myoungkyu Lee and Robert D Moser. Direct numerical simulation of turbulent channel flow up to $Re_\tau \approx 5200$. *Journal of Fluid Mechanics*, 774:395–415, 2015.

[125] Robert M Corless. Compact finite differences and cubic splines. *arXiv preprint arXiv:1805.07659*, 2018.

[126] Gopal R Yalla, Todd A Oliver, and Robert D Moser. Numerical dispersion effects on the energy cascade in large-eddy simulation. *Physical Review Fluids*, 6(9):L092601, 2021.

[127] Philippe R Spalart, Robert D Moser, and Michael M Rogers. Spectral methods for the Navier-Stokes equations with one infinite and two periodic directions. *Journal of Computational Physics*, 96(2):297–324, 1991.

[128] John Kim, Parviz Moin, and Robert Moser. Turbulence statistics in fully developed channel flow at low reynolds number. *Journal of Fluid Mechanics*, 177:133–166, 1987.

[129] Prakash Mohan, Nicholas Fitzsimmons, and Robert D Moser. Scaling of lyapunov exponents in homogeneous isotropic turbulence. *Physical Review Fluids*, 2(11):114606, 2017.

[130] Steven A Orszag. On the elimination of aliasing in finite-difference schemes by filtering high-wavenumber components. *Journal of the Atmospheric Sciences*, 28(6):1074–1074, 1971.

[131] DC Leslie and GL Quarini. The application of turbulence theory to the formulation of subgrid modelling procedures. *Journal of Fluid Mechanics*, 91(1):65–91, 1979.

[132] Thomas A Zang. On the rotation and skew-symmetric forms for incompressible flow simulations. *Applied Numerical Mathematics*, 7(1):27–40, 1991.

[133] Eitan Tadmor. Skew-selfadjoint form for systems of conservation laws. *Journal of Mathematical Analysis and Applications*, 103(2):428–442, 1984.

[134] GA Blaisdell, ET Spyropoulos, and JH Qin. The effect of the formulation of nonlinear terms on aliasing errors in spectral methods. *Applied Numerical Mathematics*, 21(3): 207–219, 1996.

[135] Claude Cambon, Nagi N Mansour, and Fabien S Godeferd. Energy transfer in rotating turbulence. *Journal of Fluid Mechanics*, 337:303–332, 1997.

[136] Fabian Waleffe. Inertial transfers in the helical decomposition. *Physics of Fluids A: Fluid Dynamics*, 5(3):677–685, 1993.

[137] Donald Coles. The law of the wake in the turbulent boundary layer. *Journal of Fluid Mechanics*, 1(2):191–226, 1956.

[138] Fernando Porté-Agel, Majid Bastankhah, and Sina Shamsoddin. Wind-turbine and wind-farm flows: a review. *Boundary-Layer Meteorology*, 174(1):1–59, 2020.

[139] Gopal R Yalla, Todd A Oliver, Sigfried W Haering, Björn Engquist, and Robert D Moser. Effects of resolution inhomogeneity in large-eddy simulation. *Physical Review Fluids*, 6(7):074604, 2021.

[140] TS Lund. The use of explicit filters in large eddy simulation. *Computers & Mathematics with Applications*, 46(4):603–616, 2003.

[141] Daniele Carati, Grégoire S Winckelmans, and Hervé Jeanmart. On the modelling of the subgrid-scale and filtered-scale stress tensors in large-eddy simulation. *Journal of Fluid Mechanics*, 441:119–138, 2001.

[142] Jessica Gullbrand and Fotini Katopodes Chow. The effect of numerical errors and turbulence models in large-eddy simulations of channel flow, with and without explicit filtering. *Journal of Fluid Mechanics*, 495:323–341, 2003.

[143] Grégoire S Winckelmans, Alan A Wray, Oleg V Vasilyev, and Hervé Jeanmart. Explicit-filtering large-eddy simulation using the tensor-diffusivity model supplemented by a dynamic smagorinsky term. *Physics of Fluids*, 13(5):1385–1403, 2001.

[144] M Germano. Differential filters for the large eddy numerical simulation of turbulent flows. *The Physics of fluids*, 29(6):1755–1757, 1986.

[145] Harmen van der Ven. A family of large eddy simulation (LES) filters with nonuniform filter widths. *Physics of Fluids*, 7(5):1171–1172, 1995.

[146] Oleg V Vasilyev, Thomas S Lund, and Parviz Moin. A general class of commutative filters for les in complex geometries. *Journal of Computational Physics*, 146(1):82–104, 1998.

[147] Alison L Marsden, Oleg V Vasilyev, and Parviz Moin. Construction of commutative filters for les on unstructured meshes. *Journal of Computational Physics*, 175(2):584–603, 2002.

[148] Sanjeeb T Bose, Parviz Moin, and Donghyun You. Grid-independent large-eddy simulation using explicit filtering. *Physics of Fluids*, 22(10):105103, 2010.

[149] S Bose, P Moin, and F Ham. Explicitly filtered large eddy simulation on unstructured grids. *Annual Research Briefs, Center for Turbulence Research*, pages 87–96, 2011.

[150] Julie S Mullen and Paul F Fischer. Filtering techniques for complex geometry fluid flows. *Communications in Numerical Methods in Engineering*, 15(1):9–18, 1999.

[151] Andreas Haselbacher and Oleg V Vasilyev. Commutative discrete filtering on unstructured grids based on least-squares techniques. *Journal of Computational Physics*, 187 (1):197–211, 2003.

[152] B De Laage de Meux, B Audebert, Remi Manceau, and R Perrin. Anisotropic linear forcing for synthetic turbulence generation in large eddy simulation and hybrid RANS/LES modeling. *Physics of Fluids*, 27(3):035115, 2015.

[153] Andrew W Cook and William H Cabot. Hyperviscosity for shock-turbulence interactions. *Journal of Computational Physics*, 203(2):379–385, 2005.

[154] C David Pruett, James S Sochacki, and Nikolaus A Adams. On taylor-series expansions of residual stress. *Physics of Fluids*, 13(9):2578–2589, 2001.

[155] S Stolz, Nikolaus A Adams, and Leonhard Kleiser. An approximate deconvolution model for large-eddy simulation with application to incompressible wall-bounded flows. *Physics of fluids*, 13(4):997–1015, 2001.

[156] Joseph Mathew, Richard Lechner, Holger Foysi, Joern Sesterhenn, and Rainer Friedrich. An explicit filtering method for large eddy simulation of compressible flows. *Physics of fluids*, 15(8):2279–2289, 2003.

[157] JA Domaradzki and Nikolaus A Adams. Direct modelling of subgrid scales of turbulence in large eddy simulations. *Journal of Turbulence*, 3(024):1, 2002.

[158] Robert H Kraichnan. Eddy viscosity in two and three dimensions. *Journal of Atmospheric Sciences*, 33(8):1521–1536, 1976.

[159] Robert H Kraichnan. Inertial-range transfer in two-and three-dimensional turbulence. *Journal of Fluid Mechanics*, 47(3):525–535, 1971.

[160] Jeffrey R Chasnov. Simulation of the kolmogorov inertial subrange using an improved subgrid model. *Physics of Fluids A: Fluid Dynamics*, 3(1):188–200, 1991.

[161] Marcel Lesieur. *Turbulence in fluids: stochastic and numerical modelling*, volume 488. Nijhoff Boston, MA, 1987.

[162] Steven A Orszag. Analytical theories of turbulence. *Journal of Fluid Mechanics*, 41 (2):363–386, 1970.

[163] MD Millionshchikov. On the theory of homogeneous isotropic turbulence. volume 32, pages 611–614, 1941.

[164] PY Chou. On an extension of reynolds' method of finding apparent stress and the nature of turbulence. *Chinese Journal of Physics*, 4(1), 1940.

[165] I Proudman and William Hill Reid. On the decay of a normally distributed and homogenous turbulent velocity field. *Philosophical Transactions of the Royal Society of London. Series A, Mathematical and Physical Sciences*, 247(926):163–189, 1954.

[166] Tomomasa Tatsumi, Shigeo Kida, and Jiro Mizushima. The multiple-scale cumulant expansion for isotropic turbulence. *Journal of Fluid Mechanics*, 85(1):97–142, 1978.

[167] Yoshimitsu Ogura. A consequence of the zero-fourth-cumulant approximation in the decay of isotropic turbulence. *Journal of Fluid Mechanics*, 16(1):33–40, 1963.

[168] Edward E O'Brien and George C Francis. A consequence of the zero fourth cumulant approximation. *Journal of Fluid Mechanics*, 13(3):369–382, 1962.

[169] J Andrzej Domaradzki and Robert S Rogallo. Local energy transfer and nonlocal interactions in homogeneous, isotropic turbulence. *Physics of Fluids A: Fluid Dynamics*, 2(3):413–426, 1990.

[170] JC André and M Lesieur. Influence of helicity on the evolution of isotropic turbulence at high reynolds number. *Journal of Fluid Mechanics*, 81(1):187–207, 1977.

[171] Robert H Kraichnan. Decay of isotropic turbulence in the direct-interaction approximation. *The Physics of Fluids*, 7(7):1030–1048, 1964.

[172] JH Ferziger. Large eddy simulation: an introduction and perspective. In *New tools in turbulence modelling*, pages 29–47. Springer, 1997.

[173] Vadim Borue and Steven A Orszag. Kolmogorov's refined similarity hypothesis for hyperviscous turbulence. *Physical Review E*, 53(1):R21, 1996.

[174] GS Winckelmans, TS Lund, Daniele Carati, and AA Wray. A priori testing of subgrid-scale models for the velocity-pressure and vorticity-velocity formulations. In *Proceedings of the Summer Program*, pages 309–328. Citeseer, 1996.

[175] Grégoire S Winckelmans and Hervé Jeanmart. Assessment of some models for les without/with explicit filtering. In *Direct and Large-Eddy Simulation IV*, pages 55–66. Springer, 2001.

[176] William J Layton. A nonlinear, subgridscale model for incompressible viscous flow problems. *SIAM Journal on Scientific Computing*, 17(2):347–357, 1996.

[177] V Deschamps. Simulation numérique de la turbulence dans un écoulement de canal plan. *La Recherche Aérospatiale*, pages 37–52, 1989.

[178] Vadim Borue and Steven A Orszag. Self-similar decay of three-dimensional homogeneous turbulence with hyperviscosity. *Physical Review E*, 51(2):R856, 1995.

[179] Vadim Borue and Steven A Orszag. Numerical study of three-dimensional kolmogorov flow at high reynolds numbers. *Journal of Fluid Mechanics*, 306:293–323, 1996.

[180] Jean-Pierre Bertoglio. A stochastic subgrid model for sheared turbulence. In *Macroscopic modelling of turbulent flows*, pages 100–119. Springer, 1985.

[181] CE Leith. Stochastic backscatter in a subgrid-scale model: Plane shear mixing layer. *Physics of Fluids A: Fluid Dynamics*, 2(3):297–299, 1990.

[182] Michele Iovieno and Daniela Tordella. Variable scale filtered navier–stokes equations: a new procedure to deal with the associated commutation error. *Physics of Fluids*, 15 (7):1926–1936, 2003.

[183] Sharath S Girimaji and Stefan Wallin. Closure modeling in bridging regions of variable-resolution (vr) turbulence computations. *Journal of Turbulence*, 14(1):72–98, 2013.

[184] C Fureby and G Tabor. Mathematical and physical constraints on large-eddy simulations. *Theoretical and Computational Fluid Dynamics*, 9(2):85–102, 1997.

[185] Fujihiro Hamba. Analysis of filtered navier–stokes equation for hybrid rans/les simulation. *Physics of Fluids*, 23(1):015108, 2011.

[186] GS Winckelmans, Hervé Jeanmart, and Daniele Carati. On the comparison of turbulence intensities from large-eddy simulation with those from experiment or direct numerical simulation. *Physics of Fluids*, 14(5):1809–1811, 2002.

[187] Charles Meneveau. Statistics of turbulence subgrid-scale stresses: Necessary conditions and experimental tests. *Physics of Fluids*, 6(2):815–833, 1994.

[188] Oleg V Vasilyev and Daniel E Goldstein. Local spectrum of commutation error in large eddy simulations. *Physics of Fluids*, 16(2):470–473, 2004.

[189] Lloyd N Trefethen. Group velocity in finite difference schemes. *SIAM Review*, 24(2): 113–136, 1982.

[190] R Vichnevetsky. Energy and group velocity in semi discretizations of hyperbolic equations. *Mathematics and Computers in Simulation*, 23(4):333–343, 1981.

[191] R Vichnevetsky. Group velocity and reflection phenomena in numerical approximations of hyperbolic equations. *Journal of the Franklin Institute*, 315(5-6):307–330, 1983.

[192] R Vichnevetsky. Propagation through numerical mesh refinement for hyperbolic equations. *Mathematics and Computers in Simulation*, 23(4):344–353, 1981.

[193] Robert Vichnevetsky. Wave propagation and reflection in irregular grids for hyperbolic equations. *Applied Numerical Mathematics*, 3:133–166, 1987.

[194] J Frank and S Reich. On spurious reflections, nonuniform grids and finite difference discretizations of wave equations. cwi report mas-e0406. *Center for Mathematics and Computer Science*, 2004.

[195] Uri M Ascher and Robert I McLachlan. Multisymplectic box schemes and the korteweg–de vries equation. *Applied Numerical Mathematics*, 48(3-4):255–269, 2004.

[196] Robert Vichnevetsky. Wave propagation analysis of difference schemes for hyperbolic equations: a review. *International Journal for Numerical Methods in Fluids*, 7(5): 409–452, 1987.

[197] Robert Vichnevetsky and Thomas Scheidegger. The nonlocal nature of internal reflection in computational fluid dynamics with spectral methods. *Applied Numerical Mathematics*, 8(6):533–539, 1991.

[198] Stavros C Kassinos, William C Reynolds, and Mike M Rogers. One-point turbulence structure tensors. *Journal of Fluid Mechanics*, 428:213–248, 2001.

[199] FR Menter and Y Egorov. The scale-adaptive simulation method for unsteady turbulent flow predictions. part 1: theory and model description. *Flow, Turbulence and Combustion*, 85(1):113–138, 2010.

[200] Ugo Piomelli, Elias Balaras, Hugo Pasinato, Kyle D Squires, and Philippe R Spalart. The inner–outer layer interface in large-eddy simulations with wall-layer models. *International Journal of Heat and Fluid Flow*, 24(4):538–550, 2003.

[201] Axel Probst, Dieter Schwamborn, Andre Garbaruk, Ekaterina Guseva, Misha Shur, Mikhail Strelets, and Andrej Travin. Evaluation of grey area mitigation tools within zonal and non-zonal rans-les approaches in flows with pressure induced separation. *International Journal of Heat and Fluid Flow*, 68:237–247, 2017.

[202] Ingrid Daubechies. *Ten lectures on wavelets*. SIAM, 1992.

[203] Nathan Halko, Per-Gunnar Martinsson, and Joel A Tropp. Finding structure with randomness: Probabilistic algorithms for constructing approximate matrix decompositions. *SIAM Review*, 53(2):217–288, 2011.

[204] Pierre Gilles Lemarié-Rieusset. Analyses multi-résolutions non orthogonales, commutation entre projecteurs et derivation et ondelettes vecteurs à divergence nuiie. *Revista Matemática Iberoamericana*, 8(2):221–237, 1992.

[205] Erwan Deriaz and Valérie Perrier. Divergence-free and curl-free wavelets in two dimensions and three dimensions: application to turbulent flows. *Journal of Turbulence*, (7):N3, 2006.

[206] Erwan Deriaz and Valérie Perrier. Direct numerical simulation of turbulence using divergence-free wavelets. *Multiscale Modeling & Simulation*, 7(3):1101–1129, 2009.

[207] Marie Farge. Wavelet transforms and their applications to turbulence. *Annual Review of Fluid Mechanics*, 24(1):395–458, 1992.

[208] Marie Farge and Kai Schneider. Coherent vortex simulation (cvs), a semi-deterministic turbulence model using wavelets. *Flow, Turbulence and Combustion*, 66(4):393–426, 2001.

[209] Naoya Okamoto, Katsunori Yoshimatsu, Kai Schneider, Marie Farge, and Yukio Kaneda. Coherent vortices in high resolution direct numerical simulation of homogeneous isotropic turbulence: A wavelet viewpoint. *Physics of Fluids*, 19(11):115109, 2007.

[210] Daniel E Goldstein and Oleg V Vasilyev. Stochastic coherent adaptive large eddy simulation method. *Physics of Fluids*, 16(7):2497–2513, 2004.

[211] Kai Schneider and Oleg V Vasilyev. Wavelet methods in computational fluid dynamics. *Annual Review of Fluid Mechanics*, 42:473–503, 2010.

[212] Charles Meneveau. Analysis of turbulence in the orthonormal wavelet representation. *Journal of Fluid Mechanics*, 232:469–520, 1991.

[213] Stephane G Mallat. A theory for multiresolution signal decomposition: the wavelet representation. In *Fundamental Papers in Wavelet Theory*, pages 494–513. Princeton University Press, 2009.

[214] Francis H Harlow and J Eddie Welch. Numerical calculation of time-dependent viscous incompressible flow of fluid with free surface. *The Physics of Fluids*, 8(12):2182–2189, 1965.